University of Hamburg

Department of Physics

3D Multimodal X-ray Imaging of a Microchip: Correlating Structure, Composition and Orientation at the Nanoscale

Dissertation

zur Erlangung des akademischen Grades

Doctor rerum naturalium (Dr. rer. nat.)

an der Fakultät für Mathematik, Informatik und Naturwissenschaften
– Fachbereich Physik –
der Universität Hamburg

vorgelegt von
Katrin **Maria Scholz**
(geb. 23.02.1985 in Großenhain)

Hamburg
2020

The work described in this thesis is done at the Photon Science division of
Deutsches Elektronen-Synchrotron, a Research Centre of the Helmholtz Association.

Gutachter/in der Dissertation:	Prof. Dr. Christian G. Schroer
	Dr. habil. Thomas Keller
Zusammensetzung der Prüfungskommission:	Prof. Dr. Daniela Pfannkuche
	Prof. Dr. Dorota Koziej
	Prof. Dr. Markus Drescher
	Dr. habil. Thomas Keller
	Prof. Dr. Christian G. Schroer
Vorsitzende/r der Prüfungskommission:	Prof. Dr. Daniela Pfannkuche
Datum der Disputation:	08.03.2021
Vorsitzender des Fach-Promotionsausschusses PHYSIK:	Prof. Dr. Günter Hans Walter Sigl
Leiter/in des Fachbereichs PHYSIK:	Prof. Dr. Wolfgang Hansen
Dekan/in der Fakultüt MIN:	Prof. Dr. Heinrich Graener

Für meinen Vati, Peter Scholz,
der auch schon für weitaus weniger
wahnsinnig stolz auf uns Kinder gewesen wäre.
Danke für alles.

For my dad, Peter Scholz,
who would have been incredibly
proud of us children for a lot less.
Thanks for everything.

Abstract

With the fast technological developments of our time often new possibilities arise to gain a deeper scientific understanding of complex processes, may these be of biological, chemical or physical nature, and materials. In natural sciences, X-ray and electron microscopy is indispensable to help uncovering these scientific backgrounds. Sophisticated microscopy methods with spatial resolutions in the nanometer range allow us to gain new insights about relations and function principles.

One example in this regard is nanotechnology continuously pushing the physical limits to build smaller structures such as transistors in microchips, thereby enhancing computing power while simultaneously lowering energy consumption of current devices. Without microchips, all these possibilities just as much as the many everyday things and gadgets of modern life would be unthinkable. Therefore, in the manufacture of these semiconductor products troubleshooting and controlling of the manufacturing processes and the resulting structures gain great attention. With continuously decreasing structure sizes, the analysis options of these manufactories reach their limits in some aspects.

Examinations using high-brilliance X-rays offer a variety of complementary analysis opportunities. Electron microscopy is commonplace in semiconductor factories [1], but it only images surfaces or transmits thin samples, partially demanding for precise preparation including destruction. Due to the high penetration depth of X-rays in matter, the usage of X-ray ptychography provides new insights into the produced microchips as comparably thick samples can be investigated with resolutions in the nanometer range.

In this thesis, the potential of imaging even the smallest structures inside a microchip is demonstrated on the example of a test chip. In addition, X-ray fluorescence helps determine the elemental composition and X-ray diffraction provides information about the crystalline states of various components. These procedures were all applied in a multimodal experiment. Through the evaluation of X-ray diffraction data using powder X-ray diffraction methods, the phases of crystalline materials are precisely determined. The diffraction data is furthermore used to determine the position, size and orientation of single grains inside the microchip. The combination with computed tomography allows for spatial assignment of these information to the internal structures and can thus point to function and structure relations.

The interplay of the various X-ray techniques provides a complementary picture of the inside of a microchip, the spatial resolution of structures, their composition, crystalline phase and orientation. It opens up new perspectives for both the investigation and development of microchips as well as of other composite solids made of different materials and crystalline states. It also offers prospects for the expansion of these investigations, for example by additional contrasts such as X-ray ptychography or visualizing active conduction.

Kurzfassung

Mit den schnellen technologischen Entwicklungen unserer Zeit offenbaren sich stets neue Möglichkeiten, verschiedene komplexere Prozesse, seien diese biologischer, chemischer oder physikalischer Natur, und Materialien besser zu verstehen. In den Naturwissenschaften sind Röntgen- und Elektronenmikroskopie dabei unverzichtbare Hilfsmittel. Hochentwickelte mikroskopische Verfahren mit Auflösungen im Nanometerbereich ermöglichen es uns, neue Kenntnisse über Zusammenhänge und Funktionsprinzipien zu gewinnen.

Ein Beispiel dafür ist Nanotechnologie, welche kontinuierlich an physikalische Grenzen stößt, um immer kleinere Strukturen wie Transistoren in Mikrochips zu bauen und dabei Rechenleistung verbessert. Gleichzeitig wird der Energieverbrauch gegenwärtiger Bauelemente gesenkt. Ohne Mikrochips wären all diese Möglichkeiten ebenso wie viele alltägliche Dinge des modernen Lebens undenkbar. Darum wird in der Herstellung dieser Halbleiterprodukte ein großes Augenmerk auf die Fehlersuche und die Kontrolle der Fertigungsprozesse sowie der entstandenen Strukturen gelegt. Mit den stetig kleiner werdenden Strukturen stoßen die Analysemöglichkeiten der Hersteller in mancher Hinsicht an ihre Grenzen.

Untersuchungen mithilfe hochbrillanter Röntgenstrahlung bieten eine Vielfalt ergänzender Untersuchungsmöglichkeiten. In Halbleiterfabriken ist Elektronenmikroskopie im täglichen Gebrauch [1], aber damit können nur Oberflächen oder sehr dünne Proben untersucht werden, was teilweise präziser Probenpräparation bedarf, welche nicht zerstörungsfrei umsetzbar ist. Neben elektronenmikroskopischen Abbildungen, wie sie bereits in Halbleiterfabriken alltäglich sind, sorgt auch die ptychographische Bildgebung dank der hohen Eindringtiefe von Röntgenstrahlen in Materie für neue Einblicke mit Auflösungen im Nanometerbereich an vergleichsweise dicken Proben.

Das Potential dieser Verfahren wird in dieser Arbeit an dem Beispiel eines Testchips demonstriert. Darüber hinaus hilft die Röntgenfluoreszenz, die elementare Zusammensetzung zu bestimmen, so wie die Röntgenbeugung Aufschluss über kristalline Zustände verschiedener Komponenten gibt. Diese Verfahren wurden in einem multimodalen Experiment angewandt und ausgewertet. Durch die Auswertung von Röntgenbeugungsdaten mit Pulveranalyseverfahren werden die Phasen der kristallinen Materialien genau bestimmt. Die Beugungsdaten dienen zudem auch der Ermittlung von Position, Größe und Orientierung von einzelnen Körnern im Mikrochip. In der Verbindung mit Computertomographie werden diese Infomationen den inneren Strukturen räumlich zugeordnet und können so Hinweise auf Funktion und Zusammenhänge der Beschaffenheit der Strukturen geben.

Das Zusammenspiel der verschiedenen Röntgentechniken liefert ein sich ergänzendes Bild über die Strukturen im Inneren eines Mikrochips, ihre räumliche Auflösung, ihre chemische Zusammensetzung, deren kristalline Phasen und Orientierung.

Außerdem eröffnet es neue Perspektiven sowohl für die Untersuchung und Entwicklung von Mikrochips als auch von anderen zusammengesetzten Festkörpern aus verschiedenen Materialien und kristallinen Zuständen. Das Vorgehen bietet Perspektiven für den Ausbau dieser Untersuchungsmöglichkeiten, beispielsweise um weitere Kontraste wie der Röntgenptychographie oder um die Abbildung aktiver Leitungsvorgänge.

Contents

CHAPTER 1

Introduction

The pursuit of knowledge as a basic endeavor of mankind enabled the way we live today and the development in all fields of life will always continue. This is especially true for all the technical possibilities which we use in our daily lives, most notably in natural science, medicine, security, transport and communication.

Over the course of less than 100 years, the electron microscope was developed (1931) [2, 3], synchrotron radiation was predicted (1944) [4] and discovered (1946) [5] and microchips were invented (1958) [6]. All these three achievements underwent tremendous development while their actual usage gained currency.

Nowadays, microchips are not only present in computers and smartphones, but in a number of devices that we rely on everyday. To get a glimpse of the fields of application, the automotive industry is picked as an example. Modern cars depend on information from many sensors about the state of diverse components, such as air pressure in wheels. But also the entertainment system, electronic driver assistance, electronic windows, windscreen wipers, light and, more importantly, all the safety arrangements, such as air bags and anti-lock break system (ABS), rely on functioning sensors and microchips [7]. Failures of these devices in the wrong moment can be an issue of life and death. For that reason, the semiconductor industry has strict controlling strategies and continuous monitoring of all production processes and devices. The factories keep their laboratory control equipment up to date, but are limited in their physical possibilities. While structure sizes on microchips steadily decrease, the spatial resolution and capabilities of electron and X-ray microscopy improved down to the nanometer and atomic regime allowing for deep insights in structure and functionality.

Current developments in electron microscopy allow for insights with resolutions on the nanometer and atomic scale [8, 9] and destructive imaging of a sample in a slice-and-view procedure [10–12]. To image inner structures non-destructively, X-rays with their high penetration depth in matter have huge potential. The advent of synchrotron radiation experiments opened up new possibilities and allowed for significantly faster data acquisition and higher resolutions than using laboratory X-ray tubes.

Another advantage of synchrotron radiation over table top systems is the high amount of coherence of X-rays. Based on coherent rays, the imaging technique ptychography was invented for electron microscopy [13]. With the work from Faulkner and Rodenburg [14] and Thibault et al. [15] this phase retrieval algorithm found the way into X-ray microscopy and developed quickly to a powerful imaging technique. Henceforth, the spatial resolution of the image obtained by ptychography is independent of the illuminating beam size.

Spatial resolutions of 50 nm to 100 nm are commonplace, but in recent years many publications show the trend to even better spatial resolutions [16–18] with continuing improvement achieved by different corrections, such as background [19, 20] and position corrections [21, 22], and broadening the fields of application.

All the progress in ptychography is supported by the availability of a variety of X-ray optics. The development of nanofocusing X-ray optics enabled focusing down to the nanometer range. Another field of application is direct imaging using different physical contrast mechanisms, for example X-ray fluorescence and X-ray absorption.

In addition, X-ray diffraction (XRD) is another X-ray signal that can be measured in parallel in scanning X-ray microscopy, opening up another wide variety of applications. In the context of this work, XRD was used for static material analysis and splits into powder diffraction based methods and grain analyses. Powder diffraction is used to determine crystalline phases, strain, texture and average crystallite sizes [23, 24]. The grain analyses focus on grain reconstruction, grain growth and strain mapping [25, 26]. The method for grain analysis is called Scanning 3D XRD, which goes back to the work from Poulsen [27]. Typically, for these analyses, the samples have a diameter of several micrometers and are sampled by a sub-micrometer beam [25, 26]. The trend, however, goes towards even smaller X-ray beams and higher sampling.

This thesis benefits from the current developments of electron as well as of X-ray microscopes and different X-ray methods and applies these to a state-of-the-art microchip. A microchip as nanoelectronic device is a complex integrated circuit embedded in insulating material. It consists of different materials in well defined shapes and at multiple length scales and thus provides different physical properties to be analyzed from different perspectives. Due to the diversity of its physical properties, the microchip is representative of a wide variety of samples, as the applied methods are not limited to analysis of this kind of sample.

The work is a methodological project with the intent to establish scanning X-ray microscopy at synchrotron radiation sources as another tool to precisely characterize nano-fabricated electronic devices and to push forward the development of multimodal X-ray experiments, which enables us to investigate the structure of matter from different perspectives.

In this context, the word multimodal is used for the combination and simultaneous application of complementary techniques, which are X-ray absorption (XRA), X-ray fluorescence (XRF) and X-ray diffraction (XRD). The aim of a multimodal experiment is the correlation of diverse information about the sample, such as chemical composition and crystallinity, and the precise spatial localization of these properties. Additionally, all the information from the different contrasts that are measured simultaneously are inherently aligned and therefore easier to correlate and to compare. With the results of each individual technique, we can draw conclusions about the density of the different structures and their elemental distribution inside the sample, about their crystallinity and about the crystal phases, grain locations and sizes. This allows us to spatially correlate the components in the sample obtained from X-ray fluorescence measurements with the atomic structure obtained from crystallographic information.

Another benefit of the simultaneity is the economy of time in comparison to a conventional experimental scheme taking one measurement after another. For that, it is advantageous that the chosen methods can be combined within the same experimental setup.

This thesis is structured as follows: A theoretical introduction of the interaction between X-rays and matter is given in Chapter 2. The applied methods X-ray ptychography, X-ray tomography, as well as two 3D XRD methods with a focus on powder and grains are introduced in Chapter 3. The main part was conducted at the PtyNAMi setup at beamline P06 (PETRA III, DESY) and the experimental setup is described in Chapter 4. As all experiments within this work used the same microchip, Chapter 5 provides a coarse background on microchip manufacturing and the structures within a microchip.

The first experimental aspect of this thesis is high-resolution imaging of the sample using the X-ray ptychography and electron microscopy combined with a focused ion beam to create cross sections in order to cut a piece out of the chip for further analysis, see Chapter 6. State-of-the-art imaging techniques, giving insights about the surface or even the inner structures of a sample, reach spatial resolutions in the tens of nanometers. With their high penetration depth, X-rays have an advantage over electrons regarding spatial analysis of inner structures. Nevertheless, the spatial resolution in electron microscopy is still higher, and provides complementary information of the microchip.

The second and larger part of this thesis is about the multimodal tomographic experiment. The experiment itself is described in Chapter 7. The data recording was done simultaneously for XRA, XRF and XRD in a step scan mode consisting of a raster grid for each discrete sampled angular projection. Compared to usual XRD experiment, the scanning scheme is altered to a discrete angular sampling compared to continuously integrated data. The analysis is split into the individual parts of XRA, XRF and XRD, which are all described in detail in Chapter 8. XRD delivered a variety of information, such as the crystalline phases, some strain and texture and also the orientation, location and size of individual grains. All results are spatially assigned and visualized in 3D views. Finally, the individual results of the multimodal experiment are correlated and compared. Chapter 9 draws final conclusions on the results and provides an outlook for prospective experiments in this field.

This work addresses the implementation of the multimodal characterization of nanoelectronic devices at a synchrotron radiation source and emphasizes the potential of high-resolution imaging techniques to gain additional insights on structure properties. The results leave room for further multimodal X-ray experiments with a nanofocused beam using additional contrasts or even operando studies. Furthermore, the successful grain reconstruction opens up new fields for 3D XRD and shows that this method is robust enough to cover a slightly altered scanning scheme.

Beyond that, with the upgrade of the 3rd generation synchrotron radiation source PETRA III to PETRA IV, experiments as presented in this thesis will benefit significantly from higher flux per area and higher coherence. A combination of the applied multimodal experiment with the high-resolution imaging technique ptychography would not need any trade-off between these two parameters. Additionally, exposure times per scan point can be reduced and spatial resolutions will further increase.

CHAPTER 2

Propagation and Interaction of X-rays

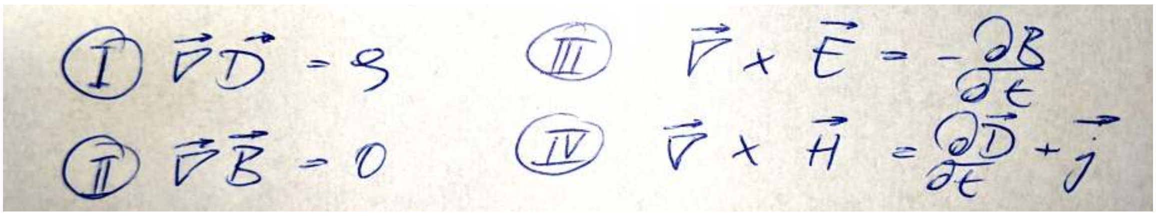

Ⓘ $\vec{\nabla}\vec{D} = \rho$ ⒾⅡ $\vec{\nabla} \times \vec{E} = -\frac{\partial B}{\partial t}$

Ⓘⅰ $\vec{\nabla}\vec{B} = 0$ ⒾⅤ $\vec{\nabla} \times \vec{H} = \frac{\partial \vec{D}}{\partial t} + \vec{j}$

X-rays are both electromagnetic waves and particles. Hence, with wavelengths λ in the range of 0.1 Å to 100 Å, this kind of radiation aligns between ultraviolet and gamma rays in the electromagnetic spectrum. However, the boundaries of X-rays to these latter rays are not clearly defined.

X-rays are called photons – as is visible light – when they are considered as particles. These particles have an energy $\hbar\omega$ and a momentum $\hbar\vec{k}$, where $\hbar = h/(2\pi)$ is the reduced Planck constant, containing the Planck constant h.

Commonly, in classical electrodynamics and literature about waves and optics, the derivation of electromagnetic waves, $\vec{E}$ and $\vec{B}$, starts with the four Maxwell equations [28]. Detailed explanation about this can be found in Jackson [29], Hecht [30], and Born and Wolf [31]. A simplified way to describe both $\vec{E}$ and $\vec{B}$ is a complex scalar wave

$$\Psi(\vec{r}, t) = \frac{1}{\sqrt{2\pi}} \int_0^\infty \psi_\omega(\vec{r}) e^{i\omega t} \mathrm{d}\omega \tag{2.1}$$

with the single spectral component $\psi_\omega(\vec{r})$ [32]. The wave field depends on space and time $(\vec{r}, t)$. Also are the spectral components $\psi_\omega(\vec{r})$ solutions to the Helmholtz equation, including the angular frequency ω and the speed of light c (in vacuum):

$$(\nabla^2 + k^2)\psi_\omega(\vec{r}) = 0, \quad \text{with wave number} \quad k = \frac{\omega}{c}. \tag{2.2}$$

Within the scope of this thesis, we take advantage of both wave and particle character of the X-rays. For this reason, we will have a closer look at the interaction processes of X-rays with matter, such as scattering, absorption and phase shift.

Furthermore, a short overview about the required coherence properties of the rays is given at the end of this chapter.

2.1 Wave Propagation

An essential part of X-ray experiments is the propagation of waves as carriers of information before and after any interaction with matter. In the propagation of a wave front in free space, each single point of a primary wave front itself is the source of a secondary wave and the wave front at a later time t is the envelope of these secondary waves [30, Chapter 4]. This description is called the *Huygens-Fresnel principle*. The propagation of the wave front $\Psi_0(\vec{r}_0)$ starting at $\vec{r}_0$ and propagating along $\vec{r}$ to $\vec{r}\,'$ with an angle θ towards the optical axis x, the horizontal direction y and the vertical direction z is described by

$$\Psi'(y',z') = -\frac{\mathrm{i}k}{4\pi}\iint \Psi_0(y_0,z_0)\frac{\exp\left(\mathrm{i}kr\right)}{r}\cos\theta\,\mathrm{d}y_0\mathrm{d}z_0, \tag{2.3}$$

with

$$r = \sqrt{(x'-x_0)^2+(y'-y_0)^2+(z'-z_0)^2}, \quad \text{and} \quad k = \frac{2\pi}{\lambda}. \tag{2.4}$$

The relevant sizes are visualized in Fig. 2.1.

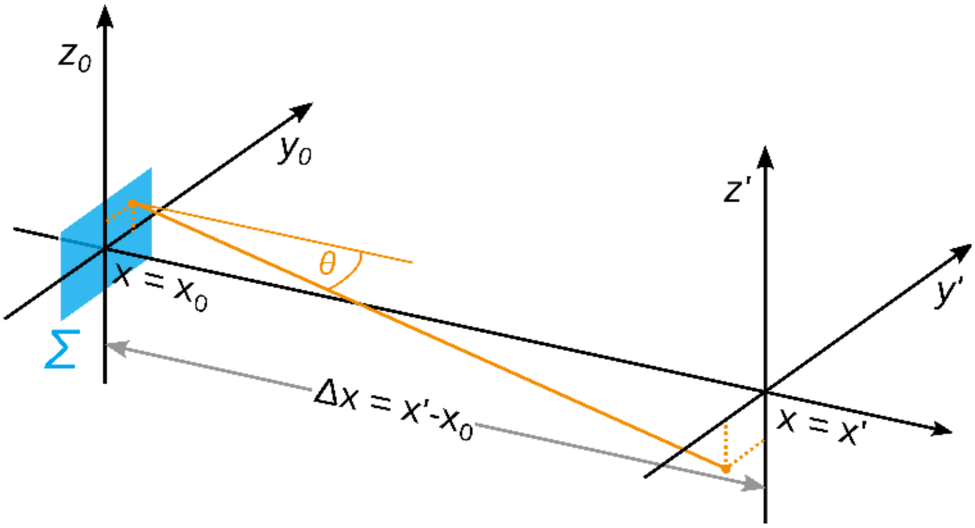

Figure 2.1: Wave propagation from the diffraction plane (y,z) with aperture Σ [33] at $x = x_0$ by Δx to the observation plane $x = x'$.

The writing of the following derivation was influenced by the works from Goodman [34], Reinhardt [35], Seiboth [33] and Kahnt [36].

For propagations over a long distance Δx in comparison to the aperture size Σ of a wave front at the starting point $x = 0$, the X-rays are approximated being paraxial $\cos(\theta \approx 0) \approx 1$. r is adjusted to this situation and the square root is binomially expanded around Δx until the second order term

$$r \approx \Delta x + \frac{(y'-y_0)^2}{2\Delta x} + \frac{(z'-z_0)^2}{2\Delta x}. \tag{2.5}$$

In the denominator of Eq. (2.3), the expansion of r is aborted after the first term according to the Fresnel approximation, but is considered until the second order term in the exponent in Eq. (2.3)

[35]:

$$\Psi'(y',z') = -\frac{\mathrm{i}k}{4\pi}\frac{e^{ik\Delta x}}{\Delta x}\iint \Psi_0(y_0,z_0)e^{\frac{ik}{2\Delta x}[(y'-y_0)]^2+[(z'-z_0)]^2}dy_0dz_0, \tag{2.6}$$

With the assumption that the aperture Σ is finite, the last equation can be rewritten as:

$$\Psi'(y',z') = \iint \Psi_0(y_0,z_0)\cdot P_{\Delta x}(y'-y_0,z'-z_0)dy_0dz_0, \tag{2.7}$$

$$\Psi'(y',z') = \Psi_0(y_0,z_0) * P_{\Delta x}(y',z'), \tag{2.8}$$

which is the expression of the wave function as convolution with the Fresnel operator $P_{\Delta x}(y_0,z_0)$ for propagations over a distance Δx, with

$$P_{\Delta x}(y',z') = -\frac{\mathrm{i}k}{4\pi}\frac{e^{ik\Delta x}}{\Delta x}e^{\frac{ik}{2\Delta x}\left(y'^2+z'^2\right)}. \tag{2.9}$$

Additionally, the quadratic terms in Eq. (2.5) can be expanded, which changes Eq. (2.6) to

$$\Psi'(y',z') = -\frac{\mathrm{i}k}{4\pi}\frac{e^{ik\Delta x}}{\Delta x}e^{\frac{ik}{2\Delta x}\left(y'^2+z'^2\right)}\iint \Psi_0(y_0,z_0)e^{\frac{ik}{2\Delta x}\left(y_0^2+z_0^2\right)^2}e^{\frac{ik}{\Delta x}\left(y'y_0+z'z_0\right)}dy_0dz_0. \tag{2.10}$$

The discussed formalism is valid for small distance propagation $\Delta x \lesssim kD^2$ with the diameter D of the aperture Σ [33, 36], which is called Fresnel approximation. A stronger approximation, the Fraunhofer approximation, stands for propagations into the far field and is defined as

$$\Delta x \gg \frac{k(y_0^2+z_0^2)_{max}}{2}. \tag{2.11}$$

This leads to the following expression of the wave field, the *Fraunhofer diffraction*:

$$\Psi'(y',z') = -\frac{\mathrm{i}k}{4\pi}\frac{e^{ik\Delta x}}{\Delta x}e^{\frac{ik}{2\Delta x}\left(y'^2+z'^2\right)}\iint \Psi_0(y_0,z_0)e^{\frac{ik}{2\Delta x}\left(y_0^2+z_0^2\right)}e^{\frac{ik}{\Delta x}\left(y'y_0+z'z_0\right)}dy_0dz_0. \tag{2.12}$$

Within the Fraunhofer approximation, the quadratic phase function $\exp\left[\frac{ik}{2\Delta x}\left(y_0^2+z_0^2\right)\right]$ goes to 1. Furthermore, with the introduction of the far-field operator $A_{\Delta x}$ [35], defined as

$$A_{\Delta x}(y',z') = -\frac{\mathrm{i}k}{4\pi}\frac{e^{ik\Delta x}}{\Delta x}e^{\frac{ik}{2\Delta x}\left(y'^2+z'^2\right)} \tag{2.13}$$

it is obvious that Eq. (2.12) is a Fourier transform with an additional factor

$$\Psi'(y',z') = A_{\Delta x}(y',z')\iint \Psi_0(y_0,z_0)e^{\frac{ik}{\Delta x}\left(y'y_0+z'z_0\right)}dy_0dz_0. \tag{2.14}$$

Further detailed descriptions can be found in handbooks such as Als-Nielsen and McMorrow [37] as a general overview about X-ray creation at large scale facilities and the possible experiments. For a more theoretical approach to the description of electromagnetic waves, their propagation and interaction with matter, the books of Goodman [34], Paganin [32], Jackson [38] as well as Born and Wolf [31] are suggested.

2.2 Interaction of X-rays with Matter

As Als-Nielsen and McMorrow describe in their book [37], there are two ways of interaction: an X-ray photon can be scattered or absorbed. This, with a closer look, includes refraction and reflection, which occur at interfaces of a material in vacuum or between different materials. These physical principles are the basis for all experiments and contrasts used in this project.

For the fundamental understanding of the principles of X-rays interacting with matter, a brief introduction is given with scattering from a single electron and from a crystal, based on the description by Als-Nielsen and McMorrow [37, Chapter 1] and the thesis of A. Lyckegaard [39, Chapter 2].

2.2.1 Scattering at a Single Atom

In terms of scattering, the electrons of an atom are described by the electron distribution $\rho(\vec{r})$. The incident wave with direction $\vec{k}_i$ scatters from the atom to the scattered direction $\vec{k}_s$, see Fig. 2.2a. In the case of elastic scattering, which is assumed in this consideration, $|\vec{k}_i| = |\vec{k}_s| = 2\pi/\lambda$. Furthermore, the scattering vector, alias momentum transfer, is described by $\vec{Q} = \vec{k}_i - \vec{k}_s$, and

$$|\vec{Q}| = 2|\vec{k}_i|\sin\theta = \frac{4\pi}{\lambda}\sin\theta. \tag{2.15}$$

The scattering of the wave at two volume elements, one at the origin and one at $\vec{r}$ causes the phase difference $\Delta\phi(\vec{r}) = \vec{Q}\cdot\vec{r}$. The scattering from the whole atom is described by an integral over the whole electron distribution with infinitesimal volume elements, resulting in the atomic form factor for a single atom:

$$f^0(\vec{Q}) = \int \rho(\vec{r})\,\mathrm{e}^{i\vec{Q}\vec{r}}d\vec{r}. \tag{2.16}$$

This equation shows that the scattering can be described by a simple Fourier transform, corresponding to considerations in the far field. This atomic form factor is extended by the dispersion corrections $f'(\hbar\omega)$ and $f''(\hbar\omega)$, which lead to the following equation.

$$f(\vec{Q},\hbar\omega) = f^0(\vec{Q}) + f'(\hbar\omega) + if''(\hbar\omega) \tag{2.17}$$

The correction terms themselves depend on the energy of the incoming X-rays and are valid for all $\vec{Q}$ values. The first correction term $f'(\hbar\omega)$ applies to the real part of the form factor and the second term $f''(\hbar\omega)$ is an imaginary correction, which is related to the absorption of the X-rays by the atom.

Materials with randomly distributed atoms, ions or molecules without any repeating structure over a recognizable range in three dimensions are called amorphous or non-crystalline.

For amorphous materials the visibility of scattering effects decrease with increasing $\vec{Q}$. Thus, in their analysis, the forward direction is of greater interest. More details to refraction effects follow in Sec. 2.2.3.

In comparison to that, when X-rays scatter at crystals, the scattering effects are enhanced by diffraction.

2.2.2 Scattering at a Crystal

Before scattering at a crystal can be discussed, the basic principle of a crystal needs to be introduced. Crystalline materials can be characterized by their lattice, a periodic arrangement of atoms in all three dimensions over a long range. A distinction in crystalline materials is made by their undisturbed range. Materials showing order over long distances in three-dimensions are monocrystalline, while the formation of crystallites with arbitrary orientations, also known as grains, is described by polycrystalline materials or powder[1] [40, Chapter 1].

2.2.2.1 Laue Diffraction

The crystal lattice as discrete periodic structure, which follows a discrete translational symmetry, is described by the Bravais lattice [41]. The smallest repeating subset of the lattice is the unit cell. It can consist of a single atom, ions or molecules in its basis described by the j atoms at their position $\vec{r}_j$. With the length of the cell edges (a, b, c) and the internal angles between these (α, β, γ), the unit cell describes the full symmetry of the crystal.

The Bravais lattice in real space, see Fig. 2.2b, pointing from the origin to another unit cell is described by

$$\vec{R}_n = u\vec{a} + v\vec{b} + w\vec{c} \tag{2.18}$$

with the lattice vectors $\vec{a}$, $\vec{b}$ and $\vec{c}$ as well as integers u, v and w. Further information on different configurations of unit cells, leading to 14 different Bravais lattices, as well as on the 230 space groups, caused by symmetry operations applied to the Bravais lattices, can be found in the Fundamentals of Crystallography [42].

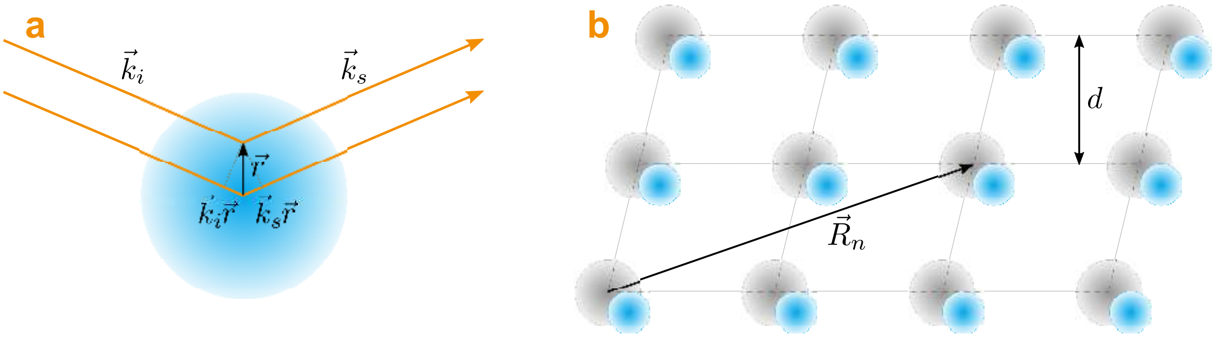

Figure 2.2: Scattering from (a) a single atom and from (b) a crystal. The incoming X-rays, see (a) with wave vector $\vec{k}_i$ scatter in direction $\vec{k}_s$. The scattering at two positions, the origin and $\vec{r}$ causes a phase difference $(\vec{k}_i - \vec{k}_s) \cdot \vec{r}$. In this example (b), the basis of the crystal unit cell consists of two atoms and the lattice plane spacing is d. Different unit cells are addressed by $\vec{R}_n$.

In this thesis only polycrystalline materials with small crystals are analyzed. For that reason, only the kinematic approximation, also known as first Born approximation [43], is relevant and dynamic effects, which are extinction and multiple reflection, can be neglected.

To continue the considerations of the scattering at a single atom, for a crystal with j atoms in the basis, first, the unit cell itself is considered. The continuous electron distributions of all j single

---

[1] In powder diffraction, the word ”powder” is used for solid substances, ceramics, glass and others equally. The crucial criteria are number and size of the individual crystallites.

atoms in the basis are discretely summed up to

$$F^{unit\,cell}(\vec{Q}) = \sum_{\vec{r}_j} f_j(\vec{Q})\, \mathrm{e}^{i\vec{Q}\vec{r}_j}, \tag{2.19}$$

including a correction of phase differences for the scattering at each atom [39, Chapter 2]. This is called the unit cell structure factor.

The transition from a single unit cell to a crystal is realized by periodicity. Subsequently, the position of any atom in a crystal is described by $\vec{R}_n + \vec{r}_j$:

$$F^{crystal}(\vec{Q}) = \underbrace{\sum_j f_j(\vec{Q})\, \mathrm{e}^{i\vec{Q}\vec{r}_j}}_{\text{unit cell}} \underbrace{\sum_n \mathrm{e}^{i\vec{Q}\vec{R}_n}}_{\text{lattice}} \tag{2.20}$$

Only when the second sum fulfills the following equation, it will be different from zero:

$$\vec{Q} \cdot \vec{R}_n = 2\pi n, \quad n \in \mathbb{Z} \tag{2.21}$$

The latter Equation requires the introduction of the reciprocal lattice. Comparable to real space, the lattice in reciprocal space is spanned by reciprocal lattice vectors ($\vec{a}^*$, $\vec{b}^*$, $\vec{c}^*$) and a set of integers, called the Miller indices (h, k, l), shortened to (hkl). Equally to the lattice vector Eq. (2.18) in real space, the $\vec{G}$ vector points to any lattice point in reciprocal space.

$$\vec{G}_{(hkl)} = h\vec{a}^* + k\vec{b}^* + l\vec{c}^* \tag{2.22}$$

The combination of Equations (2.18), (2.22) and $\vec{a} \cdot \vec{a}^* = 2\pi$ leads to the product of a lattice vector in real (R_n) and reciprocal ($\vec{G}$) space.

$$\vec{G}_{(hkl)}\vec{R}_n = 2\pi(hu + kv + lw) = 2\pi n, \quad n \in \mathbb{Z} \tag{2.23}$$

The comparison of the last equation with Eq. (2.21) gives:

$$\vec{Q} = \vec{G}_{(hkl)}, \tag{2.24}$$

which is also known as Laue condition and is equivalent to Bragg's law, see following section.

2.2.2.2 Bragg Reflection

The analysis of crystalline material – may it be monocrystalline or polycrystalline in a bulk or provided as powder of small crystallites – follows the law of Bragg:

$$n\lambda = 2d \sin\theta. \tag{2.25}$$

In this case, d describes the displacement between atomic planes, while θ is the angle between such a plane and the direction of the incident or outgoing rays. The λ in this equation outlines the dependency of this law on the wavelength, respectively energy.

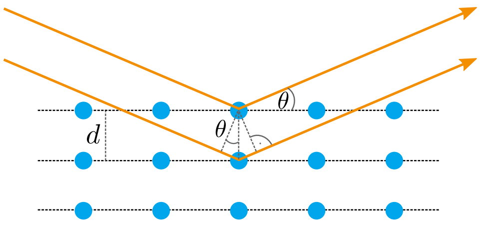

Figure 2.3: Bragg reflection. X-rays impinge on the crystal under θ and are reflected at a lattice plane. The path difference of two such rays determines their interference.

The outgoing waves interfere with each other. Depending on the path difference of these waves, the interference can be constructive ($n = 1, 2, 3, \dots$) or destructive ($n = 1/2, 3/2, 5/2, \dots$). The idea of interference of monochromatic X-rays at crystals goes back to Max von Laue, who pointed out that atoms in a crystal are arranged on a periodic lattice with very small distances between the lattice planes, called lattice constant.
The connection between the Laue condition and the law of Bragg is based on the lattice planes.

A (hkl) triplet describes a plane family, to which the $\vec{G}_{(hkl)}$ is perpendicular. The distance d between the planes can be calculated by a point in the plane, with respect to the origin, described by a lattice vector divided by a Miller index $\vec{a}/h$ multiplied by the normal vector on the planes $\vec{n} = \vec{G}_{(hkl)}/|\vec{G}_{(hkl)}|$:

$$d = \frac{\vec{a}}{h} \cdot \vec{n} = \frac{\vec{a}}{h} \cdot \frac{\vec{G}_{(hkl)}}{|\vec{G}_{(hkl)}|} = \frac{2\pi}{|\vec{G}_{(hkl)}|}. \tag{2.26}$$

By replacing $|\vec{G}_{(hkl)}|$ by $|\vec{Q}|$ and using Eq. (2.15), the vectorized Laue condition changes to the scalar Bragg's law [39, Chapter 2]:

$$d = \frac{2\pi}{|\vec{Q}|} = \frac{2\pi}{(4\pi/\lambda)\sin\theta} = \frac{\lambda}{2\sin\theta} \Leftrightarrow \lambda = 2d\sin\theta \tag{2.27}$$

2.2.2.3 Influence of Strain on Bragg Condition

The deviation of the scattering angles of crystal material from the corresponding literature values can have different causes. A main reason is that this material underlies some strain. It could either be stretched, compressed or deformed by some shear. To determine a deviation, the scattering angles θ of reflexes are measured and compared to literature values

$$\Delta\theta = -\varepsilon \cdot \tan(\theta), \tag{2.28}$$

where ε is the strain and is determined by

$$\varepsilon = \frac{d - d_0}{d_0} \tag{2.29}$$

with d_0 being the ideal d_{hlk} and d being the deviating d_{hkl}. Based on the determined strain, the stress is calculated by Hooke's law:

$$\sigma = E \cdot \varepsilon, \tag{2.30}$$

where E is the tensile module.
Other strain considerations, such as micro strain, which is usually determined by analyzing the peak broadening, were not part of this project.
Furthermore, crystallites can arrange in preferential directions. In this case, all reflections from

different crystallites accumulate in specific regions η in the diffraction pattern. These preferential directions indicate some texture in the material. There will be no detailed studies on texture in this thesis, but detailed information can be found for example in Bunge [44], Wenk and Grigull [45] or He [46].

2.2.3 Complex Refractive Index

Materials can be studied using X-rays in other ways than by diffraction. Especially for experiments including reflection and refraction, the complex refractive index is required. It is material specific and frequency dependent, which results from further considerations of Eq. (2.17) around $\vec{Q} = 0$. In this regime, $f^0(\vec{Q})$ is close to the atomic number Z, while the energy, or equivalent frequency, dependent parts $f'(\omega)$ and $f''(\omega)$ are independent of $\vec{Q}$.

In the context of transmitting materials, the binding of electrons and their answer as harmonic oscillators to the excitation by the incoming X-rays are essential. As every electron has element specific binding energies, X-rays close to these resonant frequencies cause the strongest effects on the form factor.

Detailed derivations are given in Als-Nielsen and McMorrow [37, Chapter 8]. The results are briefly summarized in the following.

The complex refractive index can be written as

$$n(\omega) = 1 - \frac{n_a}{2\pi} r_e \lambda^2 \left(f^0 + f'(\omega) - if''(\omega)\right) \tag{2.31}$$

with the wavelength λ, the electron radius r_e and the atomic number density $n_a = N_A \frac{\rho}{A}$ as product of the Avogadro constant N_A and the mass density ρ divided by the atomic mass A. In a shorter form, this is written as

$$n(\omega) = 1 - \delta(\omega) + i\beta(\omega) \tag{2.32}$$

with

$$\delta(\omega) = \frac{n_a}{2\pi} r_e \lambda^2 \left(Z + f'(\omega)\right) \tag{2.33}$$

$$\beta(\omega) = \frac{n_a}{2\pi} r_e \lambda^2 f''(\omega) \tag{2.34}$$

Considering the interaction of a wave Ψ_0 with a material of thickness Δx

$$\Psi_{\Delta x}(x) = \Psi_0 \exp\left(\mathrm{i}k \int_0^{\Delta x} n \mathrm{d}x\right) \tag{2.35}$$

and using Eq. (2.32), the resulting wave divides into the three parts:

$$\Psi_{\Delta x}(x) = \underbrace{\Psi_0 \exp\left(\mathrm{i}k \int_0^{\Delta x} 1 \mathrm{d}x\right)}_{\text{wave propagation in vacuum}} \cdot \underbrace{\exp\left(-\mathrm{i}k \int_0^{\Delta x} \delta(x) \mathrm{d}x\right)}_{\text{phase shift}} \cdot \underbrace{\exp\left(-k \int_0^{\Delta x} \beta(x) \mathrm{d}x\right)}_{\text{absorption}} . \tag{2.36}$$

Absorption of X-rays

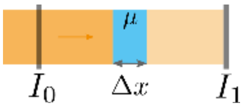

Figure 2.4: absorption scheme.

When the X-ray beam is transmitted by matter with a thickness Δx along the propagation direction, see Fig. 2.4, its intensity I_0 will be reduced due to the absorption process described by Lambert-Beer's law.

$$I_{\Delta x}(x) = I_0 \cdot e^{-\int_{x=0}^{\Delta x} \mu(x) dx} \tag{2.37}$$

As it is clearly visible in Eq. (2.37), the attenuation of the beam intensity in matter equals an exponential decay, which depends on the attenuation of absorption coefficient:

$$\mu = \frac{4\pi}{\lambda}\beta. \tag{2.38}$$

The data determined in the experiment is the attenuation or absorption coefficient μ and with the specification to the contained elements, it is converted to *mass attenuation coefficient*, which is also named *photoabsorption cross section* μ/ρ.

X-ray Phase Shift

The δ is the decrement of the real part of the refractive index. It describes the change of the phase of the X-ray wave, transmitted by matter. The resulting shift of ϕ is determined by a comparison to a propagation along same path Δx in vacuum.

$$\phi(x) = \frac{2\pi}{\lambda} \int_{x=0}^{\Delta x} -\delta(x) dx \tag{2.39}$$

2.2.4 Excitation and Fluorescence

After photo absorption, two secondary effects of the X-ray-matter-interaction can be recorded in X-ray experiments. These are called X-ray fluorescence and Auger effect.

Both effects are closely related and depend on the characteristic energies of the electrons in an atom. Providing that the energy of an incoming photon exceeds the binding energy of an electron in the atom, this electron can be ejected. In this case, the atom is in an excited state, which can be relaxed by refilling the vacancy with another electron of a higher energy level[2], see sketch in Fig. 2.5.

The energy difference occurring from the transition from the upper to the lower level can lead to two distinct effects, either X-ray fluorescence or the Auger effect. In the first case, a photon of the energy corresponding to the electron transition is emitted. This energy is characteristic for the atom and is called a fluorescence line. In the second case, the Auger effect, the remaining energy from the transition causes another electron ejection. This only happens as far as this energy matches or exceeds the binding energy of an electron in an upper level. In this thesis, we focus on the X-ray fluorescence.

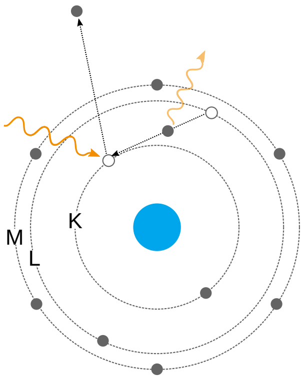

Figure 2.5: Coarse XRF scheme.

---

[2] These energy levels are also known as orbitals.

There is no preferred direction for the emitted photons, which leads to a uniform distribution of these events in all spacial directions.

2.3 Coherence

Light produced by a real physical source is never strictly monochromatic. ”If the two beams originate in the same source, the fluctuations in the two beams are in general correlated and the beams are said to be completely or partially coherent (...)” [31, Chapter 7].
Coherence describes the mutual phase relation of waves [30].
Furthermore, the coherence is distinguished in a correlation in time, the longitudinal coherence, and a correlation in space, the transversal coherence. A certain amount of coherence is necessary to visualize interference, which is essential for the imaging method ptychography, applied in this thesis.

2.3.1 Longitudinal Coherence

Longitudinal coherence is a measure for spectral purity [30, Chapter 9]. It describes the time correlation between the phases of waves with wavelengths $\lambda_1 = \lambda$ and $\lambda_2 = \lambda + \Delta\lambda$. Both waves start at the same time and same point with the same phase: To be in the same phase again, they need to fulfill the relation $n(\lambda + \Delta\lambda) = (n+1)\lambda$ with integer number n.

$$l_l = \lambda n = \lambda \frac{\lambda}{\Delta\lambda} \tag{2.40}$$

A high degree of longitudinal coherence is given for a large l_l [30]. To obtain a visual interference pattern of two scattering waves, the path length between these waves, described by vectors, needs to be smaller than the longitudinal coherence length.

2.3.2 Transversal Coherence

Transversal coherence describes spatial differences in the extended, chaotic source. Considered are two waves with the wavelength λ, starting from the source O, as origin of the wave, with source size D_O, and propagating the distance L_{OS} to the sample S, with size D_S, and beyond. With the defined transversal coherence length:

$$l_t = \frac{\lambda L_{OS}}{D_O}, \tag{2.41}$$

interference is only visible in the diffraction pattern as long as the sample size is smaller than the transversal coherence length: $D_S < l_t$, meaning the sample is illuminated coherently.
With differences in the horizontal and vertical extension of the source, two different transversal coherence lengths can be determined.

CHAPTER 3

Scanning X-Ray Microscopy

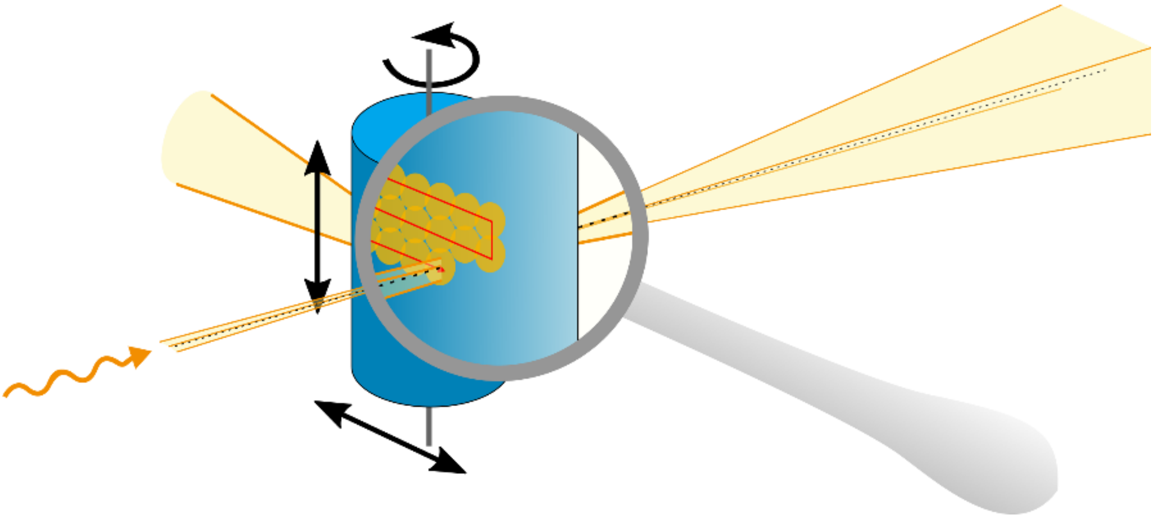

Scanning microscopy is the combination of a small beam and the scanning of it over a sample with larger dimensions than the beam. With a beam focused horizontally and vertically, as used in this work, the adjacent points build up a grid, line by line or row by row. With this principle, different properties of the sample can be imaged, for example X-ray fluorescence and X-ray diffraction. It is also required for the high-resolution imaging method named ptychography, see Sec. 3.1.

With the repetition of this grid scan at different angles, additional spatial information which is required for tomographic reconstructions, is obtained and enables the imaging of the measured contrast in three dimensions. The tomographic method and its requirements are described in Sec. 3.2.

As spatial resolution is an important measure to be pushed to its limits by many groups, a unified and mutually accepted definition allows for comparison of the achieved results. Different possibilities to determine spatial resolution are presented in Sec. 3.3.

In this thesis, two additional methods combining X-ray diffraction and a tomographic scanning scheme, are applied. The first one is based on a powder X-ray diffraction (PXRD) analysis method and the second is focused on reconstructing single grains from well separated reflections. The concept of both methods is briefly described in Sections 3.4 and 3.5, respectively.

3.1 Scanning Coherent Diffraction Microscopy – Ptychography

Ptychography is a coherent X-ray diffraction imaging (CXDI) technique combined with scanning. Originally, this technique was published in 1970 by Hegerl and Hoppe [13] with the intended use for electron microscopy. But with its application at modern synchrotron radiation sources, which have the ability to provide partially coherent beams, the algorithm was altered to image aperiodic objects. The introduction of the scanning mechanism allowed that an object can be larger than the beam size [47]. The reconstruction of both the transmission function and the illuminating complex-valued wave field at the same time [48] is a big advantage. Hence, it is used to characterize new optics, too. By propagating the reconstructed probe along the beam path it is possible to calculate the optics' wave caustic and to determine the focal position.
The general phase problem of coherent imaging is that the phase information of the wave field $\tilde{\psi}(\vec{Q})$ cannot be detected by the pixel detector, instead the absolute square of the wave is recorded as the intensity I_{det}.

$$I_{det} = |\tilde{\psi}(\vec{Q})|^2. \tag{3.1}$$

Due to the squaring, the phase information of the wave is lost. Maiden and Rodenburg [49] found a way to retrieve the phase by an iterative algorithm. The necessary for ptychography is a certain overlap of the illuminated regions of adjacent scan points. The geometry of the scanning pattern can be chosen arbitrarily with some advantages for certain patterns [50]. The ptychographic principle is described in the following section.

3.1.1 Basic Principle

In this project, we used the extended ptychographic iterative engine (ePIE) published by Maiden and Rodenburg [49] to retrieve the phase information of our objects. The basic concepts of the ptychographic data collection and data reconstruction are illustrated in Fig. 3.1. The setup for the ptychographic data collection contains a coherent incident beam $\mathcal{P}$ (yellow), which is spatially confined. At this longitudinal beam position, the object $\mathcal{O}$ is translated perpendicular to the beam path in a grid scan, while the illuminated parts of adjacent scan points overlap sufficiently (approx. 60% to 70%) [51]. The resulting exit wave ψ_i propagates to the far field. There, diffraction patterns of each scan point are recorded.
After the scanning process and with the knowledge about the distance between object and detector plane, the data can be reconstructed iteratively. This is carried out according to the scheme as sketched in the same figure, with the gray arrows and marked with capital gray letters. Here, we regard a single iteration with the consideration of the ith position $\vec{r}_i$: **A** An initial exit wave ψ_i is created out of an empty object and also a coarse guess about the illumination, i.e. shape and dimension. In the scope of this project, we used either refractive lenses (NFL or CRL) or Fresnel zone plates (FZP), which we approximate by a Gaussian beam shape. **B** The wave field is propagated into the far field, which is mathematically described by a Fourier transform of the exit wave $\tilde{\psi}_i$, see Sec. 2.1 and Eq. (2.14). **C** The amplitudes in the equation are replaced by the square root of the measured intensities I_i, compare Eqs. 2.1 and 3.1. At this position, the measured data is inserted into the algorithm. **D** This altered function $\tilde{\psi}'_i$ is propagated back to real space, which equals an inverse Fourier transform, to gain the exit wave ψ'_i. **E** This in turn

contains the update of the functions of probe and object, to be implemented as start for a new iteration.

The updated object and probe function for the ith position and diffraction pattern are [49]:

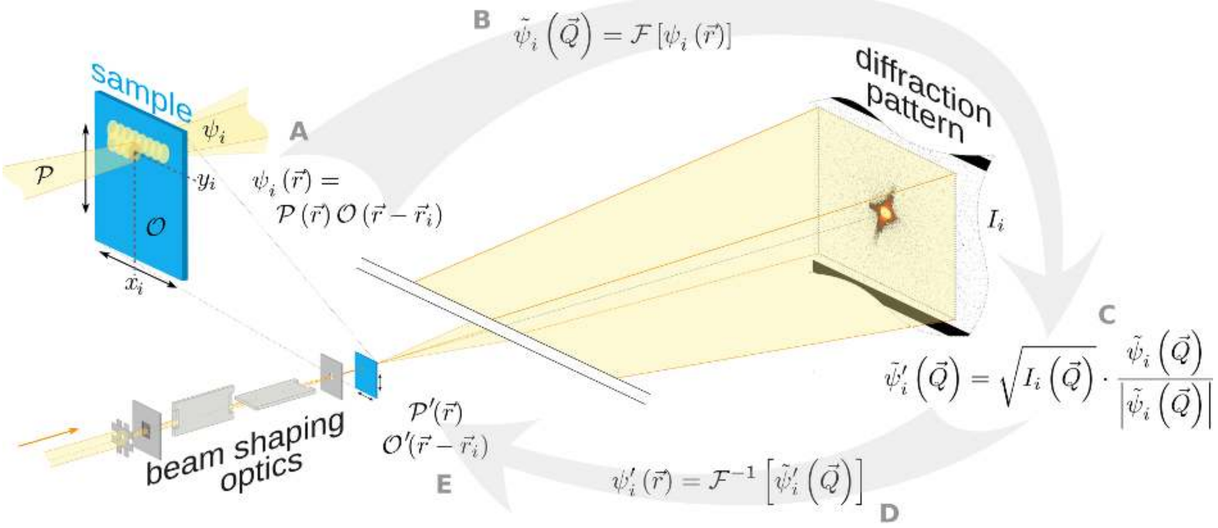

Figure 3.1: Basic principle of the ptychographic process, consisting of the scanning setup and the iterative reconstruction algorithm. After the diffraction patterns in the far field are recorded for each scan position (single yellow spot on blue object), the reconstruction according to the ePIE algorithm is performed as follows in keywords: **A** Initial guess forming the exit wave ψ_i. **B** Propagation to far field. **C** The measured intensities replace the amplitudes in the equation. **D** Back propagation. **E** Update of object and probe function in the exit wave ψ_i'.

$$\mathcal{P}'\left(\vec{r}\right) = \mathcal{P}\left(\vec{r}\right) + \beta \frac{\mathcal{O}_i^*\left(\vec{r}+\vec{r}_i\right)}{\left|\mathcal{O}_i\left(\vec{r}+\vec{r}_i\right)\right|_{max}^2}\left(\psi_i'\left(\vec{r}\right) - \psi_i\left(\vec{r}\right)\right)$$

$$\mathcal{O}'\left(\vec{r}-\vec{r}_i\right) = \mathcal{O}\left(\vec{r}+\vec{r}_i\right) + \alpha \frac{\mathcal{P}_i'^*\left(\vec{r}\right)}{\left|\mathcal{P}_i'\left(\vec{r}\right)\right|_{max}^2}\left(\psi_i'\left(\vec{r}\right) - \psi_i\left(\vec{r}\right)\right)$$

To complete one ptychographic iteration, this routine is repeated for all N scan positions or diffraction patterns, respectively. Appropriate results of both wave and transmission function are obtained after only some tenth of iterations. This is associated with the convergence of object and probe function, where changes as well as the error become negligible. The sum squared error (SSE) is measured in the diffraction plane as

$$SSE = \frac{\left(|\tilde{\psi}'(Q)|^2 - |\tilde{\psi}(Q)|^2\right)^2}{N}. \tag{3.2}$$

In reality many deviations from the simple ptychographic imaging scheme can occur. Many of these deviations were implemented in the ptychographic model, for example background and position correction. With these corrections, the number of iterations that is required for a successful reconstruction may increase.

In order to sample the diffraction patterns appropriately the maximum size of the probe beam P

is given by

$$P < \frac{\lambda L_{SD}}{2p}, \tag{3.3}$$

where λ is the wave length, L_{SD} is the distance between sample and detector and p the size of the detector pixels. The factor $1/2$ results from the Nyquist theorem [52, 53] for correct sampling. The resulting pixel size in real space Δx is determined from the relation of the wavelength λ of the illumination and the distance between sample and detector L_{SD} to the number of used detector pixels N_{det} and their size p:

$$\Delta x = \frac{\lambda L_{SD}}{N_{det}\, p} \tag{3.4}$$

3.1.2 Upsampling

The signals detected in the far field are restricted to the discrete arrangement of detector pixels. Based on the theoretical paper of Batey et al. [54] and in parallel developed in our group since 2014 [53, 55], the diffraction patterns are artificially upsampled. This corresponds to an upscaling of the field of view in real space. For this, each pixel is divided into a set of $x \times x$ subpixels, $x = 1, 2, 3, \ldots$, with the intensity value of the original pixel assigned to the sum of these. Subsequently, the intensity can freely evolve by the algorithm on the new grid with the only boundary condition that the overall measured intensity remains the same.

The effect of the upsampling is a larger field of view in real space. In situations where the illumination exceeds the field of view, the upsampling can enable a successful reconstruction nonetheless.

3.2 Tomography

X-ray computed tomography is a well established technique used to non-destructively image the inner structure of an object in 3D. Its application is versatile as with X-rays different contrasts can be measured.

Detailed descriptions about computed tomography can be found in Kak and Slaney [56] and Zeng [57]. The following sections give a brief description of the tomographical principle and its requirements.

As this thesis only uses data of experiments at synchrotron radiation sources, considerations are reduced to parallel beam projections. In case of parallel beam projections, the vertical coordinate can be decoupled. As a result, the tomographic reconstruction can be reduced to a numerical 2D problem.

3.2.1 Basic Principle

The aim of the tomographic algorithm is to reconstruct the sample function $f(x, y)$ from projections $p_\omega(u)$ of the sample at different angles ω. The sample coordinate system (x, y) is rotated by an angle ω against the laboratory system (u, v) using the rotation matrix R_ω.

$$\begin{pmatrix} u \\ v \end{pmatrix} = \underbrace{\begin{pmatrix} \cos\omega & \sin\omega \\ -\sin\omega & \cos\omega \end{pmatrix}}_{\text{rotation matrix } R_\omega} \begin{pmatrix} x \\ y \end{pmatrix} \tag{3.5}$$

A projection $p_\omega(x)$ is a set of line integrals through the sample and is known as Radon transform of the function $f(x, y)$ [56, Chapter 3]. All recorded projections are collected in a sinogram (ω, x). According to Kak and Slaney [56, Chapter 3.2], the key to tomographic imaging is the Fourier Slice Theorem. Assuming that $F(q_x, q_y)$ is the two-dimensional Fourier transform of the function $f(x, y)$.

$$F\left(q_x, q_y\right) = \int\limits_{-\infty}^{\infty} \int\limits_{-\infty}^{\infty} f\left(x, y\right) e^{2\pi i (q_x x + q_y y)} \, \mathrm{d}x \, \mathrm{d}y \tag{3.6}$$

A projection $p_\omega(x)$ of the function $f(x, y)$ in real space in direction ω is one-dimensionally Fourier transformed $P_\omega(q_x)$. This is equal to a slice of the Fourier Transform $F(q_x, q_y)$ in direction ω, see visualization in Fig. 3.2.

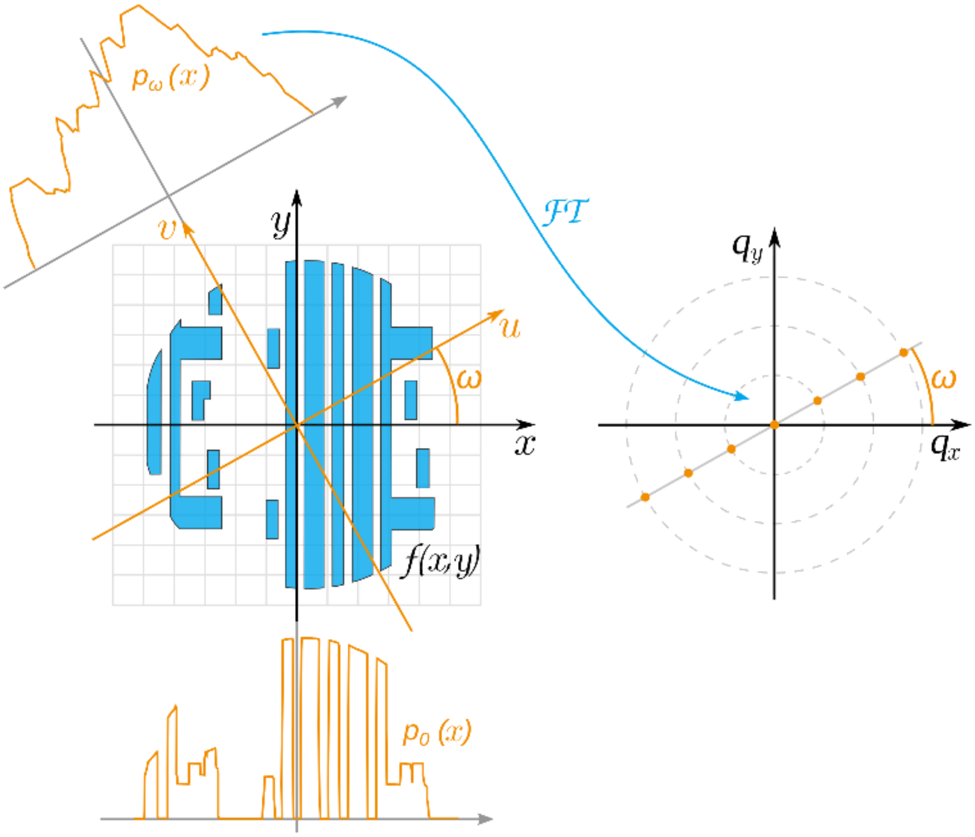

Figure 3.2: Visualized Fourier Slice Theorem. The one-dimensional Fourier transform of a projection $p_\omega(u)$ of a function $f(x, y)$ in direction ω corresponds to a slice through the two-dimensional Fourier function $F(q_x, q_y)$ in direction ω.

With projections from enough angles, see Sec. 3.2.3, the data can be reconstructed to gain an estimate of the object [56]. It needs to be considered that the further away from the center, the sparser the density of radial points. This might cause greater errors in high-frequency components as compared to low-frequency components. As the data in Fourier space is described by values at a certain radius q_r and angle ω, the coordinates can be changed to polar coordinates:

$$q_x = q_r \cos\omega \tag{3.7}$$

$$q_y = q_r \sin\omega \tag{3.8}$$

To reconstruct the sample function $f(x, y)$, the Fourier transform, see Eq. (3.6), needs to be inverted.

$$f(x, y) = \int\limits_{-\infty}^{\infty} \int\limits_{-\infty}^{\infty} F(q_x, q_y)\, e^{2\pi i (q_x x + q_y y)}\, \mathrm{d}q_x\, \mathrm{d}q_y \tag{3.9}$$

With the change to polar coordinates $\mathrm{d}q_x \mathrm{d}q_y = q_r \mathrm{d}q_r \mathrm{d}\omega$, this equation changes to

$$f(x, y) = \int\limits_{0}^{2\pi} \int\limits_{0}^{\infty} F(q_r, \omega)\, e^{2\pi i q_r (x\cos\omega + y\sin\omega)} q_r\, \mathrm{d}q_r\, \mathrm{d}\omega. \tag{3.10}$$

With adjusting the integration limits, we get

$$f(x, y) = \int\limits_{0}^{2\pi} \int\limits_{-\infty}^{\infty} F(q_r, \omega)\, e^{2\pi i q_r (x\cos\omega + y\sin\omega)} |q_r|\, \mathrm{d}q_r\, \mathrm{d}\omega, \tag{3.11}$$

where $|q_r|$ is the Jacobi determinant in this integral and represents a ramp filter $H(q_r) = |q_r|$. This can be exchanged to other filters, cutting the data at high q values and deliberately distort the result to get smoothened reconstructions.

3.2.2 Algorithms and Filters

For the reconstruction of the recorded data, there are different algorithms available, such as the filtered back projection (FBP), and different methods based on the algebraic reconstruction technique (ART) [58–61]. All reconstruction algorithms have specific advantages in different areas and not all algorithms are equally good in all situations. More information on the different reconstruction algorithms can be found in the corresponding literature [56, 57].

During this thesis, different algorithms were tested, but the best results – showing the least artifacts – were achieved using FBP with a ramp filter as obtained in the previous section, also known as Ram-Lak, short for the inventors' names Ramachandran and Lakshminarayanan [62, 63]. This and other filters, such as Shepp-Logan, Cosine, Hamming and Hann, deemphasize high frequencies and reduce artifacts [56, 57].

3.2.3 Requirements

The information about the sample is limited as it can only be recorded discretized. In order to still be able to reconstruct a meaningful tomogram, it requires a certain number of projections, dependent on the resolution and the width of the sample in real space. In order to properly sample the Fourier transform, the radial and azimuthal sampling need to match, see Fig. 3.3. The radial sampling Δq in Fourier space results from the parameters resolution or step size Δx – dependent on the used imaging method – and the sample width D_S in real space, which define the number of steps $N_{\Delta x} = D_S/\Delta x$. This number corresponds to the spacial distance Δq in Fourier space

$$\Delta q = \frac{2\pi}{\Delta x} = \frac{2\pi}{D_S} N_{\Delta x}. \tag{3.12}$$

The angular step size $\Delta\omega$ is determined by the number of steps N_ω over the half circumference $\pi \Delta q N_{\Delta x}/2$, which is sufficient to measure with parallel beam geometry,

$$\Delta\omega = \frac{\pi \Delta q N_{\Delta x}}{2 N_\omega}. \tag{3.13}$$

In order to get the same sampling in both directions $\Delta q \approx \Delta\omega$ the necessary number of projections is

$$N_\omega \approx \frac{\pi}{2} N_{\Delta x} = 1.57 \cdot N_{\Delta x}. \tag{3.14}$$

Furthermore, from the theory of communication, alias signal processing, it is known that a sufficient sampling of a signal of period p requires at least double the number of sampling points or of half period size $p/2$. This is called the Nyquist-Shannon sampling theorem [52], which is equal to the Crowther criterion and relaxation to that [64, 65].

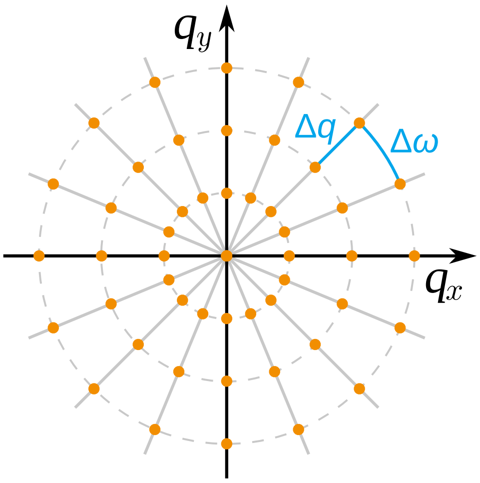

Figure 3.3: Visualization of the sampling requirements for tomography in Fourier space, given by radial Δq and angular $\Delta\omega$ sampling.

3.3 Estimation of Spatial Resolutions

For the interpretation of imaging results and their comparison to results obtained with other methods, the information about the spatial resolution is an important criterion for both two-dimensional and three-dimensional imaging. It varies with the applied contrasts and samples and indicates the smallest possible features that can be resolved. There are several possibilities to determine the spatial resolution, which will be briefly described in the following, but neither of these methods is exact or draws a full picture. For that reason, each single method results in a representative value in a certain way and has to be applied carefully. If all methods lead to the same spatial resolution, the results could be considered trustworthy.

3.3.1 Power Density Spectra

For ptychography, as applied in the experiments of this thesis, the signal is detected in the far field and the power density spectrum (PDS) shows the potential of the data set regarding spatial resolution. With further effects on the data, such as noise, the actual spatial resolution in the reconstructed image is lower. For that reason, the PDS can be considered as a limit for the achievable spatial resolution for the analyzed data set.

3.3.2 Known Features

With knowing specific structure sizes in advance, a coarse estimation about the spatial resolution can easily be made. Besides the dependency on different aspects, such as the contrast of a resolved structure, the size of a known feature can only serve as reference for the spatial resolution as it can go well beyond the smallest structure size.

3.3.3 Edge Fitting

Another method of a coarse determination of the achieved spatial resolution is the measurement of edges of sharp structures. At transitions between different structures, the edges are fitted by a Gaussian function and the full-width-at-half-maximum (FWHM) is determined. For better statistics it is ideal to choose several different edges and average the result. But nevertheless, is has to be kept in mind that not all structures necessarily have sharp transitions to their environment, which then is not a sign of weak resolution, but rather of weak transitions.

3.3.4 Determination by Fourier Ring/Shell Correlation

This method by van Heel [66] is rather new in the field of X-ray imaging. It basically determines a similarity between split and separately reconstructed data or two similar scans. It can be used to determine the spatial resolution for images, two-dimensional by the Fourier ring correlation (FRC), as well as for volumes, three-dimensional by the Fourier shell correlation (FSC). To compare achieved results, it is accepted as a valid criterion in the ptychographic community in recent years [67].

For the two-dimensional case, the FRC for rings q_i is determined as follows [66]:

$$FRC_{1,2}\left(q_i\right) = \frac{\sum_{q \in q_i} F_1\left(q\right) \cdot F_2^*\left(q\right)}{\sqrt{\sum_{q \in q_i} \left|F_1\left(q\right)\right|^2 \sum_{q \in q_i} \left|F_2\left(q\right)\right|^2}} \tag{3.15}$$

In this equation, $F_1\left(q\right)$ is the two-dimensional complex amplitude of a pixel q in Fourier space of the first image and $F_2\left(q\right)$ equivalent for the same pixel in the second image. With the same approach, a spatial resolution estimation can be made for the comparison of two volumes $V_1(\vec{r})$ and $V_2(\vec{r})$, with their Fourier space equivalents $F_1\left(q\right)$ and $F_2\left(q\right)$. In both situations, the asterisk * denotes the complex conjugate of a function.

According to equation (3.15), a curve is created. The achieved spatial resolution is determined by the crossing of this curve with the counting criterion. There are two threshold criteria to be considered: The 1-bit criterion counts for the comparison of two full data sets, while the 1/2-bit criterion is valid for the comparison of two half data sets – created out of one data set by lacking of a comparable second one.

This method has to be handled with care, because only similarities are considered. As a result, reconstructions with artifacts could be considered as highly resolved even though the result does not make sense at all. And the opposite can occur as well, when structures below the estimated spatial resolution are obviously resolved. The limit for the best possible estimation by

FRC or FSC is the reconstructed pixel or voxel size, respectively.

For completeness, by the application of FRC, another criterion, the spectral signal to noise ratio (SSNR) [68] can be used, compared to a threshold ≤ 1.

$$SSNR_{12}(k) = 2\frac{FRC_{12}(k)}{1 - FRC_{12}(k)} \leq 1 \tag{3.16}$$

The rearrangement of this equation leads to a stricter criterion for the FRC: $FRC_{12} \leq 1/3$.

3.3.5 Conclusion on Spatial Resolution Estimation

As there is no ideal method to determine the spatial resolution of a reconstructed image, the mentioned criteria can be used to limit the results. For this, the PDS can be used to determine the best achievable spatial resolution for a data set and the other limit is set by edge fitting and the identification of known features. The results of the FRC or FSC should lay in between these limits.

3.4 3D Powder X-ray Diffraction

In this thesis, powder is distinguished from grains by the size of the crystallites compared to the beam size. All crystallites with sizes comparably or larger than the size of the illuminating beam are considered as grains. Crystallites which are much smaller than the beam size are described by powders. For these small crystallites, a PXRD based method is applied.

A combination of PXRD and X-ray diffraction computed tomography (XRD-CT) using a pencil beam was first introduced by Bleuet et al. [69]. The following description uses excerpts of this paper to introduce the principle of this method.

In the work of Bleuet et al., the usage of a pencil beam for 2D phase discrimination [70–72] is extended to 3D to additionally gain depth resolution. The procedure is explained at one slice, corresponding to one vertical position z and can easily be extended to 3D by repeating the scanning and analyzing for additional vertical positions.

The sample is scanned horizontally along y, perpendicular to the probing beam, at a set of tomographic angles ω. For each scan point (y, ω), the beam samples an isotropic powder and thus is averaged over all orientations. As a result, the diffraction patterns can be azimuthally integrated to a diffractogram and can be considered as scalar.

In parallel, the complete data set of diffraction patterns is summed up and azimuthally integrated to identify major phases. In the work of Bleuet et al., it was used to build up a global sinogram, showing the general distribution in a $(y - \omega)$-overview. Additionally, particular 2θ regions are selected to build up selective phase sinograms $(y - \omega)$. These are finally reconstructed tomographically and show the spatial distribution of the different phases in the sample.

The work of Bleuet et al. introduced two more experiments with further specifications. The second experiment was used for reverse analysis, enabling Rietveld refinement [73–75] to determine different structural information, such as lattice parameters, texture and grain sizes. This requires the sampling of a high number of grains and a continuous ω coverage. The described experiment was conducted using a 1.6 µm×2.3 µm (vertical×horizontal) pencil beam, focused by a Kirkpatrick-Baez mirror system on a 200 µm sample with crystallites of approximately 100 nm. The third experiment demonstrated the extension of the 3D PXRD analysis of the first example to a multimodal experiment including a simultaneous measurement of example X-ray fluorescence (XRF) and X-ray absorption (XRA).

3.5 3D X-Ray Diffraction alias Grain Search

If crystallites are large enough, equal to or larger than the beam size, they are considered as grains and can after identification be reconstructed individually. For the explicit search for grains and the determination of their orientation, in this work an altered version of a pencil-beam 3D X-ray diffraction (XRD) was applied, which goes back to the work of Poulsen et al. [27, 76]. In recent years, the determination of grains, including their spatial location, size and orientation, developed from common 3D XRD techniques, using a full-field beam [76–78] over a box beam technique [39, 79, 80] to a pencil beam technique, which can be found as scanning 3D XRD[1] [25, 81–83].

The three mentioned acquisition schemes are illustrated in Fig. 3.4. In all three cases, the fast axis is the rotation axis with continuously scanned angles ω. For each $\Delta\omega$, for example $\Delta\omega = 1^\circ$, an integrated diffraction pattern is recorded.

In full-field beam experiments **A**, the sample is smaller than the beam and is fully sampled by one rotation. During this continuous rotation, for each distance $\Delta\omega$, an integrated diffraction pattern is recorded, with $\Delta\omega \approx 1^\circ$. The spatial resolution is given by the spatial resolution of the pixel size of the detector and the usage of two detectors in line [27]. For the box beam **B** as well as for the pencil beam technique **C**, the beam is smaller than the sample and for that reason, several sets of continuous ω rotations are conducted for each vertical and horizontal step, or each combination of these, respectively. The data acquisition for each grid point equals the acquisition for the full field case. For each $\Delta\omega$, an integrated diffraction pattern is recorded. The integration distance is equivalent.

The last scheme in Fig. 3.4 (**C**), using a pencil beam, was adapted in this work. Published Scanning 3D XRD experiments scan the sample in a grid scan with a continuous scan over ω for each scan point, with the same angular acquisition scheme as for the other schemes above. In our experiment, we first scanned all positions at one angular projection and then changed to the next discrete angle to enable the combination with other simultaneously measured contrasts. Instead of integrating over the angular range $\Delta\omega$, the data between two angles is missing.

The actual grain determination starts with a peak identification in each diffraction pattern. For this, the data in the diffraction pattern needs to have a defined size in amount of pixels and threshold in intensity. In the next step, all these peaks are indexed with a corresponding (hkl) and saved with angular information $\omega, 2\theta, \eta$, see Sec. 8.4.9. Of this huge set of indexed peaks, an algorithm sorts and compares the peaks and assigns sets of peaks to different grains. The resulting grain is described by a matrix U and can with the corresponding position information of

---

[1] This name might cause some confusion since all kinds of 3D XRD require certain scanning, even if it is only angular. For that reason, the extension 'pencil beam' is used in this thesis when referred to the 'scanning 3D XRD method explicitly.

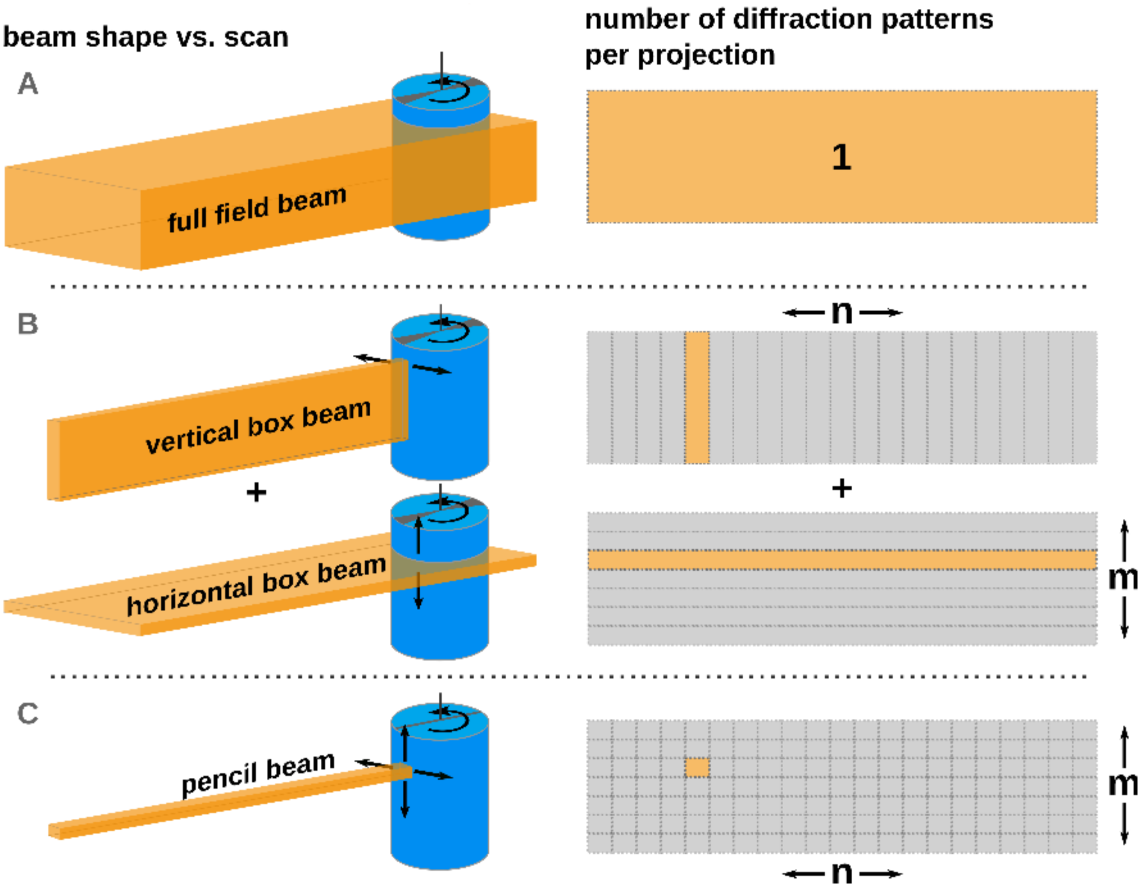

Figure 3.4: Comparison of the three different data acquisition schemes for **A** full field, **B** box scan and **C** pencil scan, especially in the context of 3D-XRD. All three schemes show the number of diffraction patterns for one static angle. To gain the full number of diffraction patterns, these numbers need to be multiplied by the number of angular steps.

the single peaks[2] be reconstructed tomographically. The matrix U describes the orientation of the grain towards the sample orientation.

The applied procedure including the programs is again described in more detail in Sec. 8.4.9.

---

[2] Here, the scan point, where the respective peak was measured is required, the angular information is not required any longer.

CHAPTER 4

Experimental Setup

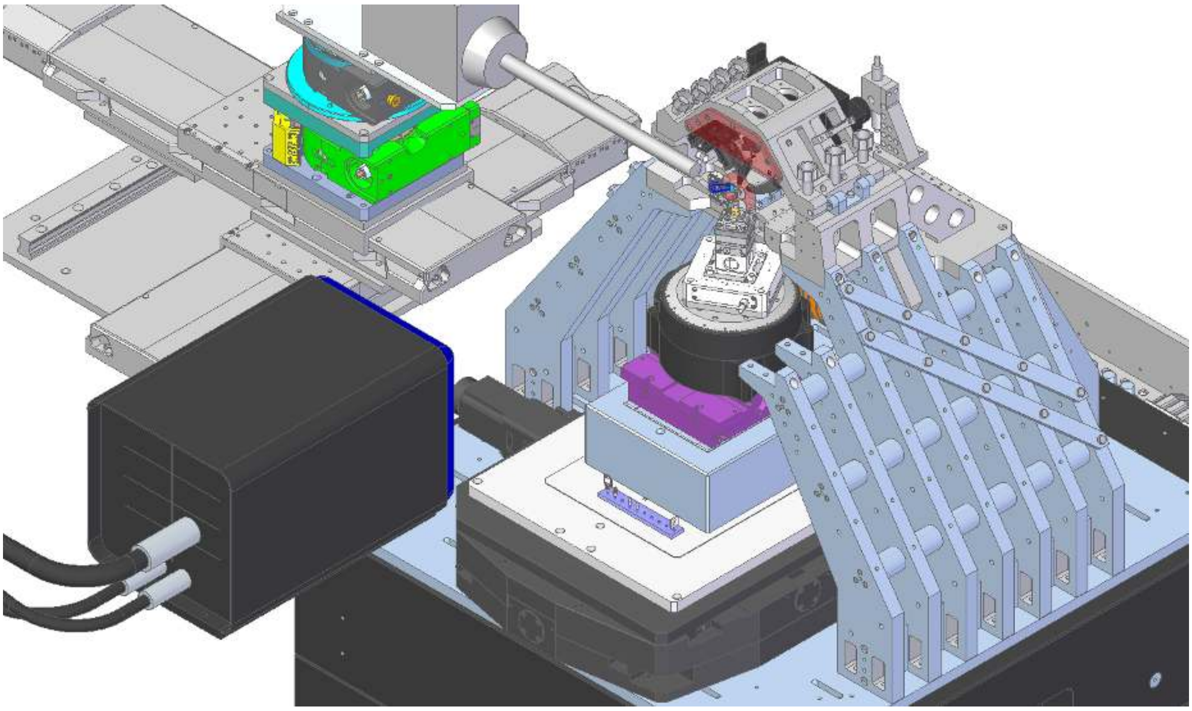

The experiments during this thesis were carried out at the hard X-ray nanoprobe end station of the P06 beamline, called ptychographic nano-analytical microscope, short PtyNAMi [84], at the synchrotron radiation source PETRA III at DESY in Hamburg, Germany, and at the coherent beamline I13-1 [85] at the Diamond Light Source (DLS) in Oxfordshire, England.

As the main part of this thesis – the multimodal experiment – was conducted at the P06 nanohutch, subsequent considerations for beamline devices and detailed explanation of specific parts are related to beamline P06 and the multimodal experiment. In the following sections 4.1 to 4.4, the basic beamline components: the optics, the sample environment as well as the detectors, are described. More details about the beamline P06, including overall dimensions, can be found in Schroer et al. [86].

For further general information, I refer to the comprehensive literature about synchrotron radiation and all the instrumentation by Als-Nielsen and McMorrow [37] as well as Attwood and Sakdinawat [87].

4.1 Basic Components

The essential components of the synchrotron beamline P06 are:

- an undulator as photon source,
- a monochromator,
- beam shaping X-ray optics,
- a sample environment including motorization, and
- at least one detector.

This beamline starts with an undulator as the insertion device, creating the photons for the experiment at the nanoprobe end station. At P06, the source is a 2 m long U32 undulator [88, 89], which creates X-rays with wavelengths in the range from 4.13 Å down to 0.248 Å, corresponding to an energy range from 3 keV to 50 keV, respectively. Along the path from the photon source to the sample position, a monochromator, slits, mirrors and lenses condition the X-ray beam according to the experimental needs. The monochromator selects photons of the chosen energy from the undulator beam, and higher harmonics, by adjusting the orientation of the crystals accordingly.

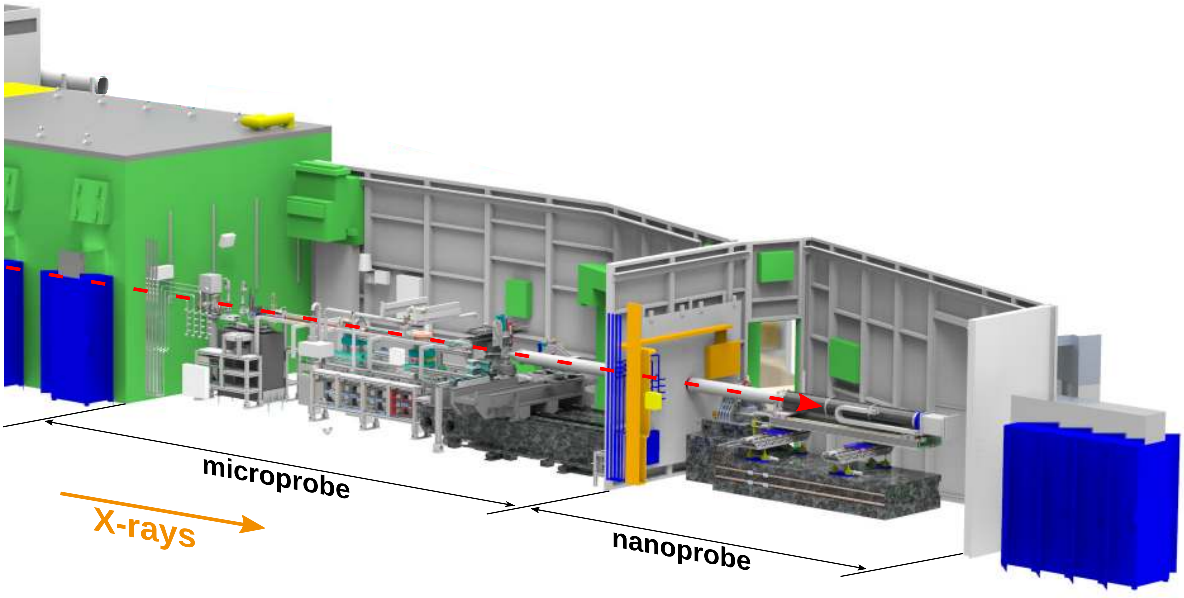

Figure 4.1: In this side view of the beamline P06, both experimental hutches, micro- and nanoprobe end stations, are visible. The multimodal experiment was conducted in the latter. The actual beam path is marked with a red dashed line.

Directly upstream of the sample, there are special X-ray optics, nanofocusing lenses (NFL), focusing the probe to the sample position. At the sample position, the probe interacts with the sample and different detectors record the diverse signals.

As Fig. 4.1 shows, the P06 beamline is divided into two distinct experimental hutches. Our experiment was conducted in the nanohutch, which is positioned at the end of the beamline.

4.2 X-ray Optical Elements and X-ray Optics

In general, optics and optical elements serve as guide for the X-rays as well as to define or shape the illumination. Based on the physical working mechanism, optics can be grouped into refractive, reflective and diffractive optics, such as lenses, mirrors and monochromators, respectively. In addition, apertures such as slits, pinholes or beamstops are used to simply block parts of the beam. For more information on X-ray optics, see Schroer and Lengeler [90] and Paganin [32]. Here, I focus on the larger and more complex optical components used within this project, sorted by the underlying working principle.

4.2.1 Diffractive Optics

The working principle of diffractive optics is the beam deflection according to Bragg's law, see Eq. (2.25). The most prominent example of such an optic at the beamlines is a monochromator. Depending on the kind of monochromator, all wavelengths $n\lambda$, with some integer n, of the incoming white beam, which hit the crystal(s) and fulfill the Bragg's law for the current inclination, pass this section of the beamline, while the rest continues in the direction of the incoming beam and is absorbed. The wavelengths $n\lambda$ for $n \geq 2$ are called higher harmonics, but they are less intense than the principal harmonic. Depending on the kind of experiment, these higher harmonics are of minor or significant relevance. In diffraction experiments, for example, they entail more complicated analyses of the multiplexed results obtained by different energies.

4.2.2 Reflective Optics

Due to the weak interaction of X-rays with matter, the index of refraction $n = 1 - \delta + i\beta$ is very close to, but smaller than one[1]. For that reason, it is not possible to build reflective optics like the ones known for visible light, for example common mirrors. The working principle of reflective X-ray optics is based on external total reflection. For diverse materials the critical angle is rather small[2] in that wavelength regime. Popular examples are Kirkpatrick-Baez mirrors [92] or higher-order rejecting mirrors, acting as low pass filter. Reflective optics are used to slightly change direction of the beam path, to guide rays and in this sense focus the rays, or to exclude higher harmonics.

Since the separation of reflections from incident X-rays with different energies is difficult, higher harmonics passing the monochromator need to be blocked. During the multimodal experiment, we used the Pt layer of the HO mirror in the optics hutch of P06 to block the higher harmonics. Its cut-off energy is at 30 keV for 2.5 mrad and so above the experimental energy of 18 keV but below the next higher order.

4.2.3 Refractive Optics

Refractive lenses for X-rays work on the same principle as lenses for visible light, except the fact that the refractive index of X-rays in matter deviates very weakly, $\lesssim 1 \times 10^{-6}$, from and is below

---

[1] Exemplary values at 18 keV for β and δ for Si: 7.2×10^{-9} and 1.5×10^{-6}, Cu: 2.2×10^{-7} and 5.3×10^{-6} and Ta: 7.4×10^{-7} and 8.5×10^{-6}, respectively. Data taken from CXRO [91].

[2] As an example, for Pt at 18 keV the critical angle $\theta_{crit} \approx 4.65$ mrad.

the refractive index[3] of vacuum $n = 1.0$. Thus, when X-rays pass through a material they show only a small change in direction. Consequently, X-ray lenses usually consist of a large stack of concave lenses with a parabolic lens shape, for example compound refractive lenses (CRLs) [93, 94] or nanofocusing lenses (NFLs) [95]. The focusing principle is described in detail in Lengeler et al. [96, 97] and Schroer [98]. The sketch in the middle of Fig. 4.2 shows the lens shape at a pair of lenses. These different X-ray focusing lenses mainly differ in the material and the production method, which lead to a difference in size and application.

4.2.3.1 Compound Refractive Lenses

Compound refractive lenses have a parabolic shape with its origin at the optical axis, see middle image in Fig. 4.2. It is realized by pressing a pair of parabolas into a material with good refractive properties, which are low absorption, but sufficient refraction at the same time. A common material for these lenses, fulfilling these criteria, is beryllium (Be). The lens with an aperture $2R_0$ is encapsulated in a casing. For the multimodal experiment, we used a single Be lens as prefocusing optics in the P06 optics hutch in order to increase the photon flux at the microscope further downstream. During the experiment at DLS, beamline I13, we used a stack of 20 CRLs[4] to focus the X-ray beam on the sample, see exemplary CRLs in Fig. 4.2 left picture.

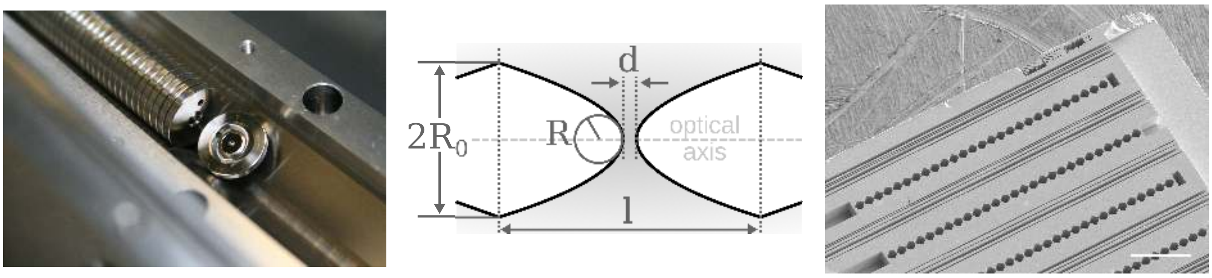

Figure 4.2: X-ray focusing optics. The picture on the left shows a stack of CRLs – with an outer diameter for the lens casing of 12 mm per lens – and the picture on the right shows an electron microscopic image of a part of a nanofocusing lens with the view of four parallel lens stacks, the scale bar is 200 µm. The construction scheme for both lens types is sketched in the middle with the radius of curvature R and the aperture $2R_0$, the thickness d and the length of the lens pair l. The lens material is colored in gray.

4.2.3.2 Nanofocusing Lenses

Another version of focusing lenses are nanofocusing lenses (NFL). To focus the incoming rays noticeably, a lens stack is etched in a plain substrate. The NFLs shown here are made of silicon. In comparison to CRLs, NFLs – being a stack of cylindrical lenses – only focus the beam in one direction. For this reason, two NFLs are combined to create a two-dimensional focus. The basic principle and further parameters of NFLs can be found in Schroer et al. [95]. The particular NFL combination we used, consisted of a stack of 108 lenses for vertical and a stack of 183 lenses for horizontal focusing[5]. At 18 keV the working distance, describing the distance from the lens

---

[3] In comparison, the refractive index for common glasses is between 1.4 to 1.5 for visible light, corresponding to yellow-orange in the visible light spectrum. These refractive indices allow for much stronger refraction and simpler optics than any refraction with X-rays.

[4] We used lenses with an aperture of $2R_0$ =300 µm and the radius of curvature R =50 µm.

[5] They have radii of curvature of the parabola of 10 µm for the NFLs and a total aperture of 40 µm.

exit to the focal plane, was about 16 mm. The beam shape and the focal size are determined in Sec. 7.3.1. Supplementary experiments, applying the ptychographic method, were conducted at 16 keV and for that reason, the lens parameters were slightly different, see Sec. 6.1.

4.3 The PtyNAMi Setup Used for the Multimodal Experiment

The whole sample positioning system of the PtyNAMi setup is a trade-off between stability and flexibility. Stability, achieved by high stiffness of the components of the setup, ensures measurements with high accuracy required for the analysis. At the same time, the setup must be versatile to serve all multimodal imaging purposes. At the bottom, a set of coarse linear motor stages provides a large scanning range in three perpendicular directions (x, y, z): one stage moving along the beam path and two perpendicular to it, separated into horizontal and vertical translational motion. Above these, a rotation stage from Micos is mounted, followed by a set of three high-precision piezo scanners, manufactured by Physics Instruments (PI) [99]. The rotation stage, a PI micos UPR 160 [100], and the piezo scanners, a PI P-733.3CL [101], are the sample stages used for the multimodal experiment. At the very top, a centering stage, that consists of two linear translational stages, Picolis$^{\text{TM}}$ 8525 [102] produced by New Focus, is essential to align the sample to the center of rotation. The upper part of the motion unit is visible in Fig. 4.3a. The usual PtyNAMi setup was slightly adjusted to the needs of the multimodal experiment by adding a large scattering shield, see Fig. 4.3b, to reduce scattering from the optical elements upstream onto the WAXS detector. The detectors were positioned in close vicinity of the sample, visible in Fig. 4.3c.

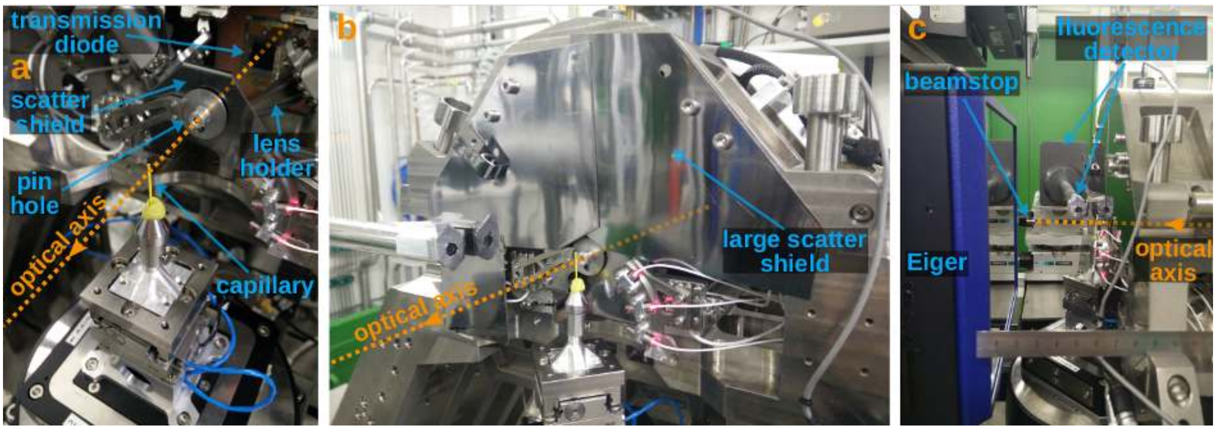

Figure 4.3: These photos show the setup with a yellow capillary, containing the powder XRD standard, on top of the scanning unit, without (a) and with (b) the large cover to suppress background scattering and with all detectors in place (c).

4.4 Detection

Measurements of distinct physical properties demand different means of detection. The principal functions and main features of the different detectors will be discussed in the following sections.

4.4.1 X-ray Camera

An X-ray camera can be used to visualize X-rays. The incoming X-rays hit a scintillator screen, which transforms the X-rays into visible light. An optical microscope magnifies the image on the screen, which is captured by a CCD chip. The X-ray camera at the PtyNAMi setup is an Optique-Peter microscope in combination with a tube lens with 2.5-fold magnification and a PCO.4000 CCD-camera [103]. The integrated optical microscope provides three different objectives with 2-fold, 4-fold, and 10-fold magnification. The effective magnifications are 5-fold, 10-fold, and 25-fold. The sensitive area of the CCD chip measures 36 mm×24 mm with a physical pixel size of 9 µm×9 µm.

4.4.2 Light Microscope

The beamline is equipped with an optical microscope from Keyence, a VH-Z100UR [104]. This microscope is used for the coarse alignment of the sample at the focal position of the X-ray optics. It is also used to find the sample's center of rotation. With the given magnifications of the zoom lens (100-fold to 1000-fold), a maximum resolution of 1 µm perpendicular to the probing beam and about 5 µm along the optical axis can be achieved.

4.4.3 PIN-Diodes

The PIN diodes[6] work with the principle of charge separation. At the beamline, the charge separation is caused by the incoming X-rays. The X-rays hit the sensitive part of the diode and produce electron-hole pairs due to ionization. These electron-hole pairs are collected by the anode and cathode of the diode. The created current is measured. The diodes we used are the transmission diode upstream of the focusing optics and the PIN-diode integrated in the beam stop. Both diodes are produced by Hamamatsu. The transmission PIN diode [105] runs without using a scintillator. The beam stop diode [106] is put in a light-tight casing to avoid the creation of signals from the light in the experimental hutch. The main difference between these two diodes is their thickness with 5 µm for the transmission diode and several hundreds of micrometers for the beam stop diode. The first diode analyses the transmitted beam and barely changes the amount of photons of the incident beam, while the second one typically absorbs most of the X-ray beam. As a result, the noise of the beam stop diode is lower. Both diodes are calibrated and the measured current is converted to $\mathrm{Ph\,s^{-1}}$. Nevertheless, Section 8.2 will show that the transmission diode could not deliver transmission values that were precise and reliable enough for our experiment.

4.4.4 Single Photon Counting Pixel Detectors

Each single pixel of the detection area is a small detection unit itself. When a photon hits the detector, it is collected by one of the sensors, as sensitive part of each pixel. The photon is transformed to an electron charge. The pulse height is compared to a certain threshold[7], which

---

[6] PIN: p-type, intrinsic and n-type semiconductor.

[7] A threshold above the electronic noise keeps data effectively noise-free [107, 108]. Additionally, these kinds of detectors do not show dark current or readout noise.

is defined in the settings and is usually set to half the X-ray photon energy. As each pixel is a fully functional detector, the incoming rays are spatially separated. At P06 we used an Eiger X 4M [109, 110] from Dectris to record the diffraction patterns for ptychographic scans and the multimodal experiment. At DLS, we used a MerlinX [111, 112] from Quantum Detectors to record the diffraction patterns during the ptychographic measurements. The main parameters of both detectors are given in the following table:

parameter	unit	Eiger X 4M Dectris	Merlin Quantum Detectors
pixel size	µm	75×75	55×55
number of pixels		2070×2167	512×512
sensitive area	mm^2	155.2×162.5	28.2×28.2
sensor thickness	µm	450	500
threshold energy	keV	2.7 - 18	5 - 17
max. count rate	Ph s^{-1} mm^{-1}	2×10^8	1.7×10^7
readout time	µs	continuous 3 µs dead time	0 / 850 / 1800 (cont./12/24 bit)
max. frame rate	Hz	750	1.2 k (burst) 100 (continuous)
counter depth	bit	20	12 or 24

Table 4.1: Parameters of photon counting detectors used for the experiment

4.4.5 Energy Dispersive Detector

The detection of the X-ray fluorescence signal is accomplished by a silicon drift detector, which is based on a diode with enhanced depletion region, where the incoming photons cause different numbers of ionizations according to their energy, for more details see Beckhoff et al. [113]. The detector measures the charge per incoming X-ray photon, converts the signal to the initial energy and subsequently assigns such an event to this energy range. This kind of detectors can handle high count rates of 900 kHz s^{-1} and provide energy resolutions of approximately 130 eV for Mn Kα. All events, entering the detector during the time of the exposure, are assigned to channels corresponding to their energy[8] and finally provide an energy spectrum.

For our experiment, we used the Vortex®-EM by Hitachi High-Technologies [114] with the readout electronics digital X-ray pulse processor xMap from XIA [115]. Besides using the data for elemental analyses, it is also used to verify the sample alignment during scans, which allows fast adjustments for subsequent scan regions in cases of drifts or misalignment.

---

[8] The full energy range, covered by the detector, is separated into a detector specific number of channels, here 2048, according to the energy resolution.

CHAPTER 5

Sample: Infineon Test Chip

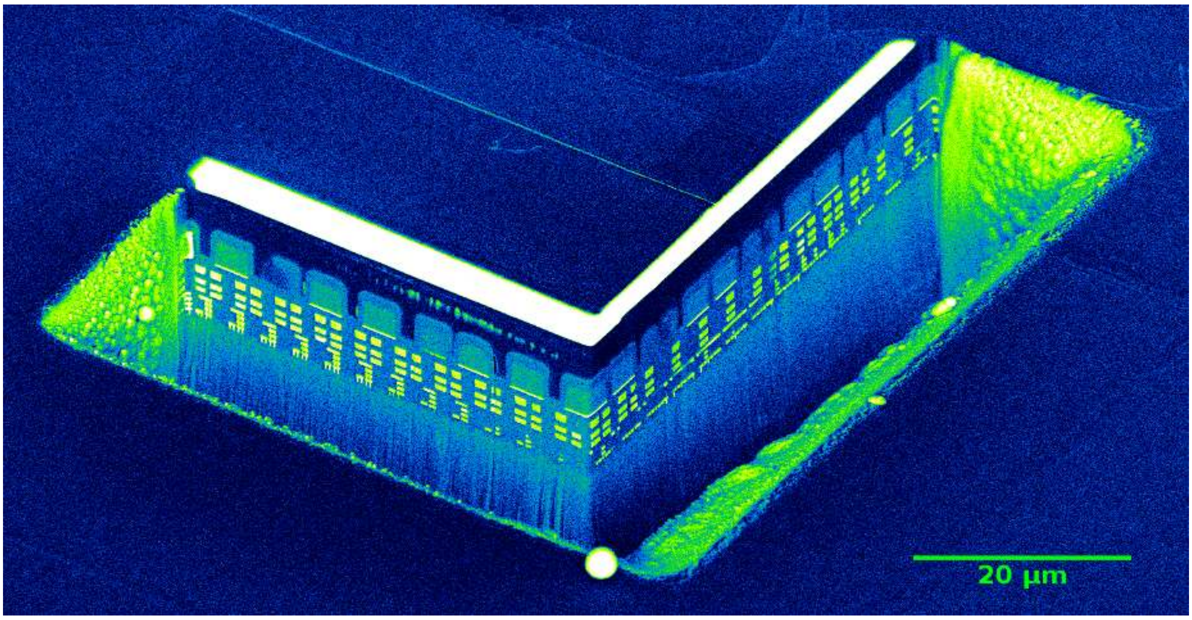

As the focus of this thesis is the development of a multimodal experiment, different experiments were applied to the same sample. We decided to use a radiation-stable sample, which provides different elements and different crystalline states. Nanoelectronic devices turned out to be good candidates for our requirements.

As a representative in the field of nanoelectronic devices, we chose a test chip produced by the semiconductor manufacturer Infineon Technologies Dresden GmbH und Co. KG. Since the experiments on the test chip sample are based on a cooperation with this company, the basic key parameters like dimensions of several metal structures in the microchip are known to us and could be used for verification of our results.

Further information on semiconductor manufacturing can be found in Hilleringmann [116] as well as Völklein and Zetterer [117].

This chapter starts with a general introduction to the manufacturing of microchips in Sec. 5.1. It continues with a closer view on the test chip and its usage as test object in Sec. 5.2 and 5.3. In Section 5.4 the aim of the analysis is outlined.

5.1 Introduction to Microchip Manufacturing

In this section, I will give a brief overview about the technology of microchip manufacturing in a simplified way at the example of the test chip.

In general, microchips are complex constructions of metal paths which are embedded in insulating material; in short, microscopic, three-dimensional electronic circuits. These electronic circuits are built on a semiconductor substrate which is provided as a bare, mono-crystalline wafer and forms the foundation for all following steps. These processing steps include doping of the wafer as well as the recurring process chain as listed in the following. Fig. 5.1 shows this process chain for a single representative layer with pictograms for each step:

A Deposition of photo resist or insulating material, e.g. oxide or nitride,
B Structure transition from a lithography mask to a photo resist,
C Development and removal of the exposed resist,
D Etching steps to transfer the structures into the insulator to form the support for conducting paths,
E Removal of remaining resist,
F Deposition of liners, also known as diffusion barriers, between insulator and conducting paths, and
G Deposition of metals to fill the paths and VIAs[1], which together build the connections in the circuit,
H Removal of excess metal.

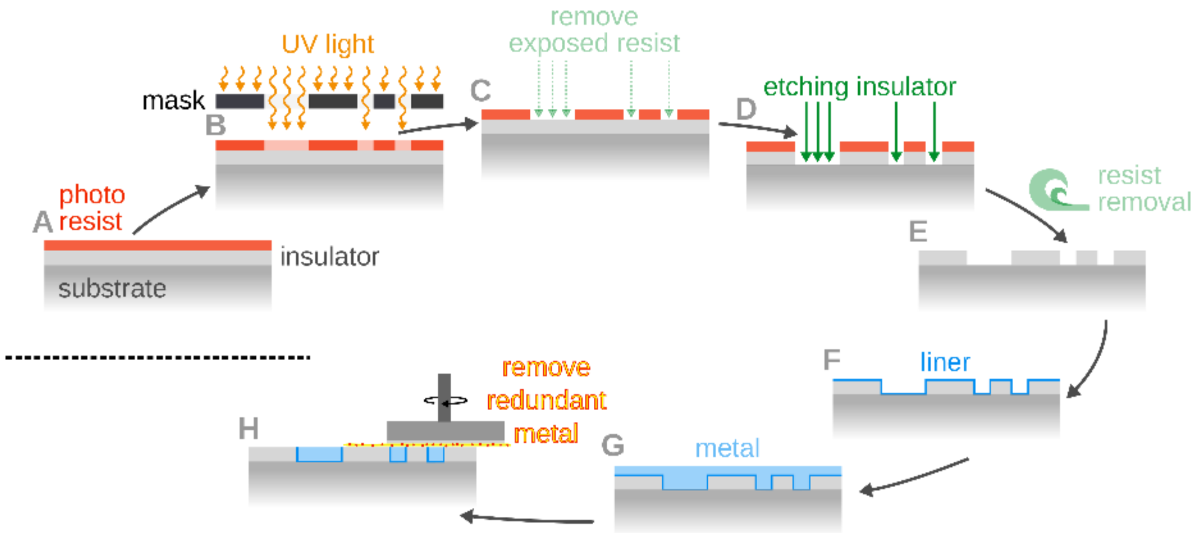

Figure 5.1: Production process for one exemplary layer of a silicon microchip. This coarse chain of deposition **A**, structuring **B** to **E**, and filling **F** to **H** is necessary to build one metal layer. These processes are repeated with different masks and dimensions to create a system of conducting paths.

Consistent with the order of the manufacturing processes, the structure stack starts from the

---

[1] Vertical interconnect accesses.

substrate, a mono-crystalline silicon (Si) wafer[2] and a dopant, i.e. boron (B) as acceptor or phosphorus (P) as donor. The first and the smallest functional elements are made of $CoSi_2$ contained in a very thin layer with a thickness of approximately 14 nm. This is followed by small electronic contacts named plugs. These plugs consist of tungsten (W) and they are present in two different heights of 250 nm and 500 nm, and their width measures 100 nm to 120 nm. To reduce the diffusion from the conducting material – the metal – into the insulating material and vice versa, all metal structures are surrounded by thin liners, alias diffusion barriers. This is important to avoid shorts between conducting paths and contacts. The tungsten plugs are surrounded by a thin titanium (Ti) coating – 10 nm to 20 nm – as liner. All these and the successive structures are embedded in the insulating material, which is based on silicon dioxide (SiO_2). Afterwards, a layer-wise system with alternating conducting paths and contacts, alias VIAs, made of copper (Cu) is built until they terminate in the outward contacts, which are made of aluminum (Al). Around all copper parts, the main liner material is tantalum (Ta) with a thickness of about 20 nm. Both liner materials Ti and Ta are partially nitrated. Each metal layer[3] is closed up by a silicon nitride (SiN)-based layer of 50 nm. With the consecutive building of conduction paths, the dimensions of these increase from the functional parts at the bottom to the connections at the top. The varying sizes, height and width, of the Cu conduction paths start from dimensions of approximately 180 nm×250 nm (width×height) at the bottom and successively increase with further steps to the top of the structure stack to approximately 1000 nm×750 nm. These circuits end with the according contacts to the motherboard or any other outer connection on the top. Consequently, the selection of specific devices, for example single resists or transistors, is realized by a conduction system from the connections at the top leading through the whole structure stack to the individual device at the bottom.

5.2 The Test Chip

The function of the test chip is the four-terminal sensing, alias Kelvin sensing. It is meant to precisely determine contact resistance of external cells, electronic components or thin films [118].

Additionally to this principal purpose, our specific test chip functions as control of different production processes, too. For that reason, there is no fully processed structure stack, from bottom to top, but the distinct regions differ in the choice of manufacturing processes. For example, in some region, the focus is set on the VIAs and thus these are produced at all heights, while other microchip structures are omitted. In other regions, the focus lies on different processing steps such as conduction paths in general or specific metal layers. The following overview summarizes the materials and expected structure sizes in the test chip. The elements in gray are present in the sample but are either too low in concentration to be imaged properly or are outside of the field of view, while materials below the detection limit or detectable energy range are not listed at all. Additionally, the deposited conducting materials crystallize in different orientations and grain sizes, which could have an influence on the functionality as well as on the

---

[2] Element specific properties, such as atomic numbers and X-ray emission lines, are listed in Tab. B.1 in the appendix.

[3] A metal layer is a layer of conduction paths, which are produced at the same time.

susceptibility to errors and is of interest for the analysis.

Most relevant components for the experiment:

Si: substrate and insulating material (as compound with O or N)
$CoSi_2$: logic structures, height: $\approx$14 nm
W: plugs, heights: $\approx$250 nm and $\approx$ 500 nm; width: $\approx$100 nm to $\approx$120 nm from bottom to top
Cu: conduction paths and contacts/VIAs, various sizes in width and height, starting from $\approx$200 nm and increasing up to the top of the structure stack
Ta: liner, $\approx$20 nm; partially nitrated
Ti: thin liner around W plugs and before final layer; partially nitrated
Al: final layer with 0.5 % Cu

5.3 The Test Chip as a Test Object

With the test chip we have a well-known and defined sample to develop new analysis techniques to investigate the different processing steps of nanoelectronic devices. Due to its sharp features, the clearly defined structures and the sharp transitions between the distinct materials, the microchip serves as a strongly scattering object. Different materials can be easily mapped using X-ray fluorescence measurements. Different crystallinity of the diverse structures allow for X-ray diffraction measurements. Some regions, like the copper conduction paths and contacts, form crystallites of different orientation. The aim here is to identify the grains' locations, sizes and orientations. Other elements form powdery structures, which are possibly stressed due to the embedding between other prominent structures. Overall, a micro chip is an excellent candidate for multimodal imaging.

In the future, the multimodal analysis approach of this project could be used for the verification of processes in chip production, e.g., by verifying crystallinities and strain in various parts of the devices. Especially nano-grain mapping inside of VIAs or plugs might be of particular interest for operando studies of electromigration in integrated circuits.

For its application as a test object, the whole wafer was thinned down to 150 µm and the single dies[4] were separated by a diamond saw. We took one of these dies for diverse analyses. The sample for the multimodal experiment was prepared according to the needs for a nanotomographic experimental setup, see Sec. 3.2. For this reason, a cone-shaped structure stack was milled out of the test chip using a focused ion beam (FIB) at the DESY NanoLab, see Fig. 5.2. All following steps to image the inner parts of this structure stack, alias 'cone', were conducted non-destructively, i.e. the cone was not further cut at any time. The diameter of this cone is

---

[4] 'Die' is the technical name for a microchip.

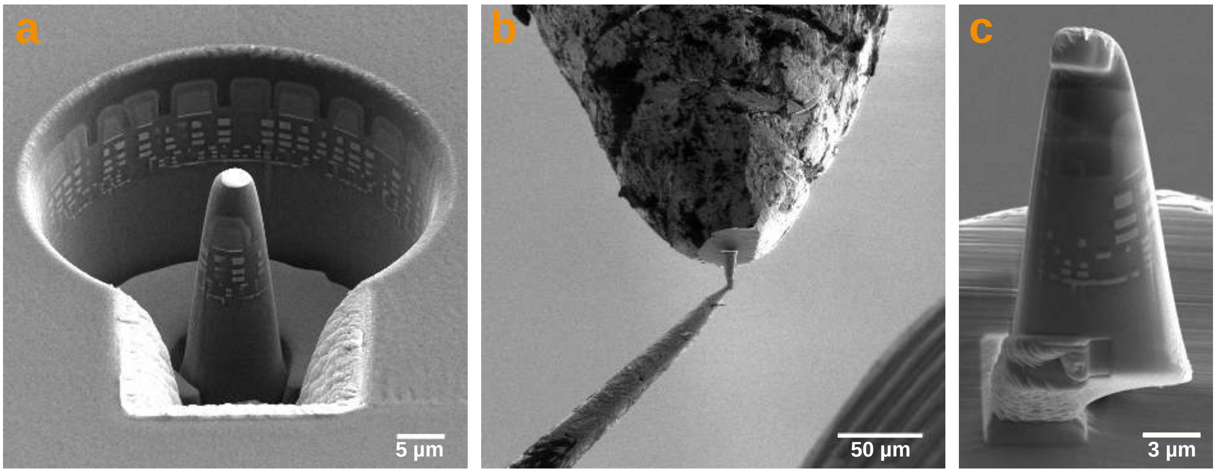

Figure 5.2: SEM images of process from milling a structure stack out of the microchip using a focused ion beam (FIB) (a) and attaching it with a needle to the tip of the sample holder (b), here both holder and sample are upside down. (c) shows the structure stack being fixed to the tip of a sample holder.

approximately 8 µm at the bottom of the structure stack, and shrinks to approximately 5 µm at the top.

5.4 Aim of Analysis

The fundamental goal of this project was the development of multimodal imaging using X-ray absorption, X-ray fluorescence and X-ray diffraction. We aimed to investigate the different contrasts and how these can be combined in order to investigate the 3D elemental distribution as well as the 3D grain distribution including their orientation and size. From the perspective of the manufacturer of the test chip it is of interest whether we can detect and locate defects, define what these defects are made of as well as detect potential sources for failures. Furthermore, the manufacturer of this test chip is interested in preferably non-destructive techniques to find specific defects or particles.

The standard imaging methods in semiconductor industries are well known and well established: electron microscopy delivers excellent views of specific cuts into microchips with a higher spatial resolution than currently achievable using X-rays. But the downside of these methods for failure analysis is that despite a very precise preparation of the area of interest, the relevant part of approximately 10 nm to 50 nm may accidentally be destroyed in a cut-and-slice imaging scheme or by the localization of the relevant position. X-ray tomography of a milled cone or structure stack, in turn, may be a solution to that problem, as the region of interest can be considerably bigger and can be analyzed without further destruction.

CHAPTER 6

High-Resolution Imaging with Ptychography and Electron Microscopy

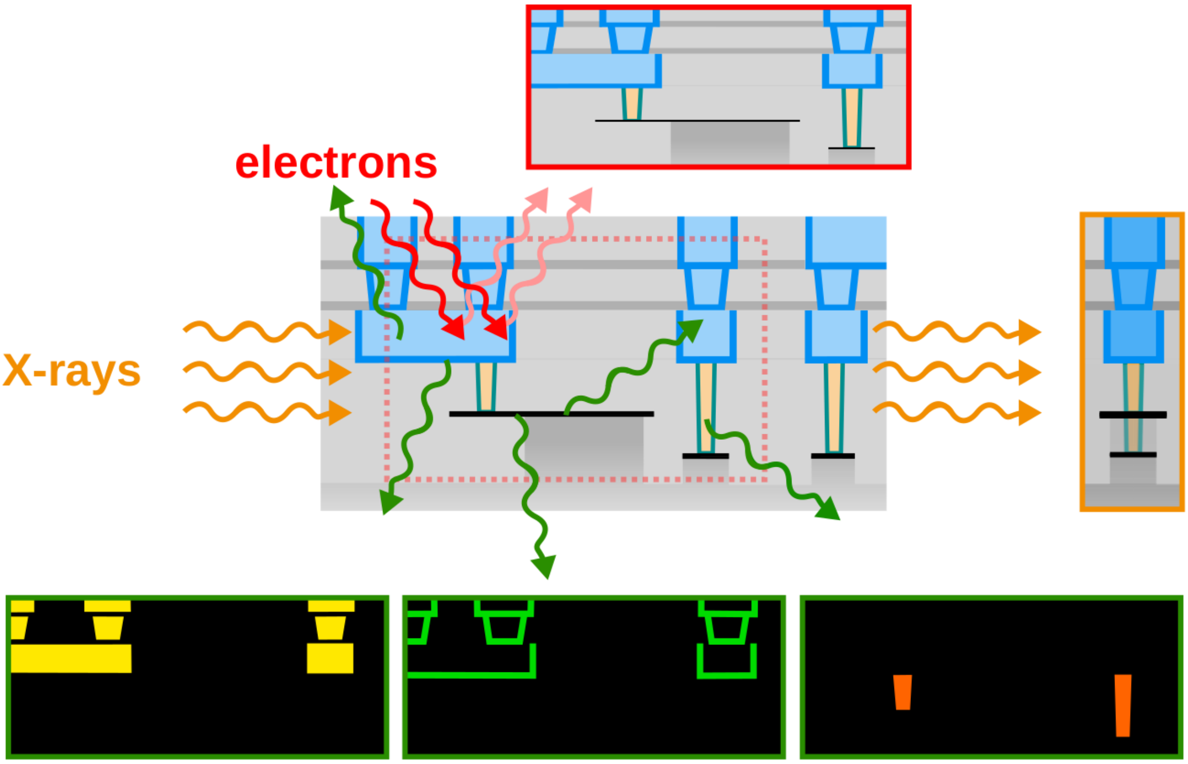

To image internal structures of the test chip with high spatial resolution, we studied it with two complementary imaging techniques: X-ray ptychography, see Sec. 6.1, and electron microscopy (EM), see Sec. 6.3. These images gave first impressions of the arrangement of the structures and were used to measure the structure sizes. Ptychography was applied to both an unprepared test chip and the extracted cone section, which is used for the multimodal experiment, see Sections 6.1.1 and 6.1.2, respectively. For the ptychography part, the achieved spatial resolution has been carefully analyzed, see Sec. 6.2.

In Sections 6.3.1 to 6.3.3, the results of imaging with electron microscopy of cross sections of the chip, including an energy dispersive X-ray spectroscopy (EDX) analysis, and results of a slice-and-view sequence are presented. This chapter closes with a comparison of both imaging methods, in Section 6.4.

6.1 High-Resolution Imaging in 2D by X-ray Ptychography

As preparation of the multimodal experiment, we used two different experiments[1] to characterize the microchip under different perspectives. The microchip was imaged ptychographically[2], first as the complete unprepared microchip and second as a smaller piece of it cut out of the structure stack, as described in Sec. 6.1.1 and Sec. 6.1.2, respectively. The imaging of the unprepared chip was normal to the chip surface, which means that the chip surface was perpendicular to the optical axis of the probing X-ray beam. Hence, it provides a top view through the complete structure stack. In turn, the cut out structure stack allows a side view of the structures, as it was probed parallel to the structure layers and so perpendicular to the view of the unmodified chip. This milled structure stack is also the sample for the multimodal tomographic experiment, detailed in Chapters 7 and 8. The following table, Tab. 6.1, shows the parameters of the experimental studies performed in advance of the multimodal experiment:

synchrotron beamline	Diamond I13-1	PETRA III P06 Nano
date	Jun 2016	Oct 2016
energy	8.23 keV	16.0 keV
monochromator	QCM[a]	DCM
HO mirror(s)	yes	no
optics	CRL	NFL
focal size	138 nm	(h) 96 nm × (v) 98 nm
sample to detector distance	5.87 m	2.12 m
detector	Merlin	Eiger X 4M
pixel size detector	55 µm	75 µm
scan mode	step	on-the-fly/continuous
field of view (FOV), v × h	2 µm × 2 µm	2 µm × 8 µm
number of steps	20×20	160×200
integration width (fly scan if $<$10 nm) or step size	100 nm	2.5 nm × 40 nm
exposure time per step	2 s	0.02 s
cropping of diffraction pattern	512×512	512×512
recon. pixel size	31.419 nm	4.278 nm

Table 6.1: Main parameters of the different ptychographic experiments.

[a] Quadrupole crystal monochromator (QCM) or ”four-bounce monochromator, containing a set of Si(111) and Si(311) crystals” [85]

When looking at the results presented in the following, it needs to be considered, that in the amplitude image, darker structures correspond to stronger absorption. For images of the reconstructed phase shift, darker structures correspond to optically denser regions of the sample, which cause a stronger negative phase shift. Ptychography is very sensitive to changes in the reconstructed object phase, hence the reconstructed phase shift usually reveals more details than the reconstructed object amplitude.

---

[1] These experiments took place at I13-1 at the Diamond Light Source and at the P06 nanoprobe at PETRA III.

[2] An introduction to X-ray ptychography is given in Sec. 3.1.1.

6.1.1 Overview over Different Chip Regions

During our beamtime at I13-I [85] at the Diamond Light Source in Oxfordshire, Great Britain, we took overview scans of different areas of the test chip. The aim of this beamtime was two-fold: We aimed to get detailed information about the composition of selected areas as well as the differences between them, and to understand current limitations in terms of spatial resolution and sensitivity regarding the different structures and materials. The selected scan areas, shown in Fig. 6.1, correspond to chip regions varying in the passed fabrication steps, as mentioned in Sec. 5.3. Thus, none of these areas represents a fully processed structure stack. The specific X-ray optical parameters under which these images were obtained are listed in Tab. 6.1. As written in Sec. 3.1.1, the ptychographic reconstructions provide the transmission function of the sample as well as the probe function at the sample position. From this result, the illumination was propagated and the Gaussian width of the focus' central lobe, produced by the CRLs, was determined to 137.9 nm (FWHM). More details to the CRL focus analysis are presented in appendix A.1.

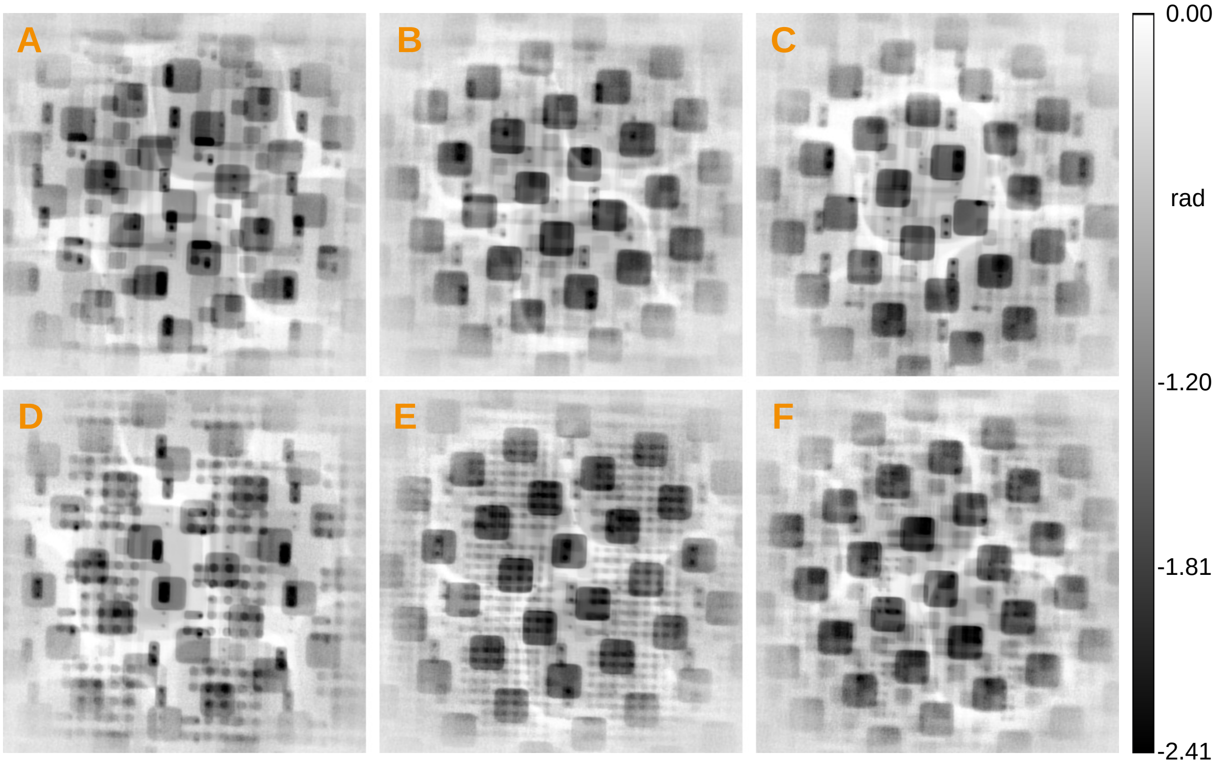

Figure 6.1: Ptychographically reconstructed phase contrast images from different regions of an unprepared microchip. The size of the images corresponds to 12.6 µm×12.6 µm. The scanned area in the center of the images is only 3.0 µm×3.0 µm.

We used region C, see top right image in Fig. 6.1, for the multimodal experiment. Figure 6.2 shows a zoom of the reconstructed phase (left) and the modulus (right) of the transmission function of the sample. In the modulus, the W plugs – smallest dots in these figures – and the Ta liner around the Cu structures appear darker since they absorb X-ray photons stronger than other structures of the same thickness, such as Cu. Thicker structures of the same material cause a stronger reduction of the transmitted amplitude and a stronger phase shift, hence appear darker in both phase and modulus images.

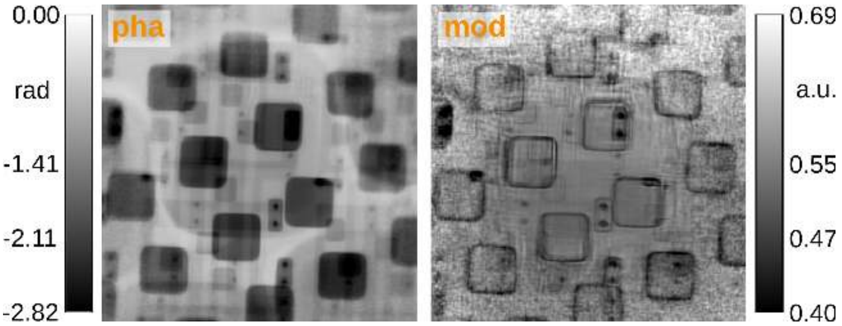

Figure 6.2: Modulus (mod) and phase shift (pha) of the transmission function for region C. The image dimensions are 8.0 µm × 8.0 µm. The object phase emphasizes the different materials and thicknesses, while the object modulus highlights the liners.

6.1.2 Pre-Characterization of the Milled Structure Stack

In preparation of the multimodal experiment, the prepared structure stack was imaged at the P06 nanoprobe end station PtyNAMi at PETRA III using X-ray ptychography. All scans in this section are reconstructed including a numerical upsampling of the diffraction patterns, see Sec. 3.1.2.

In Fig. 5.3 an overview image of the sample is shown, obtained by stitching [119] two ptychograms, one covering rather the horizontal, and another the vertical direction of the sample.

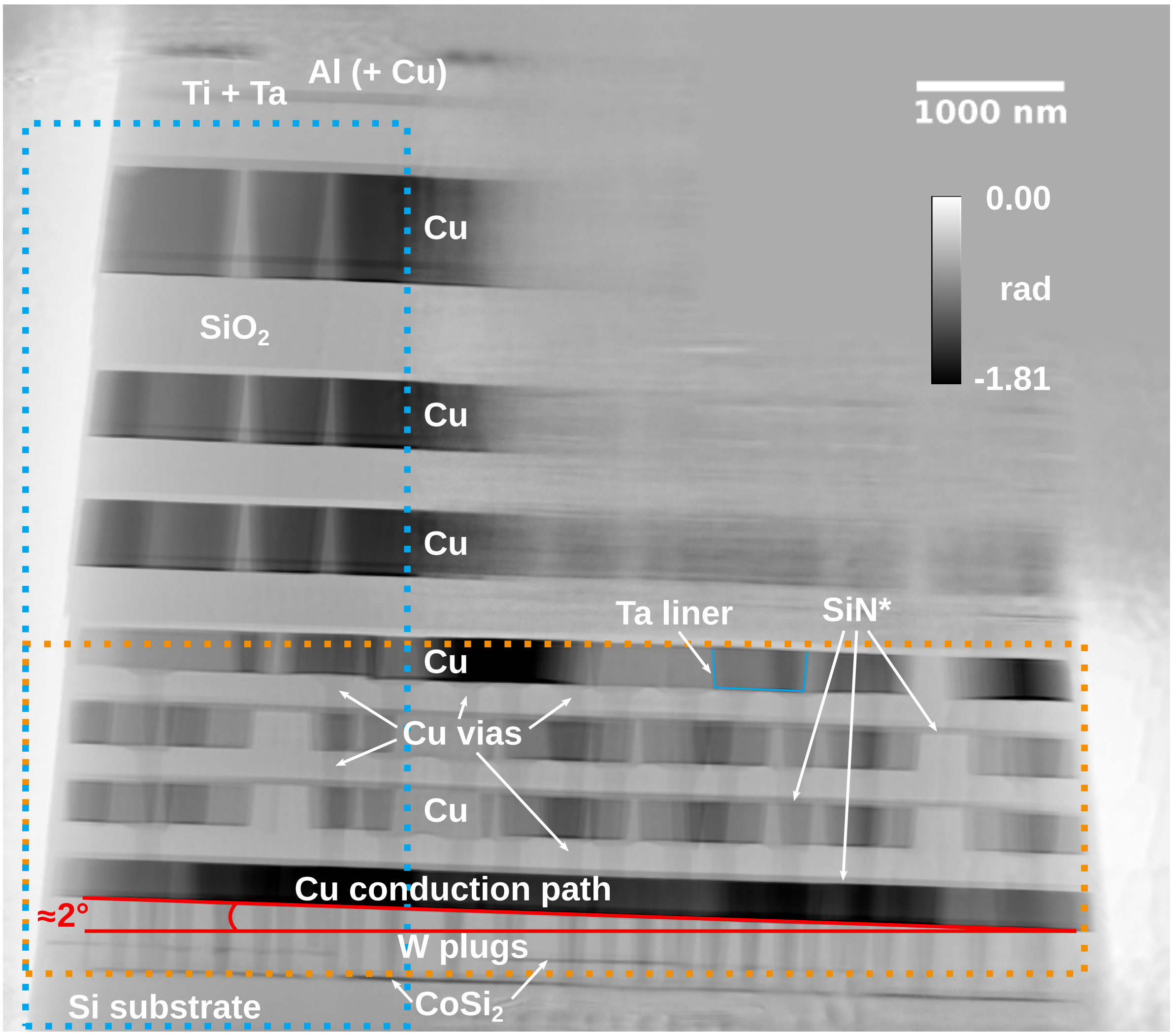

Figure 6.3: Combination of two reconstructed phase images, stitched together. The regions of the two scans are marked by a blue and an orange dotted frame for the vertical and the horizontal extended scan, respectively. The area of the horizontal scan is the same as for the multimodal experiment.

The main parameters are listed in Tab. 6.1. Differences in the specific scan parameters of the two presented scans are summarized in the following table:

scan	field of view	steps	exposure time
vertical	7.0 µm×2.5 µm	140×50	0.3 s
horizontal	2.0 µm×8.0 µm	40×160	0.3 s

Table 6.2: Scan parameters of the ptychographic scans shown in Fig. 6.3.

Figure 6.3 nicely illustrates various structural components of the test chip, which were already introduced in Sec. 5.1. At the bottom are thin $CoSi_2$ structures, which are contacted by the W-plugs above. Further up these structures are several layers of alternating conduction path and VIAs, each made of Cu, surrounded by a Ta liner. Each metal layer is closed by a thin SiN-based layer. Above the horizontal scan area, highlighted by the dotted orange frame, there are no more VIAs in this chip region, where there usually are VIAs till the last metal layer, while the Cu conduction paths continue. The sizes of the structures are considered in Sec. 6.2.2 in the context of the spatial resolution.

The pixel size of all ptychographic reconstructions, shown in images between Fig. 6.3 and 6.18 is 4.28 nm. The achieved NFL focus is analyzed in appendix A.2.

During this beamtime, the sample was imaged from different rotation angles ω. Figure 6.4 shows modulus and phase shift of the transmission function of three of these angular projections. All three projections were scanned with 200×160 steps over 2.0 µm×8.0 µm in y×x, in a flight-scan mode with an acquisition time of 0.02 s per scan point. In the scan in Fig. 6.4c, the main scanned part was substrate. For that reason, the image is cut to the part containing structures.

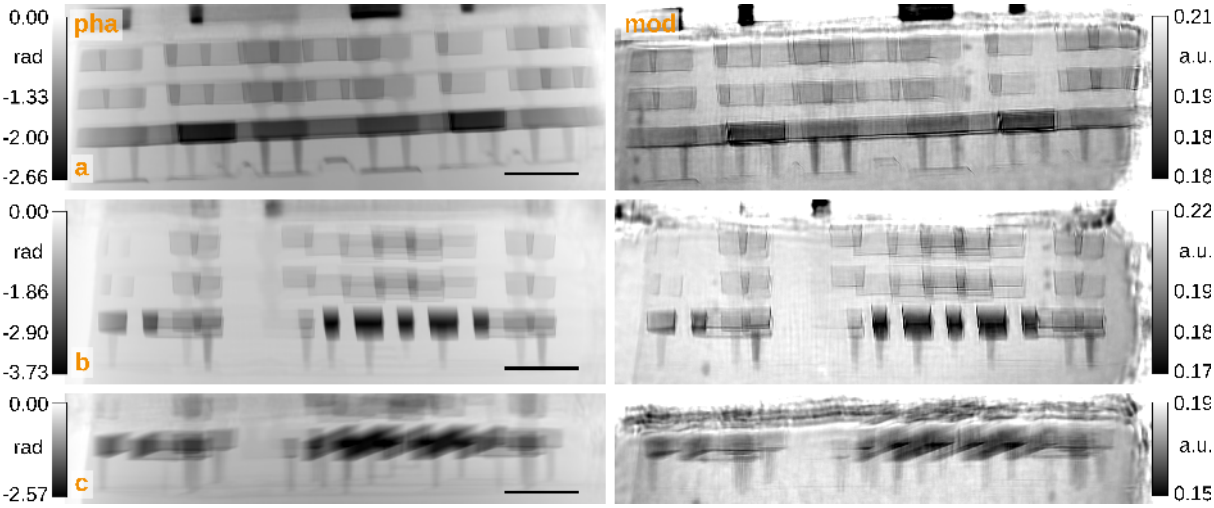

Figure 6.4: Phase (pha) and modulus (mod) of the transmission functions from the ptychographic reconstructions, positioned left and right, respectively. The scale bars represent 1.0 µm. The angular distance $\Delta\omega$ between (a) and (b) is 90° and between (b) and (c) it is $\simeq$5°.

The field of view exceeds the scanned region. For that reason, the modulus images show some reconstruction artifacts at the top, while the phase images show that the recorded information goes beyond the scanning grid. The $CoSi_2$ structures at the bottom of the structure stack are

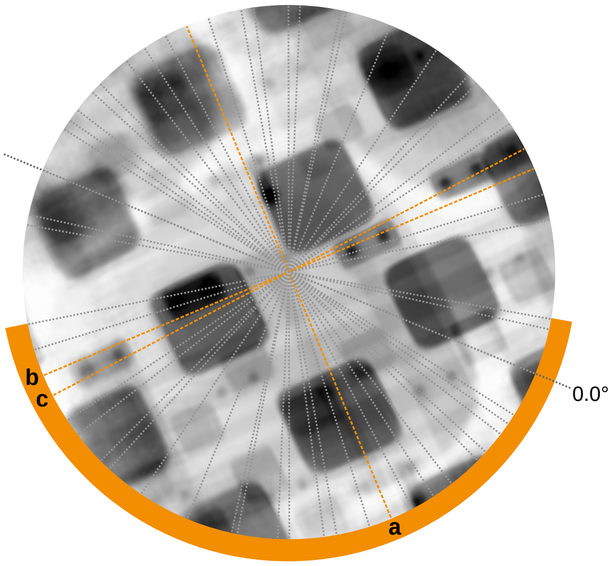

Figure 6.5: The specific viewing angles are indicated by dotted grey lines and superimposed on a ptychograph measured in planar geometry as shown in Fig. 6.1. The three orange lines mark the ptychographs of Fig. 6.4. The orange section outside the structured circle shows the angular coverage of the scans.

barely visible in the modulus, but are well presented in the phase shift. On the opposite, the liners around the conduction paths are more pronounced in the modulus, but only slightly visible in the phase shift. Further projections, 19 in total, showing the phase of the transmission function only, are presented in appendix C. Figure 6.5 shows the angular positions of the recorded ptychographs.
The sample is mounted to the tip of the sample holder with a slight tilt. Additionally, we faced a problem with the scanner motor, that showed some behavior of ω-depending slanting movements. We were not able to fully distinguish the influences of the actual sample tilt and the slanting motor movement[3]. A tilt is clearly visible at several angular positions and its maximum was determined being around 2°.

6.2 Determination of Spatial Resolution

The spatial resolution in the reconstructed images as well as the potential spatial resolution of the data itself can be determined in different ways, as described in Sec. 3.3. In the following, some of the ptychographic scans are representatively analyzed in terms of spatial resolution.

6.2.1 q-Space Resolution Estimation

The detected signal in the diffraction patterns can be used to estimate the spatial resolution which in principle can be achieved with data. As the highest spatial frequencies correspond to the smallest features, the detected signal at large scattering angles need to be considered for resolution estimations. This is illustrated in Figures 6.6 and 6.7. The first example shows some visible speckle pattern and the corresponding feature size in real space. A speckle pattern is the result of the propagated multiplication of probe and the object function in real space, which corresponds to the convolution of their Fourier transforms in reciprocal space. By the energy, the distance between sample and detector as well as the pixel size of the detector, the spatial

---

[3] The usage of the interferometer system would have helped to decouple the two causes of a tilt in the result figures. Unfortunately, during these experiments, we could not use them.

frequencies of the scattering signal can be displayed in a diffraction pattern. These correspond to sizes in real space, as marked with rings in the diffraction pattern. To increase the visibility of the scattered signal above noise, ten similar far-field diffraction patterns, from one of the ptyochgraphic scans presented in the previous section, are summed up, see Fig. 6.6. The visible signal farthest from the center position shows the best possible spatial resolution obtained with the data. It is clearly visible, that some signal above noise is going beyond the 5 nm ring. As the structures in the microchip have clear transitions rather horizontally than vertically, the signal spreads predominantly in vertical direction in the far field. The signal in the horizontal direction clearly exceed the ring marking 15 nm spatial resolution in some selected diffraction patterns. Our measurements were conducted in air. In the second example, shown in Fig. 6.7, the diffraction patterns from structured regions, presented by (b) and the orange graph in (a) were compared to empty regions, presented by (c) and the blue graph in (a). The graph and the diffraction pattern of the empty region show, that even without any sample in the beam, there are scatter effects from the interaction with air particles and components of the setup. The 'diffraction pattern' of the empty region, from scan points without any present sample, can be regarded as background. The graphs show the profiles along the boxes in both diffraction patterns, see markings in (b) and (c), starting at the center and following the direction of the arrows. The curves are disturbed by a gap between the detector panels, where no signal can be detected. These are at around 0.08 Å^{-1} and are approximately 0.01 Å^{-1} wide. For the estimation of the spatial resolution, the signal has to be clearly above the noise, which is obviously fulfilled around 0.1 Å^{-1}, corresponding to 6.3 nm, and even beyond this. The results of the actual reconstructed spatial resolution usually do not achieve these values due to the signal to noise ratio and other inconsistencies for example motion artifacts.

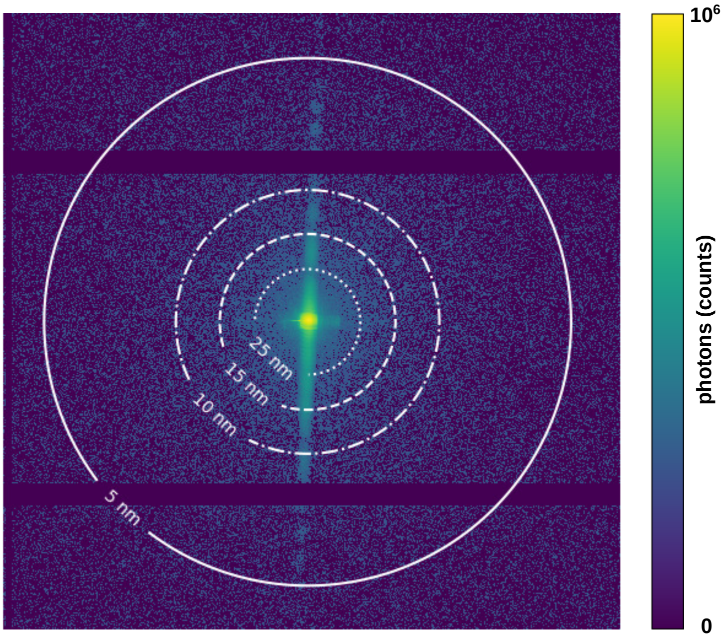

Figure 6.6: Far-field diffraction pattern obtained by summing up ten representative single patterns showing a strong scattering signal. They are taken from the horizontal scan of Fig. 6.3, marked by an orange frame. The rings mark the achievable spatial frequency.

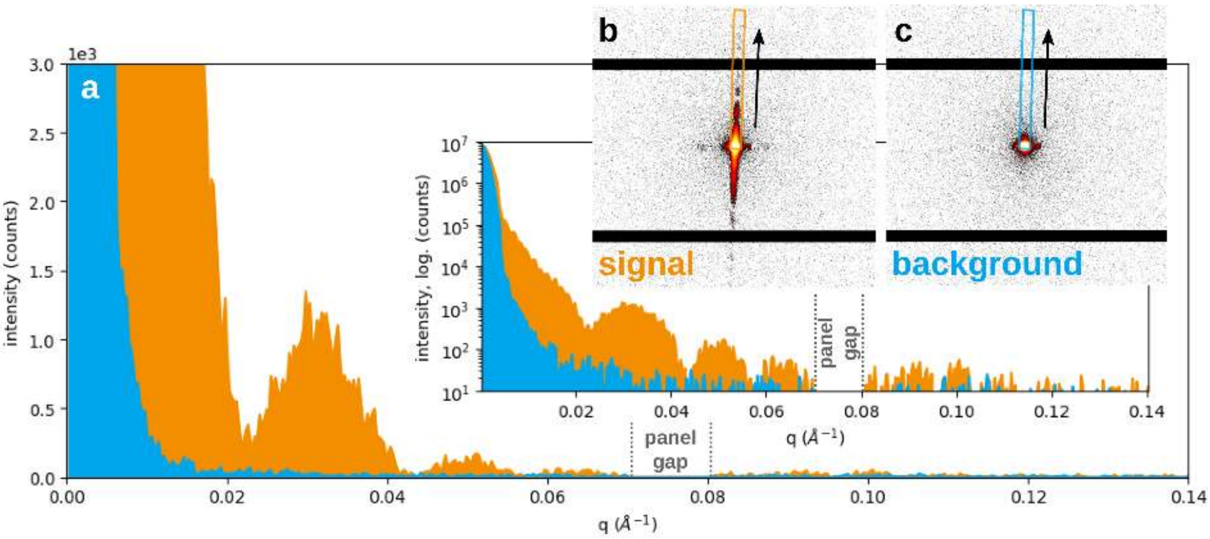

Figure 6.7: Signal compared to background (a) of one exemplary diffraction pattern with diffraction signal (b) and an empty pattern (c), which only contains background scattering. The linear plot (a) used the ten pixel wide line from center to the top in both diffraction patterns (b) and (c) with the boxes indicating the line positions, the inset shows the same plot on a logarithmic scale.

6.2.2 Known Features and Edge Contrast Analysis

Other ways to determine the spatial resolution of a dataset are applied to reconstructed images. In this regard, the following steps are the recognition of known features, determination of their reconstructed size and the analysis of edge contrasts.

The projection for these analyses, see Fig. 6.8, depicts the phase image of the transmission function and is not just a surface view. As a consequence, the determined sizes can deviate from the expected sizes when the sample is slightly tilted. In this case, structures appear extended in projection. Also when several of the same structures behind each other are slightly shifted to each other, they cause a comparable effect of extending the projected structure size.

For a coarse estimation of the spatial resolution, the smallest available features serve as reference. These are 14 nm $CoSi_2$ structures at the very bottom, marked by lines 6 and 7. The next in size are the Ta liner around the metal layers with 20 nm, marked by lines 1 and 2. Both these structures are visible. Deviations from their appearance of the thickness occur from their lateral extension. The $CoSi_2$ structures are widespread, while the liner structures are only available around the metal parts, which are more restricted in size. With a slight tilt of the sample, the more extended structures appear thicker than the structures with limited size.

The imaged sizes of the structures are analyzed from line profiles through multiple structures of the projection image, marked by lines in Fig. 6.8, and compared to the expected structure sizes, given by the chip manufacturer. The determined (det.) values corresponding to the markings and their expected (exp.) structure sizes are listed in Tab. 6.3. Since the lines 14 and 15 cover three adjacent structures – Ta liner, Cu conduction path and SiN-based layer, the sizes of these are presented from bottom ($\sim .1$) to top ($\sim .3$). Additionally, an overview of all line plots and their derivatives is shown in Fig. B.2 in the appendix, and so are the plots for lines A and B, see Fig. B.1, showing the cylindrical shape of the sample. The table reveals that the measured sizes

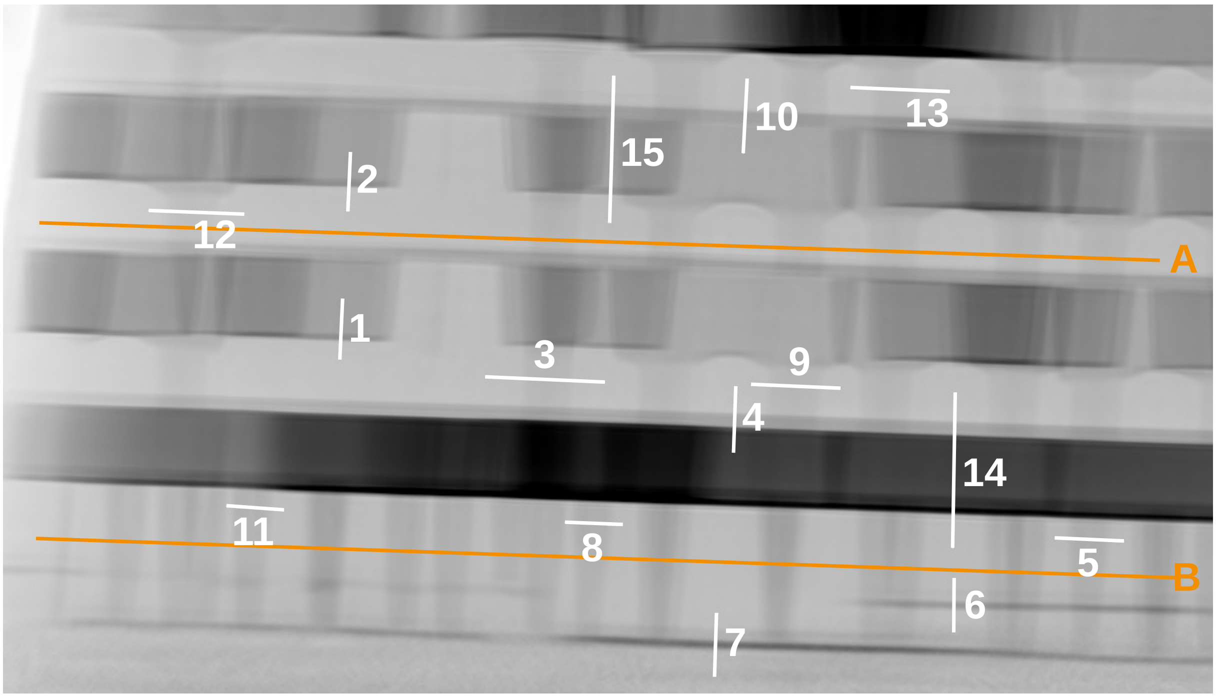

Figure 6.8: Ptychographic reconstruction, showing the phase contrast, is used to determine the sizes of different structures at 15 different, marked positions. The plots to the two long orange lines parallel to the structures can be found in appendix B.1. For structure description, see Fig. 6.3.

are close to the expected dimensions.

li.	det.	exp.	li.	det.	exp.	li.	det.	exp.	line	det.	exp.
1	21.5	20	6	22.0	14	11	128.4	120	14.3	46.9	50
2	23.6	20	7	26.0	14	12	156.8	140	15.1	24.3	20
3	156.8	140	8	122.0	120	13	137.9	140	15.2	279.9	250
4	47.8	50	9	170.0	140	14.1	20.8	20	15.3	44.1	50
5	123.4	120	10	44.6	50	14.2	247.5	250			

Table 6.3: Determined (det.) versus expected (exp.) structure sizes in nanometer at lines (li.) in Fig. 6.8.

To define the widths of transitions between adjacent materials, alias the edges, we derived the line profiles and then we took the full-width-at-half-maximum of the fitted Gaussian functions for each transition. This resulted in a mean value of 20.7 nm for the transitions and a standard deviation of 14.8 nm with the smallest transition being 8.8 nm. There is also the fact that there are transitions where the materials partially diffuse into each other. In these cases, the transition width is of course much worse than for very sharp edges. Due to different influences like tilts and diffusion, a clear statement about the achieved spatial resolution is difficult. But these influences also partially explain the deviations of the measured to the expected structure sizes.

Nevertheless, the images and the data show that a spatial resolution better than 20 nm is obtained. For the method of recognizing known features, the spatial resolution determination is restricted to the smallest structures with 14 nm height as significant benchmark. The structure measurements did not surpass 21.5 nm. In comparison to that, the smallest determined transition was 8.8 nm.

6.2.3 Spatial Resolution by FRC

To substantiate the results of the spatial resolution from the two previous sections, the ptychographic reconstructions were analyzed by Fourier ring correlation (FRC), the method is described in Sec. 3.3.4. Due to the lack of a second scan at the same position or a projection from the opposite side, two half data sets of one scan were used for the FRC, see Fig. 6.9.

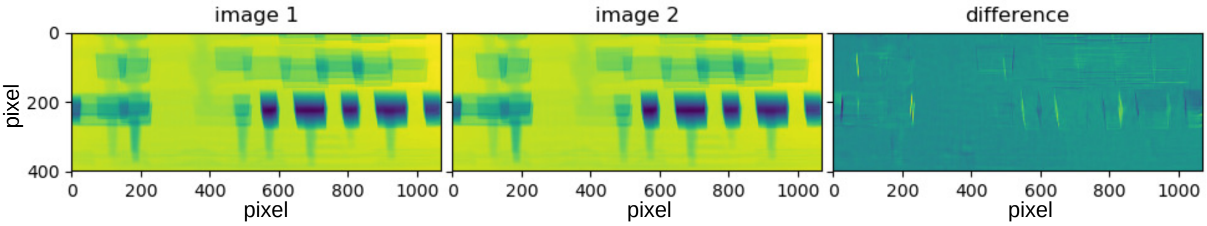

Figure 6.9: This exemplary scan was taken for the Fourier ring correlation. Image 1 and image 2 are the two individually reconstructed half datasets of the same scan. The image on the right shows the difference of these two scans. The sizes are given in pixels.

The result of the comparison of these two half data sets is plotted in Fig. 6.10. As the used image is relatively small and only limited features are visible, not all spatial frequencies could be covered and sufficiently averaged, which results in a spiky curve. In a 3D analysis, due to more sampled directions, more spatial frequencies would be sampled and the curve would be smoother.

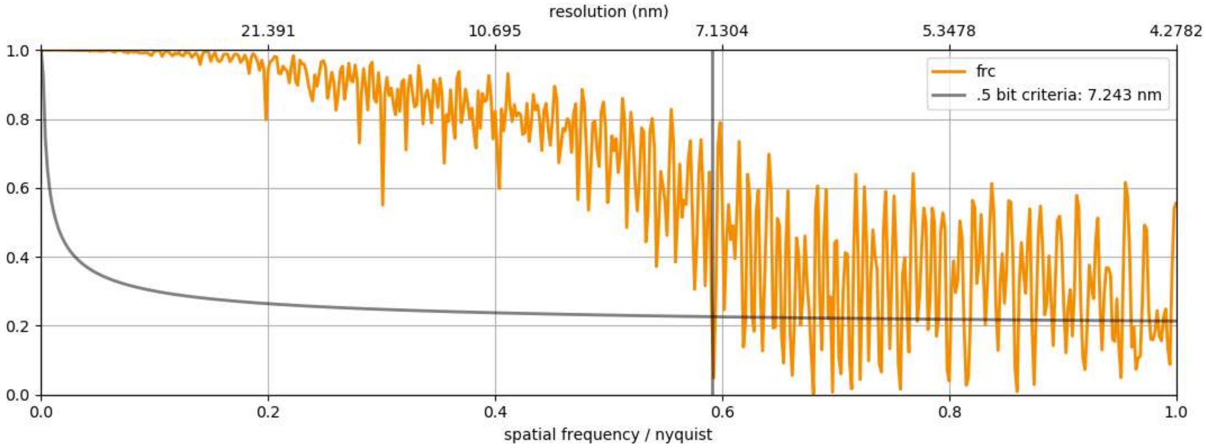

Figure 6.10: Fourier ring correlation result for the given scan, see Fig. 6.9.

The FRC estimation resulted in a spatial resolution of 7.24 nm for this data set. From the same analysis, the SSNR estimation was determined being close to the FRC result, see Fig. 6.11.

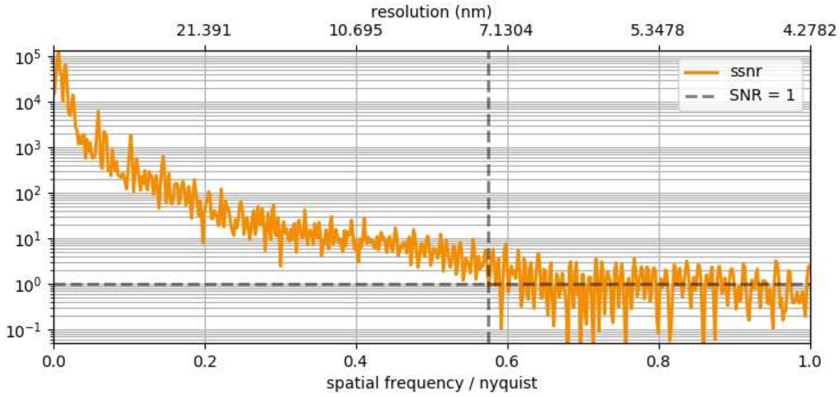

Figure 6.11: Signal to noise ratio of the presented scan, shown in Fig. 6.9, taken for Fourier ring correlation.

6.3 Imaging by Electron Microscopy

The spatial resolution achievable with EM exceeds the capabilities of X-ray microscopy. However, electrons have a very small penetration depth in most materials. In comparison, X-ray imaging based on ptychography can provide images with a spatial resolution down to around 10 nm while still passing through a thick sample. This means, that details can occasionally be better resolved with electron imaging, but the sample does not need to be cut so thin when imaging with X-rays. Hence, both techniques are used complementarily to catch the broader picture. Furthermore, the access to electron microscopes is easier and the imaging much faster. For the given reasons, we used electron microscopy to provide a preview of the structure arrangement and to reveal, what cannot be resolved with X-rays. For that, we cut the test chip at different positions and imaged the surface of these cross sections. Hence, we used these cuts to determine the structure sizes by EM and different elements by EDX. The milling of the cross sections as well as of the free standing structure stack for the multimodal experiment was done by a focused ion beam (FIB) at the DESY NanoLab[4].

6.3.1 Cross Sections of the Structure Stack

With the cross sections, we could – in this case destructively – analyze the structures in shape and appearance. Additionally, we could measure the sizes of the structures presented in the current area of the microchip. This information is used to compare and evaluate the results from X-ray experiments, shown in Secs. 6.1 and 6.2.

Differences between electron and X-ray microscopy are shown in Sec. 6.4. In the scanning electron microscope (SEM) images in Fig. 6.12, the surface of the milled regions is visible, and different gray scales depict different atomic masses. Consequently, materials with heavier nuclei appear brighter, since they cause more electrons to scatter from them[5]. For example the Cu (Z = 29) conducting paths show up in light grey, while W (Z = 74) plugs are even brighter, almost white. The Ta (Z = 73) liner also stand out from the Cu-parts with high contrast and appear in a similar gray scale as W.

---

[4] The milling and imaging was done by the group of Thomas Keller, especially by Satishkumar Kulkarni. I participated in the milling procedure and guided him to the regions of interest.

[5] The emphasis of different masses is visible in images generated by the detection of backscattered electrons using an in-lens detector called T1 [120]. SEM images, which rather present topographic differences predominantly use secondary electrons, detected by the Everhart-Thornley detector (ETD).

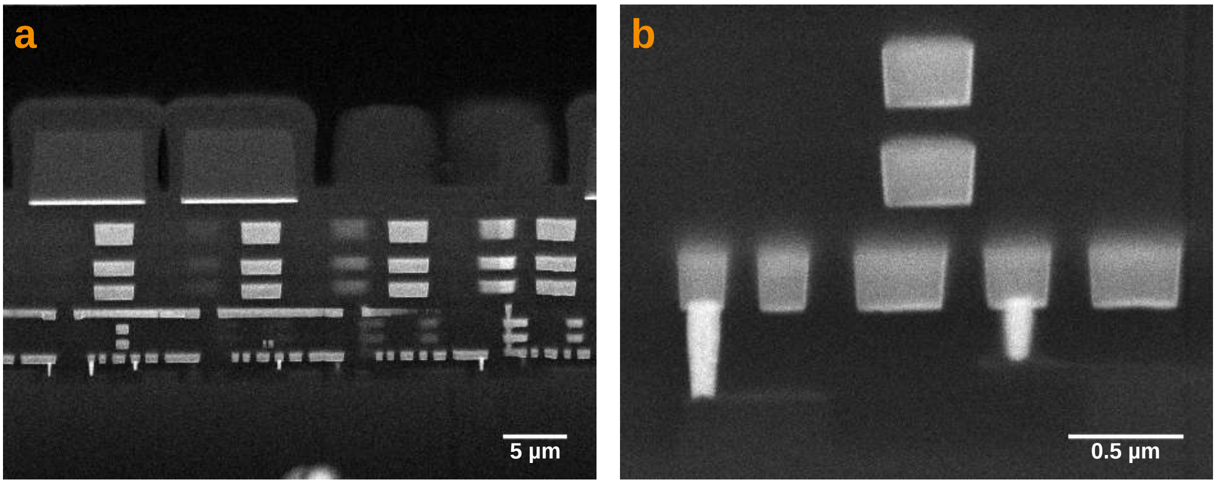

Figure 6.12: These cross sections of the microchip, imaged with electron microscopy, reveal the inner functional parts of the device at the cut position in a coarse view (left) and a more detailed view (right).

6.3.2 Energy Dispersive X-ray spectroscopy

With respect to the multimodal experiment, see Chapters 7 and 8, eight different regions were additionally analyzed by energy dispersive X-ray spectroscopy, short EDX, to gain an overview of the contained elements and their distribution within the sample.

The energy dispersive X-ray spectroscopy has the same working principle as X-ray fluorescence except the excitation of the bound electrons is realized by energetic electrons from the electron gun instead of X-ray photons generated in an undulator. Moreover, the cross sections of the emitted photons in an EDX experiment is weaker than in an X-ray fluorescence (XRF) experiment. Furthermore, with the additional EDX analysis the strengths of the electron microscope versus the X-ray microscope and the chemical analysis of each are compared in Section 6.5.

The results of three regions are presented in Fig. 6.13, showing the selected regions as electron micrographs and the corresponding EDX results in Fig. 6.14. The remaining regions can be found in the overview gallery of the results of this analysis in appendix D. The EDX results of the cross sections are repeated in the appendix.

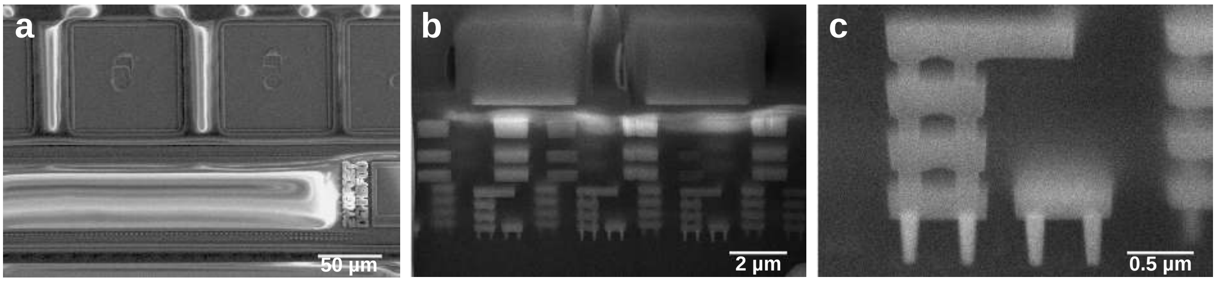

Figure 6.13: Electron microscopic images, representing three different areas with different magnifications for the EDX analysis, see results of (a) to (c) in Fig. 6.14.

The EDX results are shown from top to bottom in Fig. 6.14. The first image in Fig. 6.13 and the corresponding EDX images in Fig. 6.14a show the top view onto the chip, while the other two regions represent cross sections within the microchip. The images (a) and (b) in Figure 6.14 show the elements Al, Si, Cu and Ta, while (c) shows the same elements but W instead of

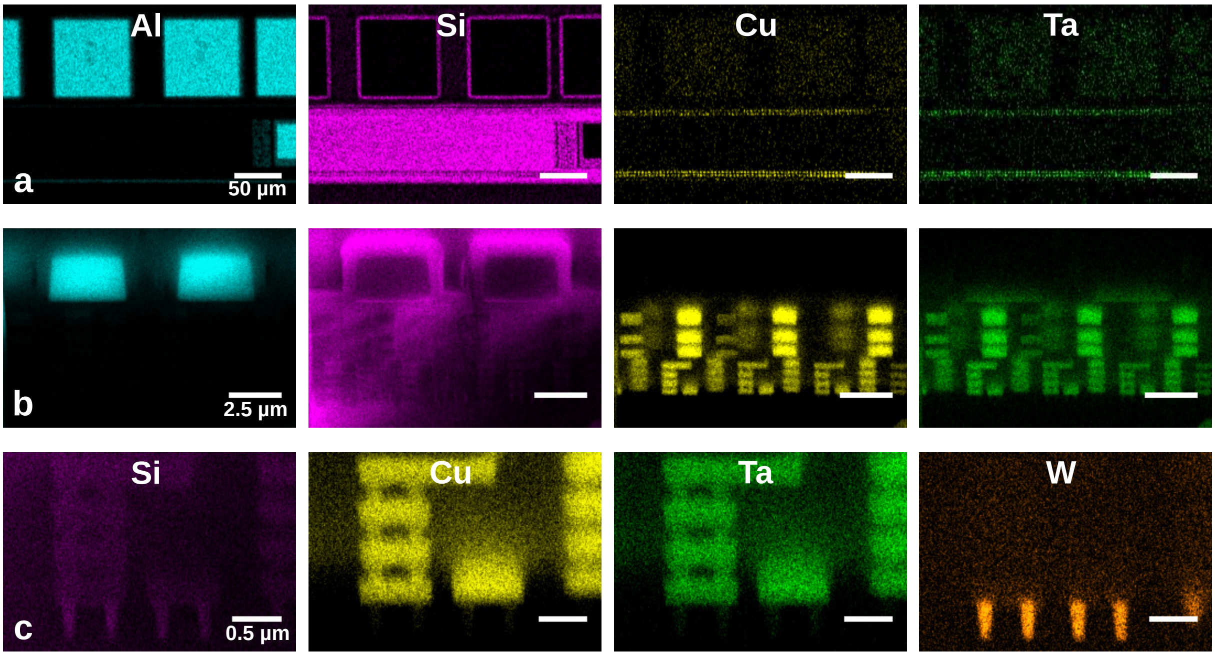

Figure 6.14: Results of the EDX analysis of the microchip in top view (a), on the milled surface (b) and on the milled surface with higher magnification (c), compare EM images in Fig. 6.13.

Al. While (a) and (b) are concentrated on the top part of the structure stack, the element Al is included instead of W, and vice versa for (c), focusing on the bottom of the structure stack. While Figure 6.14 (a) highlights the top part of the electronic device mainly consisting of Al structures, vertical internal structures – built upon various elements such as Cu, Ta, and W – are emphasized in (b) and (c). For some cross sections it was also searched for the elements Co and Ti, but neither could be resolved. The concentration of these elements seems to be too low for the parameters of the setup[6]. In comparison, the Al image (light blue) highlights the big contact pads at the very top. In all images, except top row (a) in Fig. 6.14, Si was detected but rather weakly presented, despite its ubiquity through the whole chip as substrate and insulator material. In contrast, Cu is clearly resolved as it is the main content of the conduction paths. Even Ta could be clearly resolved at the metal structures, despite that it only functions as liner around them. The W plugs at the bottom are clearly visible as well.

6.3.3 Electron Microscopy Slice-and-View

Based on the microchip cross sections, the DESY nanolab started a slice and view project. Beginning with a cross section in the structure stack, the micro chip is alternatingly imaged using SEM and milled down using a focused ion beam (FIB). In total 80 imaged slices with a milling distance of 20 nm were generated with this method. The milled structures are lost and structural changes in the volume between two frames cannot be imaged. All the single images were put together to build a 3D stack. The slices in this stack were aligned and the structures were segmented by a former Nanolab summer student John O'Sullivan using Avizo (Thermofischer

---

[6] We faced the same challenges in the multimodal experiment with X-ray fluorescence results. In that case, the detector position was traded off the elements emitting a low dose of photons against the elements emitting a huge amount of photons, see Sections 7.2.2 and 8.3.2.

GmbH) [121, 122]. With the results gained by the EDX analysis, the chemical information was added to the reconstructed physical structures.

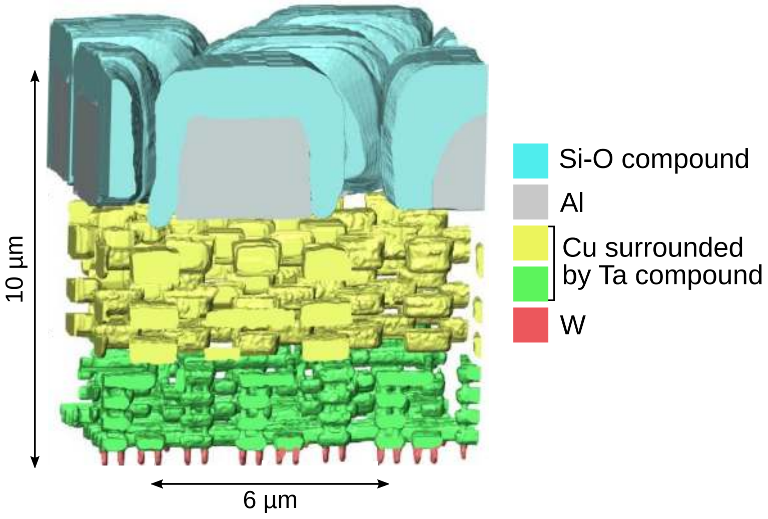

Figure 6.15: This 3D model is the result of a slice and view project at the DESY Nanolab. The coloring of this model is based on the according elemental composition from the EDX measurements, see legend to the right. The Cu and Ta regions are additionally separated by the size of the structures.

The colors in Sections 6.3.2 and 6.3.3 are chosen to match. In Fig. 6.15, unaltered inherited from a Nanolab documentation, different shapes and sizes of the Cu structures surrounded by Ta are additionally segmented into green and yellow structures. Consequently, in Fig. 6.15 all green structures themselves have similar structures and are about the same size. This is the same for all yellow structures, which are on average bigger than the green ones.

Only the distribution of the Si-O compound is unexpected, since it is available as insulator throughout the whole microchip at each non-metal position and not just at the top, compare Fig. 6.14, second row.

6.4 Comparison of Ptychography and Electron Microscopy

In this section, the overview scans from Sec. 6.1.1 were taken to assign the regions with the different components to the different FIB-sections. This is demonstrated for one exemplary region in Fig. 6.16. This image shows a comparison between the phase shift of the transmission function, gained from the ptychographic reconstruction, to two perpendicular cuts into the microchip prepared by focused ion beam (FIB) and subsequently imaged with an electron microscope (EM). The black arrows in the ptychographic image represent the approximate cut regions and directions of the according EM images, from left to right. Especially the horizontal line does not perfectly fit the position, but it matches most of the structures in this comparison. Additionally, the electrons penetrate into the surface and image the content of some tenth of nanometer in depth. For this reason, there are more structures visible than actually cut by the two black lines V and H. To emphasize the equivalent components, they are highlighted with the same color. To allow for a better comparison between the various different structures in each of the images, not all structures are fully colored but just the edges highlighted by a dotted line. Another comparison is shown in Figures 6.17 and 6.18 with ptychographic projections, which were recorded with a view on the vertical construction of the structures. The structures in microchips arrange parallel to the outer borders of the chip. In Fig. 6.17 and Fig. 6.18 the chip

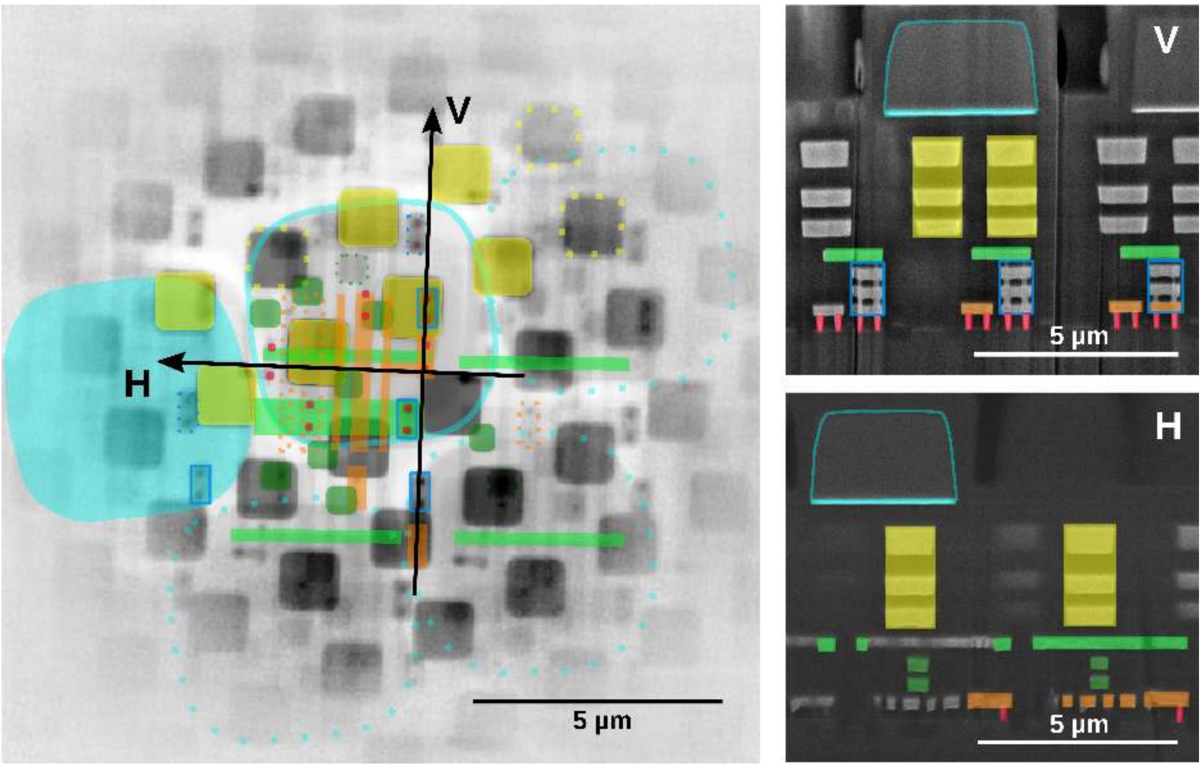

Figure 6.16: This set of images compares the structures from top view as transmission image (ptychographic phase shift) on the left to two cross sections of the same chip region (electron microscopy images) on the right. The letters V and H mark the vertical and horizontal cut direction as visible in the ptychographic image, respectively. Same colors refers to similar structures.

was cut parallel to these borders and thereby 90° to each other. We recorded two ptychographic scans at approximately the same directions as these cross sections, see object phase in (a) and object modulus of the transmission function in (b) of the two figures compared to the EM images in (c). The main distinction between the X-ray ptychographic images and electron micrographs is the imaging in transmission versus the imaging of the surface of some chip region, respectively. With a complementary usage of both methods, more details were revealed.

The most noticeable distinction is that in EM images the shades highlight the differences of atomic masses of the structure materials, while ptychographic images emphasize the differences of the structures' electron densities. Conspicuous examples are the visibility of the $CoSi_2$-structures at the bottom as well as the different compounds of the surrounding Si. The thin $CoSi_2$-structures are only slightly visible in the electron microscopic images, but stand out in the phase of the transmission function of the object, compare (c) versus (a) of Figures 6.17 and 6.18.

In the other case, all EM images in this chapter, which include the structures at the bottom, reveal a difference between the different Si compounds below and above the $CoSi_2$ structures – highlighted by adjusted contrast in inset in Fig. 6.18, while there is no noticeable difference in both ptychographic images, the modulus and the phase.

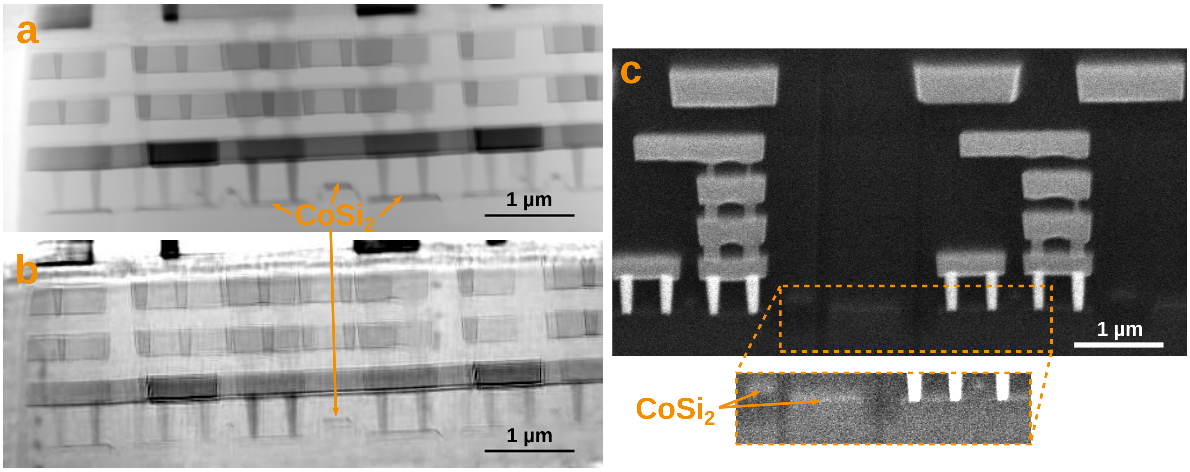

Figure 6.17: Ptychographically reconstructed phase (a) and modulus (b) of the microchip with a similar view as the electron microscopic image of the cross section in (c). This view corresponds to the H line and view in Fig. 6.16 and is perpendicular to the view shown in Fig. 6.18.

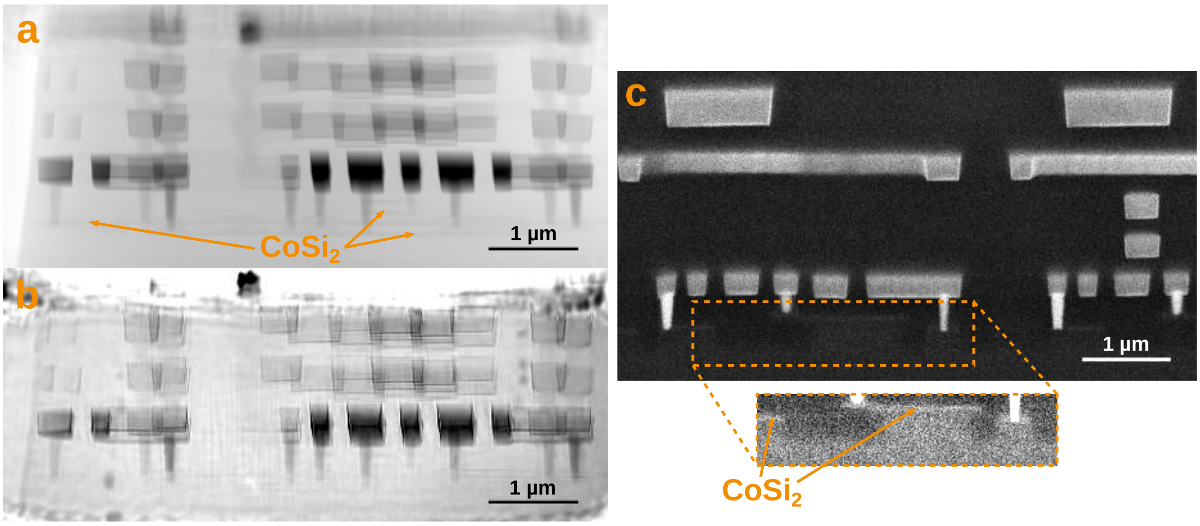

Figure 6.18: Ptychographically reconstructed phase (a) and modulus (b) of the microchip with a similar view as the electron microscopic image of the cross section in (c). This view corresponds to the V line and view in Fig. 6.16 and is perpendicular to the view shown in Fig. 6.17.

6.5 Conclusion on X-ray versus Electron Microscopy

In the comparison of the two different high-resolution imaging methods, we see, that neither of the two methods clearly protrudes beyond the other. With the mentioned advantages on both sides, these methods rather complement each other.

The EM images show high resolutions together with an easy access to an electron microscope as well as a fast implementation. The micrographs are a direct result of a session at such a microscope without the need for post-processing. They show the surface of a chosen region, even of a cross section. With an integrated FIB, these cross sections can be done at the EM directly. Elemental information can be obtained by an EDX analysis of the diverse surfaces. In our results, the structures made of different materials were well resolved, but not all elements were found. The concentrations of the Co and Ti structures may have been too weak and compared to the other elements, their energies were too low, to be detected. At some regions, even the Si search showed some results, which is not surprising, since it is available in the whole sample. Additionally, through the combination of EM and FIB in one machine, a three-dimensional view can be obtained in a slice and view procedure. This however requires the assembly of the single images in an extra program, for example Avizo, to model the 3D volume including the correct positioning of the image distances and the correction of possible shifts. A downside of this method is the destroyed sample afterwards.

In comparison to that, the sample was imaged by X-ray ptychography. This method does not work without a reconstruction algorithm. In return, X-rays have a large penetration depth, which enables the imaging of a several micrometer thick sample in transmission and even enables high-resolution X-ray tomography, both without further destruction of the sample. Usually, the parallel measurement of XRF is included in these measurements, too. However, during our experiment at P06, it was not activated.

In our measurements, we were able to image the 14 nm $CoSi_2$ structures at the bottom as well as the 20 nm Ta liners. The spatial resolution determined by edge contrast surpassed 9 nm and by Fourier ring correlation (FRC) it reached even 7.24 nm. The latter one is close to the plotted signal over background, showing potential for 6.3 nm. The q-space estimation in the diffraction patterns even went beyond 5 nm.

CHAPTER 7

Multimodal X-ray Experiment

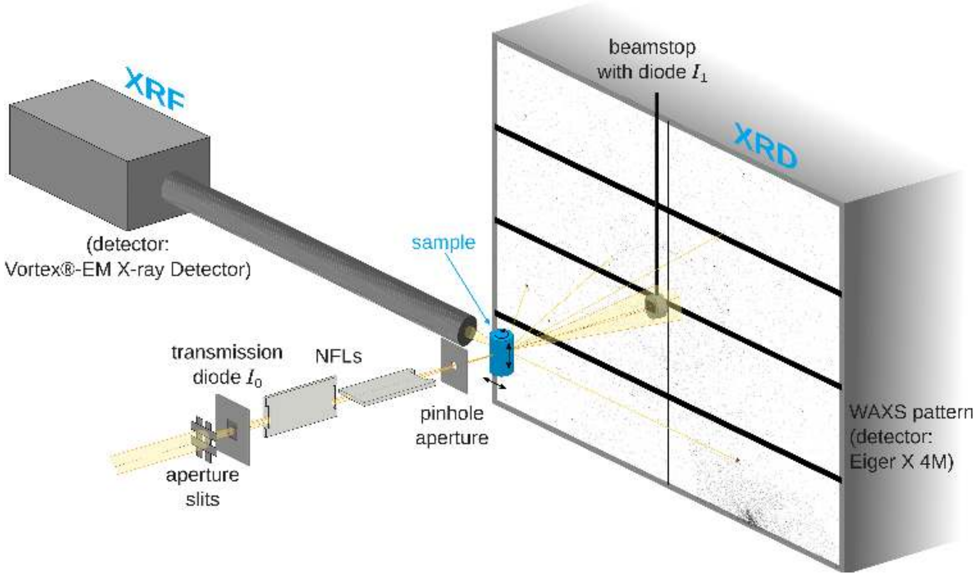

The application of complementary contrasts on a nanoelectronic device is realized by the parallel acquisition of X-ray absorption (XRA), X-ray fluorescence (XRF) and X-ray diffraction (XRD). The experimental realization of this parallel acquisition is discussed in this chapter. In the beginning, the experimental parameters are introduced, see Sec. 7.1. This is followed by Sec. 7.2, describing how the scanning scheme is adjusted to the requirements of the chosen combination of contrasts. The contrasts themselves are briefly described in Secs. 7.2.1 to 7.2.3. Hence, the accomplishment of the experiment with all preparation steps at the beamline is described in Sec. 7.3.

7.1 Experimental Parameters

For our measurements, we used a Si (111) double crystal monochromator (DCM). The relative energy bandwidth is $1 \times 10^{-4} \mathrm{dE/E}$. For stability reasons, we used the DCM in a break state[1]. Furthermore, slits coarsely define the beam shape by cutting away outer parts of the beam as well as unwanted scattering. Moreover, in order to reduce the contribution of X-ray photons with higher energies originating from higher harmonics, we used so-called horizontal offset mirrors (HO) mirrors installed at P06. This is particularly important for the XRD measurements. To reduce vibrations of these, the cooling of the HO mirrors was switched off. The multimodal experiment was set up in the hard X-ray regime at 18 keV, corresponding to the wavelength of $\lambda = 0.6888$ Å. At this energy, the transmission of X-rays through the sample is sufficiently high and all the fluorescence lines of all relevant materials can be excited. Most importantly, for XRD we had to consider the limitations of the experimental setup, which were the minimum sample-to-detector distance and the field of view of the detector. With the final sample-to-detector distance we covered an angular range of $2\theta \approx 50^\circ$. Additionally, due to the chosen energy, we achieved a sufficient $\vec{q}$-range for the XRD data, which reaches approximately $\vec{q} = 7.7$ Å^{-1}. Since the XRD peaks were expected to be rather weak in intensity, the scan time was chosen accordingly. In order to increase the incoming photon flux, we used compound refractive lenses (CRLs), positioned in the optics hutch downstream of the HO mirrors, as prefocusing lenses. These lenses bundle the diverging X-ray beam further upstream of the experimental station towards the sample position.

Parameters of the Multimodal Experiment

- **Beamline:** P06 nanoprobe, PETRA III, DESY Hamburg
- **Ring parameters:** 40 bunch mode at 95 mA and 100 mA
- **Undulator:** 2 m long U32 undulator
- **Energy:** 18 keV, corresponding to a wavelength of $\lambda = 0.6888$ Å
  - sufficient transmission for chosen sample
  - all relevant[a] fluorescence lines below exciting energy
  - reasonable $\vec{q}$-range[b] for XRD analysis ($\vec{q} = 7.7$ Å^{-1} for $2\theta \approx 50^\circ$)
- **Monochromator:** Si (111) double-crystal monochromator (DCM) in a braked state (stability)
- **Flux settings:** 1.5×10^8 Ph/s/mm^2 with prefocusing by CRL (potentially reduced coherence)
- **Higher Harmonics:** HO mirrors, no cooling (mechanical stability)

[a] Each element in the sample should be excited and emit characteristic photons.

[b] At least the 2θ angles of five (hkl)-families per crystal structure should be covered.

---

[1] After the monochromator reaches the target position, the servo actuator is switched off as the monochromator causes high frequency vibrations in the control mode, which degrades the beam stability, see Kristiansen et al. [123]

Due to the usage of prefocusing CRLs, the photon flux was increased by a factor of five[2], which considerably reduced the scan time. In return, when using the prefocusing lenses, the degree of coherence can decrease depending on the new position of the secondary source, see Schroer [124]. However, the degree of coherence was not measured during this project, neither with nor without prefocusing lenses. With the chosen contrasts for the multimodal experiment, the degree of coherence does not affect the measurements. For possible extensions of the multimodal experiment, for example by ptychography, a compromise of photon flux and coherence is essential. The relevant parameters of the multimodal experiment are summarized in the gray box.

7.2 Multimodal Acquisition Scheme

The data, characterizing the different structures in the sample, was recorded using a 3D step scan procedure: 2D translation and 1D rotation. For a single 2D projection, we applied a grid step scan. The rotation of the sample was added to enable three-dimensional mapping of sample features and to record tomographic data sets for the different contrasts XRD, XRF and XRA in parallel. The grid step scan was repeated for $N = 136$ evenly distributed discrete angles over the range of 180°. However, common 3D-XRD experiments cover the full angular range of 180° continuously [26], in contrast to the discrete acquisition scheme we applied. The difference is emphasized in Fig. 7.1: For continuously acquired angular steps (upper sketch), all diffraction signal within the measured angular range is obtained. Diffraction information from diffraction angles between the discrete angular steps is of course missing in this scanning scheme. For this experiment a continuous scanning scheme was not possible as the scanning unit could not deliver the demanded repeatability for the lateral scan positions. As comparison, other 3D-XRD experiments have lateral step sizes of 250 nm and larger. Our step size was 100 nm and the structures were about the same size. But despite very precise alignment of the sample to the axis of rotation, drifts of the motors or other reasons for lateral deviations could not be compensated. The deviations were larger than the sizes of the structures with widths of several scan points. Thus, the projection wise scanning scheme allowed for prompt corrections of these lateral deviations.

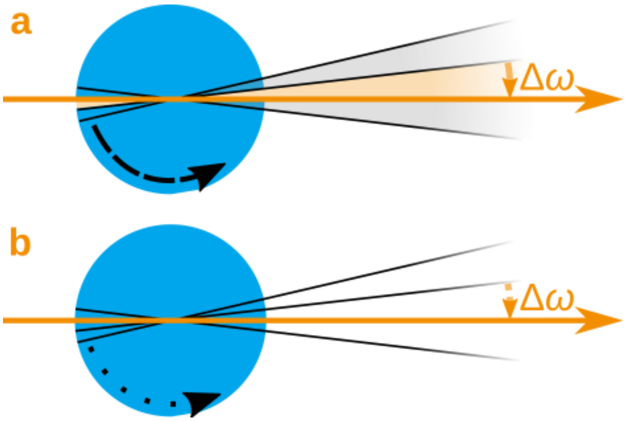

Figure 7.1: Continuous (a) versus discrete (b) angular scanning scheme. In (a), the sample is illuminated continuously. Diffraction patterns are integrated over $\Delta\omega$, see orange wedge. With (b), in turn, the sample is only illuminated at the static stops each $\Delta\omega$.

---

[2] The photon flux, measured by the calibrated PIN diode, without and with CRLs was 3.3×10^7 Ph/s/mm^2 and 1.5×10^8 Ph/s/mm^2, respectively.

Furthermore, the origin of the contained elements, obtained by X-ray fluorescence, could not straightforward be allocated without a grid scan, which equally applies for the X-ray absorption. In contrast, diffraction only occurs at specific angular values. Discrete angle scanning has a huge influence on the analysis, as will be observed later.

Nevertheless, with XRD being not usually applied at this beamline, we had to carefully adjust all constraints – first of all, physically clearing all the effects and influences which affect the background. Moreover did we try to gain as much diffraction signal as possible with the given capabilities and resources. This includes tuning the incoming beam with prefocusing lenses to get a sufficient amount of flux and moving the detector for the diffraction data as close as possible.

In the following three subsections, the parts of the multimodal experiment are explained individually. The sample was moved perpendicular to the beam path, covering directions y and z, and rotated ω around the center of the rotation, which is parallel to the z-axis of the sample. At each scan position, data for each of the three applied techniques is recorded. The slits, the lenses and the pinhole, see Figure on page 59, are not further mentioned or marked in the following Figures 7.2 to 7.4.

7.2.1 X-ray Absorption - XRA

To determine the sample induced attenuation of the probing beam according to Eq. (2.37), the intensity of the incident beam I_0 and of the outgoing beam I_1 are measured. Both detectors, in our case a transmission diode upstream of the sample and a PIN diode downstream of the sample – depicted in Fig. 7.2, are calibrated to the same reference. In the experiment, the single PIN-diode was integrated in the central beam stop. This covered two functions at the same time: The beamstop blocked the central beam by absorbing all photons in this area and the integrated diode measured these blocked photons.

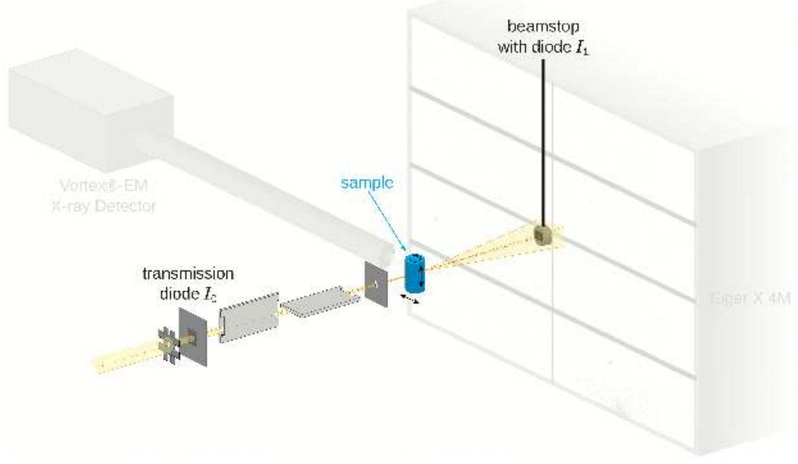

Figure 7.2: Setup to measure the absorption of a sample. The incoming intensity I_0 of the probe (yellow) upstream of the sample (blue) and the transmitted intensity I_1 downstream of the sample are measured.

The blocking of the central beam is important to prevent the WAXS detector from being damaged by too high count rates[3] and continuous X-ray exposure of the panel gaps.

---

[3] The detector is designed to cover a certain count rate. Above this rate, incoming photons are not counted linear anymore and might damage the pixels at some point [107].

7.2.2 X-ray Fluorescence - XRF

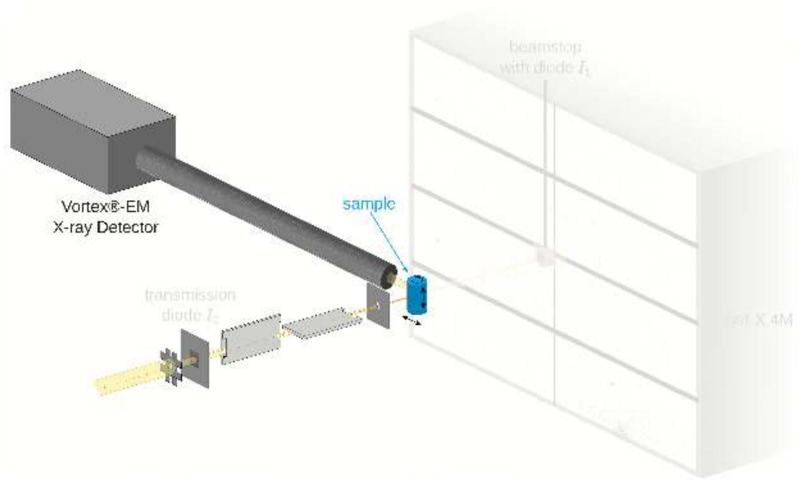

Figure 7.3: Setup to measure the X-ray fluorescence signal. Here, the detector (dark gray) is positioned perpendicular to the probe path (yellow) and detects the emitted light from atoms excited by the X-rays along the path through the sample (blue).

The fluorescence detector was positioned perpendicular to the beam path to minimize the elastic and Compton scattering background in the measured XRF spectra. The detected signal is proportional to the total number of emitted rays by detecting only a small solid angle. To calculate the quantitative concentration of each element, the fluorescence detector has been calibrated by standard reference samples. For our experiment, one X-ray fluorescence spectrum was detected per scan point. The signal was sorted to different channels, corresponding to a certain energy range – the exact range was determined in the calibration procedure during the analysis of the data. X-ray fluorescence photons emitted after the interaction of the sample with the incoming X-ray beam can be absorbed within the sample before reaching the XRF detector. This effect is called self-absorption, which depends on the emitted energy, the sample thickness and material composition on the path from the excited atom to the detector.
During the experiment, the fluorescence detector needed to be moved away from the sample because the amount of photons emitted from Cu structures was too high and caused dead times due to event overflow. The final detector position was a trade-off between events of elements available in lower amounts, such as Co in smaller structures, and the huge amount of Cu. With this position, the detector dead times for the Cu regions were still high, but acceptable and correctable, see analysis in Sec. 8.3.2. Additionally, for setup reasons, we had to remove the collimator.

7.2.3 X-ray Diffraction - XRD

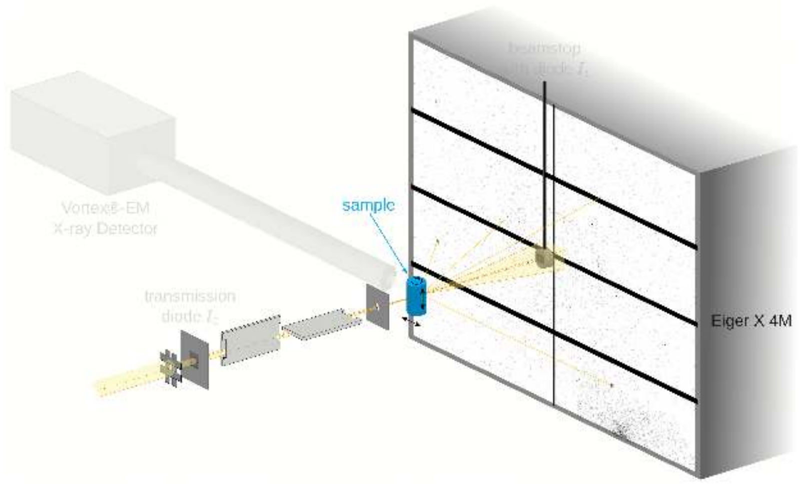

Figure 7.4: Setup to measure the WAXS signal of a sample. In the diffraction setup, the detector is positioned downstream of the sample and detects scattered X-rays from the interaction of the probe (yellow) with crystalline parts of the sample (blue).

The section to measure the X-ray diffraction of a sample makes up the largest part of the setup. The reason for that is the large detector, which is needed to cover a large solid angle (2θ) behind the sample. In this part, the sole function of the beamstop is to block the central beam, while the WAXS detector records the diffraction signal. The applied scanning scheme enabled the analysis based on both powder diffraction and single Bragg peaks. The powder diffraction methods use the azimuthal integration over single or summed diffraction patterns to generate appropriate diffractograms. The Bragg peak based techniques exhibit position and orientation of single grains. In this work, both approaches find their application.

7.3 Performing the Experiment

To conduct such an experiment, several steps in advance of the actual measurement are necessary. These are the alignment of the optics, the measurement of a XRD standard and most important, the sample alignment to the probing beam. Basically, the alignment subdivides into positioning of the sample in the beam, close to the focal plane, and to the axis of rotation. Finally, the actual data acquisition is conducted.

7.3.1 Alignment of Lenses

To ensure a defined beam, nanofocusing lenses (NFLs) suitable for focusing at 18 keV incident beam energy were aligned. The shape of the focus as well as the beam path around the focal plane were reconstructed using ptychography [48], see Fig. 7.5. The determined full-width-at-half-maximum focal size was 76.9 nm in the vertical direction and 65.5 nm in the horizontal direction, see the graphs in Fig. 7.6. The spot size on the sample was bigger, since we moved the sample out of focus by 250 µm, see Sec. 7.3.4. Additionally, the averaged maximal flux, determined from diffraction patterns of this scan without sample, is approximately 6.6×10^7 Ph mm^{-2} s^{-1}. During this scan, the prefocus was not used. The pixel size[4] is 3.80 nm.

---

[4] The pixel size is determined by Eq. 3.4 using the parameters: $E = 18$ keV, $d_{SD} = 2120$ mm, $s_{pix} = 0.075$ mm and the number of used pixels from center to edge is 256.

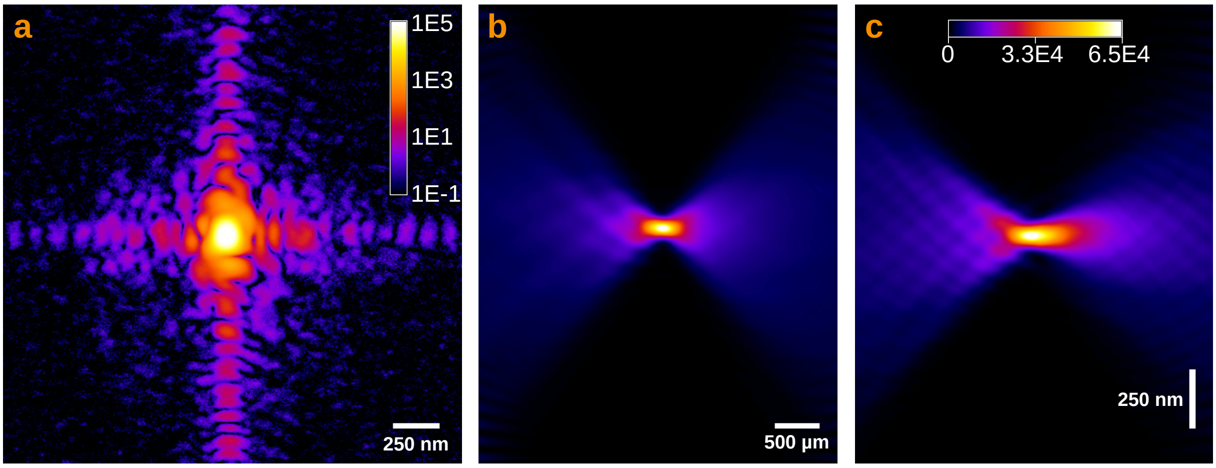

Figure 7.5: Reconstructed beam shape and profile from aligned NFLs: (a) is a intensity plot of the illumination function at the focal position, brightest colors show the most intense features. (b) and (c) show the horizontal and vertical beam profile around the focal position, respectively, propagated ± 2 mm along the optical axis.

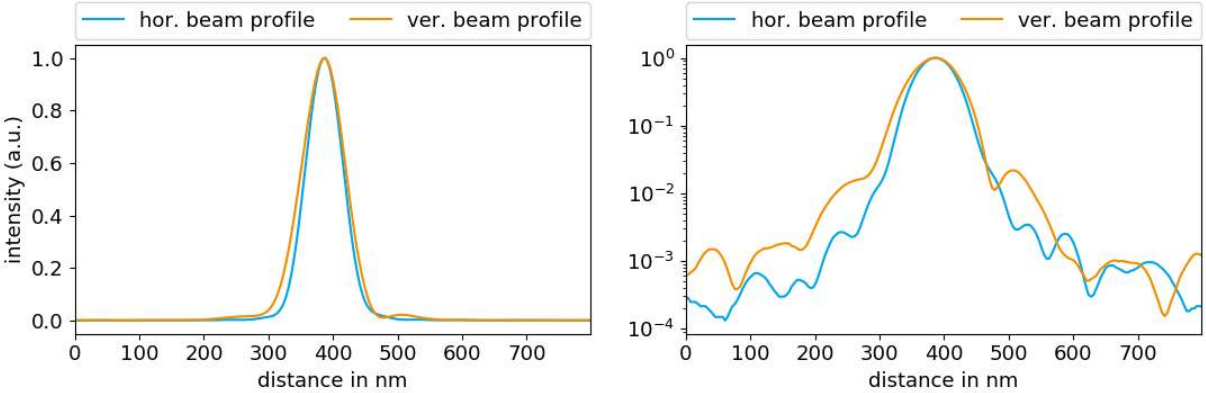

Figure 7.6: These line plots trough the central spot of the focus show the normalized intensity of the beam horizontally and vertically in linear scale (left) and logarithmic scale (right).

7.3.2 Removing the Physical Background

Usually, the experimental hutch of the nanoprobe at P06 – where our multimodal experiment took place – is used and designed for measurements in the far field or at specific angular positions to measure individual Bragg peaks. Thus, the background is clean for small scattering angles, but the beam shaping part is constructed to be relatively open to provide a high flexibility and easy accessibility. For wide-angle XRD experiments, however, it is required to cover a large area of scattering. In our case, all scattering from the central beam up to $2\theta \approx 53^\circ$ is detected. This was achieved by setting up the detector closely behind the sample. The sample to detector distance, which we achieved, was 83.8 mm, allowing for save movements of the sample. Before we could start the data acquisition, we had to clean the diffraction signal from background scattering, see Fig. 7.7a showing the initial condition without shielding the detector. Only a small part at the bottom right could not be blocked for technical reasons, see Fig. 7.7b for the final condition. In both cases of Fig. 7.7, the XRD standard sample was already mounted.

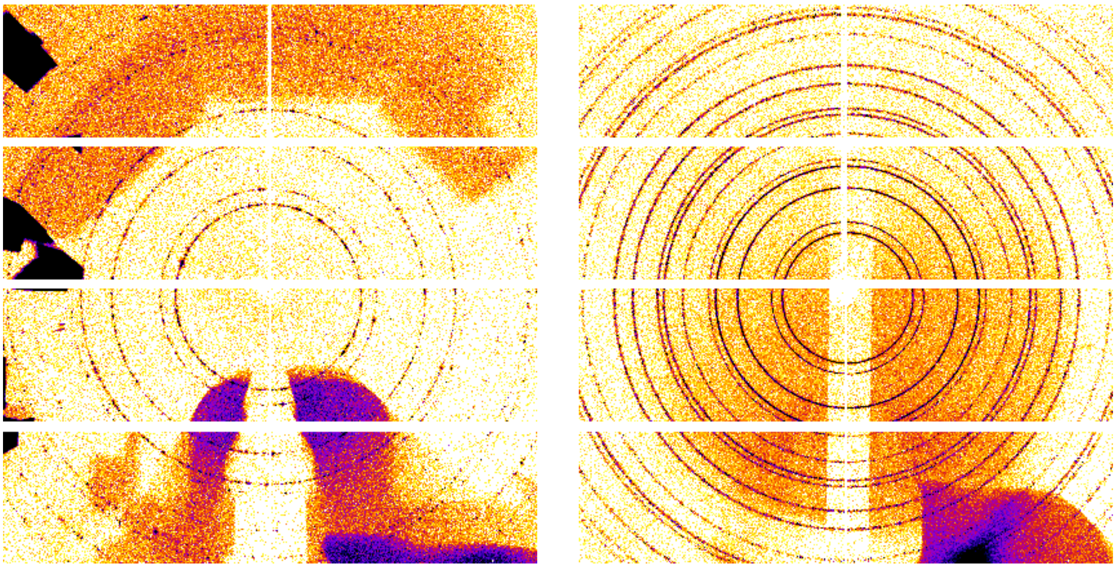

(a) Initial state, before cleaning **(b)** Final state, after cleaning

Figure 7.7: These two images visualize (a) the necessity and (b) the realization of cleaning the diffraction signal from background scattering. Since the background cleaning was carried out while the calibration standard was mounted, scattering rings are visible. Additionally, in b) the detector was moved closer to the sample and hence, there are more rings in the field of view than in a). Also, the exposure times differ: a) 10 s, b) 30 s.

7.3.3 Measurement of Powder XRD Standard CeO_2

In XRD experiments, it is very important to precisely determine the orientation of the detector relative to the optical axis. This was realized by illuminating a well known standard sample and fitting the diffraction orders measured on the detector. In our case, we used a CeO_2 powder, which is commonly used to calibrate the experimental geometry. By using the known 2θ scattering angles of CeO_2, the distance between sample and detector as well as slight tilts of the detector out of the plane perpendicular to the beam path are analyzed. Later on, these parameters were used for the analysis of the XRD data obtained from the milled microchip.

This powder was provided in a yellow capillary and was mounted onto the sample stage, see Fig. 4.3. We illuminated the CeO_2 powder with the focused beam and recorded 100 images over $\Delta\omega = 20°$, which were exposed for 10 s each. These images were summed up and analyzed. The results of this analysis are presented in Chap. 8.

7.3.4 Data Recording

After the setting up was completed, the measurement of the sample began. We had to consider the object thickness relative to the smallest structures, which both contributes to the necessary amount of steps in horizontal direction per angle and the number of angles to be probed.

Due to limited time during a beamtime, the chosen parameters are a trade-off between exposure time and step size, to get a certain amount of projections for a reasonable tomogram. For that reason, we moved the sample out of the focal plane by approximately 250 µm along the beam path. Additionally, without using ptychography at this point and for that reason no necessity of overlapping scan points, we decided to move in discrete steps rather than continuously.

The experiment was conducted with the following parameters: The determined beam size was 110.0 nm±0.4 nm×116.9 nm±0.4 nm. The step sizes were 100 nm×120 nm in horizontal and vertical direction, respectively. With a sample width of approximately 8 µm to 8.5 µm, we had to scan at least 85 steps. The scanning height was 3 µm and was sampled in 25 steps. With the step size of 0.1 µm the necessary number of projections $N_\omega = 134$, according to Eq. (3.14) by the Nyquist-Shannon sampling theorem or Crowther criterion.

The data was acquired projection-wise and the tomographic data was recorded in a 3-way filling scheme to cover most angles to gain at least a sparse tomogram in case of any problem. It finally led to 136 steps distributed in equally spaced angles over 180°, which matches the required N_ω. Between projections, every once in a while, we had to adjust drifts in height and sideways.

Scan parameters[a]**:**

- steps (v×h): 25×85, snake scan[b], fast axis: vertical
- step sizes (height×width): 120 nm×100 nm
- 136 angles over 180° in steps of 1.3333°
- time per scan point: 0.2 s exposure plus overhead of ≈0.6 s (motor movement and data writing)

---

[a] A summary on the experimental parameters can be found on page 60.

[b] In a snake scan, the fast axis changes the scan direction alternatingly.

The total time of the experiment was about 45 h, while the net exposure time only summed up to roughly 16 h.

7.3.5 PIN-Diode Malfunction

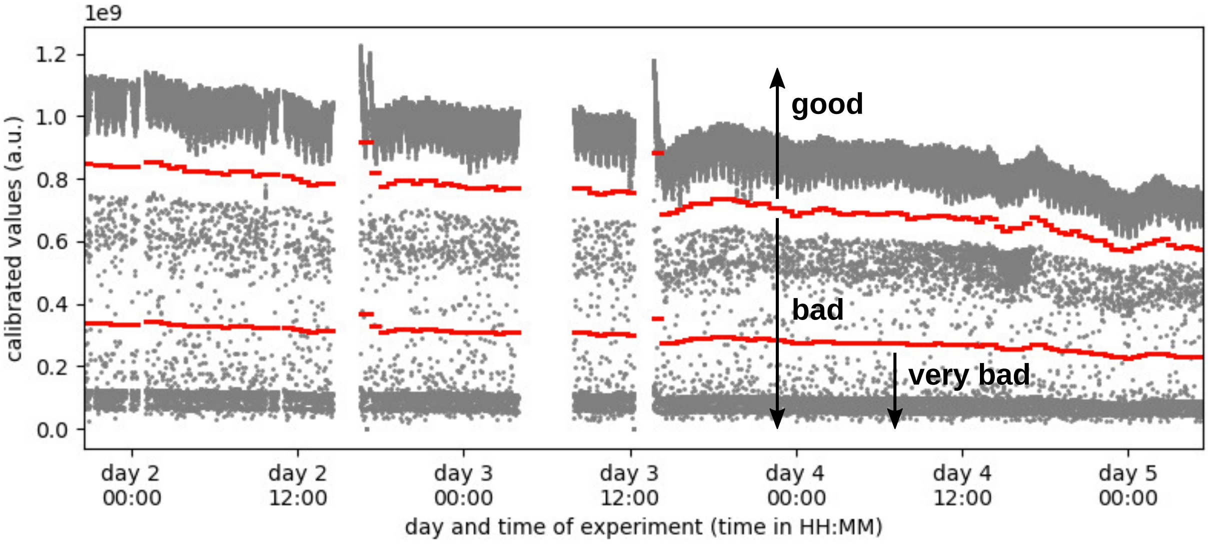

Figure 7.8: Plot of calibrated beamstop diode values over the whole 3D scan. The starting time is 20:30 at day 1. The overall decay of the diode values due to general saturation is visible. The two red lines, upper and lower one, indicate the thresholds per scan for the separation to "bad pixels" in general and additionally to "very bad pixels" as part of the "bad pixels", respectively. This means, that only values above the upper red line are regarded as real values.

During the experiment, the single projections were measured one after another. The absorption of the probe was measured by the pin diode in the beamstop, which was read out by a Keithley multimeter. Over the whole 3D scan, the values of the pin diode decreased, which could be an effect of general saturation of the diode, see Fig. 7.8. In addition to that, there were some false values in each projection right from the beginning on. After four fifth of the whole scan time, at day 4 between 12 and 18 o'clock, this effect got worse. By pausing the scan routine between two scans for 9 min, the effect was reduced to the status at the beginning of the data taking. This is visible in the comparison of the projection images of these scans with bright pixels representing the real signal and the highlighted gray to black dots marking the failure points, see Fig. 7.9. The remaining false pixels appear more arbitrary, comparable to the beginning of the whole measurement. Unfortunately, every scan had at least some false pixels. But in general, the number of pixels that suffered from a malfunction were negligible. The percentage of ”bad pixels”, which are declared as pixels deviating from the ”healthy pixels”, compared to all pixels per projection is below 6 %, compare Fig. 7.10. The distinction between ”good” and ”bad” pixels is set by thresholds of the pixel values. Due to the decrease of the general diode values, the threshold is adaptable in the sense that the differentiation is applied projection-wise. For each projection, the respective maximum of all pixels of the current projection represents the 100 % value, the ”bad pixels” lay below 75 % and of these, the sub group ”very bad pixels” counted all pixels below 30 %. The variation of the real signal, white to light gray pixels, due to the structures of the sample are almost not visible in this image. In turn, some measurement failures are more prominent, sticking out as pixels with a darker gray or in black. The effect of accumulating false pixels at the borders of the images are caused by a bug of the old control software. It causes a loss or timing problem of the first point of a scanning line. Due to the applied snake scan mode, which alternates the scan direction every column, these missing points appear periodically on both sides, with a few exceptions. Some other dark pixels occur in regular distances and depict the biggest deviation from the real values. In conclusion, all projections needed to be post-processed to remove the distortions, see iterative correction in the analysis chapter in section 8.2.3. Nevertheless, the reason for these bigger, regular malfunctions are still unsettled, but the probability of a loose contact between conduction paths and diode is high compared to other possibilities. Altogether, we rather exclude a pure electronics failure,

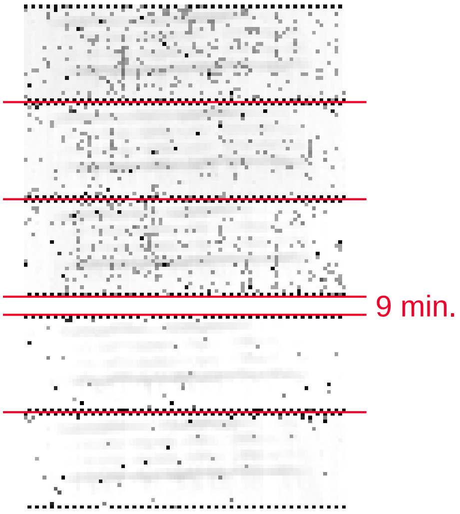

Figure 7.9: These five images, separated by red lines, show five consecutively taken projections of the PIN-diode signal. The three upper projections were acquired before, the last two after a short break. In this case, the grey scale is adjusted to highlight scan points in which the PIN diode delivered a bad signal, represented by gray to black pixels. The brighter pixels mark sample and background.

due to the fact that the effect was reduced after pausing the scans.

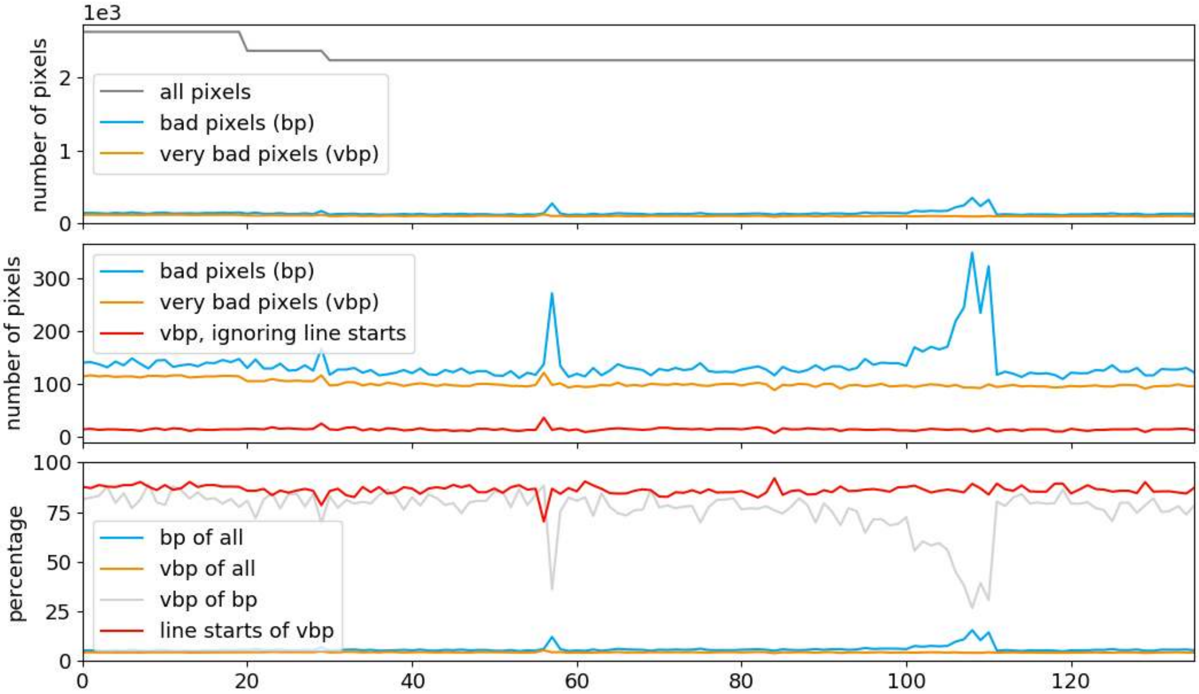

Figure 7.10: Comparison of faulty pixels, called ”bad pixels” (bp) and ”very bad pixels” (vbp). The separation is done by a percentual threshold of the pixel values. The x-axis represents the 136 scans. Faulty line starts are excluded or extracted in the 2nd and 3rd graph, respectively. After 20 and 30 scans, the scan width and with that the amount of pixels per scan was reduced.
The scan width changed two times during the experiment. That is why the total number of pixels is higher at the beginning of the top plot.

CHAPTER 8

Multimodal X-ray Data Analysis

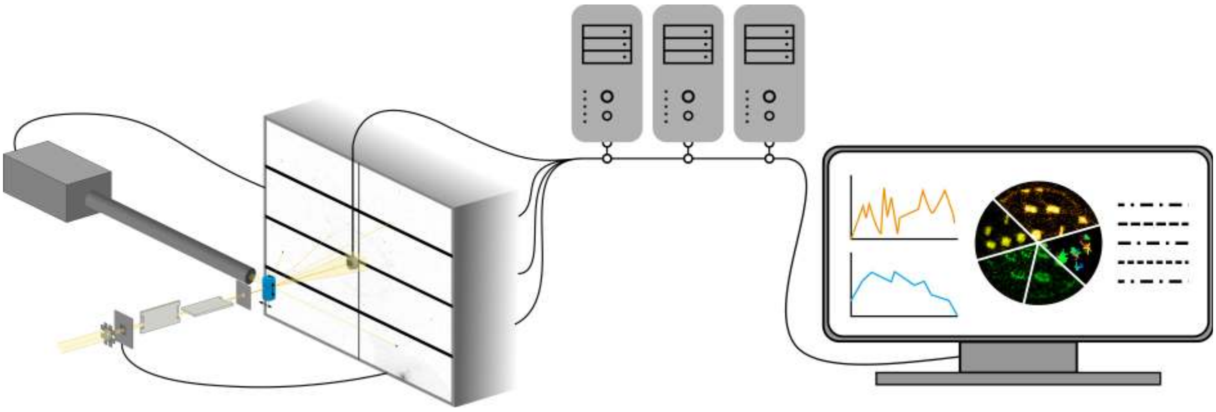

In this chapter, the analysis of the multimodal X-ray data is addressed. It starts with basic preparation steps. But despite continuously emphasizing the parallelism in the previous chapters, the analysis is done individually for each of the three applied contrasts – X-ray absorption (XRA), X-ray fluorescence (XRF) and X-ray diffraction (XRD) – and combined afterwards.

The analysis starts with the alignment of the projection within a stack and across the different contrasts in Sec. 8.1. In the following, the contrasts are analyzed separately. The analysis of the first contrast, XRA, is presented in Sec. 8.2. This is continued by the analysis of the XRF contrast in Sec. 8.3. As last of the three measured contrasts, after the calibration of the detector geometry XRD is analyzed from different perspectives in Sec. 8.4.

Finally, in Section 8.5 the results of all contrasts are combined and compared.

8.1 Data Alignment

With regard to the comparison of the results, obtained from the different contrasts, a consistent three-dimensional data alignment is required. In this thesis, the term 'data alignment' denotes the adjustment of all projections relative to each other concerning their vertical and horizontal positions relative to the center of rotation. During the experiment, in advance of the data acquisition, the sample was aligned to the focus of the probing X-ray beam. This means, the center of the specimen is physically aligned to the optical axis and close to the focus as well as to the center of rotation within an accuracy of at least the step size of 100 nm. Deviations from the alignment occurred during scanning and reasons for this are manifold. We identified thermal drifts and an angular dependent scanner problem as the main reason for translational deviations between different projections. With respect to the sample structures in the range of 120 nm to 250 nm, the sampling was relatively coarse. An alignment precision matching the sampling size was desired. Due to that fact, the sole alignment of the setup is not sufficient for the satisfactory three dimensional reconstruction of the data set. The correlation of the different contrasts to a 2D projection is inherently given by the scanning scheme and the simultaneous data acquisition for all three contrasts. For that reason, we need to post process the relative alignment between the recorded 2D projections, which is determined using only one of the contrasts. The resulting relative alignment parameters are then applied to all other contrasts as well, to generate consistent sinograms.

In practice, both the fluorescence and the absorption contrast are suitable to align the data, as both depict the structures very clearly. Because of clearer transitions between regions on and off the sample, I chose the fluorescence contrast to align the data.

In order to gain a higher alignment accuracy, each pixel was divided into 4×4 subpixels. This means, a projection of the original size of 26×101 pixels was upsampled to 104×404 pixels. In principle, the alignment has to undergo a process of translation, shearing and rotation of the images, see Fig. 8.1.

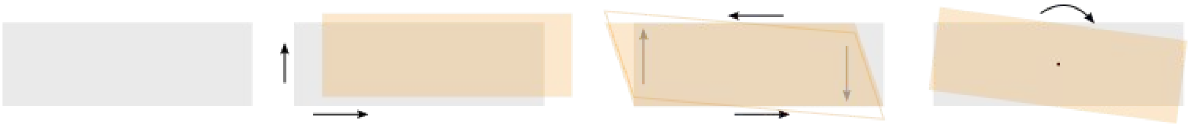

Figure 8.1: From left to right: original image, translations (horizontally and vertically), skews or shearings, and rotations. All of these options were tested and only the translation were found to have a noticeable influence. For that reason and to simplify the analysis for this project, we concentrated on translational correction only.

After trying several alignment strategies, a combination of automated alignment based on cross correlation and manual alignment[1] provided the most satisfying results. Different combinations of affine transformations were considered during the alignment procedure, but the slight physical tilt of the sample on its holder in combination with the scanner problem, causing a sheared scanning, were not separable. Additionally, the effect of the shearings, with a maximum shear of three pixels over the full width of 101 pixels by a total height of 26 pixels, were negligible. Moreover, an exemplary implementation of correcting shearings caused visible, unwanted steps

---

[1] For facilitated manual alignment, a Python tool developed by Maik Kahnt was used.

in the structures, even with applying the corrections at sub-step sizes. As a consequence, only translational corrections were implemented.

Finally, the validation for a successful alignment are continuous sinograms for each height, see Fig. 8.2. As a result of successful vertical alignment, the dark lines in the uncorrected sinogram shown in Fig. 8.2 on the left disappear as shown in the same Figure on the right. A correct horizontal alignment can be recognized by smooth and closed sinusoidal trajectories.

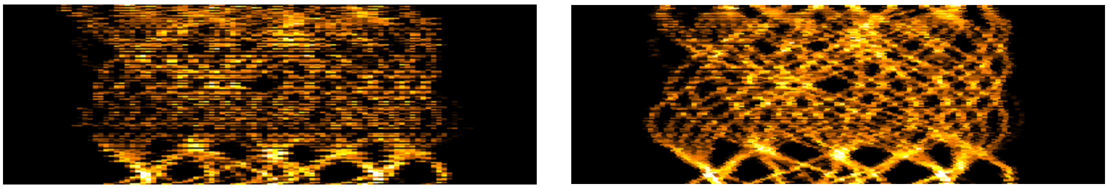

(a) Tungsten before alignment. **(b)** Tungsten after alignment.

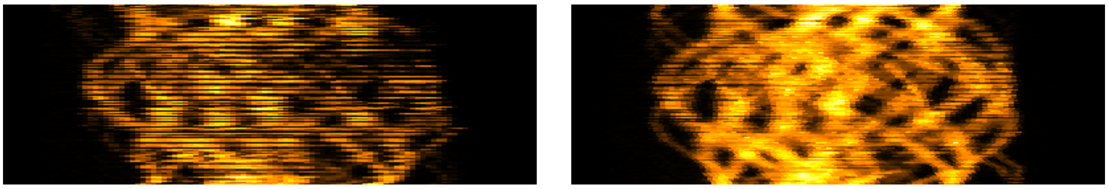

(c) Copper before alignment. **(d)** Copper after alignment.

Figure 8.2: XRF data before, (a) and (c), and after, (b) and (d) alignment, vertical and horizontal, for two exemplary elements and heights, tungsten (a and b) and copper (c and d). By the adjustment of the heights, the stripes, visible in the left images, are clearly reduced.

In total, misalignment of up to ±0.8 µm for the full scanning width of 10.0 µm and up to ±0.4 µm for the height of 3.0 µm was corrected during the registration procedure. The alignment of the projections to each other is a major part of the tomographic reconstruction. Without alignment, the images would be smeared out, artifact-prone or, dependent on the degree of misalignment, would not even show real structures. In all further analysis steps, the determined shift parameters are applied to the individual contrasts.

8.2 Analysis of X-ray Absorption Data

This section describes the transition from raw transmission data to attenuation coefficients μ and further to the three-dimensional reconstruction of the data. The steps for this transition are: **I** calibration, **II** normalization to the ring current, **III** elimination of false pixels and **IV** calculation of the transmission I_1, compare the overview in Fig. 8.3. The whole analysis is divided in the preparation of the single projections and the tomographic reconstruction. The transformation from raw data to absorption coefficients is done individually for each pixel (x, y) per projection ω. It demands a uniform calibration of the values measured upstream and downstream of the sample to one selected reference to get the values I_0 and I_1, respectively. The transmission is calculated by the Lambert-Beer law, see Eq. (2.37).

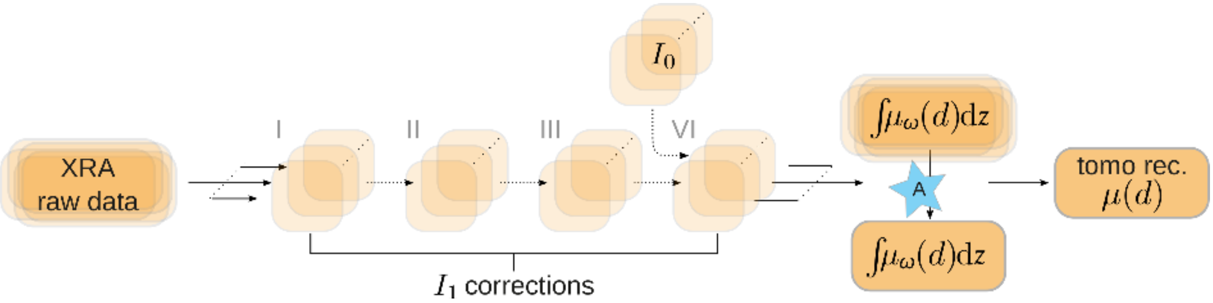

Figure 8.3: Analysis procedure applied to the X-ray absorption data. It is completed by the alignment, marked by the blue star, and the following tomographic reconstruction. The d represents the position within the sample $d(x, y)$, at a constant height z where y is perpendicular to the optical axis and x the coordinate along the optical axis.

Basic two-step procedure to get the attenuation coefficient from the raw data:

I generate I_0 and I_1 values from raw data
II determine $\int \mu \mathrm{d}z$ per pixel

The achieved values per pixel (y, z) of a projection represent the attenuation of the X-ray beam by the whole width of the sample along the optical axis x.

In principle, this is the required preparation for the tomographic reconstruction of the XRA data. Nevertheless, this process needed to be extended in this project due to fluctuations of the beam current and instable measurements of the diodes. Figure 8.4 shows the initial situation for an exemplary projection angle. The three signals, gained from (a) the transmission diode, (b) the diode in the beamstop and (c) the ring current from the machine are plotted in the graph (d). This figure points out the necessity of data preparation by visualizing the influence of the ring current on the measured diode signals. In addition, as mentioned in Sec. 4.4.3, the transmission diode was too noisy[2], see inset in Fig. 8.4, which shows a part of the scan without sample. Hence, only the beamstop diode was used to determine the absorption values. Additionally, the influence of the ring current is taken into account and above all, the failures in the beamstop diode are addressed. These corrections will be explained in detail in the following Secs. 8.2.1 to 8.2.4. Finally, the XRA analysis is completed by the tomographic reconstruction of the data as well as the comparison to known mass attenuation coefficients[3] μ/ρ in the literature, see Secs. 8.2.5 and 8.2.6.

---

[2] The fluctuation of the transmission diode values in air regions is approximately three times that of the beamstop diode values in the same regions, false pixels ignored.

[3] alias photoabsorption coefficients

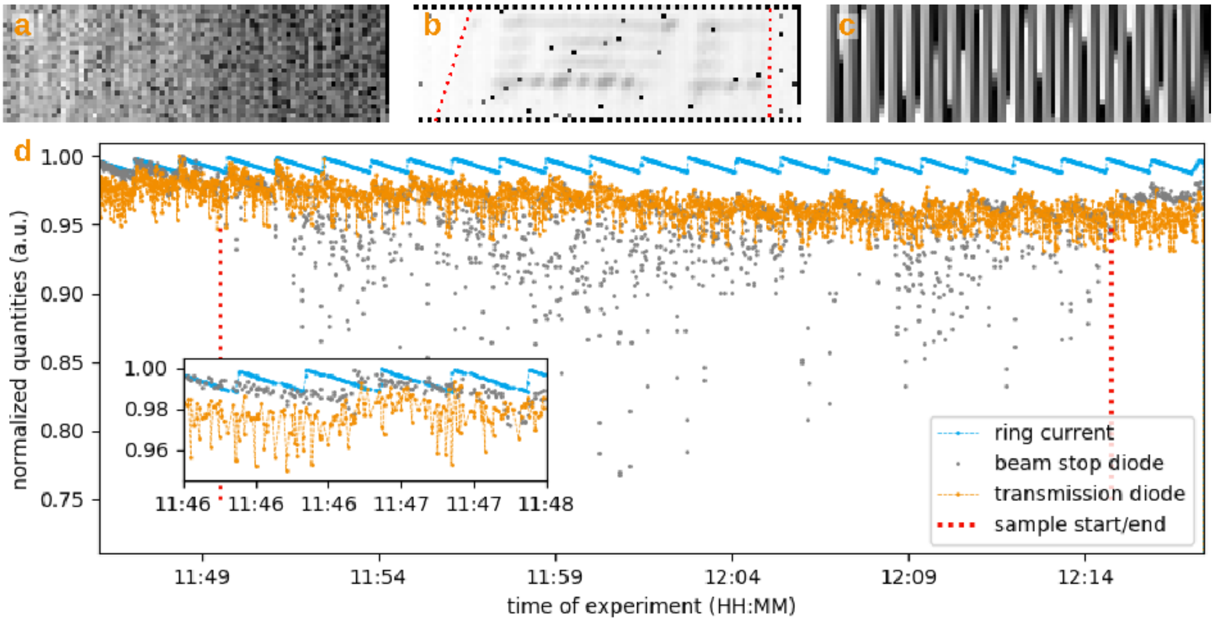

Figure 8.4: Unprocessed projection images and plotted data of one representative scan. The images show (a) the raw signals of the transmission diode and (b) the diode in the beamstop as well as (c) the ring current. The graph (d) shows the different signals in direct comparison over time. In the graph and in (b), start and end of the sample region are marked in red. The inset enlarges the vacuum region at the beginning of the scan.

8.2.1 Calibrating Data

To determine the photon absorption of the sample, the incoming signal is measured upstream and the transmitted signal is measured downstream of the sample. Based on the Lambert-Beer law, see Eq. (2.37), the absorption coefficient μ is the natural logarithm of the quotient of those two measurements. With the usage of two separate diodes, a calibration of these to the same reference is essential. Due to the high level of noise in the transmission diode signal, which was used to measure the incoming photon flux I_0, we decided to solely use the signal of the beamstop diode. In this case, the incoming flux cannot be determined simultaneously to the attenuated intensity signal I_1 behind the sample. Instead, the average of the signals from regions without sample was used as reference I_0. By the usage of only one diode, a calibration is redundant.

8.2.2 Ring Current Correction

The signal of the ring current is used to correct variations in the diode signal due to the top up mode. In Fig. 8.4, the influence of the ring current on the diode signals is shown using one exemplary scan. Commonly, the ring current is automatically measured by the DESY machine system and archived for later access. Unfortunately the temporal resolution of this automatically saved data is lower than the time between exposure points. The ring current is saved each 2 s while the time between exposures is approximately 0.6 s and the actual exposure is 0.2 s. For that reason, the extracted values for the ring current were interpolated to the times of each single exposure. To correct the diode values by the ring variations, the ring current signal was normalized and multiplied with the diode signal. The temporal gaps in Fig. 8.5 match the gaps in recording experimental data. Due to some saturation effects of the diode, the measured signal is lower after the fifth day.

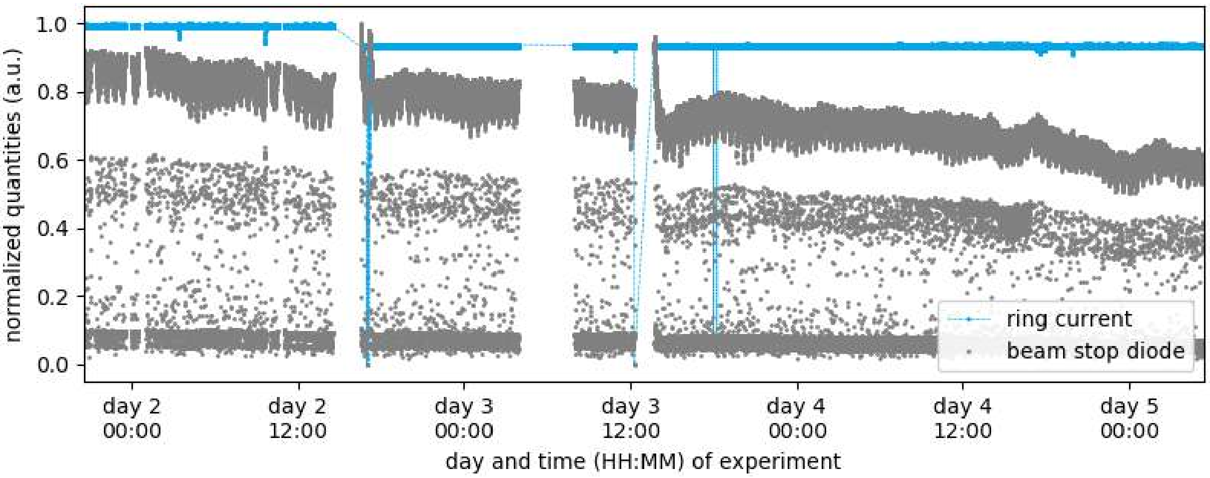

Figure 8.5: This plot shows the normalized data of the relative ring current (in blue) and of the beamstop diode (in gray) over the whole tomography scan time. A change in the ring current from 100 mA to 90 mA is visible at approximately the first quarter of the plot. But this current change has no influence on the analysis. Additionally, a general decay of the signal over the full time is visible, caused by some diode saturation.

8.2.3 Correcting False Pixels

The diode in the beamstop randomly measured false values, cf. Sec. 7.3.5. Here, we correct these false pixels, which is done on each projection individually. The starting point is a projection with false values, cf. example in Fig. 8.6. The good pixels, representing real values, are visible in nuances of orange, while pixels considered as false or bad appear in red and black.
Initially, all pixels below a threshold, set to 75 % transmission, compare upper red line in Fig. 7.8, were identified as false and were corrected. The correction of the faulty pixels was done by interpolation with nearest neighboring pixels in an iterative process. The correction process follows the conditions as listed here, in the order of most to least important, developed together with Lukas Grote, who implemented the Python code.

- The closest neighbors are considered for interpolation.
- Preferably, avoid using already interpolated pixels for interpolation.
- Use direction – horizontal or vertical – with smaller difference of values.
- When no pixels can be interpolated by using the closest neighbors, the second nearest neighbors are used in a subsequent iteration instead, compare Fig. 8.6 A to D.

An exemplary projection is presented in Fig. 8.6, with an enlarged view on an area with an accumulation of false pixels, showing the changes between the iterations. If the red pixel in A is exchanged by a green dot in B, the horizontal neighbors were used to interpolate this faulty pixel, while the blue dot represents the vertical interpolation, respectively. The structures present in the sample are mostly arranged in multiple horizontal planes. Hence, the interpolation using the horizontal neighboring pixels would be preferable to the interpolation using the vertical neighbors. However, the algorithm sticks to the rules as listed above, where the horizontal interpolation is not prioritized. Yet, the choice of horizontal interpolation over vertical is in most cases automatically fulfilled by the rule to use the value with the minor change between the used neighbors.

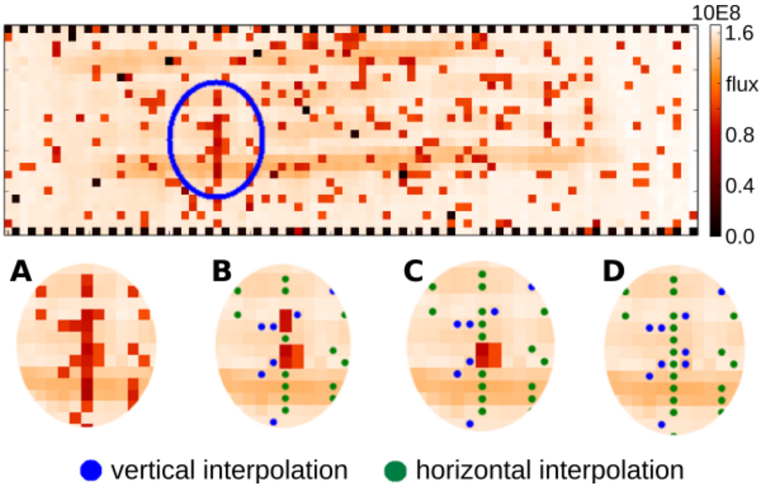

Figure 8.6: The interpolation process to correct the absorption values is displayed at a projection with one of the highest failure rates:
A - original image,
B - first iteration,
C - second iteration,
D - third iteration.
The colored dots mark the interpolation direction which was applied to correct the value at this position.
By courtesy of Lukas Grote [125].

On average, one to three iterations were necessary per projection. Less than 10 % of all projections needed up to six iterations. Despite the correction of all these deviating pixels values, a residual error remains in the final projections due to slight smoothing of the edges of sample features through interpolation. This will cause a reduced resolution in the tomographic reconstructions, compared to a failure free data acquisition.

8.2.4 Determination of Absorption Coefficients

As mentioned earlier, the signal of the transmission diode is far too noisy, thus the beamstop diode data from the empty regions of the scan area serve as reference I_0 for the determination of the absorption coefficients.

8.2.4.1 Definition of Reference Regions

Due to the sample being prepared as a cone, at each angular step ω the scans started and ended in a region next to the sample. These scan positions in empty regions are used as the reference signal I_0 for the XRA analysis. To differentiate the sample regions from reference regions, per projection the signal was separated by a threshold to define regions on and off the sample.

In principle, both contrasts XRA and XRF could be used to identify these regions. With XRD data, it is in general more difficult to distinguish sample regions from its surroundings, for example by using the sum of a diffraction pattern per scan point.

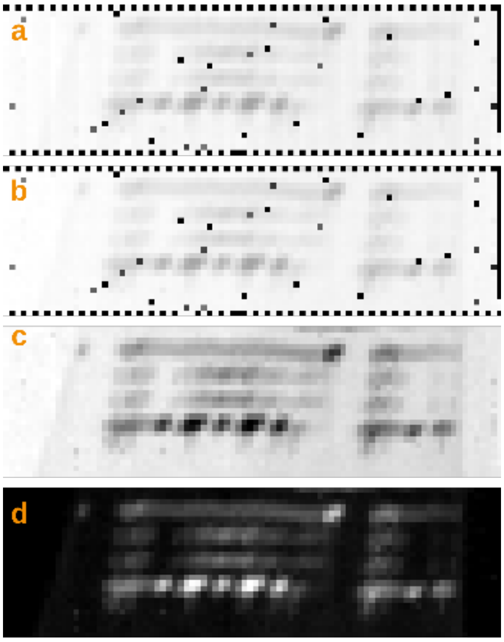

Figure 8.7: Analysis steps for an example projection. (a) shows the raw signal of the pin diode, which is calibrated and corrected to the ring current in (b), compare I and II in Fig. 8.3 and the summary box. In (c) the image is interpolated III and (d) depicts the resulting $\int \mu(x,y)\mathrm{d}z$, IV.

On the one hand not all parts of the sample are crystalline enough to create diffraction signal and on the other hand, the available crystals do not diffract the beam for an angular position ω if the Bragg condition is not met.

In the end, the XRF data for Ga was used, as the sample is covered by Ga and Pt due to the sample preparation with the focused ion beam (FIB), cf. Sec. 5.3. It only occurs at the edges of the sample and for that reason clearly shows the transition from sample to the surrounding. Besides the threshold, which identifies the transition, the search region was restricted to 25 pixels from the edges of the image, as the sample is located in the middle of all projections with slight shifts to the left and right. For the left part of the image, the search routine starts at each line from the left and ends at the first position, that exceeds the threshold and vice versa for the right part. All those pixels, until the threshold is reached, are considered as part of the sample free reference region.

8.2.4.2 Determination of Attenuation per Scan Point

As it is visible in Figure 8.5, the graph of the raw values from the beamstop diode show a general decay. With the projection-wise calculation of the absorption coefficients, referenced to itself, the influence of the decay vanishes. There are two cases to consider for the calculations: In case one, the mean reference value of the scan start $I_{0_{start}}$ is comparable to the mean reference value of the scan end $I_{0_{end}}$ of a projection. Hence, the determination is done per scan point (y, z) with the value $I_1(y, z)$ and the mean of all reference pixels I_0 of this projection. In the second case, there is a noticeable gradient between the two reference values. Thus, the gradient between $I_{0_{start}}$ and $I_{0_{end}}$ is considered and the reference value $I_{0_{adjust}}(y, z)$ is adjusted per scan point to account for the gradient of the reference I_0 during the recording of a single scan. At this state of the XRA analysis, step IV in Fig. 8.3 closes the preparation process, which handles all projections individually. In Fig. 8.7 all steps of the preparation procedure are presented exemplarily for one projection.

Summary of the procedure to transform raw data to attenuation coefficient:

- I calibrate pin-diode values
- II correct these values to the relative ring current
- III interpolate the image to remove false pixels
- IV define empty region, take mean there as I_0 and determine $\int \mu \mathrm{d}z$

8.2.5 Tomographic Reconstruction of the XRA Data

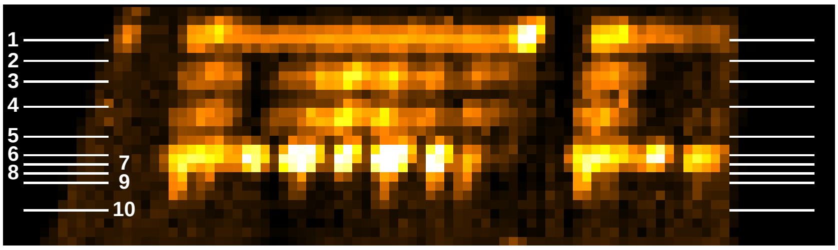

Figure 8.8: XRA projection with white reference lines for the slices presented in Fig. 8.9.

The last and final step of the XRA data reconstruction is the combination of all the projections to generate a three-dimensional XRA volume. For this, the alignment parameters are applied to the data stack and the tomographic reconstruction, as described in Sec. 3.2, is executed. Briefly summarized, the projection stack transformed to a stack of sinograms with one sinogram for each height in the recorded projections. A reverse Radon transform is applied to each of the sinograms to reconstruct the 3D volume, which in turn is a stack of 2D tomographic slices at different heights. Figure 8.9 shows selected slices, representative for the successful tomographic reconstruction. The lines in Fig. 8.8 from top to bottom represent the heights of the slices in Fig. 8.9 starting at the top row from left to right and ending at the bottom right.

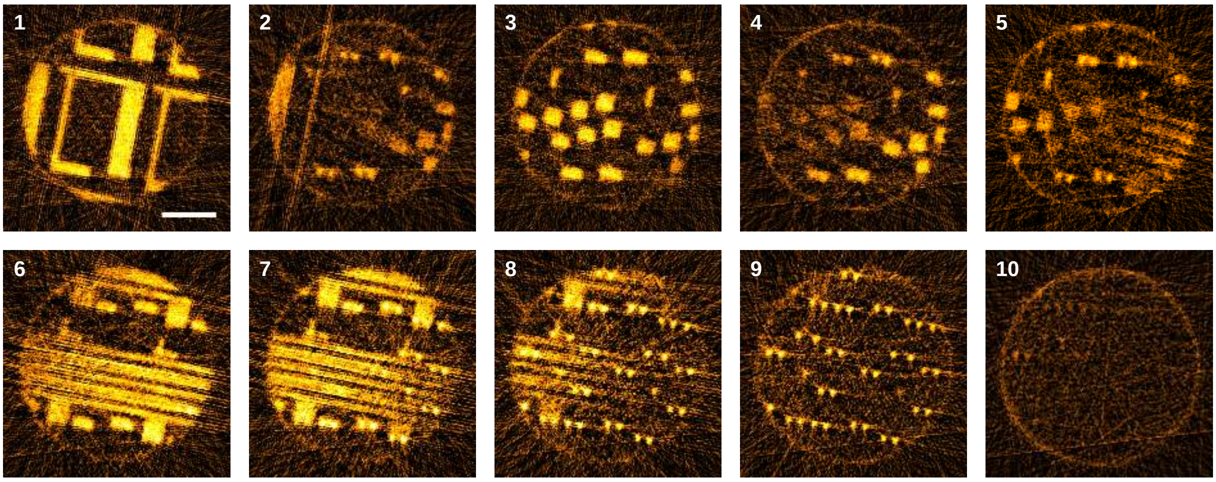

Figure 8.9: XRA reconstructions, the colors represent attenuation coefficients from 0.0 (dark) to 1.5×10^{-3} per pixel (bright), the scale bar is 2 µm. The slices belong to the marked vertical positions in Fig. 8.8.

8.2.6 Comparison of Measured to Listed Absorption Values

Based on the knowledge about the elemental composition of the microchip, we compare the reconstructed attenuation coefficients of the structures to the coefficients of the corresponding elements at the incident photon energy of 18 keV in literature. From Chapter 6, we know that most of the structures are made of copper and the plugs at the bottom are made of tungsten. Additionally, silicon is present at all layers, either as a compound in the structure stack or in pure form as substrate. For this reason, the determination of the mean attenuation coefficients μ in the structures is done for Cu, W and Si at four representative two-dimensional slices, see Tab. B.4 in the appendix. These are converted to the mass attenuation coefficients $[\mu/\rho] = \frac{cm^2}{g}$

by dividing through the element specific density $[\rho] = \frac{g}{cm^3}$. The result of this comparison is summarized in Tab. 8.1.

element	markers in Tab. B.4	ρ (g/cm^3)	lit. μ/ρ (cm^2/g)	meas. $\pm$ tol. μ/ρ (cm^2/g)
Cu	$\#1 - \#22$	8.96	44.84	41.52 ± 2.87
W	$\#23 - \#28$	19.3	81.79	21.69 ± 0.81
Si	$\#29 - \#32$	2.33	5.512	4.98 ± 1.5

Table 8.1: Summary of a comparison between literature absorption values and measured values. The underlying data is listed in the appendix, Tab. B.4. The literature values for ρ and μ/ρ are taken from the Center for X-ray Optics [126].

By comparing the measured and literature values, it becomes obvious, that the copper as well as the silicon is well represented by our data with only slight deviations. Yet the tungsten plugs do not fit to the literature value. This can be explained by the structure size versus the voxel size of 100 nm^3. Compare 120 nm to 140 nm for the W plugs and 100 nm step sizes. In a voxel, the average attenuation inside of this volume is reconstructed. Therefore, during the acquisition, the structures are not sampled by one scan point only, which means that the result is the average of these structures and their environment, resulting in much lower or divergent values.

8.2.7 3D XRA rendering

The stack of 2D slices can also be rendered as a 3D volume, cf. Fig. 8.10, for better understanding of the relative arrangement of the different structures in space.

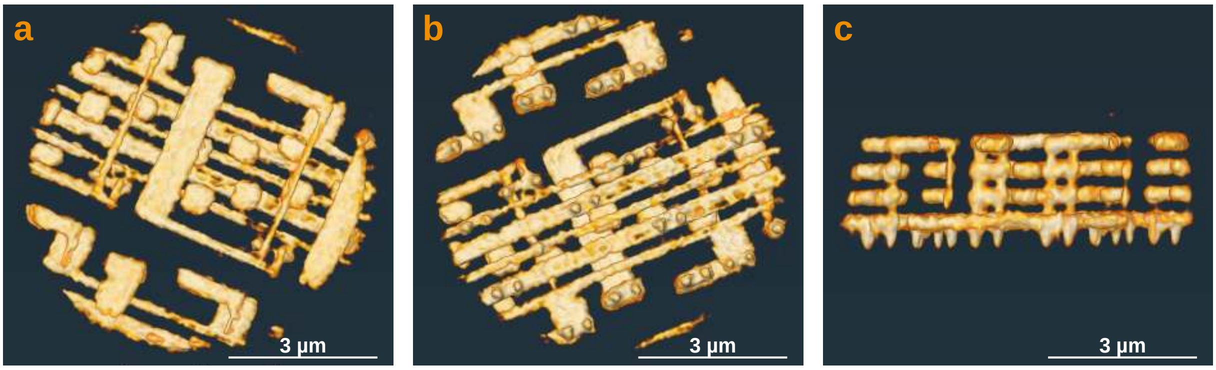

Figure 8.10: 3D model of XRA results. The metal parts of the sample, which conduct the current through the stack, are depicted in (a) a top view, (b) a bottom view and (c) a side view.

8.3 Analysis of the X-ray Fluorescence Data

This part of the analysis determines the elements of the sample and their spatial distribution. The analysis of the X-ray fluorescence data divides into the transition from raw XRF data to elemental information, to the live time correction of these, and finally, to the tomographic reconstruction, see Sections 8.3.1, 8.3.2 and 8.3.3, respectively. In the latter, the element specific data is reconstructed tomographically and depicted in 3D.
The complete work flow is depicted in Fig. 8.11.

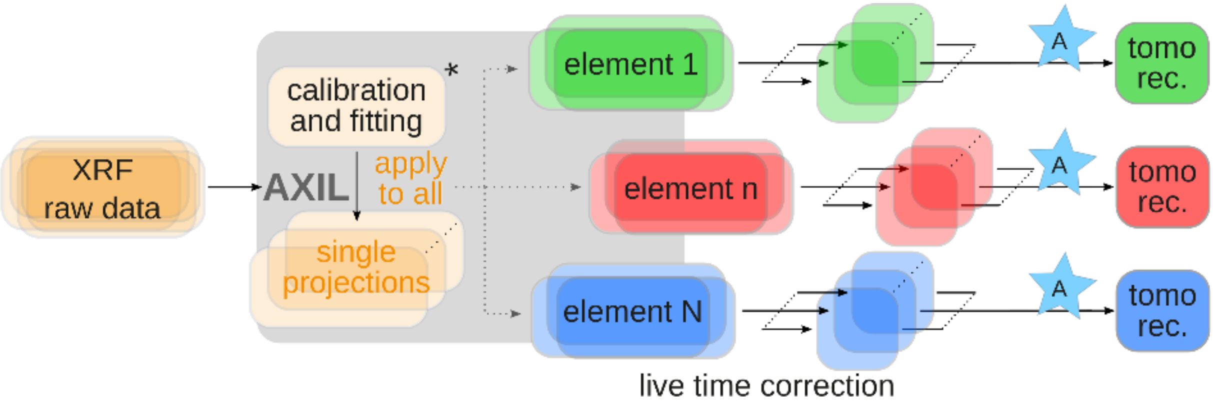

Figure 8.11: Flowchart for XRF analysis, depicting the process from raw data to tomographic reconstructions for the $n = 1 \ldots N$ elements. The data calibration and fitting for the XRF analysis – marked with $\star$ – is done at one representative scan and is then applied to all scans.

8.3.1 Extraction of Elemental Information from Raw Data

The major part of the XRF data analysis, which is the fitting of the XRF raw data to extract the elemental distribution, was carried out with the program 'Analysis of X-ray spectra by Iterative Least squares', short AXIL [127, 128]. Alternative XRF data analysis programs are for example the python module PyMca [129] or GeoPixe [130]. The underlying working principle of all these analysis tools is similar.
At the beginning, the raw data, provided as both one $\sim$.spe and one $\sim$.edf file per scan point, is extracted. These files contain the X-ray fluorescence spectrum of that respective scan point. The spectrum is divided into 2048 channels, containing the detected photon events, energy-dispersively separated.
The following numbers shall serve to get an impression of the analyzed data. The raw data of the 136 scans, with 2236 scan points per scan for the majority of scans[4], has on average 2×10^6 events per scan, which makes on average 923 counts per scan point as sum of all channels. The number of events for the channel with the highest counts per scan is on average 52.
The average mean value of events over the full measurement is at 0.22 counts.
The summed up extracted spectra of one representative scan have been used to define a general

---

[4] The measurement started with 2626 scan points and was reduced twice, first to 2366 scan points and finally to 2236, which equals the amount of pixels in a 101 × 26, 91 × 26 and 86 × 26 scanning grid, respectively.

calibration and fitting for this experiment. The fitting contains general settings such as the limits of the actual data, the channel width and the definition of measured elements. The calibration includes the assignment of the channels to certain energy ranges. Subsequently, all scans were analyzed on the basis of these calibration and fitting parameters. Furthermore, the background is calculated [128] and peaks are fitted as Gaussians with non-Gaussian tails. Further effects of the creation and detection of XRF photons are explained in the appendix B.3. Within a batch process for each single projection, the spectra of every scan point of that projection were analyzed individually. The general parameters were applied to the respective spectrum, then the background was calculated and removed and subsequently, the peaks were fitted and assigned to the according elements.

The result of this batch process is one text file per projection, which contains the extracted data per scan point and lists the elements and the collected number of photons for each element and scan point accordingly. In the subsequent step, the data of these files is transferred to matrices for each projection and element. The elements used for the spectral fit were Co, Cu, Ta and W in the sample as well as Ga and Pt, see Fig. 8.12. The emission lines of the fitted elements are listed in Tab. B.1 in the appendix.

The latter two elements, Ga and Pt, are remnants from the preparation of the sample using a focused ion beam and are located at the sample surface.

Furthermore, we expected to get titanium (Ti) extracted from the spectra, as it should be available around the W plugs in small amounts as a thin liner. It is even visible in the total spectrum, see upper graph in Fig. 8.12, but the analysis does not show clearly assigned regions as the signal is rather randomly distributed. As a result, not a single clear structure could be resolved in any projection or volume showing the extracted Ti signal. Potential other materials were not found and some peaks stay undetermined while they do not match any material that is

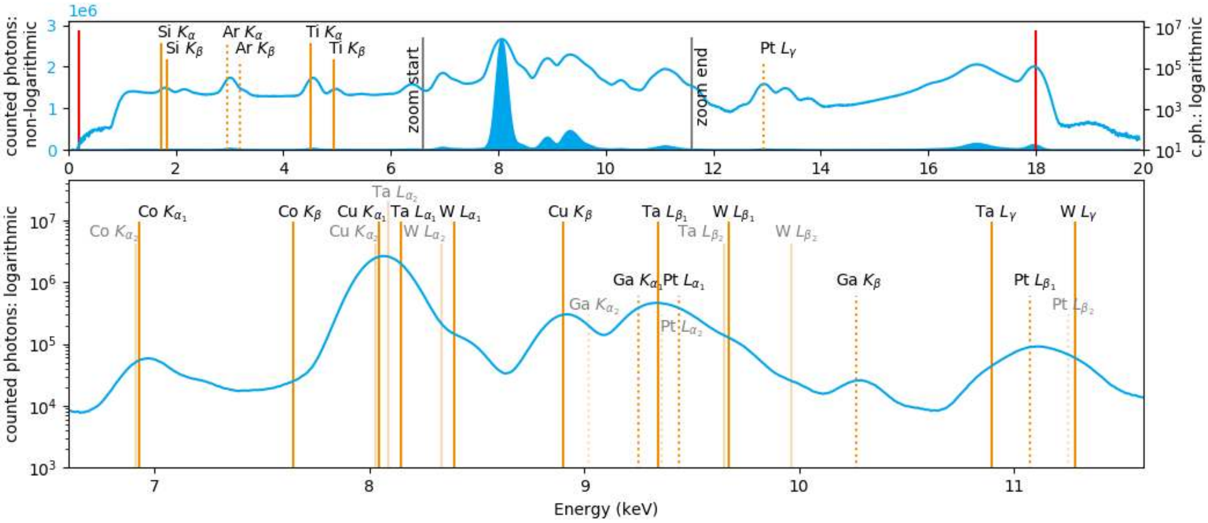

Figure 8.12: Uncorrected, summed up X-ray fluorescence spectrum for the whole measurement. In the full detected spectrum in linear (filled graph) and logarithmic scale (line plot) in the upper plot, the substrate Si as well as Ti are clearly visible. The lower plot, enlarging the marked region of the upper plot, shows most of the emission lines of the sample. The characteristic photon energies are given in the Siegbahn notation [131]. The relevant lines are the α_1 and β lines, further lines are faded. The labels for the XRF emission lines for Ga and Pt are put to lower positions in the graph to separate the content of the microchip and elements from preparation.

expected in the microchip. For example the emission lines of iron[5] (Fe) fit quite well, but this is very unlikely contained in the microchip. In turn, the setup, which is made of Invar to a large extend, contains Fe. However, Invar also consists to approximately $1/3$ of nickel[6] (Ni) which cannot be seen in the spectrum.

For conclusions about the absolute quantitative distribution of the elements, the implementation of data from foils for standards would have been necessary. In this first attempt of the multimodal experiment, we did not measure any reference standards and thus present relative qualitative results.

8.3.2 Live Time Correction

As described by Bonetto and Riveros [132] and Ran Yan et al. [133], during XRF measurements, not all events are registered: With an X-ray photon entering the XRF detector, pulses are initiated and recorded. During this time of recording, the detector cannot respond to any other second incident X-ray photon. This time period to process the pulses is called dead time as many photons at the same time can accumulate, but none is counted. The result is a lower effective count rate.

During our experiment, instead of the duration the detector was unable to count further photons, the active time, called live time was measured per scan point. These live times were used to correct the projection maps gained from the analyzed spectra to create a more realistic distribution of events. With the live time correction, the adjusted spectrum has a higher Cu peak. The live time correction was applied to the elemental projections individually after the analysis with AXIL[7].

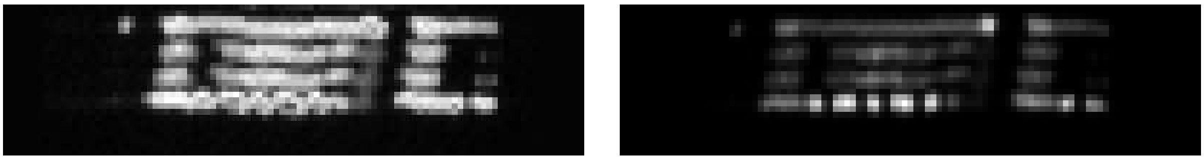

Figure 8.13: One exemplary Cu projection without (left) and with (right) live time correction.

The live time values were not measured during the first 22 scans. Instead, these missing live time maps were created of the live time maps of adjacent angular positions. The difference between projections using calculated and measured live time maps is noticeable, but the overall results show significant enhancements compared to uncorrected results or reconstructions with 22 missing scans.

8.3.3 Tomographic Reconstruction of the XRF Data

The procedure of the tomographic reconstruction of the XRF data equals the one for XRA, see Sec. 8.2.5. In comparison to XRA, the XRF data results in a 3D volume for each analyzed element: Cu, W, Ta and Co. Beginning with the alignment, the shift parameters are applied to

---

[5] Fe K-lines: K_{α_1} = 6.40 keV; K_{α_2} = 6.39 keV, K_{β_1} = 7.06 keV

[6] Ni K-lines: K_{α_1} = 7.48 keV; K_{α_2} = 7.46 keV, K_{β_1} = 8.26 keV

[7] The live time correction can be directly included in the AXIL analysis. At the time of the analysis of the raw data, we did not consider the live time correction.

the data stacks, as described in Sec. 8.1. Sinograms for each element, and each height are generated and finally tomographically reconstructed, filtering included. An extract of the results is shown in Fig. 8.14 and 8.15. In the first figure, Fig. 8.14, the four individual projections show which structures correspond to which element. In the middle, all four elements are combined, to show their relative positions.
Additionally, the heights of selected 2D tomographic slices, which are presented in Fig. 8.15, are marked with white lines and numbers.

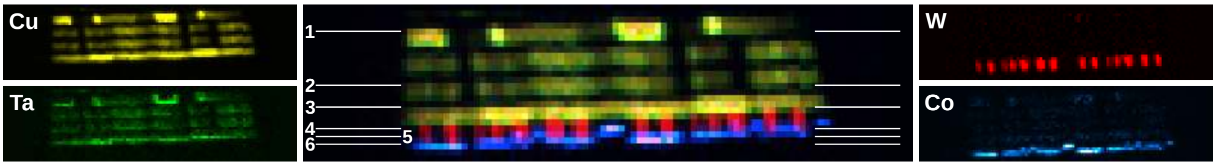

Figure 8.14: X-ray fluorescence projections separated into four different elements (left and right). The large image in the middle shows the combination of all four elements and includes the heights selected for representative tomographic reconstructions in Fig. 8.15. The full width of such a projection is 10 µm.

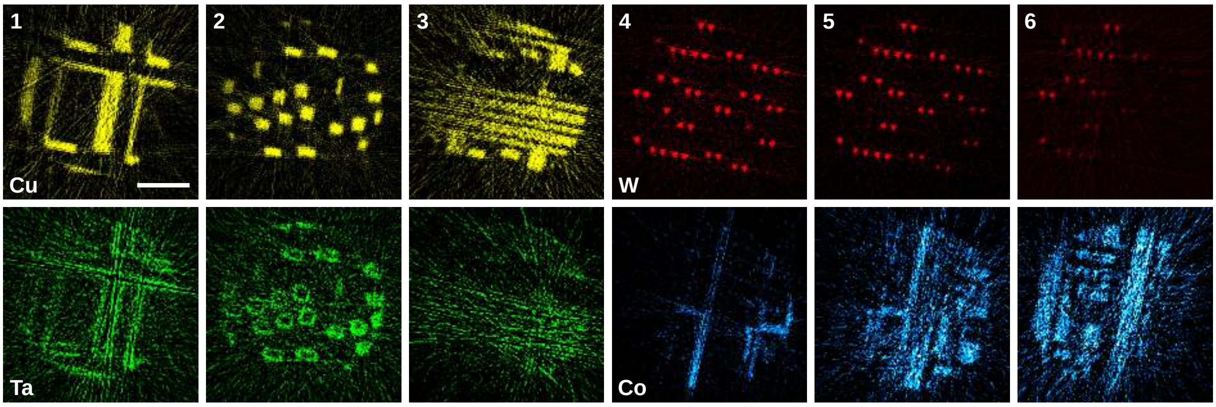

Figure 8.15: Selected slides of the tomographic reconstruction of X-ray fluorescence data. The heights are marked in Fig. 8.14. The scale bar in the first image is 2 µm.

The tomographs of Cu and W show smoother structures than the tomographs of Ta and Co. The sparse resolution of the Ta structures is justified by the fact that these structures are very thin and only sampled by a fraction of the beam. The Cu structures in comparison exceed the size of one scan point and the beam size. For the latter structures, the angular sampling seems to be sufficient. The same is valid for the W structures, which fill at least the width of one scan point. The reason for the irregular Co patterns is partially similar to the explanation for Ta with the difference that these structures are thin in vertical direction an extended horizontally. Additionally, due to a trade-off regarding the positioning of the detector during the experiment, reducing the dead time in the Cu regions but still getting signal of elements with emission lines at lower energies, the Co signal is relatively weak in general.

8.3.4 Self-Absorption Correction

To achieve quantitative tomographic reconstructions, attenuation effects of rays through the sample require correction [134]. In a sample, both the incident X-ray beam through the sample as well as the secondary XRF photons created in the sample are attenuated while propagating

through the sample. As a result, dependent on the size of the sample, the signal in the XRF sinogram degrades from the side towards the XRF detector to the side away from it.
With approximately 8 µm in diameter, our sample is relatively thin compared to the analyzed sample in the work by Schroer [134]. At these sizes, the probability for secondary photon-sample interactions is very low. Additionally, there are no obvious gradients visible in the sinograms, see example in Fig. 8.16 in comparison to Schroer [134].

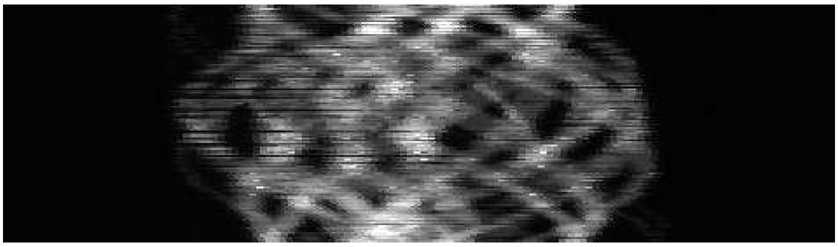

Figure 8.16: Exemplary Cu sinogram. There is no visible gradient in intensity between left and right side.

Nevertheless, we[8] exemplarily applied the self-absorption correction by Schroer to one slice of the Cu tomograph. Cu was chosen for this self-absorption correction as it should be most influenced by the absorption of the other elements, Pt, Ga and Ta, in the same layer with higher emission energies. In case of a relevant selfabsorption effect, the order of highest to lowest absorption energies and emission lines above the emission line of the element of interest needs to be followed. For the example slice, the results of the XRA analysis of this height as well as the tomographs of Pt, Ga and Ta were included in the correction. After the correction, no significant changes can be noticed for the thin sample used in this work.

8.3.5 3D XRF tomographs

The tomographically reconstructed fluorescence data was used to create 3D volumes as combination of all four extracted elements, with approximately the same orientation as used for the XRA results, is shown in Fig. 8.17. Additionally, the results are presented in an overview of individual 3D models for each element and as combinations of these, see Fig. 8.18.

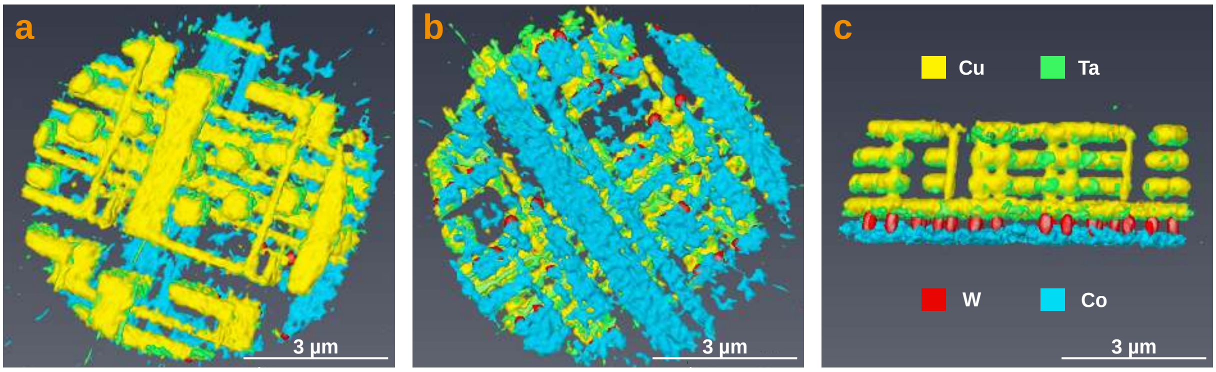

Figure 8.17: Combined 3D model of XRF results. The different elements are shown in different colors, see (a) top view, (b) bottom view and (c) side view.

The gained 3D view perfectly reflects the microchip construction, as also seen in Chap. 6. It starts with the functional structures at the bottom represented by the Co, shown in blue. The W

---

[8] Our former master student Lukas Grote also applied Schroer's self-absorption correction with the same result presented in his master thesis [125].

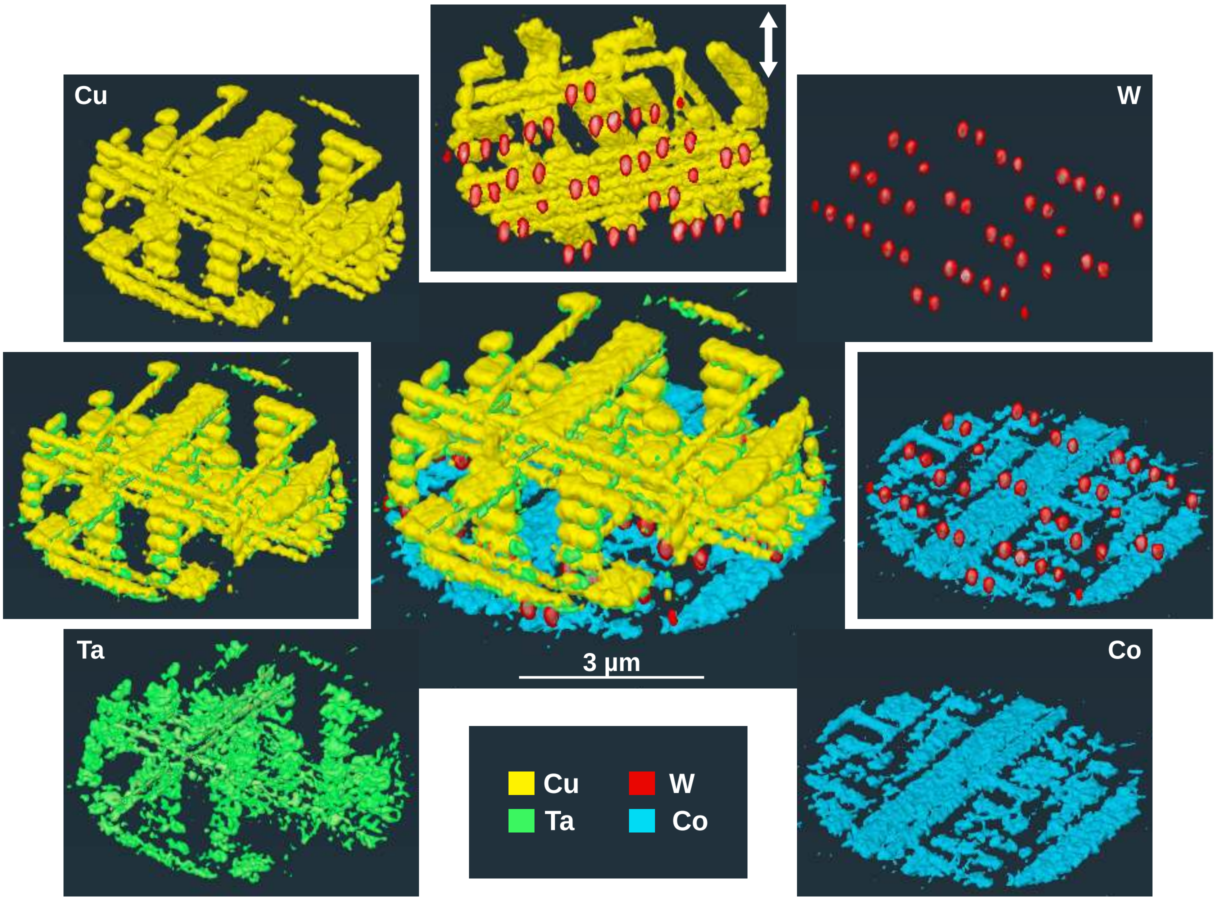

Figure 8.18: 3D models of XRF results. The different elements are shown as individual 3D rendering as well as in combined views. Except the very top image, all have the same orientation. In the upper one, the view is from the bottom to the top to see, where the W plugs are connected to the Cu pads and paths.

plugs above, marked in red, build the connection between these Co containing structures below and the conduction paths made of Cu above. The Cu paths, depicted in yellow, build a complex net with alternating conduction paths and contacts. These Cu structures are surrounded by a thin Ta liner, presented in green. The 20 nm liner structures of Ta around the Cu pads, paths and contacts are clearly visible, but could not be higher resolved than the step size of 100 nm.

8.4 Analysis of the X-ray Diffraction Data

In contrast to the two previously analyzed contrasts, XRA and XRF, with scalar data, the analysis of the XRD data is more complex. Different methods were used and the data was interpreted from different points of view as depicted the overview in Fig. 8.19. With this part of analysis being more extensive than the ones before, it can be regarded as the core of this project. In addition to that, the results of the different methods will be complementary within this contrast. This section starts with two data preparation steps, the background correction of the diffraction patterns in Sec. 8.4.1 and the detector geometry calibration in Sec. 8.4.2. This is followed by general considerations of the data as diffraction patterns and as diffractograms including expectations of the peak coverage, see Sec. 8.4.3. The data is analyzed by powder X-ray diffraction (PXRD) methods as summed up data and for each height individually, see Secs. 8.4.4 and 8.4.5, respectively. Salience in the diffraction patterns and in the diffractograms are discussed in Sec. 8.4.6. Subsequently, the analysis changes to spatially resolved analyses. These are separated into powder and single grain analyses, see Secs. 8.4.7 and 8.4.9, respectively.
With the information about the sample from the manufacturer as well as from general knowledge about microchips, basic parameters are estimated for the materials present in the sample, see Tab. B.2 in the appendix. Actual present materials in the sample partially are compounds and the exact composition was unknown before the analysis.

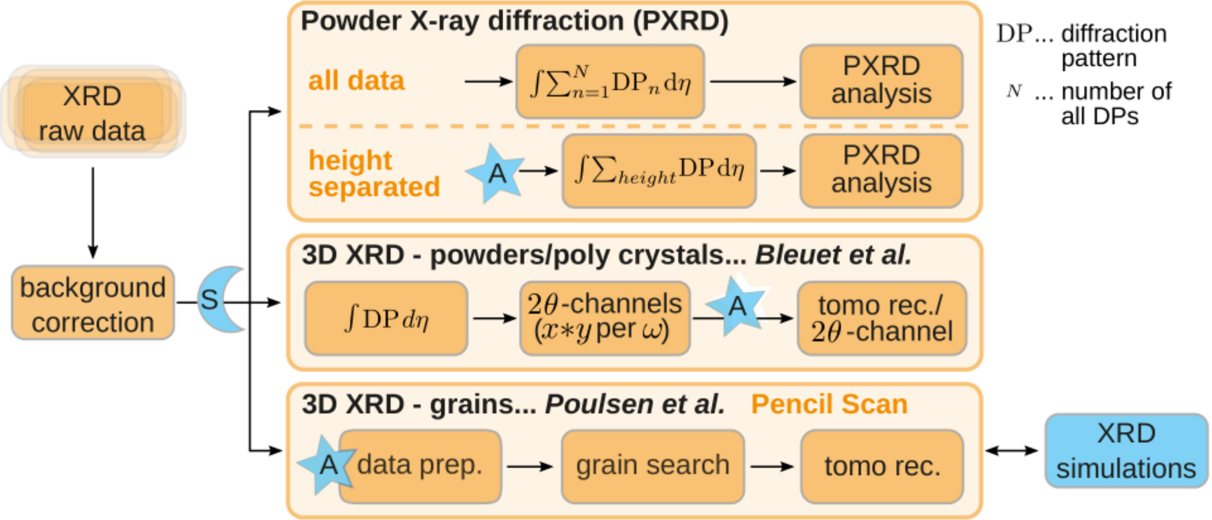

Figure 8.19: The XRD data is analyzed from different points of view. This chart shows the main ways of analysis applied by us. It also includes symbols for alignment and calibration, which are represented by a star and a moon, respectively.

8.4.1 Background Correction

Due to the fact that we took the data in an open environment, the background scattering, as interaction of X-rays with particles in the air, caused noise in all scan points. This weakens the contrast for signals coming from the sample, see uncorrected summed up diffraction pattern in Fig. 8.20a. For this reason, the background was reduced. A background image was created by averaging all diffraction patterns from scan points in empty regions as determined in XRA

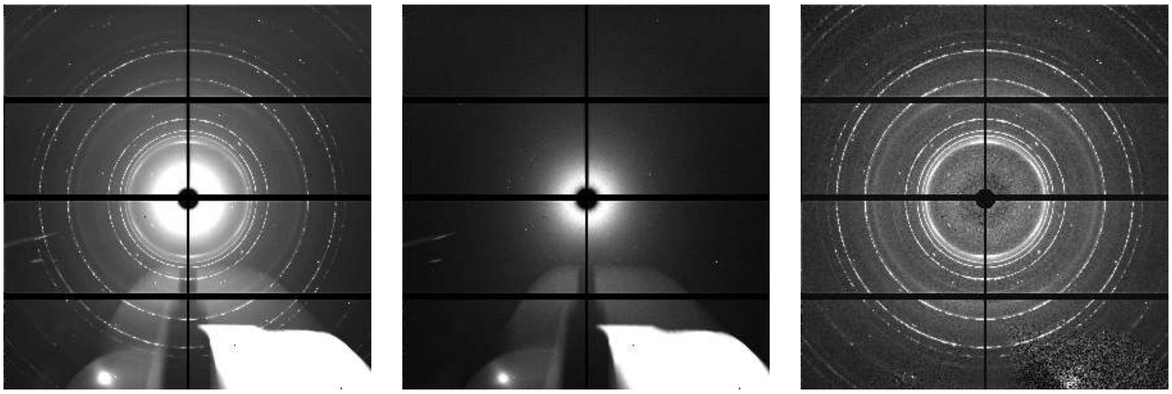

(a) All diffraction patterns integrated.

(b) Background, created from DPs at empty scan positions.

(c) Integral of background corrected diffraction patterns.

Figure 8.20: These pictures from left to right depict the transition from (a) integrated raw diffraction patterns to (b) background and (c) background corrected diffraction patterns. At the bottom of the images, parasitic scattering effects from the beam path upstream of the sample, which could not be blocked entirely during the experiment, stick out in (a) and (c), but are strongly reduced in (c).

analysis, see Sec. 8.2.4. The averaging takes fluctuations over the whole scan into account and leads to a smoothed background image, see Fig. 8.20b. Subsequently, the background image was subtracted from each diffraction pattern. The influence of the background reduction on the data is visualized for the summed up diffraction pattern, compare Fig. 8.20a to Fig. 8.20c. In the latter image, it is obvious that due to the background correction, weaker events become visible which were inconspicuous before. The subtraction of the background image does not remove the background signal completely, as the propagation of the diffracted X-rays through air and secondary effects within the sample cause additional background, but it reduces it significantly. The enhancement of the data by background correction is also visible in the diffractogram of the data set, see Fig. 8.21.

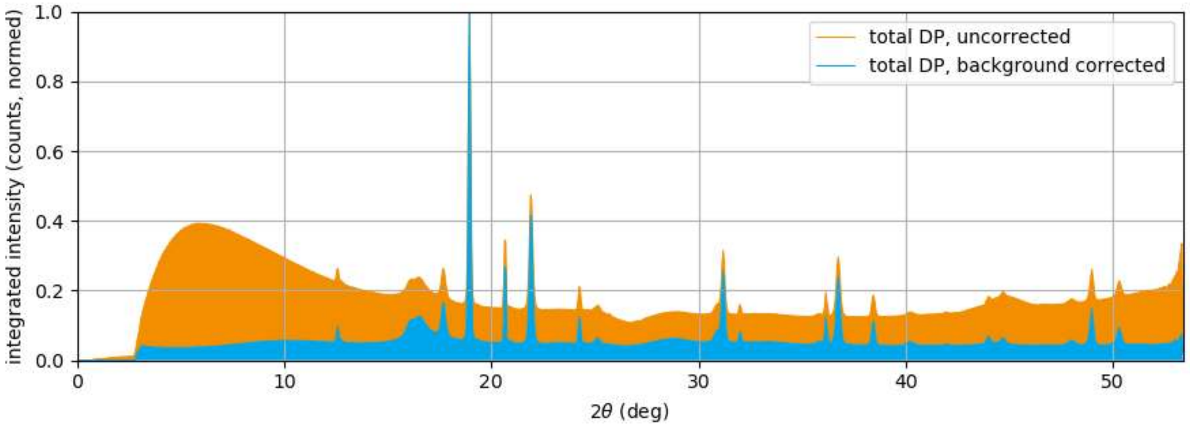

Figure 8.21: Comparison of the diffractograms of all diffraction patterns summed up without (orange) and with (blue) background correction.

The creation of a background image resulted in the following values for the full background image, all values given in counts: mean = 0.015, median = 0.005 and max = 1.877. By considering the first quadrant of the background figure only, the values slightly change to: mean = 0.006, median $= 0.005$, and max $= 0.08$. Compared to the background, in the diffraction patterns some peaks, formed by accumulations of a few pixels with very low values from 1 to 3, will not be detected as peaks any longer.

8.4.2 Evaluation of the CeO$_2$-Standard as XRD Setup Calibration

The evaluation of the calibration standard is essential for the XRD analysis, as it provides the following basic parameters: the location of the center of the diffraction pattern, the distance from the sample to the detector, and the deviations of the detector from being perfectly aligned towards the optical axis in terms of rotation and tilt, which can alternatively be described in three rotation parameters (rot_1 (tilt z), rot_2 (tilt y) and rot_3 (tilt x))[9], compare Fig. 8.22.

To calibrate the detector geometry, we used two different programs, fit2D and Dioptase, which are similar in usage. In each of the programs the calibration image – the summed up diffraction pattern of the calibration scan, see Sec. 7.3.3 – is loaded. Then, the powder, here CeO$_2$, is chosen in the settings and some points in the inner rings are set as initial reference peaks. Eventually, a mask is inserted to exclude panel borders and other effects of the scan from the calculation, which are not peaks of the powder. Estimated values for the sample-to-detector distance and known parameters such as wavelength and pixel size are included in the search mask. Subsequently, the algorithm compares the measured diffraction rings, identified by the peaks marked in red circles in Fig. 8.23a, to the known theoretical values and determines the correct center position, distance and detector rotation. In the display 'cake diagram', plotting the azimuth η over 2θ, Fig. 8.23b, the peaks that fall in the same 2θ region and thus build the diffraction rings, must form a straight vertical line. The calculation would not be correct, if these lines showed a sinusoidal behavior. Additionally, the data can displayed as a diffractogram,

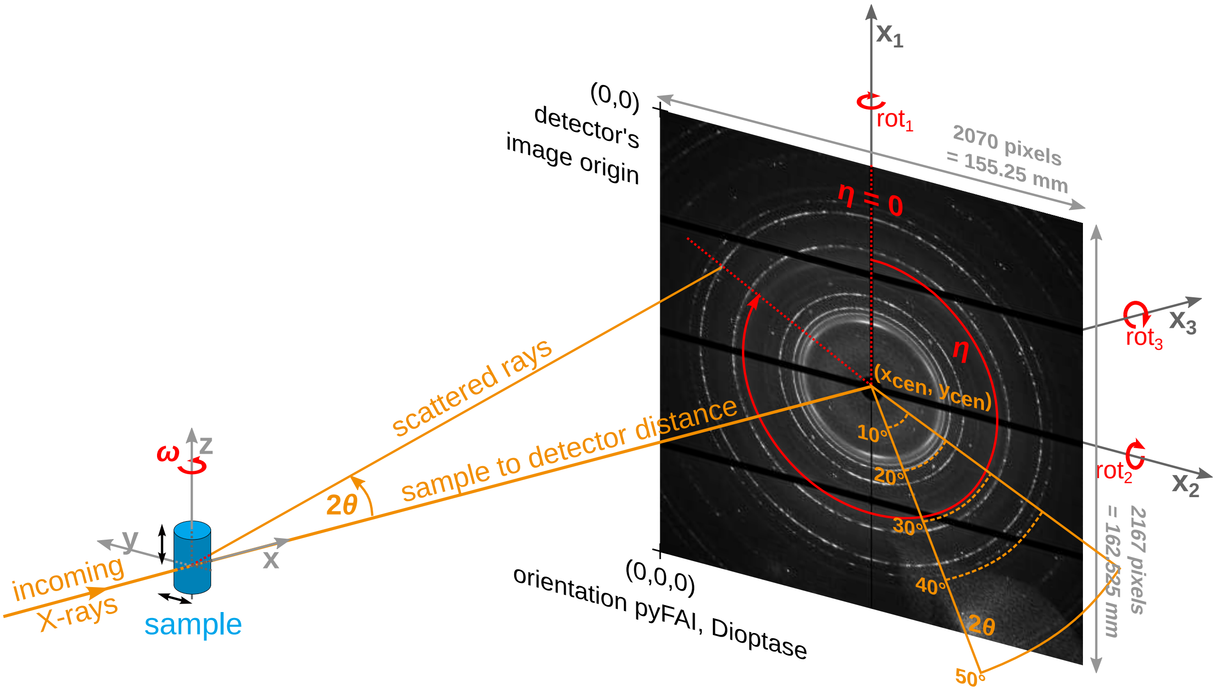

Figure 8.22: XRD coordinate schemes, as used within the analysis.

---

[9] A tilt or rotation around x can only be fitted when something is indexed.

shown in Fig. 8.23c, which represents the azimuthal integration with the total intensity of each ring over the diffraction angles 2θ.

(a) Calibration tab. **(b)** 'Cake diagram', $(\eta - 2\theta)$. **(c)** Diffractogram XRD standard.

Figure 8.23: XRD calibration procedure. These pictures show the results of the calibration using the CeO_2 powder measurement as calibration standard in Dioptase. In (a), some peaks of the inner rings are set. Additionally, a mask to block the panel gaps and the identified peaks on different rings are visible. (b) shows a correct calibration by arranging the peaks in straight vertical lines. The diffractogram in (c) is the result of the azimuthal integration after the correct calibration. The calibration was done without correction of the big blob at the bottom right in (a).

Due to the usage of two different programs, the results were averaged to gain following values in the gray box.

XRD detector geometry parameters

parameter description	Dioptase	Fit2D	$\overline{X}$	$\pm$
sample-to-detector distance in mm	83.78	83.79	83.79	0.01
coordinate of direct beam X in pixels	1036.47	1036.94	1036.71	0.24
coordinate of direct beam Y in pixels	1075.93	1075.45	1075.69	0.24
rotation angle of tilting plane in °[a]	145.47	155.53	150.50	5.03
angle of detector tilt in plane in °	0.41	0.45	0.43	0.02

---

[a] This angle seems to be very large. From the alternative description in three rotations, the value never exceeded 6°. With further testing of different angles, there were no noticeable influences in the results.

8.4.3 General Analysis

Before focusing on specific analysis methods such as the phase determination or searching for and reconstructing of single grains, I provide a general impression of the recorded data.

With the applied scanning scheme and step sizes of horizontally 100 nm and vertically 120 nm, the expectations of the results need to be related to the scanned structures. For the smallest structures, being 14 nm in vertical direction for $CoSi_2$ and approximately 20 nm for the Ta-liner in vertical and horizontal direction, only a coarse positioning can be achieved. In comparison to that, the W-plugs, with horizontal dimensions from 120 nm to 140 nm, and the Cu-structures of around 250 nm are in the range of and larger than the step size and for that reason are better imaged. Furthermore, due to the discrete angular scanning scheme, we missed a certain amount of Bragg reflections. To estimate, how many peaks per grain we were able to detect at all with this scheme, a total 42 differently orientated Cu grains were simulated by PolyXSim [135, 136].

The expected numbers of peaks for these grains were between 64 and 76 for a continuous measurement with the same parameters for energy and detection range 2θ. For the estimation of peak detection, the rotation angle ω of the Bragg peaks is the relevant information. The angular positions were compared to the measured angles of our experiment. Since the peaks could appear over a certain angular range, six tolerances were used to test, whether a peak could be detected or not, see Tab. 8.2.

tolerance	min.	avg.	max.
± 0.1°	5 %	**14 %**	26 %
± 0.2°	6 %	**30 %**	42 %
± 0.3°	29 %	**45 %**	62 %
± 0.4°	48 %	**60 %**	75 %
± 0.5°	63 %	**75 %**	86 %
± 0.6°	80 %	**89 %**	97 %

Table 8.2: Expected amount of peaks for measurements at discrete angles ω, with $\Delta\omega = 1.333°$, compared to continuous acquisition (100 %).

The percentage of peaks within six tolerance ranges from ± 0.1° to ± 0.6° were determined. The first tolerance range of 0.1° represents a poor angular extension of the peaks. With a range of $\Delta\omega\pm$ 0.677°, the measurement is comparable to a continuous scanning scheme. In Figure 8.24, the comparison of the peak positions to the tolerance range is illustrated for three grains at an extracted section of the full angular range. The tolerance range in this figure goes to maximum ± 0.5°, and the peaks represented by red crosses are not covered within this range.

Additionally, it needs to be considered, that the peak position can also be on a detector panel gap. In this case, the peak cannot be detected. This was not included in the upper estimation. But the simulation shows that half of the angular step size, and with that double as much angular

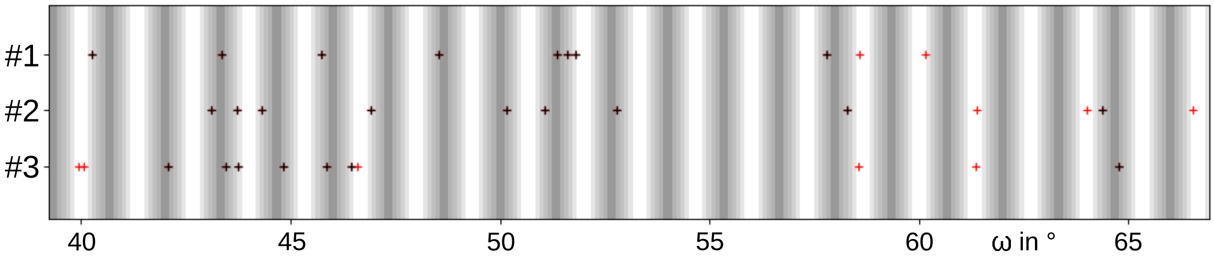

Figure 8.24: Visualization of peaks for three arbitrary Cu grains, #1 to #3. The center of mass of the peaks appear at certain ω positions, marked by crosses. The detection tolerances are marked in overlaying gray from ± 0.1° to ± 0.5°. The red crosses were not even detected within the biggest illustrated tolerance range of ± 0.5°.

projections, would be sufficient to measure most of the peaks for this setup.

Additionally, with the PXRD analysis applied on this data, it is not possible to get information about grain sizes, which usually is a part of this analysis. At least chemical phases can be determined, i.e. a specific material and its structure.

The summed up diffraction pattern is also used to illustrate the azimuth η over the diffraction angle 2θ, see Fig. 8.25. In this view, different crystalline states become visible. Straight homogeneous lines represent polycrystalline phases in contrast to monocrystalline phases, which only have peaks at specific orientations, only at some η per corresponding scattering angle. Furthermore, with the deviation from a straight line, it is obvious that some structures are strained. In comparison to the cake diagram, the diffractogram is plotted at the bottom of the image.

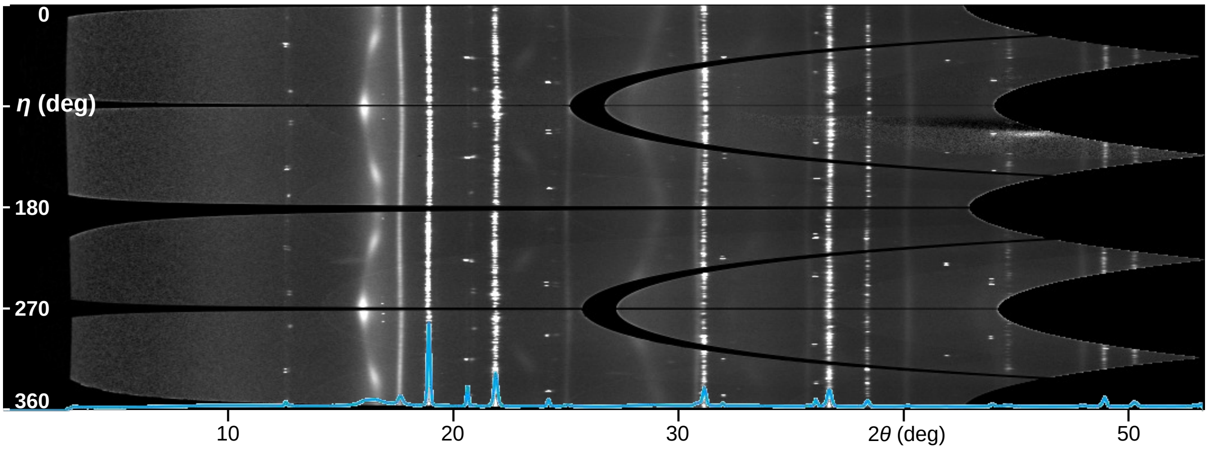

Figure 8.25: Azimuth over scattering angle, alias 'cake diagram' of summed up diffraction pattern. Highest intensities appear brightest.With the separation into the different projection angles it is clearly visible that not all directions η contribute in the same way to the major peaks, for example the one at $2\theta =$ 20.5° to 21.0° or that at around 24.0°. The blue line at the bottom is the corresponding diffractogram.

8.4.4 Powder X-Ray Diffraction Analysis – Overall Diffractogram

In common powder diffraction measurements, the sample is rotated during the exposure and one diffraction pattern is acquired for a full rotation of either 180° or 360°. In the case of an actual powder, due to the rotation, the Bragg peaks of that material are not clearly separated any longer and all peaks accumulate in Debye-Scherrer rings. For solid or grainy samples, the results are similar to the Cu reflections in our data and also accumulate in specific rings. These rings are used to determine the crystalline phase of a material. Different sets of rings belong to different crystalline phases. All peaks of an (hkl)-family corresponding to one element or elemental composition accumulate in one ring. Usually, PXRD is used to analyze samples of a single material with different oxidation states, arranged in crystallites of arbitrary orientation, provided as powder or bulk sample. PXRD is also used to determine stress and average strain of the sample as well as textures.

The sample is a bulk sample with mixed materials. Furthermore, as the data was recorded at static positions and with a finite beam smaller than the imaged structures, the diffraction patterns had to be summed up for a meaningful powder X-ray diffraction analysis. In the diffraction pattern in Fig. 8.27 it is visible, that some structures are made of bigger crystallites, alias grains, and other structures are made of smaller grains and are therefore equivalent to a powder in that regard. The grainy structures build interrupted rings with varying width, while the powdery structures show smooth and homogeneous rings. A third class, the clearly separated and single peaks originate from a monocrystalline part of the sample.

As starting point for the analysis of the XRD data, all diffraction patterns were added and azimuthally integrated, taking into account the geometry parameters. The resulting diffractogram is the basis for further analysis steps with the aim of analyzing the general distribution of the elements or elemental compositions of the structures and their crystallinity. Furthermore, with the average over the peaks of all scan points and rotation angles, the crystalline phases are better imaged, even if the image shows rather single spots instead of rings. For the first phase assignment, the software Topas[10] [137] was used. This program makes use of a huge library of data and provides different fitting algorithms, such as the Rietveld refinement. For a precise statement about the sample the peak statistics of our data were not sufficient. Basically, the intensity distribution among the different phases follows certain rules. Due to strong intensity differences, not all peaks could be assigned. In addition to that, deviations due to strain and probable effects due to crystal edges of small grains complicated the assignment. Furthermore, due to the applied discrete measurement, we miss a significant percentage of peaks. With this, the literature values of the single phases, dependent on specific intensity distributions among the peaks, varied from the expectations. As a result only the distinctive phases of pure Cu, W and Si could be assigned.

In Fig. 8.26 the contribution of the angular positions to the single peaks is presented. It depicts the azimuthally integrated data per scan, which are the diffractograms per projection angle. They are presented in a comparable arrangement where higher intensities appear brighter. The ω range, presenting the projection angles, goes from 0° to 180° in 135 steps and the scattering angles 2θ, with its maximum at approximately 53°, are split into 1068 channels. With the separation into the different projection angles it is clearly visible that not all directions contribute to major peaks, for example the one at $2\theta \approx$ 20.5° to 21.0° or that at around $2\theta \approx$ 24.0°. Additionally, the phases assigned by Topas are marked on top and at the bottom of the image. The remaining reflections were assigned manually by comparing the found 2θ angles against published lattice constants for the elements known to be inside the sample. The expected scattering angles 2θ are listed in Tab. B.3 in the appendix.

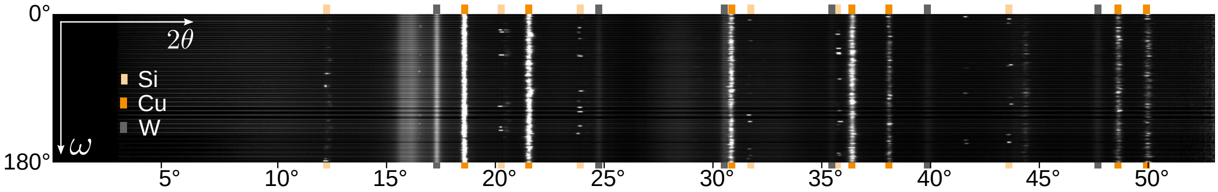

Figure 8.26: Azimuthal integration per angular projection. The brightness indicates the intensity of the data. The colored markers on the top and bottom show which 2θ position belong to which identified element.

In Figure 8.27, the phase assignment is extended by Ta and $CoSi_2$. In comparison to the angular

---

[10] The analysis was done by Martin Etter in my presence.

distribution in Fig. 8.26, Fig. 8.27 shows the direct overlay of an extract of the diffraction pattern and the diffractogram of the summed up data. With this overlay the contribution of single peaks compared to powder rings is emphasized. In this total diffraction pattern, the $CoSi_2$ peaks vanish in the noise. For that reason, only the first three peaks are visible and marked.

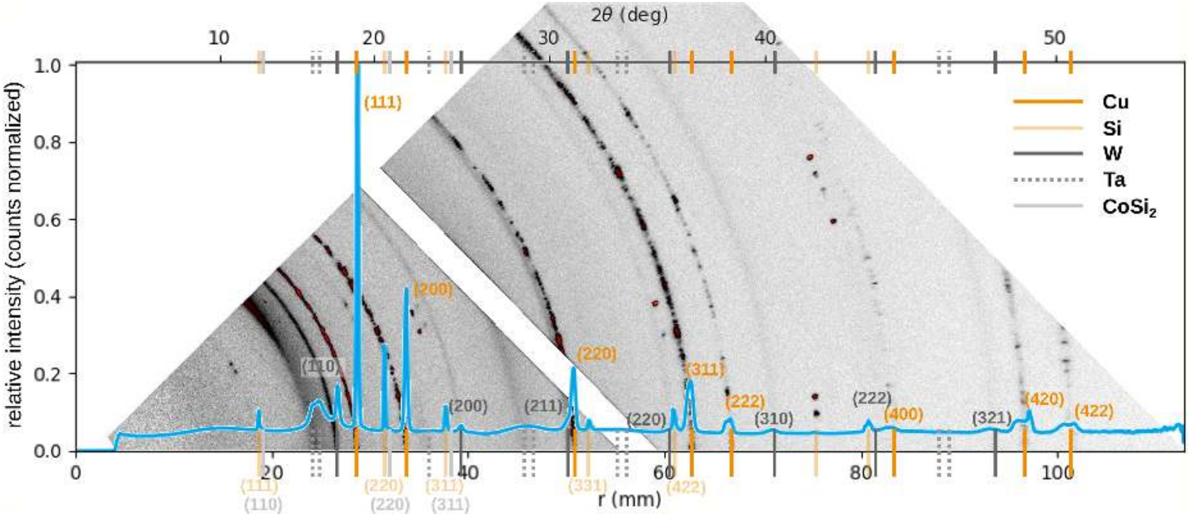

Figure 8.27: Overall diffractogram with phases marked. Angular distances are displayed at top of the graph.

8.4.5 Powder X-Ray Diffraction Analysis – Height Separated

As the structures and their composition change with different layers, the diffraction signal changes accordingly. Overall, the Cu signal exceeds the signal of other scattering materials in the total diffractogram, despite not occupying all heights. For that reason, for each height only the corresponding diffraction patterns were summed up and at heights with less Cu, other diffraction signals are pronounced. The position of the heights in the sample are shown in Fig. 8.28.

Figure 8.28: Height references for the results presented here are marked in a summed up projection on the right and at approximate heights in an EM image on the left.

With the separation of the distinct heights subtle differences in the peak distribution emerge in those regions otherwise diminished by Cu signal. This is visible in both the summed diffraction patterns and the diffractograms of the individual heights. The latter is presented as an overview in Fig. 8.29. Looking at the lower part of this graph, it is obvious that with the absence of the most prominent scattering element, weaker signals emerge. To emphasize the differences, I selected three heights for a direct comparison of the diffractograms and diffraction patterns in Fig. 8.30 and Fig. 8.31, which were marked in the same colors in Fig. 8.29.

Most conspicuous about these heights are the different kinds of diffraction signals. Starting with the first of the selected heights, height 10 shows a variety of diffraction signals. Most prominent

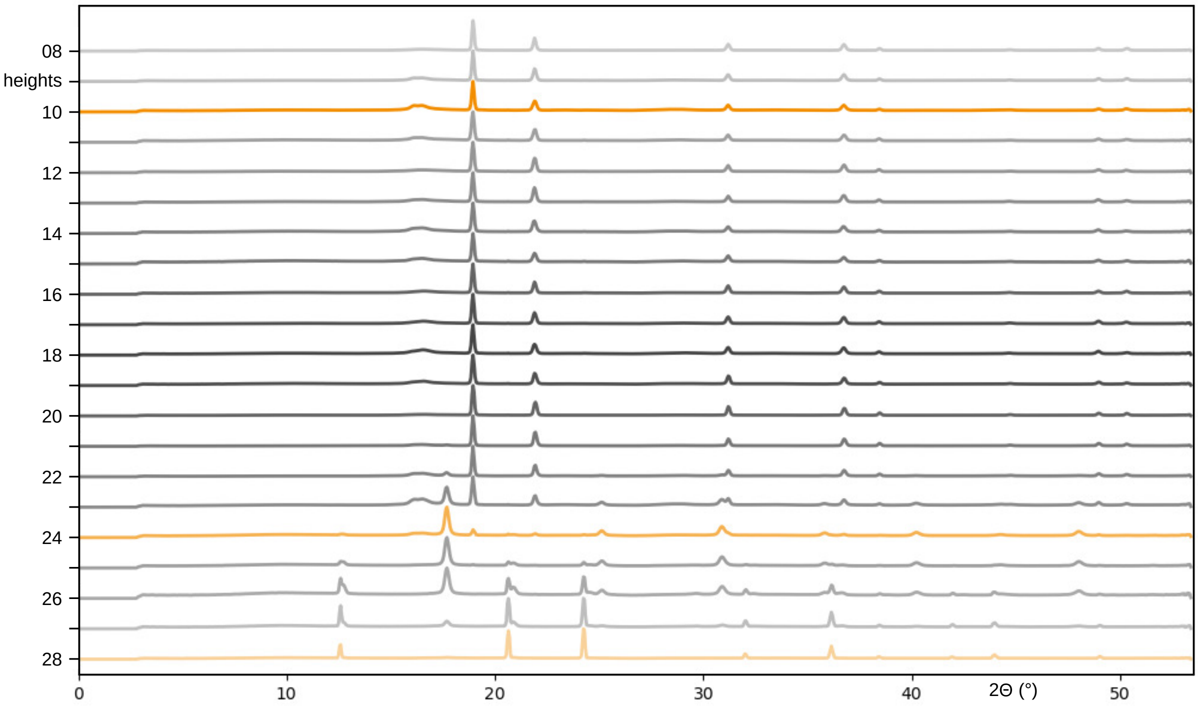

Figure 8.29: Overview of azimuthal integration per height with normalized intensity values.

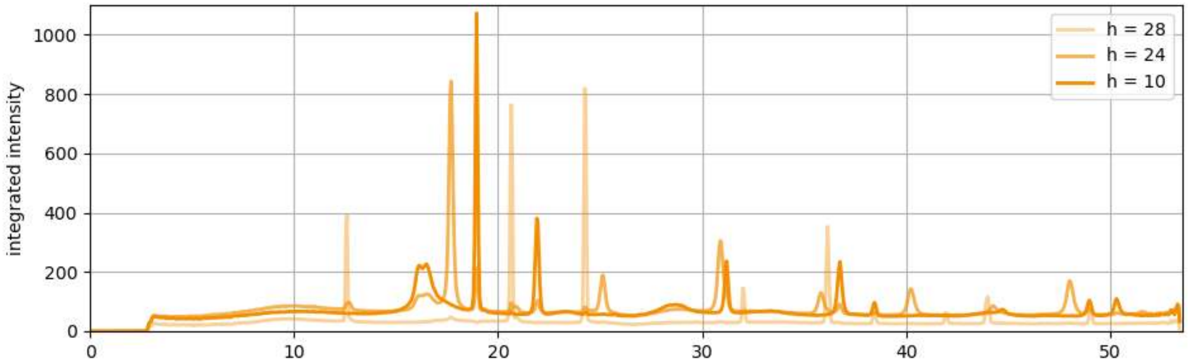

Figure 8.30: Azimuthal integration of selected heights in direct comparison. The selected heights are plotted in the same colors in Fig. 8.29.

are the diffraction rings visibly being built of single Bragg peaks. There are weaker rings from more polycrystalline structures. In the diffraction pattern of height 24, it is striking that the rings seem to be equidistant and are more consistent than peaks or rings at other heights. The higher homogeneity of the rings is an indicator for smaller crystallites, comparable to powder. In comparison, the lowest height, height 28, shows selected reflections only. From these three heights we see that – taking the selected heights from top to bottom – there are grainy and polycrystalline structures as well as a monocrystalline bulk material, respectively.

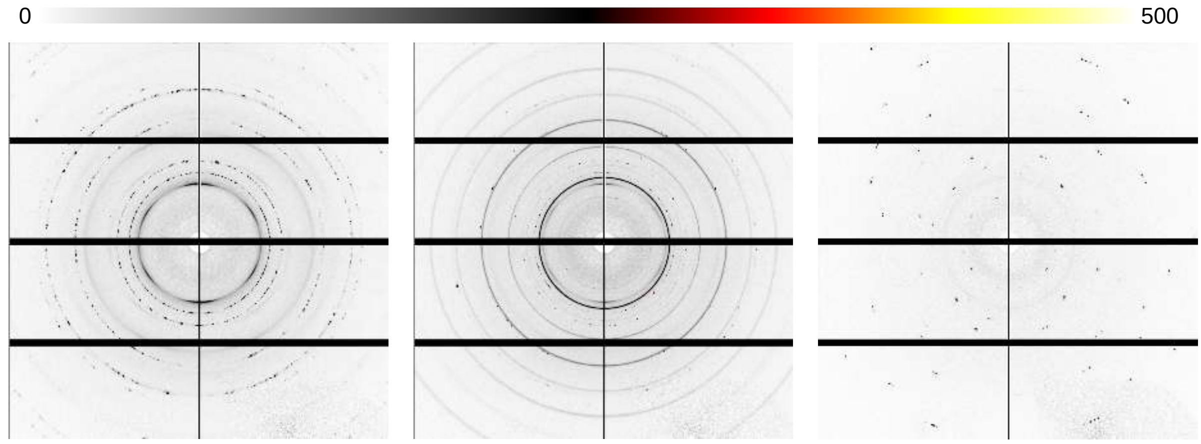

(a) Height 10 **(b)** Height 24 **(c)** Height 28

Figure 8.31: Summed up diffraction patterns to the selected heights in Fig. 8.30.

8.4.6 Strain and Texture

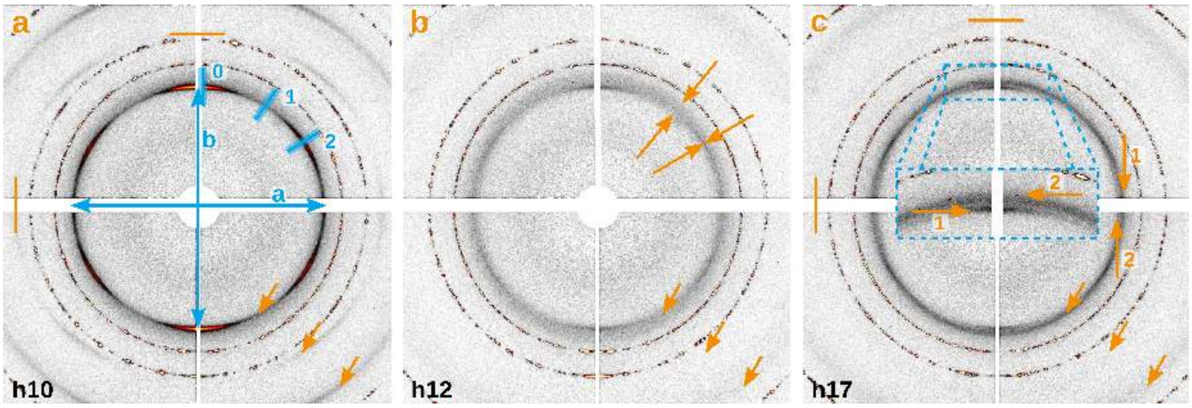

Figure 8.32: Summed up diffraction patterns, zoomed to center, showing XRD signal of nitrated tantalum at three different heights. The three orange arrows in the fourth quadrant point at the same three diffraction ring positions in all shown diffraction patterns. From a) to c) the signal shows different behaviors, originating from the Ta structures under different conditions.

When looking more closely at the diffraction patterns, various things become apparent. The different diffraction signals do not only separate in spotty and smooth rings, they also reveal strain and texture of some structures by forming elliptical rather than circular rings and accumulation of peaks in preferential directions, respectively.

In this part I concentrate on the signals originating from the Ta structures. The PXRD analysis did not reveal the strained element. Figure 8.32 shows three selected heights, demonstrating the differences within the Ta structures. In all three images, the positions of the Ta-related rings are marked by three (unnumbered) orange arrows in the fourth quadrant. One of the most obvious appearances is the elliptical shape of these rings, see Fig. 8.32a, which is even more emphasized by the neighboring two intense, circular and spotty rings originating from Cu.

With the structures themselves, the signals change across the heights. The three chosen heights in Fig. 8.32 show that the signal can be (a) sharp and intense, (b) diffuse, broadened and weak, or (c) divides into two rings with distinct strain, highlighted in Fig. 8.32c by the inset and the arrows with orange marks 1 and 2. The second ring is relatively weak in all images and is not visible in (b) at all. Additionally, in all heights, the signal clearly accumulates in preferential directions, at the positions of two, four, six, eight, ten and twelve o'clock in fewer and stronger manifestation, which is most prominent in (a). This accumulation in preferential directions is an indication for texture.

A direct comparison of the three heights is visualized in Fig. 8.33 for three different positions, see three blue marks, labeled with 0, 1 and 2 in Fig. 8.32. The width of the first order reflection ring varies from approximately eight to thirty pixels, see orange line in marks 0 and 2 in Fig. 8.33 versus all lines at position 1, respectively. Marks 0 and 2 are set on preferential directions and mark 1 is set at a position between these two. At the preferential directions, the height 10 predominates the other two, but there is no difference to height 17 at mark 1. Furthermore, a splitting of the ring at height 17 is visible in Fig. 8.32c as well as by the gray line in Fig. 8.33 mark 0.

Despite the visualization of strain and texture, we wanted to determine the correct Ta-N-compound. As written in Chapter 5, page 36, the liners are partially nitrated. By comparing the lattice constants and lattice types for possible Ta-N compounds [138] to the detected signals, Ta(N) was estimated as most promising phase. It arranges in base-centered-cubic crystal structures, with approximately 2.5 % N. Besides the lattice constants, the intensity of the first peak compared to the others was a criterion for the comparison of the actual compound, see Nie et al. [138]. Other potential compounds were TaN, which arranges in an fcc lattice, and Ta_2N, which has a hexagonal structure. The lattice constants for the three different types Ta-N are around $a = 3.35$ Å for Ta(N), $a = 4.4$ Å for TaN and $a = 2.3$ Å for Ta_2N. Among the mentioned compounds, only Ta(N) resulted in a consistent value for the lattice constant for all measurable rings. The differences in allowed reflections for the different lattices were taken into account.

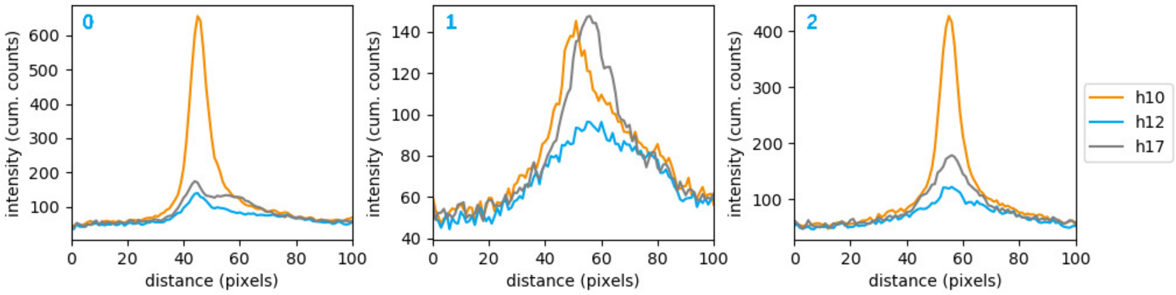

Figure 8.33: Line profiles at blue marks 0, 1 and 2 in Fig. 8.32a, measured at all three heights. The line profiles were averaged over a width of 20 pixel.

As the rings are deformed to ellipses, the strain is determined by the difference from the expected 2θ distance. In Figure 8.32a, the ellipse is extended in horizontal direction, while in Figure 8.32b the extension in the vertical direction prevails. To emphasize the difference of the strain at different heights, the horizontal orange line at the top and the vertical orange line on the left of Fig. 8.32a and 8.32c mark the second reflection ring.

To determine the strain, the axes of the elliptical diffraction rings were measured manually. An automated ellipse fitting did not show any useful result due to the weak structure of the data. The reflections do not build a continuous ring and the transition between signal and background blend into each other. The attempts to emphasize the signal over the background by applying dilation and erosion in various ways failed too. The results of the manual measurements, done at different heights individually as well as at the summed up diffraction pattern are presented in the following table:

orders	dir.	heights	a$_a$ (Å)	a$_b$ (Å)	d$_a$ (Å)	d$_b$ (Å)	ε_a	ε_b
1 (110)	$\leftrightarrow$	all	3.358	3.48	2.373	2.463	–0.004	–0.042
2 (200)	$\leftrightarrow$	all	3.330	3.500	1.666	1.750	0.003	–0.047
3 (220)	$\leftrightarrow$	all	3.341	3.474	1.181	1.228	0.001	–0.039
1 (110)	$\updownarrow$	3 (16–18)	3.443	3.346	2.434	2.366	–0.03	0.001

Table 8.3: Measured values a. . . lattice constant, d. . . lattice distance and ε . . . strain for horizontal ($\sim_a$) and vertical ($\sim_b$) axes of ellipses with greater extend in directions $\leftrightarrow$ or $\updownarrow$. The reflection order or (hkl)-family is given in the first column. The reference values are the lattice constant a$_0$ $=$3.343 Å as well as the corresponding distances between adjacent (hkl) lattice planes d$_{0,(110)}$ $=$2.364, d$_{0,(200)}$ $=$1.672 and d$_{0,(220)}$ $=$1.182.

The table shows strong average negative strain of -0.043 in horizontal direction at all heights that contain Ta. The fluctuations of the strain values as result of fluctuations of the measured ellipse axes at (110) are $\varepsilon \pm$ 0.003. The negative sign signifies a deviation to greater diffraction values 2θ and thus indicates a compression of the crystal lattice. According to the comparison of the results in Tab. 8.3 and the corresponding heights in Fig. 8.28, the liner is compressed over its larger dimension. At three specific heights, h16 to h18, compare heights in Fig. 8.28, the diffraction patterns show some compression of the liner material in vertical direction, too. There is no explanation, why the vertical compression is only visible at these three heights, since the liner alternates between horizontal extension at the bottom of all metal structures and vertically aligned at the side walls. Also is a greater visibility of any compression expected at the bottom of each metal layer as the liner material is larger extended there.

The strain could be caused by the embedding of the thin liner between the Cu structures and the insulator material. Both the Cu structures and the insulator are greater extended than the liner and in the case of the Cu metal structures, are available in crystallized state. Moreover, both surrounding materials[11] of the liner have larger lattice constants: a_{Cu} $=$3.615 Å, a_{Si} $=$5.431 Å and $a_{\mathrm{Ta(N)}}$ $=$3.343 Å.

The explanation to the determined strain values is sketched in Fig. 8.34. An explanation based on the results could be a general compression of the liner material in all directions, see red arrows in (b), and some relaxation in direction of the neighboring materials, or adaptation to their lattice constants, see black arrows. In this case, the compression is maintained over the long distance, but relaxed to normal distances in the shorter directions. Other materials in the sample, such as Cu or W, did not show deviations of the lattice constants and with that are not strained. Moreover are the other structures larger and allow for relaxation of the material. The liner material, some Ti compound, around the W plugs could not be resolved by any contrast. For that reason, no strain could be determined either.

---

[11] The insulator material could not be fully identified with any of the applied methods. It is assumed so be either a SiO_2, which is available in different phases or even amorphous or some Si_3N_4. All crystalline phases of the insulator have lattice constants close to that of Si.

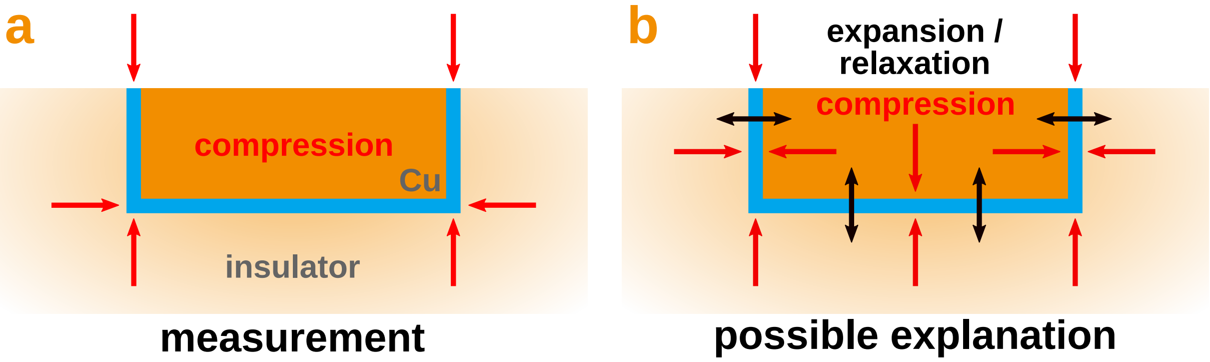

Figure 8.34: Sketch to explain determined strain on the liner (blue). The arrows show the change of the crystal lattice of the liner structure. The two different images show the behavior of the crystal lattice of the liner between Cu and insulator from (a) the results of the measurement and (b) in a possible explanation of the results.

8.4.7 Powder 3D-XRD

This part of the analysis is conducted according to the work of Bleuet et al. [69], which is briefly depicted in Sec. 3.4. It is based on the evaluation of diffractograms, the azimuthal integration of the diffraction patterns from a raster scan. From the lateral information in combination with the sample rotation, for each phase or even peak, a tomographic reconstruction can be achieved. The challenge for this analysis is a proper peak fitting. The diffraction data accumulates in Voigt profiles, which is the convolution of a Gaussian with a Lorentzian profile. It can also be evaluated as pseudo Voigt, which is a linear combination instead of a convolution of Gaussian and Lorentzian. During the analysis, I tried all three kinds of profiles for the fitting, pseudo Voigt, Gaussian and Lorentzian. Neither of these mapped the shape of the peaks very well, but the fitting process was efficient enough to determine the peak positions. From the fitting at the diffractograms per height and at the total diffractogram, 41 peaks were selected, as visible in Fig. 8.35.

The peaks can be grouped by their affiliation to a crystal phase and with that to the element or elemental composition they belong to. The analysis continued with the channels of these central peak positions, marked in orange in Fig. 8.35. Subsequently, the collection of the data of each

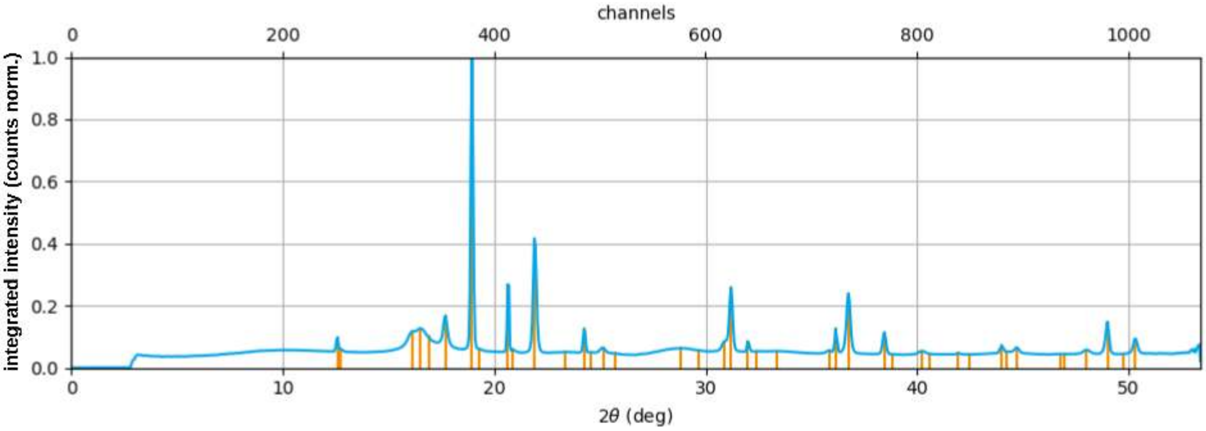

Figure 8.35: Total diffractogram with selected peaks. Only the peak positions are used for further analysis.

of the selected peak positions at each height and scan point resulted in a set of 41 sinograms. Finally, these sinograms were tomographically reconstructed.

Representative, some heights are selected to show the results, see Fig. 8.36 and 8.38. The heights in the sample are referenced in Fig. 8.28. Each of the presented examples is the result of the center position of the peaks, not the integrated information about the full-width-at-half-maximum. The W and Ta structures show typical powder X-ray diffraction behavior and the shape of the structures is clearly reconstructed, no matter which of these peaks is chosen, see Fig. 8.36 and 8.38. In comparison to that, parts made of Si, $CoSi_2$ and Cu are monocrystallin – in case of the substrate – or arrange in small crystal grains. Due to this, no structures can be reconstructed, see top row in Fig. 8.36 as well as the two lower rows in Fig. 8.38. Instead, only special crystal orientations contribute to the peak position. The direct comparison of Cu with Ta for the same layers in Fig. 8.36 shows the difference of grainy to polycrystalline structures.

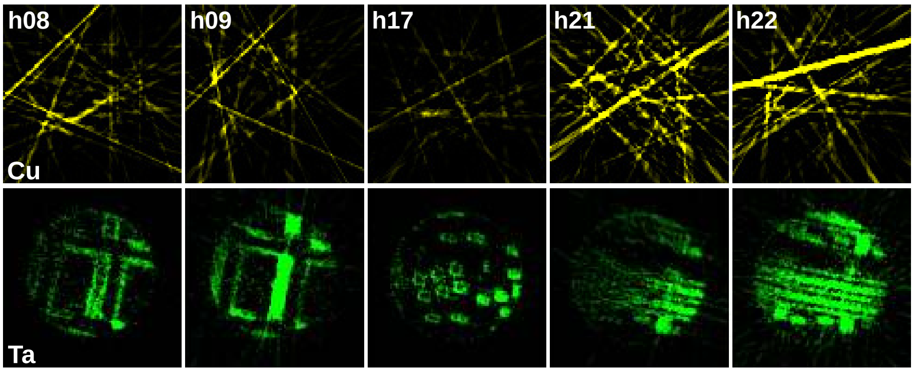

Figure 8.36: Selected heights of PXRD tomographs for grainy Cu and powdery Ta, showing only one peak per element.

The conduction paths are build of Cu grains. The contributing Cu peaks are not sufficient to reconstruct the structures in the tomographs. Single reflections coming from isolated Bragg peaks cannot sum up to a full sinogram because at each different angle, they fulfill the Bragg condition for another (hkl) combination and therewith scatter to another 2θ or are not in Bragg condition at all. Only the permutations of positive and negative values of h, k and l[12] will contribute to the same peak region, depending on the underlying crystal structure. For that reason, the Cu parts were analyzed differently, see the following section, Sec. 8.4.9.

Analyzed under the powder XRD conditions, the combination of all Cu peaks leads to roughly visible Cu structures, see Fig. 8.37. As the intensity among the Cu peaks varies strongly, each peak image needed to be normalized before all were combined to see the originating structures.

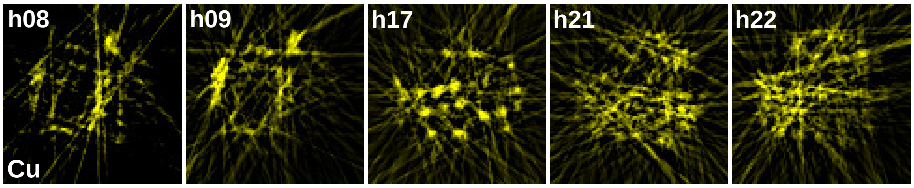

Figure 8.37: Combination of all detected Cu peaks. Underlying structures become visible.

The lower part of the scanned sample shows results of the monocrystalline Si substrate, the above laying thin $CoSi_2$ structures, adjusting to the crystal order of the substrate they are build on, and the polycrystalline W plugs, see Fig. 8.38. The $CoSi_2$ data is very weak and for that reason, the reconstruction is rather noisy. Additionally, it seems to build small crystals and,

---

[12] For example: $[2\,2\,2]$, $[\bar{2}\,2\,2]$, $[2\,\bar{2}\,2]$, $[2\,2\,\bar{2}]$, $[\bar{2}\,\bar{2}\,2]$, $[\bar{2}\,2\,\bar{2}]$, $[2\,\bar{2}\,\bar{2}]$ and $[\bar{2}\,\bar{2}\,\bar{2}]$, which build one (hkl)-family.

compare the explanation for the Cu structures, the shape of the $CoSi_2$ structures could not be resolved. Furthermore, these sample regions were not covered by all the 136 angles, which leads to an even worse reconstruction. Besides the incomplete angular coverage of the substrate region, the Si only contributes with specific angles. Since it is not divided into smaller grains, the angular response would even be less than for grainy regions despite a full angular coverage.

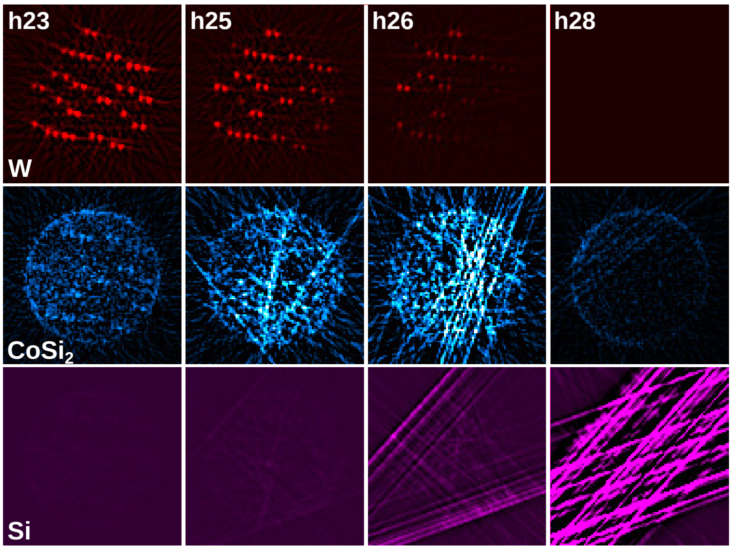

Figure 8.38: Selected heights of PXRD tomographs for W, $CoSi_2$ and Si. The powdery W leads to homogeneous sinograms and the tomographic reconstruction shows the actual structures. The $CoSi_2$ structures are made of grains and do not contribute to continuous sinograms, as it is the case for Cu. The Si substrate is monocrystalline and only fulfills the Bragg condition at certain rotation angles ω.

The formation of grains or powders is also influenced by the fabrication processes. The deposition of thin liners or small plugs is different than the process to form conduction paths. Additional healing processes could also support the formation of crystal grains.

8.4.8 3D PXRD tomographs

The 3D visualization in Fig. 8.39 shows the results for the powdery phases in the sample, here shortened by Ta and W. The liner builds a coat around the conduction path and as such is a continuous layer. Below, the W plugs are visible just as in Fig. 8.18.

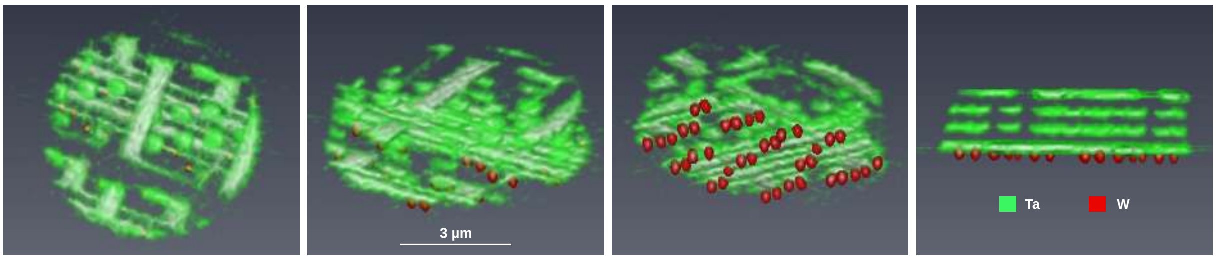

Figure 8.39: 3D models of powder XRD results for the powdery phases of Ta and W. In comparison to the XRF results, here the Ta structures are more continuous. The views are chosen to be similar to the presentations of the XRF and XRA results.

8.4.9 Single Crystal 3D-XRD or Grain Search

The evaluation draws on the work 'Three-Dimensional X-Ray Diffraction Microscopy' by Poulsen and the 'box scan technique' introduced by Lyckegaard, respectively, see Sec. 3.5. This analysis is focused on the localization of single grains and the determination of their orientation. For that reason, it is only useful for the Cu structures in this work, as the reflections for the other materials, forming smaller, rather powdery grains, are not separable. Within the 3D-XRD community, these analyses are even extended to pencil beam experiments and can be found under the name scanning 3DXRD.

Necessary preparation steps as well as the actual analysis of the peaks was conducted in python. For the particular analysis we used the programs provided by FABLE, especially ImageD11 and grainspotter [139]. All modules are described in detail [140, 141]. An overview over the steps for the grain search is given in Fig. 8.40.

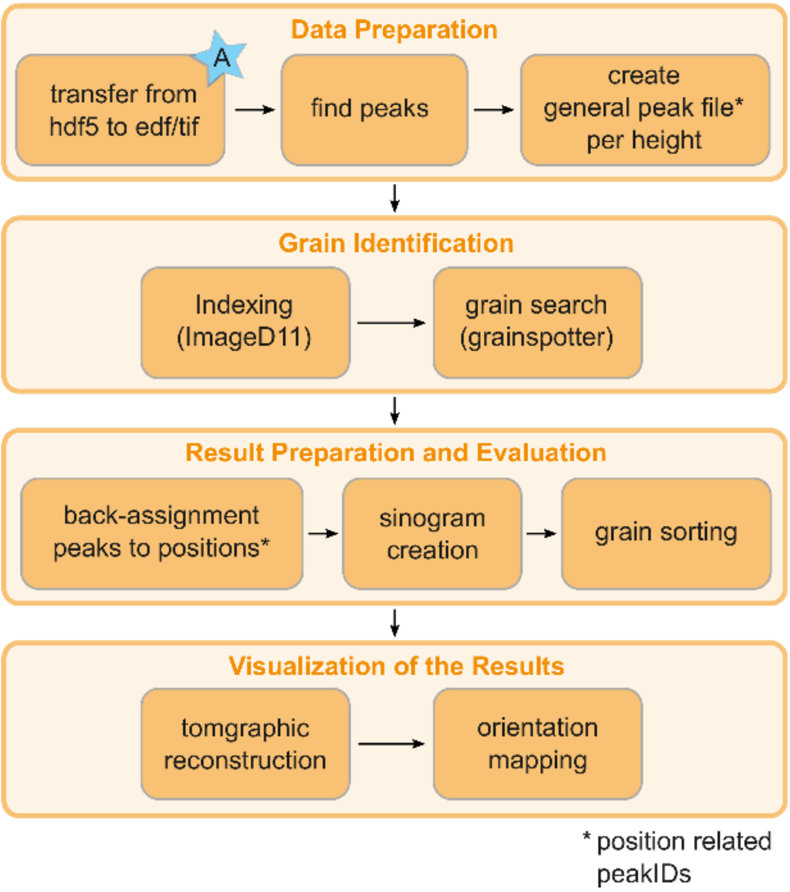

Figure 8.40: The grain search analysis follows the steps in this scheme.

The grain analysis started with the data preparation. The first two steps use the diffraction patterns directly. The recorded ∼.hdf5 files, containing several diffraction patterns of adjacent scan points, were extracted to single diffraction patterns, ∼.tif or ∼.edf. This transfer included the correction of the alternating scan direction of the data, the background correction as well as the alignment. The following steps were applied to each height separately.

After that, the module 'findpeaks.py' was used to identify peaks and write them into a peak file per scan point.

For each scan point, separated by height and position, the diffraction patterns of all 136 projection angles were used to search for peaks that fulfill the chosen peak criteria: accumulated pixels were identified as peaks when they consist of at least 4 pixels with counts ≥ 4. When a peak expands over several projection angles, the angle at the center of mass is written to the peak file.

In the subsequent step, all these single peak files were combined to a general one for each height. For a later assignment to the original peak position, we included a specific naming of the peak-IDs, which leads back to the original positions. With this step, the data preparation is concluded.

The identification of the grains starts with the peak indexing using ImageD11, which is available as GUI or in script version. The requirements for the indexing are the peak file, the geometry parameters from the calibration as well as the crystal information about the current crystal structure. Within ImageD11 it was possible to adjust the geometry parameters automatically. Based on these requirements, the g-vectors, see Eq. 2.22, for the peaks are calculated. As output, we gained the adjusted geometry parameters and the indexed peaks as a g-vectors file and a finalpeaks.log file.

With these files, fed into grainspotter via an initialization file, short 'ini'-file and with additional search parameters, the assignment of peaks to a certain grain starts. The search parameters were tested in in advance. As long as a found grain does not meet the chosen criteria, it will not result in the list of found grains. In the following, the grain search parameters to find Cu grains with space group 225 are described. As the peak files contain peaks of the full data set, specific 2θ regions with ± 1° around the central peak values for the different phases were implemented in the 'ini'-file. The search region also comprises the ranges for η $=$0° to 360° and ω $=$0° to 180° as well as the angular step size $\Delta\omega$ $=$1.3333°. Furthermore, the number of (hkl)-families was set to 5, which corresponds to 5 rings. The angle step size in Euler space was set to 4 and ...n σ: 2. Besides the above mentioned criteria, the following values were chosen after an intense testing procedure.

cuts		**uncertainties**	
measurements	$\geq$ 25	$\sigma 2\theta$	0.5°
completeness	$\geq$ 0.6	$\sigma\eta$	0.2°
uniqueness	$\geq$ 0.5	$\sigma\omega$	0.7°

The grain search by grainspotter results in a file containing the different found grains including their orientation and all the associated peaks.

Taken from the results of a single height, of 86 identified grains, the measured versus expected peaks are in a range from approximately 60 % to 87 %. The minimal number of peaks is influenced twofold, first by the measurement principle and the discretely scanned angles, second by the parameter in the 'ini-file' (completeness of 60 %). With a lower completeness value, there could be more grains detected. But with this adjustment, the algorithm is open for an increasing number of false grains, too. Furthermore, with fewer peaks, the reconstruction as well as the validation check is more complicated. On average, around 68 % of the expected peaks, determined by the grainspotter due to the chosen parameters, are measured.

Subsequently, all peaks of a grain are back-assigned to their origin position, which is based on the extended peak-IDs. With all the information about the peaks, starting from position and all angular information, ω, η and 2θ, the extent of the grain at each projection angle is determined by the search for peaks with the same parameters in neighboring positions. The intensity values for these peaks are normalized at each projection angle and finally put together in a picture. The result of this is a sinogram per grain. At this step, the quality of the grain search results can be evaluated. The choice of the parameters for the grain search are a trade-off between finding as many grains as possible and get reasonable results. Whether the results are reasonable or not, is directly revealed by the sinograms which are formed by the data that form a grain. To verify the identified grains, the sinograms were sorted to three categories: good, intermediate and bad, as visualized in Fig. 8.41. The good ones build a clearly visible sinogram with few exceptions or outliers. The grains which end in the intermediate pool show roughly sinusoidal behavior, but they data points spread too far from the curve or there are more than one sinograms contained

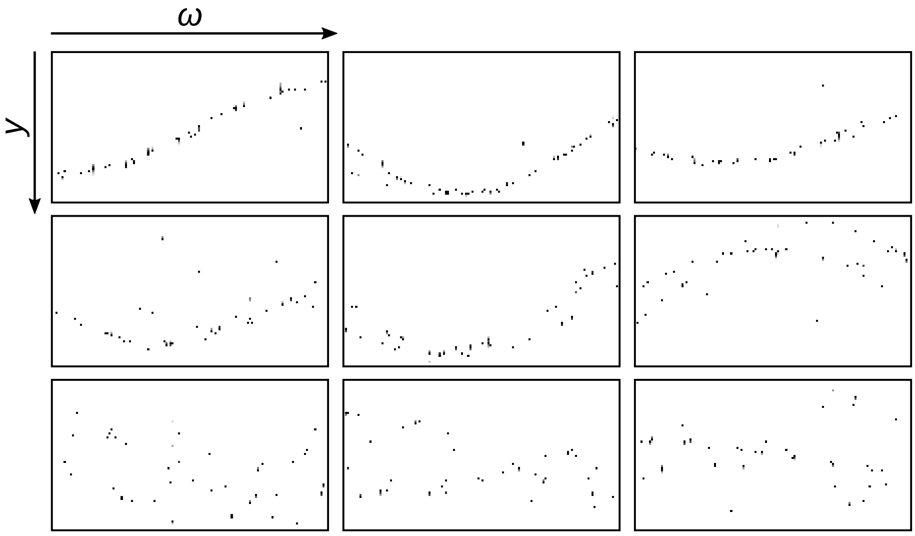

Figure 8.41: Exemplary sinograms, each representing one found grain. Due to their unambiguity they are classified as good, intermediate and bad, as presented in first to third row, respectively. The images are inverted for visualization reasons. For a good sinogram, only one sinusoidal path should be visible.

in one. Bad sinograms show a random distribution of spots. The decision about reasonable grains can also partially be made according to the difference values between expected and measured values in the result file.

With these criteria for the sinograms, the data was sorted out manually and further reconstruction steps were done using only those grains classified as good. The rate of reasonable grains varies with slight adjustments of the grain search parameters as well as slightly with the height. After testing out parameters, we chose the set with the highest amount of good grains relative to an acceptable rate of bad grains. We were not able to define parameters which result in good grains only. The examples in Fig. 8.41 also show, that the size of the grains barely exceed a two pixel width in a single projection and the data is relatively sparse in projection angles as well.

After the sorting, each good sinogram was reconstructed individually. Some exemplary results are presented in Fig. 8.42.

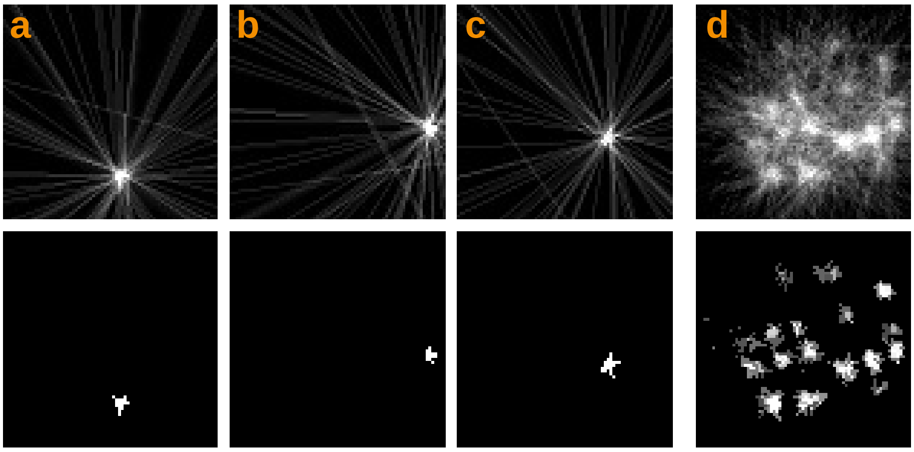

Figure 8.42: Reconstructed grains. Original and reduced view of three single grains (a) to (c), and the combination of all detected and good grains (d). In the reduced view, per grain only values from 50 % to maximum value are used.

The subsequent step was the adjustment of the tomographs to isolate the grains and get their position and approximate shape. In a trial-and-error principle, this was achieved by setting a threshold of 50 % of the maximum value per grain to reduce reconstruction artifacts.

Furthermore, with the information from the grain result file, the reconstructed grains can be mapped with their orientation[13], see Fig. 8.43. The procedure to achieve the orientation mapping

---

[13] The orientation mapping was achieved with the help of some python code from Silvio Achilles. An alternative

uses the found grain direction in Euler angles [143] and projects these stereographically or by an equal area principle [144]. For the orientation distribution, only one stereographic triangle as inverse pole figure is required, as other triangles in the projection are symetrically equivalent [145].

The depiction is given with colors of the inverse pole figure with the sample in normal direction (ND). The presented figure shows three adjacent heights, where the same color means same orientation and shows that some grains reach over all three heights. The upper pictures show the grains with different orientations while the lower figures present the distribution of the different orientations. In some Cu structures, several grains overlap. The actual distribution cannot be clearly resolved and some grains share a voxel, which could be horizontal as well as vertical. The orientations among the grains in Fig. 8.43b are random and relatively homogeneous, while in comparison the orientations between neighboring structures in (a) and (c) are more alike. Furthermore, some structures are occupied by a single grain and others are shared by several smaller grains. Overall, there is no preferred orientation and a detailed texture analysis for these Cu grains is not necessary.

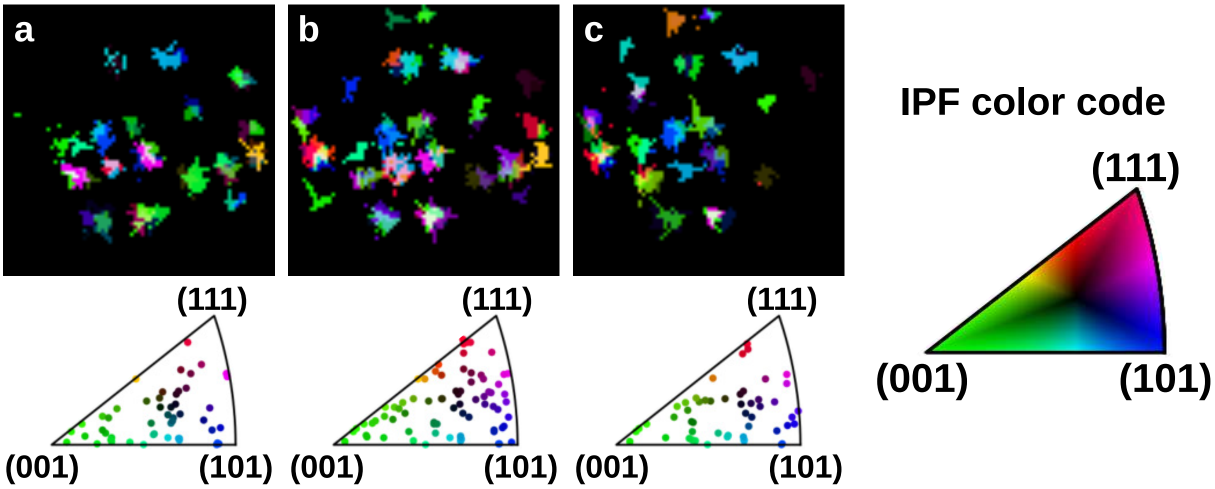

Figure 8.43: Orientation mapping of exemplary heights from a to c: h16 to h18 with sample in normal direction (1,0,0) with orientation distribution in an inverse pole figure. Each found grain is assigned with its crystal orientation, represented by a specific color of the color coding. The height in (a) is the same as in Fig. 8.42d. The color coding of the inverse pole figure is given on the right.

8.5 Combination of all Three Contrasts

By comparing the results of all three applied methods, each single method has some advantages over the others. The XRA analysis leads to the distribution of the absorption coefficients. The XRF analysis shows the elemental distribution. The XRD analysis provides different crystal information such as the kind – powdery, arrangement in grains or monocrystalline –, the phases, size and orientation of grains as well as strain and texture.

As there is no elemental distinction in the XRA analysis, the results appear very smooth and even the transition between the layers is visible. In comparison to the analysis of the XRF data, in the XRA results, the structures made of $CoSi_2$ are not visible at all, since its absorption is

---

solution is provided by a Matlab toolbox called MTEX [142].

similar to that of the surrounding Si and SiO_2.

When comparing XRF versus XRD, in general, it appears that the structures are better resolved by XRF. Furthermore is XRF sensitive to all elements with energies in the detection range, while XRD is only sensitive to any kind of crystalline material. The identification of different grains within a structure of a single material and the determination of its orientation is a unique advantage of the XRD analysis. On top of that, it provides information about texture and strain of the material, which can not be accessed otherwise.

In Figure 8.44 the comparison is shown for four selected heights. The XRF results split into the analyzed elements. Compared to the XRA results, the structures from (a) to (c) appear narrower in the XRF Cu column, which is explained by the additional Ta liner around the Cu. The comparison of the reconstructed Ta structures from XRF and XRD data, the latter achieves a better representation of the liner.

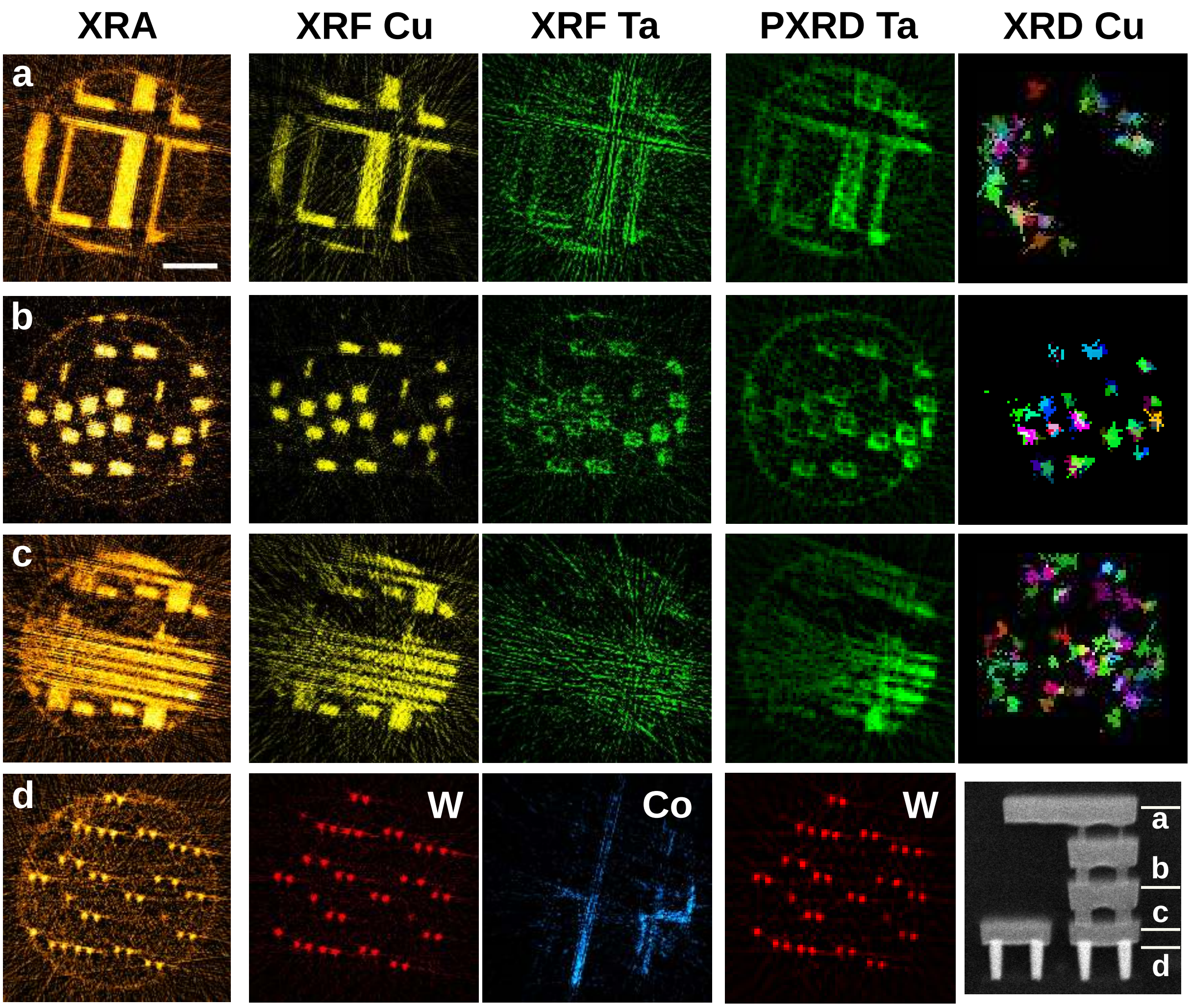

Figure 8.44: Comparision of the results from the XRA, XRF and XRD analyses. For four different heights, with a reference image at the bottom right, the structures are well presented by all techniques with certain differences. The elements change for the last row and the last column shows the results from grains search. The scale bar is 2 µm.

A direct comparison between the results from XRF and the grains search in Fig. 8.45 reveals that in general, the positions of the structures match well, but the reconstructed grains exceed the structures reconstructed by the XRF signal. The explanation for larger structures by grain reconstruction lays in the way the data is detected. For the XRD data, the side lobes of the beam are not negligible and even when the central beam samples a region next to a relevant structure, some lower parts of the whole beam shape may diffract from neighboring grains. This is different for XRF, where mainly the central beam contributes to the detected data. Furthermore, the grain search did not succeed for all Cu structures, as some regions stay empty or are not fully filled with some corresponding grain.

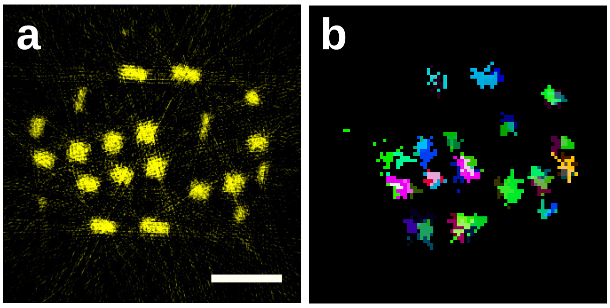

Figure 8.45: Direct comparison of Cu structures reconstructed from (a) XRF and (b) XRD analyses at one height. The scale bar is 2 µm. The grain search algorithm, with results in (b) was not successful to find grains in all Cu structures in (a). The reconstructed grains (b) exceed the structures reconstructed from XRF data due to tomographic reconstruction artifacts and a higher influence of the beams side lobes on the XRD signal.

With XRA analysis, a coarse view is generated, showing the full width of the structures. A fuller picture of the structures, presenting the composition can be achieved using XRF, up to a visualization of the $CoSi_2$ structures and XRD adds additional information to these structures, for example that these are polycrystalline like $CoSi_2$ or build larger grains like Cu. This comparison shows that the combination of these methods is complementary. Further contrasts would contribute with additional information.

8.6 Conclusion on the Multimodal Experiment

The applied multimodal approach is novel in the sense that it first and foremost combines different XRD techniques itself and other contrasts – XRA and XRF – measured all simultaneously and in addition to that it was implemented in smaller step sizes as usual for XRD experiments. Furthermore, the kind of sample with mixed elemental composition in well defined structures is uncommon for these methods, but opens a broader field of application for XRD.

With the results of the XRA analysis, the conduction paths through the whole scanned region could be depicted. The reconstructed absorption values matched the literature values for the expected elements in the structures, allowing to distinguish the elements and structures already by their absorption coefficient alone.

The analysis of the XRF signal lead to four different structure volumes, concentrating only on the four main elements contained in the sample. These four volumes show the relative position of the different elements and highlight their individual tasks in an overlay of these. The potential of the XRD data exceed these of the other two contrasts. We were able to comment on strain and texture as well as on specific compositions and crystal structures. Furthermore, some grains could be reconstructed and be matched to the structures reconstructed by the other two contrasts. The scanning scheme, using discrete angular steps rather than continuous, may lead to some disadvantages concerning the quantitative XRD analysis, which are for example the exact determination of the intensity ratios for a correct Rietveld refinement and the grain search. But through the combination with other contrasts, it offers more diversity of sample characterization, too.

Despite the limited sampling due to time restrictions of the experiment, we achieved successful tomographs for all contrasts and even single grains were identified. Nevertheless, compared to the measured structures and the possibilities of the beamline, there is some room for improvement. On one hand, a finer sampling, in lateral scan positions as well as angular, would improve the results for the smaller structures, the diffusion barriers and the logical structures at the bottom. On the other hand, it will also apply to the quantitative XRD analysis. Another point of consideration is the tilt of the sample, which is visible in the results, but it is unclear to which amount the sample was actually tilted and what part of tilt belongs to an unwanted behavior of the scanner stages. This had a huge effect on the alignment of the data.

During the whole beamtime, radiation damage was neither explicitly examined nor was it noticed otherwise. We could not see any changes of the structures even after very long exposure. A quantitative radiation damage investigation would need two comparative measurements, one at the beginning and one at the end of the experiment with preferably identical or at least mirrored sample orientation and matching scan parameters. A proper method would be the comparison of the phase shift between two ptychographic scans, for example. But the sample was not scanned ptychographically after the multimodal experiment. A required estimation about the applied radiation dose can be determined from the diffraction patterns of the scans in between.

CHAPTER 9

Conclusion and Outlook

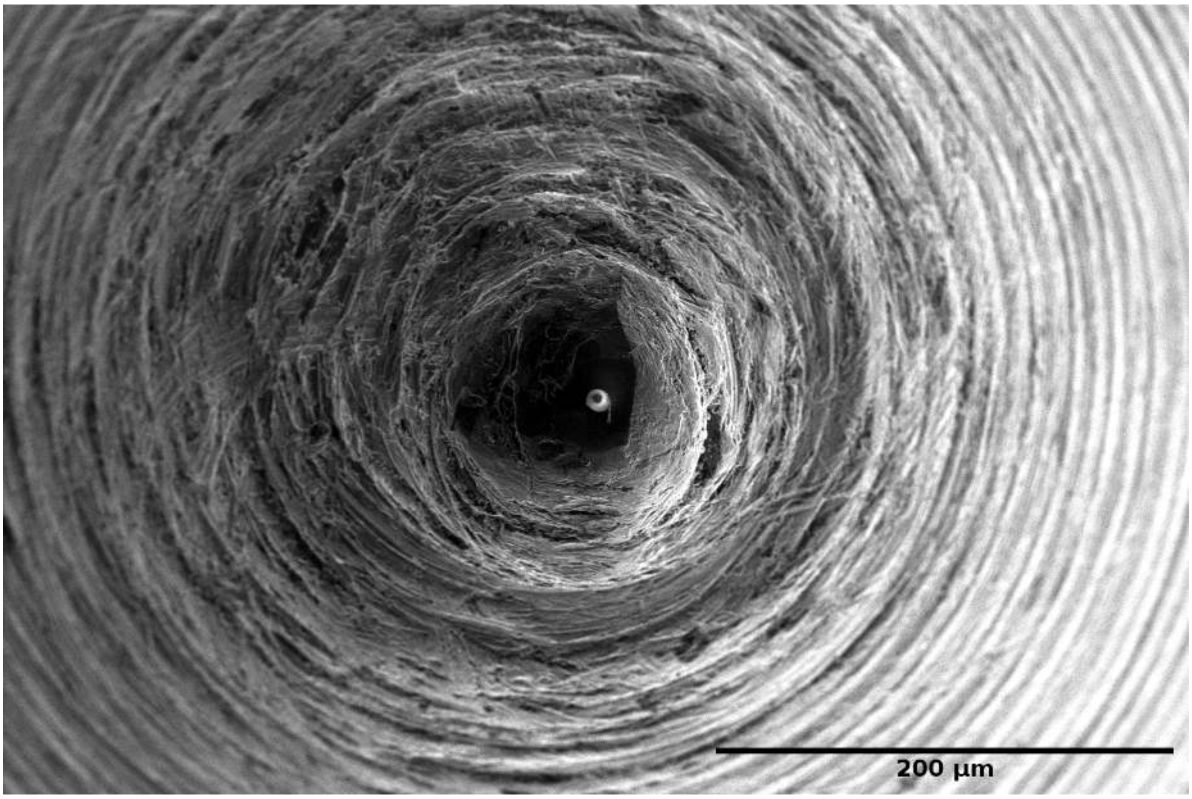

This chapter starts with a brief résumé on the results from the high-resolution imaging and the multimodal experiment.
This project proved that there is much potential in combining contrasts. But in turn there are many things which can be improved or by what the experiment can be extended. The needs of the microchip manufacturer are discussed in Sec. 9.2. The Sections 9.3 and 9.4 point to what needs to be considered in future experiments to further strengthen the results. Additionally, prospect of improvements and extensions is given in the last three Sections, 9.5 to 9.7.

9.1 Conclusions

The different experiments with and on the microchip, conducted within this work, demonstrate the versatility of electron and X-ray imaging methods. With X-ray ptychography the inner structures of relatively thick samples were imaged. For the top views, the X-rays had to transmit about 150 µm matter with a structured region of approximately 10 µm to 15 µm. The images of the milled piece reveal even very thin structures and emphasize different electron densities of the diverse structures as transmission signal. In comparison to that, images obtained by electron microscopy show the surface of the different sections. Additionally, the elemental composition could be assigned to most of the structures by including energy dispersive X-ray spectroscopy (EDX). Furthermore, through a slice-and-view project, the structures could be modeled in 3D.

Both ways, using either the electron or the X-ray microscope, here with ptychography, resolved structures with a width of 14 nm and below and both have advantages over the other method, as especially visible by direct comparison.

The multimodal project delivered diverse information about the sample in a simultaneous measurement. Very often, at P06, in both the microprobe as well as in the nanoprobe, X-ray fluorescence is combined with other contrasts, such as high resolution imaging by ptychography, may it be in 2D or 3D. Usual step sizes for X-ray fluorescence measurements are in the same range or even below the applied step sizes in the multimodal experiment, indicating possible improvements ’ready for use’. X-ray absorption is usually not measured individually. From the diffraction patterns of ptychographic measurements in the far field, the central beam could be analyzed separately to gain this information.

The X-ray diffraction part of this experiment is exceptional in that sense that it is usually measured continuously, with larger beam sizes and with that larger step sizes. The results prove that despite missing information, the phases could still be analyzed and grains could be reconstructed. However, a full Rietveld refinement was not possible due to missing angular segments. In this case, information was missing and the proportions or the intensities of the different peaks to one phase did not match the database.

Also, the grain search needed some work around and the grain shapes are not perfectly reproduced. The applied threshold to the reconstructed grains was a trade off between visualizing the shape of a grain and removing reconstruction effects. With only twice the number of angular projections most of the expected peaks would be detected. A higher number of angles combined with a smaller step size would provide a remedy and would significantly improve the results as well as the analysis itself. Another important fact in this context is the sampling of the grains with a beam of similar size, which also has an impact on the reconstruction of these. Usually, in 3D X-ray diffraction (XRD) experiments, the beam is much smaller than the grains. Nevertheless, the achieved results are unprecedented through the combination of the way they are achieved, the applied step size and the resulting reconstructed grain sizes with diameters down to approximately 200 nm.

A drawback in this experiment was the alignment combined with the shifts and the required corrections for every or at least every second scan. With the current state of the beamline, the interferometers take care of these parameter and simplify the data alignment.

Altogether, this experiment was successful and enabled the continuation and extension of multimodal experiments at an X-ray microscope, as described in the following sections.

9.2 Industrial Use Case

The interest of the manufacturer Infineon Technologies GmbH is set on the high-resolution 3D imaging with spatial resolution of 20 nm and better, which could be achieved by a ptycho-tomo experiment. This could be used for critical samples in the physical failure analysis, where current methods reach their limits: Conventional methods put a marker on top of the microchip where a section will be cut out of the whole stack to be analyzed with a transmission electron microscope (TEM). The disadvantage of this method is the precision of the sample preparation and the accompanying miss of the region of interest. With an X-ray analysis, the restriction of the cutting size is less strict due to the high penetration depth. So the area around the marker can be chosen much more coarse to guarantee the defect to be in this stack. This area can be of the size of several micrometer. This, in turn, not only enables to guarantee the defect being caught, but it also depicts defects in a larger environment to see possible influences which might have caused it. The latter is of higher importance to distinguish the defect's cause, whether it is structural related or caused by the production machines.

For the analysis, the knowledge about the sample enabled the comparison with the experimental results obtained during this thesis. Altogether, the results provide a detailed view into the device in such a way which is not straightforward possible non-destructively in these large dimensions of the sample with other methods.

9.3 Further Steps for General Improvement of the Scanning

Due to the unavailability of an essential component for the originally proposed experiment, the actual experiment was changed to the multimodal experiment one week before the beamtime. With this quick alteration of the experiment, new requirements came up and a beamstop with an integrated PIN-diode including suitable positioning stages and the XRD calibration standard as well as some analysis software needed to be organized. As our group had minor experience with XRD experiments at that time, not all requirements, such as estimations for the angular sampling for the different XRD techniques in the extend necessary, were considered.

With the following considerations, the experiment itself as well as the results will be significantly enhanced. During the multimodal experiment, a former control software was used, which caused an overhead of ≈0.6 s between two scan points on top of the 0.2 s exposure time.

Since then, with the change to the new control software for all following experiments, the overhead problem does not exist any longer and the remaining overhead time is negligible. Also the scan routines and read out mechanisms themselves were improved a lot in the meantime. Especially the ptychographic scans profit from an on-the-fly measurement scheme [146] for faster acquisition. For all kinds of experiments at the nanoprobe at P06, motor positions and vibrations of the setup are tracked with an interferometer system. Not only is this advantageous for a correct 2D reconstruction, it also supports the 3D alignment.

Another influence on the scanning time is an increase of the photon flux. This may be achieved by the use of different optics direct upstream of the sample – for example diamond lenses [147]

– or a better set of prefocusing lenses. As the conducted multimodal experiment did not explicitly depend on high coherence, these means to increase the flux are unproblematic.
Additionally, there is always unwanted scattering which does not occur from the sample. This scattering is caused by hitting different parts along the beam path and especially by the propagation through air with all the particles as scatterers despite optimal adjustment of all components. The part of the air scattering could be drastically reduced with conducting the experiment in a vacuum environment. But there might always remain some scattering from other sources, e.g. from the beam shaping parts. This scattering needs to be reduced to gain results belonging to the sample only by adding further scattering shields. The implementation of further shields at the P06 nanoprobe is challenging as it might reduce the required flexibility of the optics and minimizes the space between the optics section and the sample tower.

9.4 Further Analysis of the XRD data

For X-ray tomographic experiments, the transverse as well as the angular sampling rate is adjusted to the size of the sample and the expected structure sizes. For the planning of comparable future XRD experiments with discrete angular sampling an expectation estimation of the peaks for the possible crystalline structures in advance of the experiment is highly demanded. With grain simulations beforehand, the ideal or necessary angular step size $\Delta\omega$ can be defined for a satisfactory reconstruction. This all needs to match the planned energy and the capabilities of the optics as well as these of the positioning motors and detectors and will result in smaller beam and step sizes. The peak detection rate should be at least 80 %.
From simulations earlier in this thesis, see Sec. 8.4.3, for the same experiment, the double number of angular steps, meaning half the step size, would be sufficient to improve the grain search as well as phase identification in powder analysis.
With a finer sampling, the analysis on strain and the influence on deviations on the peak positions as well as the peak sizes could be advanced. The same accounts for a detailed texture analysis [148], which was only mentioned in this thesis.
In another approach, 3D XRD can be used to differentiate between different oxidized states instead of resonant measurement with the advantages of further information such as texture and strain if present. This, of course, is only possible for crystalline samples, but it would reduce the requirement to measure at different energies [35]. Usually, XRD is applied to samples with different phases of an element or compound and barely structured. With this work, the field of application is extended to samples of mixed materials and predefined structures.

During the grain analysis, despite intense parameter testing, we faced the many false results, with peaks laying outside of the sinusoidal curve. In an extra approach, we wanted to circumvent the inclusion of such peaks that cannot belong to the current grain. This was achieved by a routine called voxelized indexing. The whole setting up, including scripting and testing for this routine was done by our masters student Silvio Achilles and the results are included in his thesis. In this routine, only peaks whose positions originate from the same pixel in a 2D view and for this reason build a sinogram, are included in the search for grains in this region. If a grain exceeds the size of one pixel, the resulting orientation should match neighboring pixels and can be combined afterwards. A sketch for this is presented in Fig. 9.1. In this approach, the variance of the positions during the scanning or from the alignment might be problematic, if no tolerance is considered between neighboring pixels. For the analysis with the voxelized indexing, the parameters for the grainspotter need to be carefully tested and evaluated. With the concentration on peaks which only appear on a sinusoidal curve, the criteria could allow to set the parameters less strict. Some results of this approach are included in the master thesis of Silvio Achilles [149].

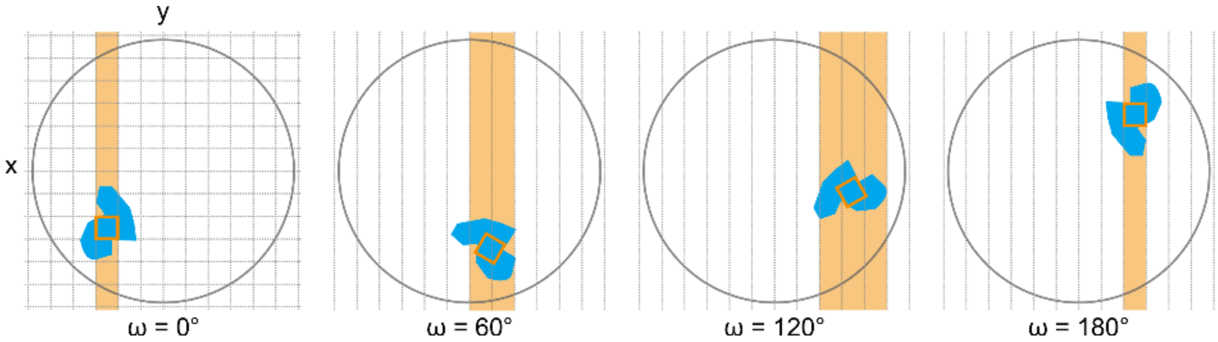

Figure 9.1: In the voxelized indexing the index files are adjusted, that for example only the orange positions can be used for the grain search. A found grain will result in a perfect sinusoidal curve and belong to the marked voxel at $\omega = 0$.

9.5 Inclusion of Ptychography as an Additional Contrast

The potential of high-resolution imaging, as presented in Chap. 6, could build the basis for further expansions of the presented multimodal project. In Chapter 6 a spatial resolution of approximately 7.2 nm was achieved. Further estimations of the diffraction patterns even showed signal beyond 5 nm, which is achievable for such samples in future reconstructions by appropriate background reduction, such as the use of a flight tube.

The inclusion of the high resolution imaging technique ptychography was out of the question for this experiment for several reasons. Despite being a very attractive supplement to this project, the missing equipment – first of all the additionally needed detectors – was the main impediment. With the inclusion of ptychography in a future multimodal experiment, a high coherence of the probing photons is essential. At the current setup, this needs to be guaranteed as a trade-off between a good level of coherence for ptychography or other contrasts depending on it and flux for XRD and in addition to that, the capability of the detectors to handle this amount of photons per area and time. To gain enough photons in a Bragg peak during the multimodal experiment, the dwell time per scan point was higher than required for a ptychographic measurement.

The trade-off will no longer be problematic at PETRA IV, as the coherence will be better. Furthermore, a combination of the presented multimodal experiment with ptychographic measurements in the far field require two additional pixel detectors. Of the in total three pixel detectors, two will be placed close to the sample at the same distance to the sample to record the WAXS signal, leaving a gap between these two. The remaining detector, is necessary to record the SAXS signal in the far field.

An additional advantage of this altered setup is the larger two-theta range for the XRD measurement, when covered with two detectors, depending on the kind of detector. It only has to be kept in mind, that the two XRD diffraction patterns must be combined with respect to the correct alignment of the detectors to each other – by using an XRD standard – to one bigger image for the analysis.

In combination with a high-resolution imaging method, the number of projections needs to be adjusted. However, with resolutions of assumed 7.5 nm and an exemplary sample width of 5 µm and a sample height of 3 µm, the required amount of projections would exceed 1000 angular steps, see Sec. 3.2.3. Using a step size of 50 nm instead, the amount of angular steps would relax to 150 angles matching the tomographic requirements. With on-the-fly scan modes and sufficient flux for diffraction signals[1] even with short exposure times of approximately 0.1 s, this could still lead to reasonable experiments within two to four days[2] for a full tomogram including some overhead for positioning and data writing, depending on the applied criterion.

9.6 Prospect to High-Resolution 3D Imaging

There are different possibilities to generate 3D images of a sample: computed X-ray tomography, limited angle tomography and laminography. In terms of highly resolved 3D images, all three methods need to be combined with a high resolution 2D imaging method such as ptychography. The decision on the 3D method depends on the sample and the objective of the analysis. For comparably small samples, which can be fully rotated and illuminated from all sides, X-ray tomography is the most robust method. It is a well developed 3D method, but with novel developments such as '3D ptycho tomo', the required amount of data points for each ptychogram could be considerably reduced, see work from Kahnt [36, 150]. With this, the beam time is used more efficient without a noticeable reduction of the 3D information.

The other two methods come into play if the sample is laterally extended and a non-destructive imaging is required, for example for further tests or later use of the sample after the imaging. This can be achieved by both limited angle tomography (LAT) as well as with laminography (Lami)[3]. A prominent example for ptyLami is the investigation of a microchip at the cSAXS group of the PSI by Holler et al. [18, 151]. The advantage of ptyLAT over ptyLami and ptyTomo is the application of reaction cells or chambers for in-situ experiments. But with the limited angular range, a considerably part of the required sinograms is missing. To artificially solve this problem, a deep learning algorithm could be applied, see Xiaogang Yang [152]. Another way to improve sparsely scanned LATs or laminograms is the usage of sparse or compressed sensing [153–156]. Instead of improving data sets, which lack of the required amount of projections, it could be used to optimize scan time beforehand. Using the advantages of the ptycho tomo algorithm, the overlap between the scan points for ptychography could also be reduced. Besides the high resolution 3D imaging, tomography, limited-angle tomography and laminography could also be used with other contrasts, for example X-ray fluorescence (XRF). Both methods for laterally extended samples have been applied in this group and are currently analyzed. Even in

---

[1] And optimized optics to reduce side lobs and to concentrate the focused photons in the central beam.

[2] (Sample width/step size $\times$ sample height/step size) $\times$ exposure time $\approx$ (5000 nm/50 nm $\times$ 3000 nm/50 nm) $\times$ 0.1 s $\times$ 150 angles $=$ 90 000 s $\approx$ 25 h.

[3] For better readability, in combination with ptychography, the prefix 'pty' is added to the abbreviations for the 3D methods.

combination with ptychography, we gained some experience in X-ray laminography, which will be further developed in the future.

9.7 In-situ/Operando Experiment

With this kind of sample, the effect of crystallization on the electronic behavior as well as strain in electronic devices can be evaluated under real conditions of an actual working and used microchip. Future multimodal experiments, comparable to the presented one, will also include electrical measurements to image for example the conduction in a running microchip or comparable electronic device.

Some people in our group successfully conducted experiments on solar cells and the imaging of conduction processes [157, 158]. The experience in this field could be used to adapt the imaging to comparable conduction measurements of microchips and other electrical components to detect possible structural or manufacturing problems.

APPENDIX A

Focus Plotting and Determination

A.1 CRL Focus

The ptychographic scans during the beamtime at Diamond I13-1 were all recorded with the same parameters and the same optics. The focus is determined for one of these scans. Fig. A.1 shows the intensity of the probing wavefield at the focal plane (a), the caustic of the beam around the focal position (b) and the profile of a horizontal line through central spot at the focal position.

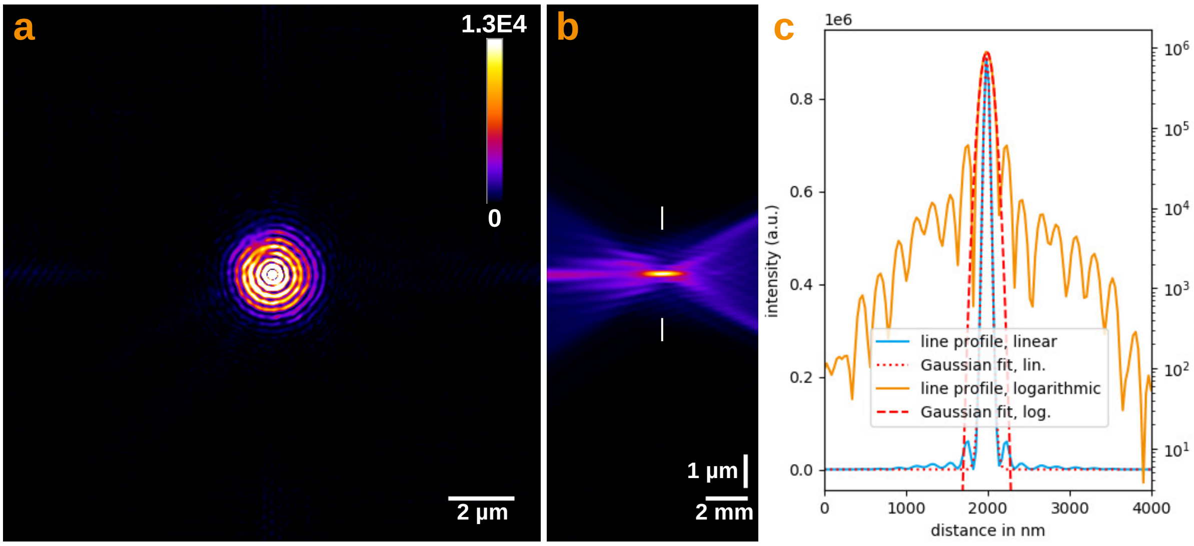

Figure A.1: CRL focus of scans during beamtime at I13-1 (DLS). From left to right: illumination at the focal plan in a linear scale, beam caustic along the optical path and the beam profile at the focal plane, plotted linear and logarithmic with the Gaussian fit.

The central part of the beam has a full width at half maximum of (137.9 ± 1.6) nm. This analysis was referred to on page 43. See the corresponding ptychographic scans there, too.

A.2 NFL Focus

The ptychographic scans during the preparation beamtime at the P06 nanoprobe (PETRA III) were all conducted using the same optics. The experimental energy for these scans was 16 keV. Figure A.2 presents the wave field at the focal position. It contains the wave field at the focal position in linear (a) and logarithmic (c) scale, the horizontal (d) and vertical (e) beam caustics, which span 4 mm along the beam path, and the line plots through the focal spot in (b).

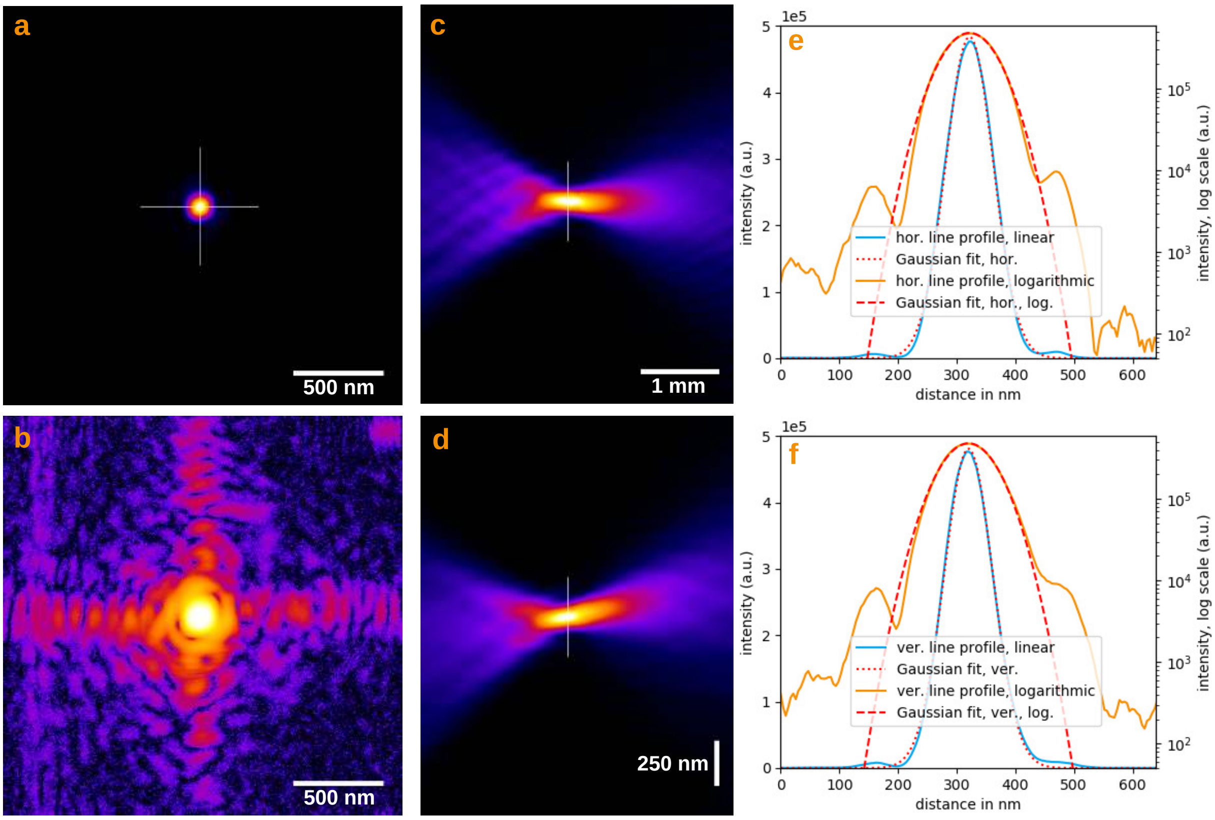

Figure A.2: NFL focus of scans during beamtime at the P06 nanoprobe (PETRA III) in advance of the multimodal experiment. The composition contains the wave field at the focal plane (a) as well as the logarithmic wave field (b), the horizontal (c) and vertical (d) beam caustic around the focal plane and the corresponding line profiles in (e) and (f), respectively. The line profiles through the focus are plotted linear and logarithmic. Additionally, the Gaussian fits to both lines are plotted in the same graph.

The determined full widths at half maxima are (95.7 ± 0.3) nm for the horizontal and (97.8 ± 0.4) nm for the vertical direction. The ptychographic scans, taken during this beamtime, are presented in Section 6.1.2.

APPENDIX **B**

Data Sheets

B.1 Structure Size Determination at Ptychographic Reconstruction

The reconstructed structures were measured at one exemplary ptychographic scan, shown in Fig. 6.8. The plots and values to this are shown here, Fig. B.1 and Fig. B.2.

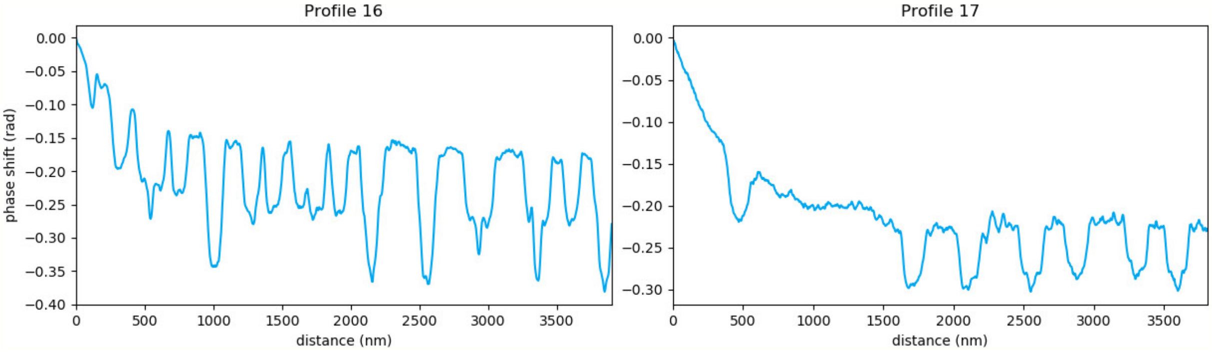

Figure B.1: These two plots show the profiles to the lines A (left) and B (right) in Fig. 6.8. With these plots, the cylindrical shape of half of the sample is visible in the projected phase shift of the structures.

To determine the positions of the structure edges, the line profiles are derived. The peaks in the derivative function of the plots in Fig. B.2 are fitted with a Gaussian function. As result, the peak position of the fitted Gaussian profile is taken as the position of the structure edge. See according figure and results in Section 6.2.2.

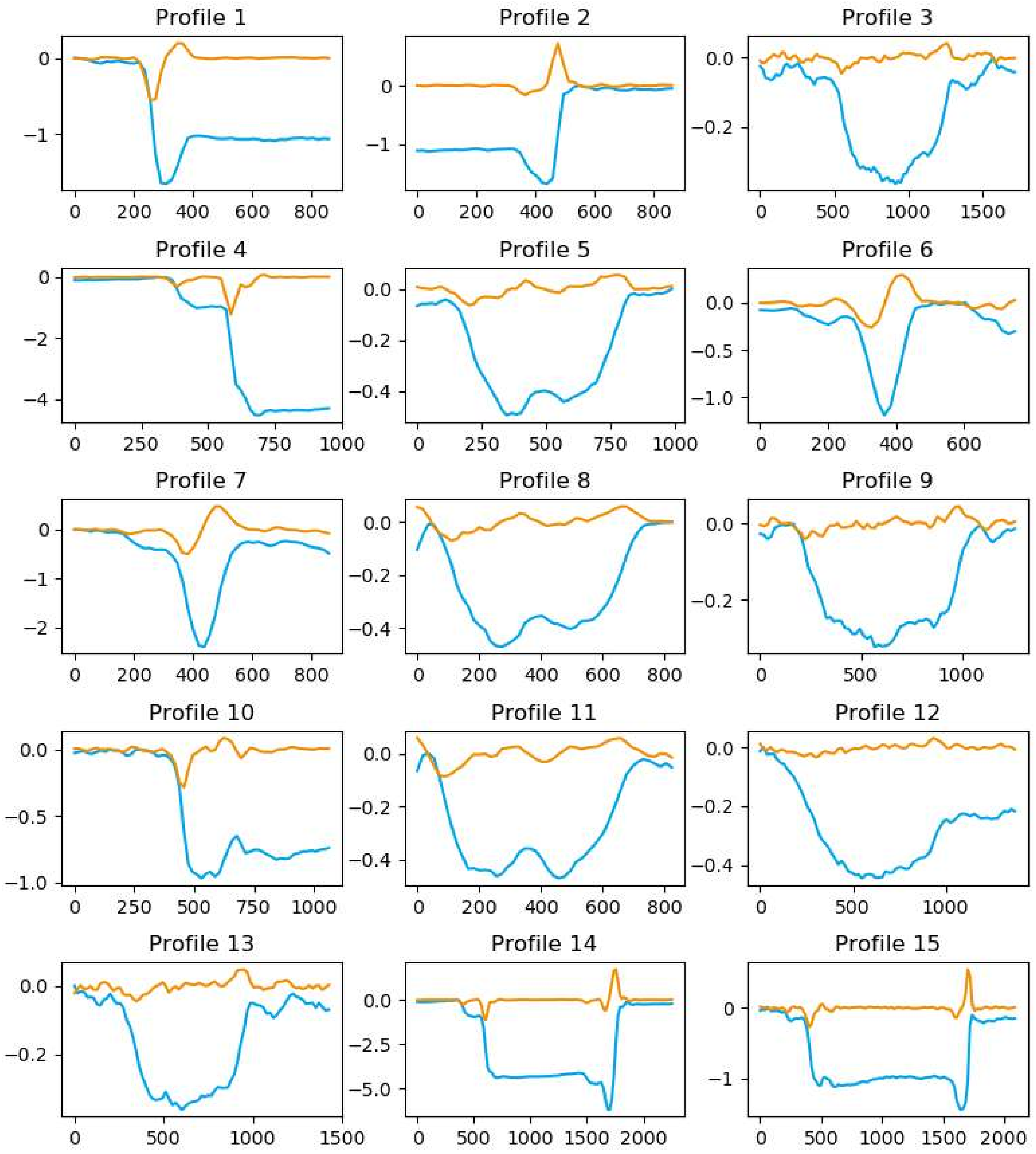

Figure B.2: Line profiles through structures in the ptychographically reconstructed phase images (blue) and their derivatives (orange) to lines in Fig. 6.8, all phase shifts given in rad. These profiles are used to determine the structure sizes. The x-axis show distances in nanometers and the y-axis presents the projected phase shifts of the structures in radian.

B.2 X-ray Fluorescence - Emission Lines

The following table lists the elements expected to be in the microchip and the values of emission lines being used for the analysis of the XRF spectra. The data is taken from the X-ray data booklet [159]. In case of free spaces in the table, these emission lines do not exist, while the gray values represent emission lines which are out of interest for our given energy range, which means that these emission lines are below the detectable energy or above the probe energy 18 keV.

El.	Z	Kα_1	Kα_2	Kβ_1	Lα_1	Lα_2	Lβ_1	Lβ_2	Lγ_1	Mα_1
B	5									
Al	13	1.487	1.486	1.557						
Si	14	1.740	1.740	1.836						
P	15	2.014	2.013	2.139						
Ti	22	4.511	4.505	4.932	0.452	0.452	0.458			
Co	27	6.930	6.915	7.649	0.776	0.776	0.791			
Cu	29	8.048	8.027	8.905	0.930	0.930	0.950			
Ga	31	9.252	9.225	10.264	1.098	1.098	1.125			
Ta	73	57.532	56.227	65.223	8.146	8.088	9.343	9.652	10.895	1.710
W	74	59.318	57.982	67.244	8.398	8.335	9.672	9.962	11.286	1.775
Pt	78	66.832	65.112	75.748	9.442	9.362	11.071	11.251	12.942	2.051

Table B.1: This table shows the XRF emission lines for the expected elements (El.) in the sample in keV. Gray values are out of the detectable energies and empty cells mean that this emission line does not exist.

To get back to the sample chapter, this table was referenced on page 36. The XRF analysis continues on page 81.

B.3 X-ray Fluorescence Effects

The following effects of the XRF measurement need to be considered during the analysis of the spectra [160]:

Rayleigh Peak	elastic scattering of the incident X-rays, $E_i = E_R$
Compton Peak	inelastic scattering of the incident X-rays, the energy is lower than the Rayleigh peak $E_C < E_R$ and is wider than the other peaks
Sum Peaks	detection artifact: two photons enter the detection region at exact the same time, their energy is added, e.g. $E = K_\alpha + K_\beta$
Escape Peaks	detection artifact: the energy of the emitted photon is partially absorbed by the detector material, e.g. Si: $E = K_{\alpha(Cu)} - K_{\alpha(Si)}$
Peak Overlaps	with the presence of different elements in the sample, the peaks may lay close to each other and their Gaussian distributions overlap

To return to the main part of the thesis, you may go back to page 82.

B.4 X-ray Diffraction - Crystal Information

Values and information taken from http://www.webelements.com with crystallographic abbreviations hcp - hexagonal close-packed, ccp - cubic close-packed, and bcc - body-centered cubic. Data for CoSi$_2$, tha data is taken from [161].

Phase	Z	space gr.	sg.no.	structure	Length (Å)			Angle (°)		
					a	b	c	α	β	γ
Si	14	Fd$\bar{3}$m	227	diamond	5.431	5.431	5.431	90	90	90
Ti	22	P6_3/mmc	194	hcp	2.951	2.951	4.686	90	90	120
Co	27	P6_3/mmc	194	hcp	2.507	2.507	4.069	90	90	120
Cu	29	Fm$\bar{3}$m	225	fcc	3.615	3.615	3.615	90	90	90
Ta	73	Im$\bar{3}$m	229	bcc	3.301	3.301	3.301	90	90	90
W	74	Im$\bar{3}$m	229	bcc	3.165	3.165	3.165	90	90	90
CoSi$_2$	-	Fm$\bar{3}$m	225	fcc	5.356	5.356	5.356	90	90	90
β-Si$_3$N$_4$	-	P6_3		hcp	7.595	7.595	2.902	90	90	120
Ta(N)	-			bcc	3.343	3.343	3.343	90	90	90

Table B.2: Lattice parameters for the materials contained in the sample.

Return here to Page 87.

The following table shows the expected 2θ of reflections (hkl), including permutations, for the elements in table B.2 for 18 keV. The table does not show an angle for forbidden reflections. Values given in gray are principally available, but are out of the measured region.

(hkl)	Cu	Si	CoSi$_2$	W	Ta	Ta(N)
	fcc	fcc (diam.)	fcc	bcc	bcc	bcc
(110)	-	-	-	17.70	16.97	16.75
(111)	18.99	12.61	12.79	-	-	-
(200)	21.97	-	-	25.14	24.09	23.78
(211)	-	-	-	30.92	29.61	29.21
(220)	31.27	20.67	20.96	35.85	34.32	33.88
(310)	-	-	-	40.25	38.53	38.03
(311)	36.84	24.28	24.63	-	-	-
(222)	38.54	-	-	44.29	42.37	41.82
(321)	-	-	-	48.05	45.95	45.35
(400)	44.80	-	-	51.60	49.33	48.67
(330)/(114)	-	-	-	54.99	52.54	51.84
(331)	49.07	32.09	32.55	-	-	-
(420)	50.44	-	-	58.24	55.62	54.87
(422)	55.65	36.2	36.72	64.42	61.47	60.62

Table B.3: XRD reflection angles for the elements of the sample for all phases, alias (hkl)-groups, in the angular range of the detector, given in 2θ for direct comparison of the values with the diffractogram.

The XRD analysis continues on Page 93.

B.5 X-ray Absorption Region Measures

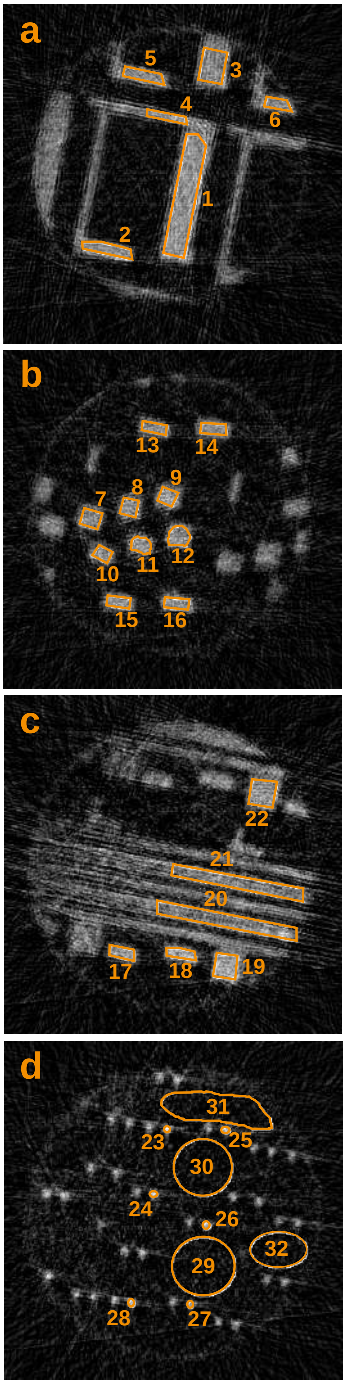

img	mark	exp. ele- ment	meas. μ per pixel	meas. μ/ρ in cm^2/g	mean μ/ρ cm^2/g
a	1	Cu	9.750×10^{-4}	43.527	41.52
	2		9.100×10^{-4}	40.625	
	3		8.932×10^{-4}	39.875	
	4		8.770×10^{-4}	39.152	
	5		8.793×10^{-4}	39.254	
	6		9.675×10^{-4}	43.192	
b	7		8.725×10^{-4}	38.951	
	8		9.144×10^{-4}	40.821	
	9		9.978×10^{-4}	44.545	
	10		9.171×10^{-4}	40.942	
	11		9.480×10^{-4}	42.321	
	12		9.084×10^{-4}	40.554	
	13		8.734×10^{-4}	38.991	
	14		9.006×10^{-4}	40.205	
	15		9.764×10^{-4}	43.589	
	16		9.202×10^{-4}	41.080	
c	17		9.679×10^{-4}	43.21	
	18		1.069×10^{-3}	47.723	
	19		1.079×10^{-3}	48.17	
	20		8.157×10^{-4}	36.415	
	21		8.403×10^{-4}	37.513	
	22		9.563×10^{-4}	42.692	
d	23	W	1.120×10^{-3}	23.212	21.69
	24		1.024×10^{-3}	21.223	
	25		1.031×10^{-3}	21.368	
	26		1.053×10^{-3}	21.824	
	27		9.938×10^{-4}	20.597	
	28		1.057×10^{-3}	21.907	
	29	Si	3.151×10^{-5}	5.409	4.98
	30		1.410×10^{-5}	2.421	
	31		3.438×10^{-5}	5.902	
	32		3.599×10^{-5}	6.179	

Table B.4: XRA reference regions and measured (meas.) attenuation coefficients for comparison to literature values. This table contains the images (img) of the four selected slices of the three-dimensional tomographic reconstruction with the marks of the measurement regions (mark). The table on the right shows the measured mean values of each region, represented by the according number, and the calculated mass attenuation coefficient μ/ρ. The last collumn of the table gives the mean value for the elements. The average values are compared to literature values in the summary on page 79.

APPENDIX C

Ptychography Image Gallery

During an earlier experiment, many ptychograms were acquired at different projection angles. Unfortunately, they are not all taken at the same height and they do not fully span the necessary 180° in a sufficient sampling to tomographically reconstruct a volume. Nevertheless, these projections serve as good references for the contrasts used for the multimodal experiment. Back to the page 45.

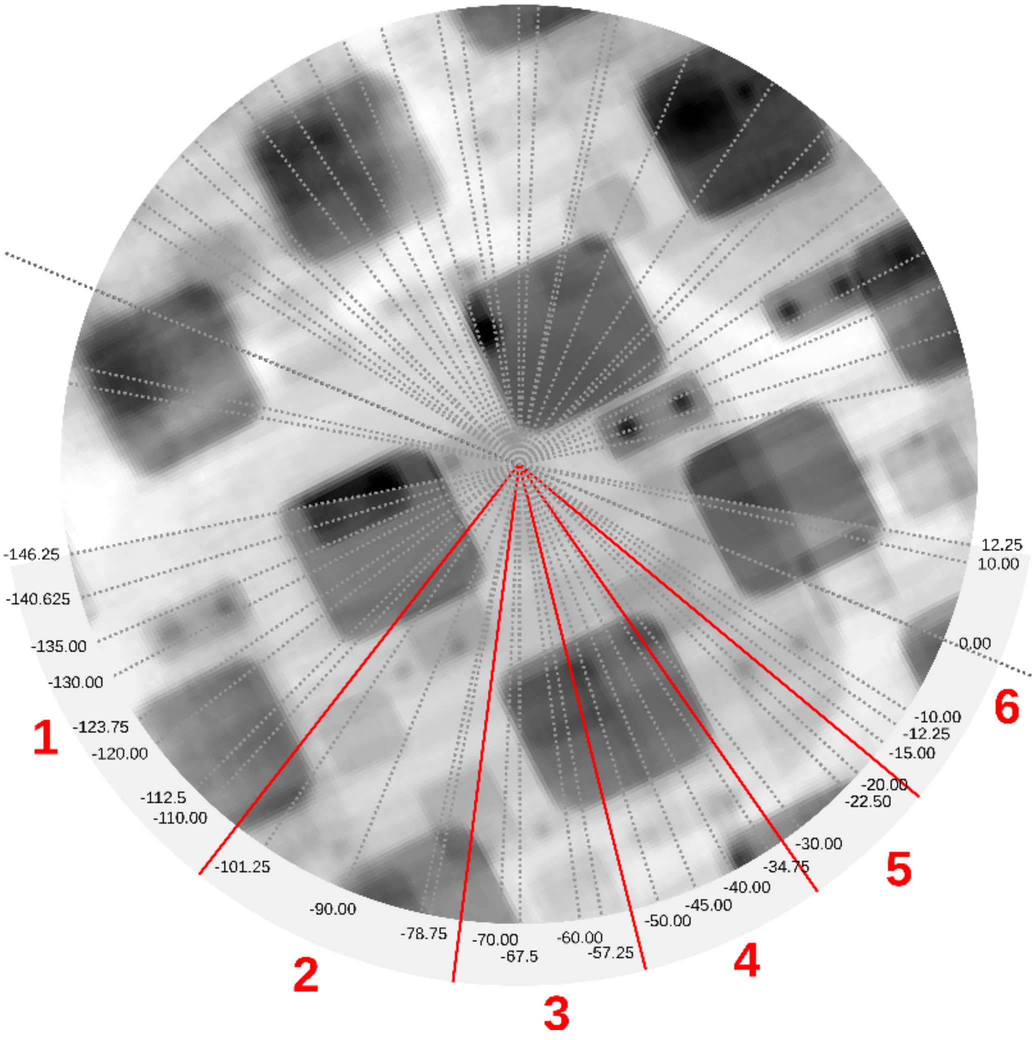

Figure C.1: Angular positions (in deg.) of the ptychographic projections in the Figures C.2, C.3 and C.4. The ptychograph underneath is a top view of the actual position and direction of the milled part and the other ptychograms, respectively.

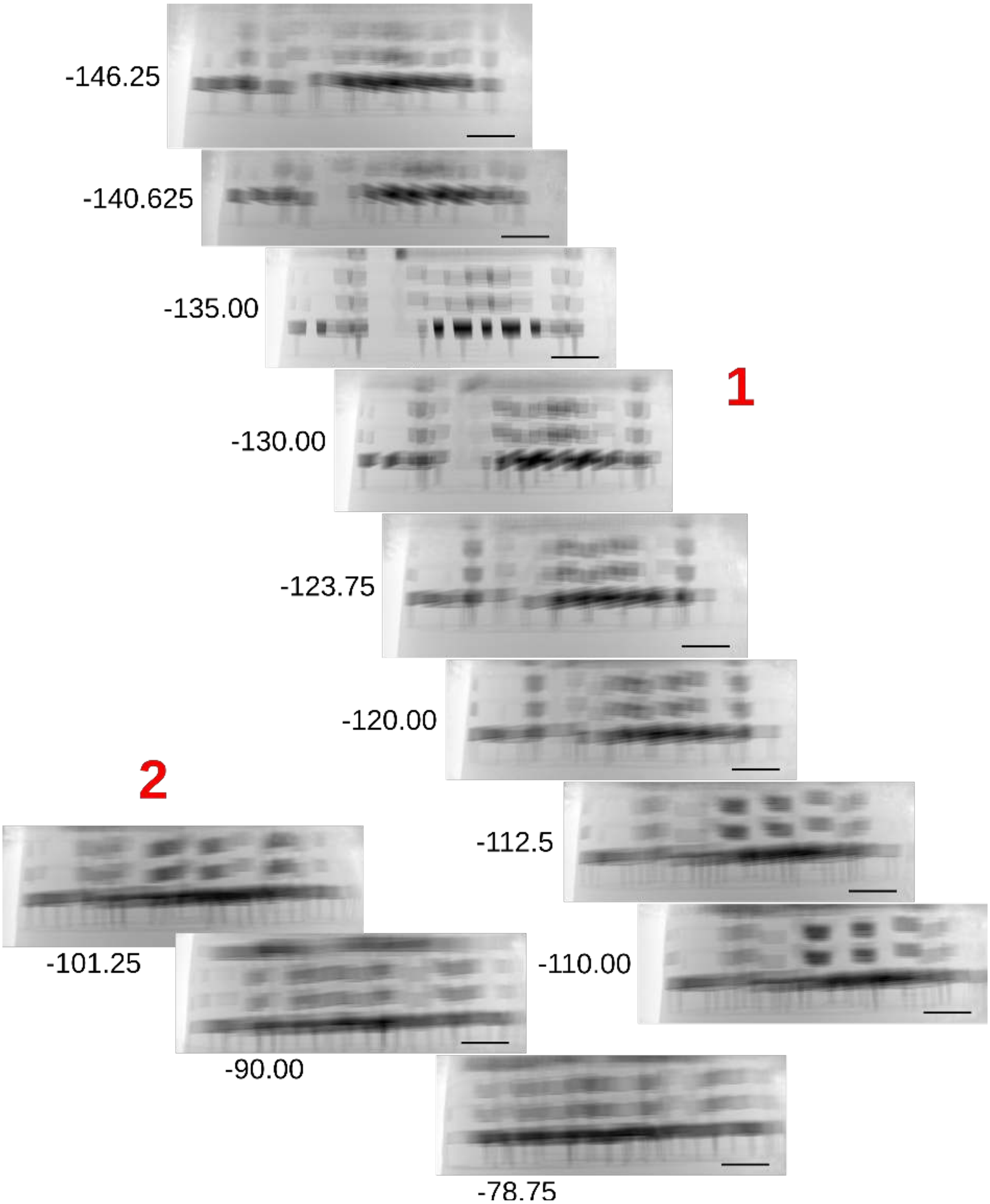

Figure C.2: Ptychographs of angular positions as sketched in see Fig. C.1.

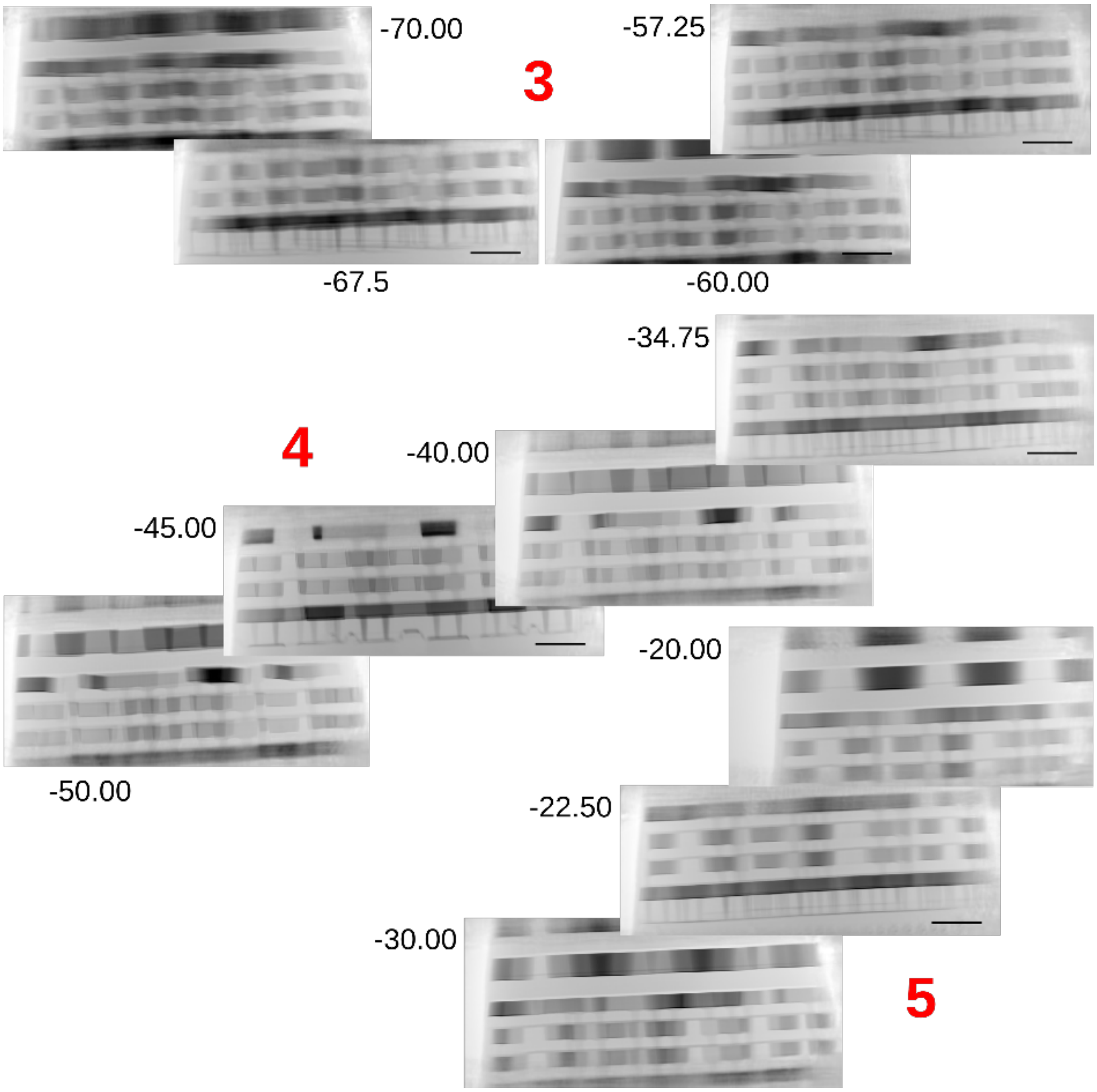

Figure C.3: Ptychographs of angular positions as sketched in see Fig. C.1.

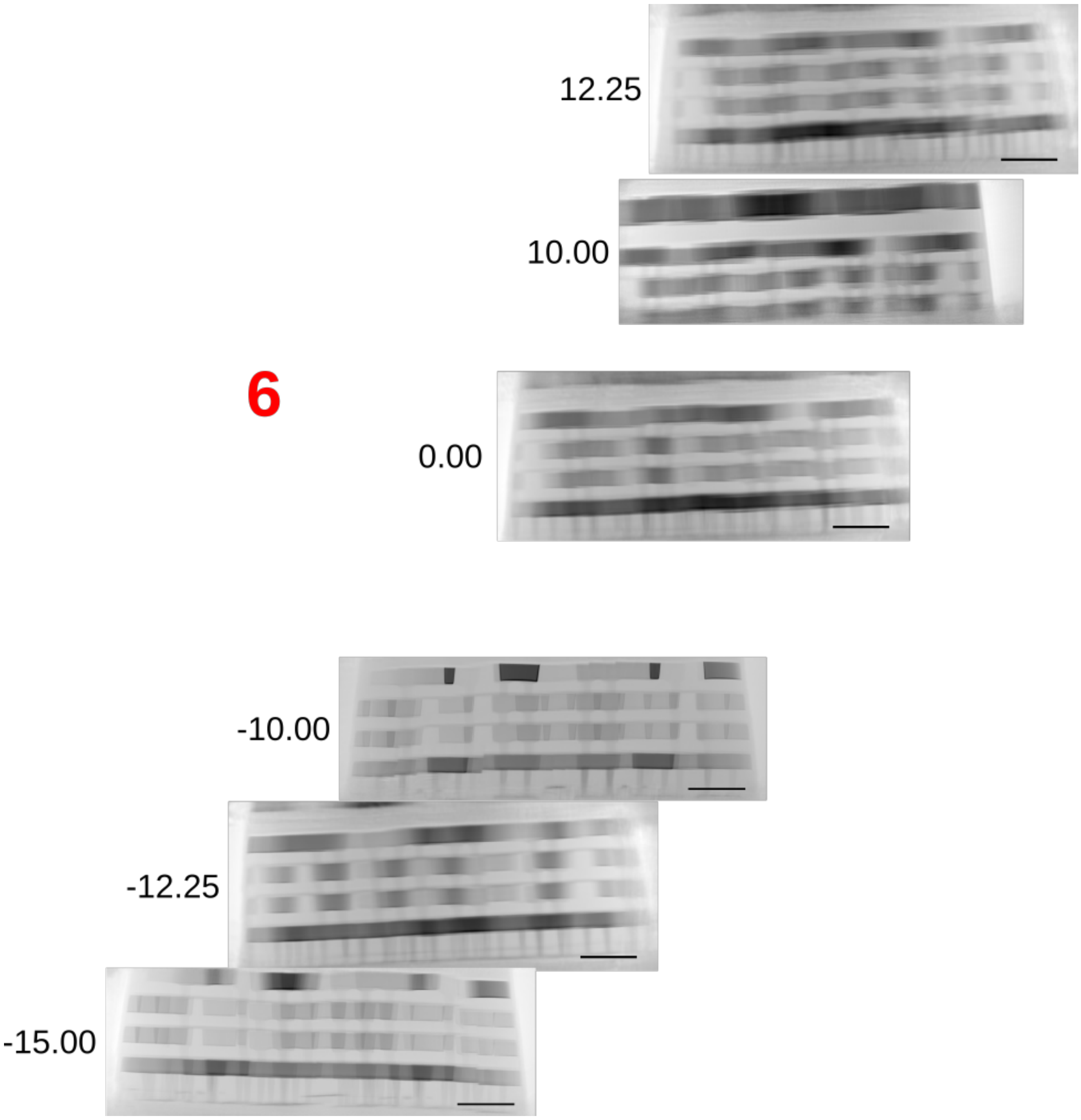

Figure C.4: Ptychographs of angular positions as sketched in see Fig. C.1.

APPENDIX D

EDX Image Gallery

Additionally to the electron microscopic imaging of different chip regions in top view and as cross sections, see Fig. 6.13, the elemental composition of these regions was probed by energy dispersive X-ray spectroscopy (EDX). The results are shown in Fig. D.2, which is separated in two groups, showing regions with Al, Si, Cu and Ta for the first four rows and Si, Cu, Ta and W for the last three rows, respectively.

The imaging chapter continues on page 52.

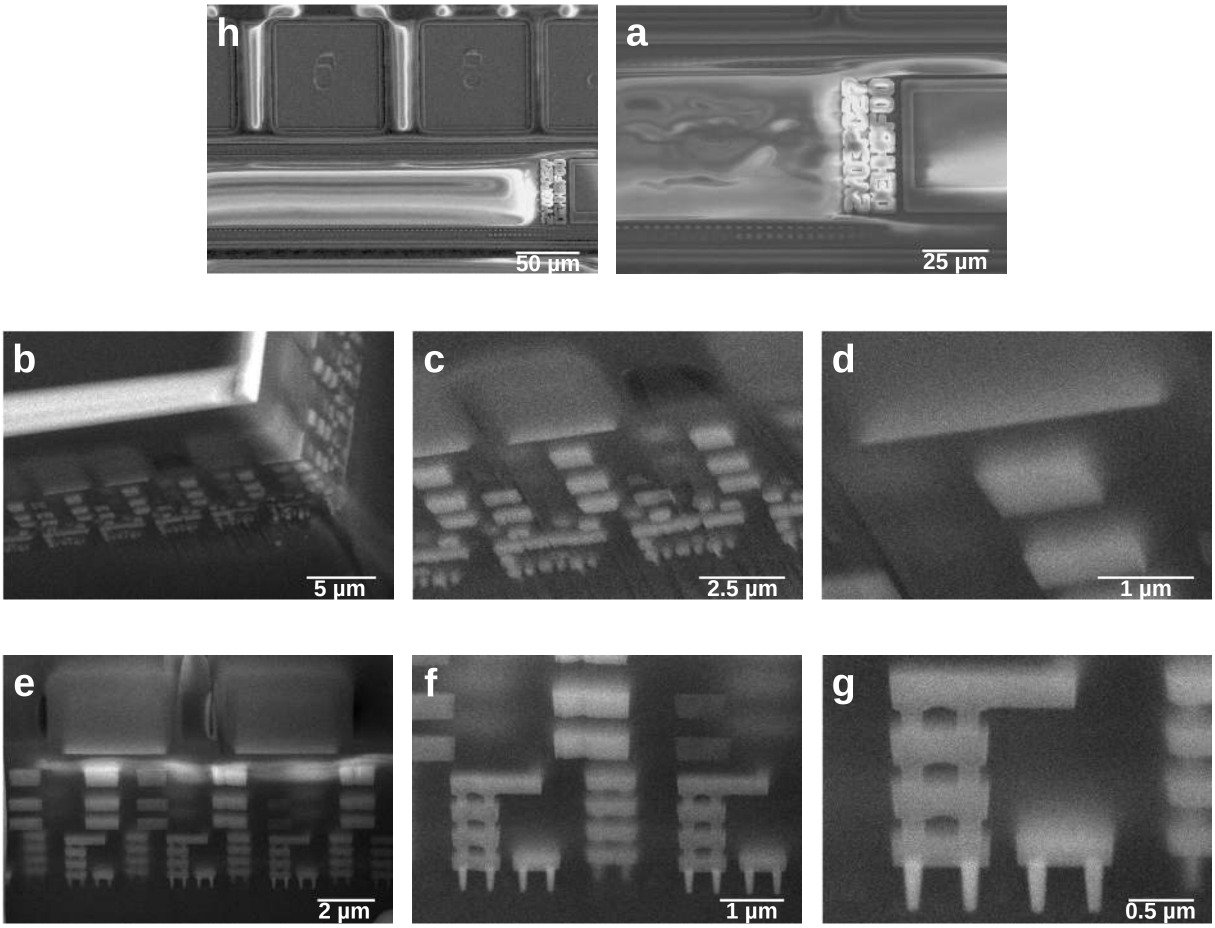

Figure D.1: Electron microscopic images of the microchip.

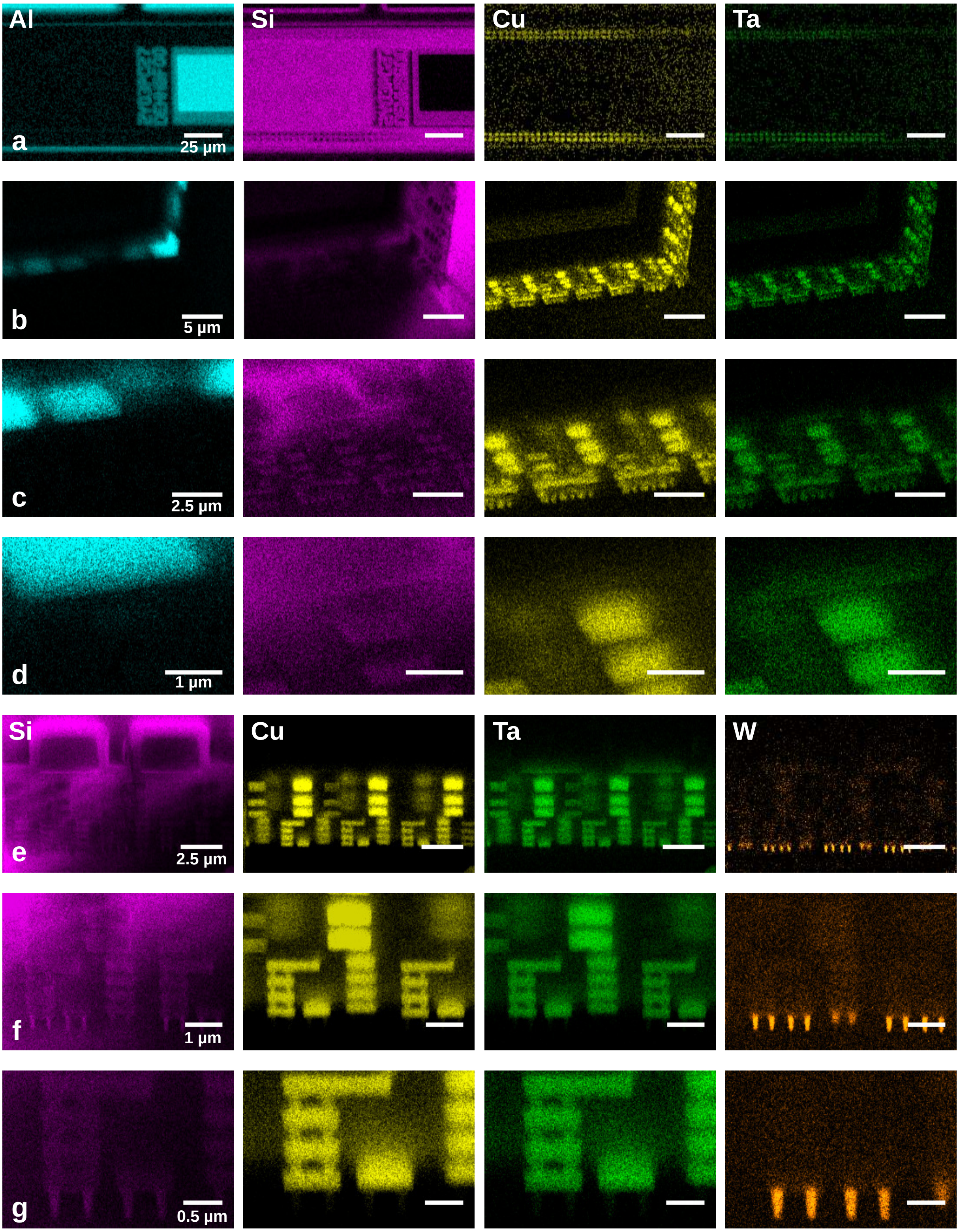

Figure D.2: EDX images of the microchip. The elemental analysis belongs to the EM images of Fig. 6.13.

Bibliography

[1] Haleh Ardebili, Jiawei Zhang, and Michael G. Pecht. “8 - Defect and failure analysis techniques for encapsulated microelectronics”. In: *Encapsulation Technologies for Electronic Applications (Second Edition)*. Ed. by Haleh Ardebili, Jiawei Zhang, and Michael G. Pecht. Second Edition. Materials and Processes for Electronic Applications. William Andrew Publishing, 2019, pp. 317–373. DOI: https://doi.org/10.1016/B978-0-12-811978-5.00008-0 (cit. on pp. iv, v).

[2] Max Knoll and Ernst Ruska. “Beitrag zur geometrischen Elektronenoptik. I”. In: *Annalen der Physik* 404.5 (1932), pp. 607–640 (cit. on p. 1).

[3] Martin M. Freundlich. “Origin of the electron microscope”. In: *Science* 142.3589 (1963), pp. 185–188 (cit. on p. 1).

[4] D. Iwanenko and I. Pomeranchuk. “On the maximal energy attainable in a betatron”. In: *Physical Review* 65.11-12 (1944), p. 343 (cit. on p. 1).

[5] F.R. Elder, A.M. Gurewitsch, R.V. Langmuir, and H.C. Pollock. “Radiation from electrons in a synchrotron”. In: *Physical Review* 71.11 (1947), p. 829 (cit. on p. 1).

[6] Leslie Berlin. *The man behind the microchip: Robert Noyce and the invention of Silicon Valley*. Oxford University Press, 2005 (cit. on p. 1).

[7] *Customized Chips at Volkswagen*. URL: https://www.volkswagenag.com/en/news/stories/2017/09/customized-chips.html (visited on 12/16/2020) (cit. on p. 1).

[8] Christian Kisielowski et al. “Detection of single atoms and buried defects in three dimensions by aberration-corrected electron microscope with 0.5-Å information limit”. In: *Microscopy and Microanalysis* 14.5 (2008), p. 469 (cit. on p. 1).

[9] Maria Benelmekki and Andreas Erbe. “Chapter 1 - Nanostructured thin films–background, preparation and relation to the technological revolution of the 21st century”. In: *Nanostructured Thin Films*. Ed. by Maria Benelmekki and Andreas Erbe. Vol. 14. Frontiers of Nanoscience. Elsevier, 2019, pp. 1–34. DOI: https://doi.org/10.1016/B978-0-08-102572-7.00001-5 (cit. on p. 1).

[10] *FEI, Slice and View Software*. URL: https://analyticalscience.wiley.com/do/10.1002/micro.1924/full/ (visited on 12/16/2020) (cit. on p. 1).

[11] Lorenz Holzer and Marco Cantoni. “Review of FIB-tomography”. In: *Nanofabrication using focused ion and electron beams: Principles and applications* 559201222 (2012), pp. 410–435 (cit. on p. 1).

[12] Marco Cantoni and Lorenz Holzer. “Advances in 3D focused ion beam tomography”. In: *Mrs Bulletin* 39.ARTICLE (2014), pp. 354–360 (cit. on p. 1).

[13] Reiner Hegerl and W. Hoppe. “Dynamische theorie der kristallstrukturanalyse durch elektronenbeugung im inhomogenen primärstrahlwellenfeld”. In: *Berichte der Bunsengesellschaft für physikalische Chemie* 74.11 (1970), pp. 1148–1154 (cit. on pp. 1, 16).

[14] Helen Mary Louise Faulkner and J.M. Rodenburg. “Movable aperture lensless transmission microscopy: a novel phase retrieval algorithm”. In: *Physical review letters* 93.2 (2004), p. 023903 (cit. on p. 1).

[15] Pierre Thibault, Martin Dierolf, Andreas Menzel, Oliver Bunk, Christian David, and Franz Pfeiffer. “High-resolution scanning x-ray diffraction microscopy”. In: *Science* 321.5887 (2008), pp. 379–382 (cit. on p. 1).

[16] Robert Hoppe et al. “High-resolution chemical imaging of gold nanoparticles using hard x-ray ptychography”. In: *Applied Physics Letters* 102.20 (2013), p. 203104 (cit. on p. 2).

[17] Juliane Reinhardt et al. “Beamstop-based low-background ptychography to image weakly scattering objects”. In: *Ultramicroscopy* 173 (2017), pp. 52–57 (cit. on p. 2).

[18] Mirko Holler et al. “Three-dimensional imaging of integrated circuits with macro-to nanoscale zoom”. In: *Nature Electronics* 2.10 (2019), pp. 464–470 (cit. on pp. 2, 114).

[19] Bjoern Enders, Martin Dierolf, Peter Cloetens, Marco Stockmar, Franz Pfeiffer, and Pierre Thibault. “Ptychography with broad-bandwidth radiation”. In: *Applied Physics Letters* 104.17 (2014), p. 171104 (cit. on p. 2).

[20] Huibin Chang et al. “Advanced denoising for X-ray ptychography”. In: *Optics express* 27.8 (2019), pp. 10395–10418 (cit. on p. 2).

[21] Manuel Guizar-Sicairos and James R. Fienup. “Phase retrieval with transverse translation diversity: a nonlinear optimization approach”. In: *Optics express* 16.10 (2008), pp. 7264–7278 (cit. on p. 2).

[22] Fucai Zhang et al. “Translation position determination in ptychographic coherent diffraction imaging”. In: *Optics express* 21.11 (2013), pp. 13592–13606 (cit. on p. 2).

[23] Emmanuel Garnier. “Powder Diffraction. Theory and Practice. Edited by RE Dinnebier and SJL Billinge. Cambridge: RSC Publishing, 2008. Pp. xxi+ 582. Price (hardcover): GBP 59.00. ISBN (online): 978-1-84755-823-7; ISBN (print): 978-0-85404-231-9.” In: *Acta Crystallographica Section A: Foundations of Crystallography* 65.1 (2009), pp. 51–51 (cit. on p. 2).

[24] Eric J. Mittemeijer and Paolo Scardi. *Diffraction analysis of the microstructure of materials*. Vol. 68. Springer Science & Business Media, 2013 (cit. on p. 2).

[25] Johan Hektor, Stephen A. Hall, N. Axel Henningsson, Jonas Engqvist, Matti Ristinmaa, Filip Lenrick, and Jonathan P. Wright. “Scanning 3DXRD Measurement of Grain Growth, Stress, and Formation of Cu6Sn5 around a Tin Whisker during Heat Treatment”. In: *Materials* 12.3 (2019), p. 446 (cit. on pp. 2, 24).

[26] N. Axel Henningsson, Stephen A. Hall, Jonathan P. Wright, and Johan Hektor. “Reconstructing intragranular strain fields in polycrystalline materials from scanning 3DXRD data”. In: *Journal of Applied Crystallography* 53.2 (2020) (cit. on pp. 2, 61).

[27] Henning Friis Poulsen. *Three-dimensional X-ray diffraction microscopy: mapping polycrystals and their dynamics*. Vol. 205. Springer Science & Business Media, 2004 (cit. on pp. 2, 24).

[28] James Clerk Maxwell. “VIII. A dynamical theory of the electromagnetic field”. In: *Philosophical transactions of the Royal Society of London* 155 (1865), pp. 459–512 (cit. on p. 5).

[29] John David Jackson. *Classical electrodynamics*. John Wiley & Sons, 2007 (cit. on p. 5).

[30] Eugene Hecht. *Optik*. Walter de Gruyter GmbH & Co KG, 2018 (cit. on pp. 5, 6, 14).

[31] Max Born and Emil Wolf. *Principles of optics: electromagnetic theory of propagation, interference and diffraction of light*. Elsevier, 2013 (cit. on pp. 5, 7, 14).

[32] David Paganin. *Coherent X-ray optics*. 6. Oxford University Press on Demand, 2006 (cit. on pp. 5, 7, 29).

[33] Frank Seiboth. “Refractive Hard X-Ray Nanofocusing at Storage Ring and X-Ray Free-Electron Laser Sources”. In: (2016) (cit. on pp. 6, 7).

[34] Joseph W. Goodman. *Introduction to Fourier optics*. Roberts and Company Publishers, 2005 (cit. on pp. 6, 7).

[35] Juliane Reinhardt. “Resonant Hard X-ray Ptychography for High-Sensitivity Imaging with Chemical Contrast”. PhD thesis. Universität Hamburg, 2017 (cit. on pp. 6, 7, 112).

[36] Maik Kahnt. “3D nano-tomography using coherent X-rays”. PhD thesis. Universität Hamburg, 2019 (cit. on pp. 6, 7, 114).

[37] Jens Als-Nielsen and Des McMorrow. *Elements of modern X-ray physics*. John Wiley & Sons, 2011 (cit. on pp. 7, 8, 12, 27).

[38] John David Jackson. “Classical electrodynamics”. In: John Wiley & Sons, 2007. Chap. 6 (cit. on p. 7).

[39] Allan Lyckegaard. “Development of tomographic reconstruction methods in materials science with focus on advanced scanning methods”. PhD thesis. Technical University of Denmark, 2011 (cit. on pp. 8, 10, 11, 24).

[40] Georg Will. *Powder diffraction: The Rietveld method and the two stage method to determine and refine crystal structures from powder diffraction data*. Springer Science & Business Media, 2006 (cit. on p. 9).

[41] Robert A. Evarestov. *Quantum chemistry of solids: LCAO treatment of crystals and nanostructures*. Vol. 153. Springer Science & Business Media, 2013 (cit. on p. 9).

[42] Carmelo Giacovazzo, Hugo L Monaco, Davide Viterbo, F. Scordari, G. Gilli, G. Zanotti, and M. Catti. *Fundamentals of crystallography*. Vol. 7. Oxford University Press Oxford, 2002 (cit. on p. 9).

[43] Max Born. “Quantenmechanik der stoßvorgänge”. In: *Zeitschrift für Physik* 38.11-12 (1926), pp. 803–827 (cit. on p. 9).

[44] H.-J. Bunge. *Texture analysis in materials science: mathematical methods*. Elsevier, 2013 (cit. on p. 12).

[45] H.-R. Wenk and S. Grigull. “Synchrotron texture analysis with area detectors”. In: *Journal of applied crystallography* 36.4 (2003), pp. 1040–1049 (cit. on p. 12).

[46] B.B. He. “Texture analysis”. In: (2019) (cit. on p. 12).

[47] John M Rodenburg and Helen M.L. Faulkner. “A phase retrieval algorithm for shifting illumination”. In: *Applied physics letters* 85.20 (2004), pp. 4795–4797 (cit. on p. 16).

[48] Pierre Thibault, Martin Dierolf, Oliver Bunk, Andreas Menzel, and Franz Pfeiffer. “Probe retrieval in ptychographic coherent diffractive imaging”. In: *Ultramicroscopy* 109.4 (2009), pp. 338–343 (cit. on pp. 16, 64).

[49] Andrew M. Maiden and John M. Rodenburg. “An improved ptychographical phase retrieval algorithm for diffractive imaging”. In: *Ultramicroscopy* 109.10 (2009), pp. 1256–1262 (cit. on pp. 16, 17).

[50] Xiaojing Huang, Hanfei Yan, Ross Harder, Yeukuang Hwu, Ian K. Robinson, and Yong S. Chu. “Optimization of overlap uniformness for ptychography”. In: *Optics Express* 22.10 (2014), pp. 12634–12644 (cit. on p. 16).

[51] Oliver Bunk, Martin Dierolf, Soren Kynde, Ian Johnson, Othmar Marti, and Franz Pfeiffer. “Influence of the overlap parameter on the convergence of the ptychographical iterative engine”. In: *Ultramicroscopy* 108.5 (2008), pp. 481–487. DOI: 10.1016/j.ultramic.2007.08.003 (cit. on p. 16).

[52] Claude E. Shannon. “A mathematical theory of communication”. In: *The Bell system technical journal* 27.3 (1948), pp. 379–423 (cit. on pp. 18, 21).

[53] Felix Wittwer. “Untersuchung der Auflösung der Beugungsbilder in der Ptychographie”. Masterthesis. Technische Universität Dresden, 2015 (cit. on p. 18).

[54] D. J. Batey, T. B. Edo, C. Rau, U. Wagner, Z. D. Pešić, T. A. Waigh, and J. M. Rodenburg. “Reciprocal-space up-sampling from real-space oversampling in x-ray ptychography”. In: *Phys. Rev. A* 89 (4 Apr. 2014), p. 043812. DOI: 10.1103/PhysRevA.89.043812 (cit. on p. 18).

[55] Felix Wittwer, Robert Hoppe, Frank Seiboth, Juliane Reinhardt, Maria Scholz, and Christian G. Schroer. “Ptychography with a Virtually Enlarged Illumination”. In: *Microscopy and Microanalysis* 24.S2 (2018), pp. 46–47 (cit. on p. 18).

[56] Avinash C. Kak and Malcolm Slaney. “Principles of computerized tomographic imaging”. In: *IEEE Engineering in Medicine and Biology Society* (1988) (cit. on pp. 18–20).

[57] Gengsheng Lawrence Zeng. *Medical image reconstruction: a conceptual tutorial.* Springer, 2010 (cit. on pp. 18, 20).

[58] Richard Gordon, Robert Bender, and Gabor T. Herman. “Algebraic reconstruction techniques (ART) for three-dimensional electron microscopy and X-ray photography”. In: *Journal of theoretical Biology* 29.3 (1970), pp. 471–481 (cit. on p. 20).

[59] Gabor T. Herman, Arnold Lent, and Stuart W. Rowland. “ART: Mathematics and applications: A report on the mathematical foundations and on the applicability to real data of the algebraic reconstruction techniques”. In: *Journal of theoretical biology* 42.1 (1973), pp. 1–32 (cit. on p. 20).

[60] Peter M. Joseph. “An improved algorithm for reprojecting rays through pixel images”. In: *IEEE transactions on medical imaging* 1.3 (1982), pp. 192–196 (cit. on p. 20).

[61] Anders H. Andersen and Avinash C. Kak. “Simultaneous algebraic reconstruction technique (SART): a superior implementation of the ART algorithm”. In: *Ultrasonic imaging* 6.1 (1984), pp. 81–94 (cit. on p. 20).

[62] G.N. Ramachandran and A.V. Lakshminarayanan. “Three-dimensional reconstruction from radiographs and electron micrographs: application of convolutions instead of Fourier transforms”. In: *Proceedings of the National Academy of Sciences* 68.9 (1971), pp. 2236–2240 (cit. on p. 20).

[63] Y. S. Kwoh, I. S. Reed, and T. K. Truong. “A generalized |03c9|-filter for 3-D reconstruction”. In: *IEEE Transactions on Nuclear Science* 24.5 (1977), pp. 1990–1998. DOI: 10.1109/TNS.1977.4329147 (cit. on p. 20).

[64] Richard Anthony Crowther, D.J. DeRosier, and Aaron Klug. “The reconstruction of a three-dimensional structure from projections and its application to electron microscopy”. In: *Proceedings of the Royal Society of London. A. Mathematical and Physical Sciences* 317.1530 (1970), pp. 319–340 (cit. on p. 21).

[65] Chris Jacobsen. “Relaxation of the Crowther criterion in multislice tomography”. In: *Opt. Lett.* 43.19 (Oct. 2018), pp. 4811–4814. DOI: 10.1364/OL.43.004811 (cit. on p. 21).

[66] Marin Van Heel and Michael Schatz. “Fourier shell correlation threshold criteria”. In: *Journal of structural biology* 151.3 (2005), pp. 250–262 (cit. on p. 22).

[67] Niccolo Banterle, Khanh Huy Bui, Edward A. Lemke, and Martin Beck. “Fourier ring correlation as a resolution criterion for super-resolution microscopy”. In: *Journal of structural biology* 183.3 (2013), pp. 363–367 (cit. on p. 22).

[68] Pawel A. Penczek. “Resolution measures in molecular electron microscopy”. In: *Methods in enzymology*. Vol. 482. Elsevier, 2010, pp. 73–100 (cit. on p. 23).

[69] Pierre Bleuet, Eléonore Welcomme, Eric Dooryhée, Jean Susini, Jean-Louis Hodeau, and Philippe Walter. "Probing the structure of heterogeneous diluted materials by diffraction tomography". In: *Nature materials* 7.6 (2008), pp. 468–472 (cit. on pp. 23, 99).

[70] E. Dooryhée et al. "Non-destructive synchrotron X-ray diffraction mapping of a Roman painting". In: *Applied Physics A* 81.4 (2005), pp. 663–667 (cit. on p. 23).

[71] Eleonore Welcomme, Philippe Walter, Pierre Bleuet, J.-L. Hodeau, Eric Dooryhee, Pauline Martinetto, and Michel Menu. "Classification of lead white pigments using synchrotron radiation micro X-ray diffraction". In: *Applied Physics A* 89.4 (2007), pp. 825–832 (cit. on p. 23).

[72] Alain Manceau et al. "Deciphering Ni sequestration in soil ferromanganese nodules by combining X-ray fluorescence, absorption, and diffraction at micrometer scales of resolution". In: *American Mineralogist* 87.10 (2002), pp. 1494–1499 (cit. on p. 23).

[73] H. M. Rietveld. "A profile refinement method for nuclear and magnetic structures". In: *Journal of Applied Crystallography* 2.2 (June 1969), pp. 65–71. DOI: 10.1107/S0021889869006558 (cit. on p. 23).

[74] Robert E. Dinnebier, Andreas Leineweber, and John S.O. Evans. *Rietveld Refinement: Practical Powder Diffraction Pattern Analysis using TOPAS*. Berlin, Boston: De Gruyter, 17 Dec. 2018. DOI: https://doi.org/10.1515/9783110461381 (cit. on p. 23).

[75] L. B. McCusker, R. B. Von Dreele, D. E. Cox, D. Louër, and P. Scardi. "Rietveld refinement guidelines". In: *Journal of Applied Crystallography* 32.1 (Feb. 1999), pp. 36–50. DOI: 10.1107/S0021889898009856 (cit. on p. 23).

[76] Henning F. Poulsen, Dorte Juul Jensen, and Gavin B.M. Vaughan. "Three-dimensional X-ray diffraction microscopy using high-energy X-rays". In: *MRS bulletin* 29.3 (2004), pp. 166–169 (cit. on p. 24).

[77] Henning O. Sørensen et al. "Multigrain crystallography". In: *Zeitschrift für Kristallographie-Crystalline Materials* 227.1 (2012), pp. 63–78 (cit. on p. 24).

[78] Henning Friis Poulsen and G.B.M. Vaughan. "Multigrain crystallography and three-dimensional grain mapping". In: (2019) (cit. on p. 24).

[79] Allan Lyckegaard, Henning Friis Poulsen, Wolfgang Ludwig, Richard W. Fonda, and Erik M. Lauridsen. "Box-scan: A novel 3DXRD method for studies of recrystallization and grain growth". In: *Materials Science Forum*. Vol. 715. Trans Tech Publ. 2012, pp. 518–520 (cit. on p. 24).

[80] Allan Lyckegaard et al. *3D grain reconstruction from boxscan data*. Tech. rep. NAVAL RESEARCH LAB WASHINGTON DC, 2010 (cit. on p. 24).

[81] Yujiro Hayashi, Yoshiharu Hirose, and Yoshiki Seno. "Polycrystal orientation mapping using scanning three-dimensional X-ray diffraction microscopy". In: *Journal of Applied Crystallography* 48.4 (2015), pp. 1094–1101 (cit. on p. 24).

[82] Yujiro Hayashi, Daigo Setoyama, and Yoshiki Seno. "Scanning three-dimensional x-ray diffraction microscopy with a high-energy microbeam at SPring-8". In: *Materials Science Forum*. Vol. 905. Trans Tech Publ. 2017, pp. 157–164 (cit. on p. 24).

[83] Axel Henningsson. "Scanning-3DXRD Reconstructions-A Novel Reconstruction Method for Intragranular Orientation and Strain Fields In Crystalline Materials." In: *ISRN LUTFD2/TFHF-19/5232-SE (1-68)* (2019) (cit. on p. 24).

[84] Andreas Schropp et al. "PtyNAMi: ptychographic nano-analytical microscope". In: *Journal of Applied Crystallography* 53.4 (Aug. 2020), pp. 957–971. DOI: 10.1107/S1600576720008420 (cit. on p. 27).

[85] Christoph Rau. “Imaging with Coherent Synchrotron Radiation: X-ray Imaging and Coherence Beamline (I13) at Diamond Light Source”. In: *Synchrotron Radiation News* 30.5 (2017), pp. 19–25. DOI: 10.1080/08940886.2017.1364530 (cit. on pp. 27, 42, 43).

[86] Christian G. Schroer et al. “Hard x-ray nanoprobe of beamline P06 at PETRA III”. In: *AIP conference proceedings*. Vol. 1741. 1. AIP Publishing LLC. 2016, p. 030007 (cit. on p. 27).

[87] David Attwood and Anne Sakdinawat. *X-rays and extreme ultraviolet radiation: principles and applications*. Cambridge university press, 2017 (cit. on p. 27).

[88] Markus Tischer, Andreas Schoeps, U. Englisch, M. Barthelmess, J. Pflüger, and J. Skupin. “Status of the PETRA III Insertion devices”. In: (2008) (cit. on p. 28).

[89] Andreas Schoeps, Pavel Vagin, and Markus Tischer. “Properties of the insertion devices for PETRA III and its extension”. In: *AIP Conference Proceedings*. Vol. 1741. 1. AIP Publishing LLC. 2016, p. 020019 (cit. on p. 28).

[90] Christian G. Schroer and Bruno Lengeler. “X-Ray Optics”. In: *Springer Handbook of Lasers and Optics*. Springer, 2012, pp. 1461–1474 (cit. on p. 29).

[91] *The Center for X-ray Optics*. URL: https://henke.lbl.gov/optical_constants/getdb2.html (visited on 02/24/2020) (cit. on p. 29).

[92] Paul Kirkpatrick and A. V. Baez. “Formation of Optical Images by X-Rays”. In: *J. Opt. Soc. Am.* 38.9 (Sept. 1948), pp. 766–774. DOI: 10.1364/JOSA.38.000766 (cit. on p. 29).

[93] Christian G. Schroer et al. “Parabolic compound refractive lenses for hard x rays”. In: *Advances in X-ray optics*. Vol. 4145. International Society for Optics and Photonics. 2001, pp. 274–284 (cit. on p. 30).

[94] A. Snigirev, V. Kohn, I. Snigireva, A. Souvorov, and B. Lengeler. “Focusing high-energy x rays by compound refractive lenses”. In: *Appl. Opt.* 37.4 (Feb. 1998), pp. 653–662. DOI: 10.1364/AO.37.000653 (cit. on p. 30).

[95] Christian G. Schroer et al. “Nanofocusing parabolic refractive x-ray lenses”. In: *Applied physics letters* 82.9 (2003), pp. 1485–1487 (cit. on p. 30).

[96] B. Lengeler, C.G. Schroer, M. Richwin, J. Tümmler, M. Drakopoulos, A. Snigirev, and I. Snigireva. “A microscope for hard x rays based on parabolic compound refractive lenses”. In: *Applied physics letters* 74.26 (1999), pp. 3924–3926 (cit. on p. 30).

[97] Bruno Lengeler et al. “Refractive x-ray lenses”. In: *Journal of Physics D: Applied Physics* 38.10A (2005), A218 (cit. on p. 30).

[98] Christian G. Schroer. “Hard X-ray Microscopy and Microanalysis with Refractive X-Ray Lenses”. Habilitation. RWTH Aachen University, 2004 (cit. on p. 30).

[99] PI. *PI web page*. URL: https://www.physikinstrumente.de/de/ (visited on 11/11/2020) (cit. on p. 31).

[100] PI. *UPR-160 AIR Bearing Rotation Stage*. URL: https://www.pi-usa.us/fileadmin/user_upload/pi_us/files/product_datasheets/Air_Bearing_Rotation_Stages_UPR-Air_Family.pdf (visited on 11/11/2020) (cit. on p. 31).

[101] Physikinstrumente. *PI P-733.3CL*. URL: https://www.physikinstrumente.de/de/produkte/piezo-nanopositioniertische/pifoc-objectivscanner-pinano-probentische-fuer-die-mikroskopie/p-7333-xyz-piezonanopositionierer-20125/ (visited on 11/11/2020) (cit. on p. 31).

[102] New Focus. *Picolis^{TM} 8525*. URL: https://www.newport.com/medias/sys_master/images/images/he3/h79/8797240164382/Picolis-Linear-Stage-Datasheet.pdf (visited on 11/11/2020) (cit. on p. 31).

[103] Optique-Peter. *PCO.4000 with Microscope*. URL: http://optiquepeter.fr/wp-content/uploads/2019/03/OHP-Synchrotrons-2019-03.pdf (visited on 11/11/2020) (cit. on p. 32).

[104] Keyence. *VH-Z100UR*. URL: https://www.keyence.de/products/microscope/digital-microscope/vh_lens/models/vh-z100ur/ (visited on 11/11/2020) (cit. on p. 32).

[105] Hamamatsu. *Photo Diode without Scintillator*. Transmission Diode with 5 µm thickness, not available anymore. URL: http://www.hamamatsu.com (visited on 01/23/2017) (cit. on p. 32).

[106] Hamamatsu. *S1226-18BQ*. URL: https://www.hamamatsu.com/eu/en/product/type/S1226-18BQ/index.html (visited on 11/11/2020) (cit. on p. 32).

[107] Roberto Dinapoli et al. "EIGER characterization results". In: *Nuclear Instruments and Methods in Physics Research Section A: Accelerators, Spectrometers, Detectors and Associated Equipment* 731 (2013), pp. 68–73 (cit. on pp. 32, 62).

[108] I. Johnson et al. "Eiger: a single-photon counting x-ray detector". In: *Journal of Instrumentation* 9.05 (2014), p. C05032 (cit. on p. 32).

[109] Dectris. *Eiger X 4M*. URL: https://www.dectris.com/support/manuals-docs/eiger-x-for-synchrotron/eiger-x-4m/ (visited on 11/11/2020) (cit. on p. 33).

[110] Roberto Dinapoli et al. "EIGER: Next generation single photon counting detector for X-ray applications". In: *Nuclear Instruments and Methods in Physics Research Section A: Accelerators, Spectrometers, Detectors and Associated Equipment* 650.1 (2011), pp. 79–83 (cit. on p. 33).

[111] Quantum Detectors. *MerlinX*. URL: https://quantumdetectors.com/n/products/merlinx/ (visited on 11/11/2020) (cit. on p. 33).

[112] R. Plackett, I. Horswell, E.N. Gimenez, J. Marchal, D. Omar, and N. Tartoni. "Merlin: a fast versatile readout system for Medipix3". In: *Journal of Instrumentation* 8.01 (2013), p. C01038 (cit. on p. 33).

[113] Burkhard Beckhoff, Birgit Kanngießer, Norbert Langhoff, Reiner Wedell, and Helmut Wolff. *Handbook of practical X-ray fluorescence analysis*. Springer Science & Business Media, 2007 (cit. on p. 33).

[114] Hitatchi. *Vortex®-EM*. URL: https://www.hitachi-hightech.com/hhs-us/product_detail/?pn=ana-vortex-em (visited on 11/11/2020) (cit. on p. 33).

[115] *XIA xMap*. URL: https://www.xia.com/dxp-xmap.html (visited on 12/19/2020) (cit. on p. 33).

[116] Ulrich Hilleringmann. *Silizium-Halbleitertechnologie: Grundlagen mikroelektronischer Integrationstechnik*. Springer-Verlag, 2018 (cit. on p. 35).

[117] Friedemann Völklein and Thomas Zetterer. *Einführung in die Mikrosystemtechnik: Grundlagen und Praxisbeispiele*. Springer-Verlag, 2013 (cit. on p. 35).

[118] *Basis for Kelvin Contacts*. URL: http://www.loranger.com/loranger_edc2/html/PDFs/Why_Kelvin_Contacts.pdf (visited on 09/23/2020) (cit. on p. 37).

[119] Stephan Preibisch, Stephan Saalfeld, and Pavel Tomancak. "Globally optimal stitching of tiled 3D microscopic image acquisitions". In: *Bioinformatics* 25.11 (2009), pp. 1463–1465 (cit. on p. 44).

[120] Amwar Ul-Hamid. "Components of the SEM". In: *A Beginners' Guide to Scanning Electron Microscopy*. Springer, Cham, 2018, pp. 15–76. DOI: 10.1007/978-3-319-98482-7_2 (cit. on p. 51).

[121] ThermoFischer. *Avizo*. URL: https://www.thermofisher.com/de/de/home/industrial/electron-microscopy/electron-microscopy-instruments-workflow-solutions/3d-visualization-analysis-software/avizo-materials-science.html (visited on 11/11/2020) (cit. on p. 54).

[122] Peter Westenberger. “AVIZO-3D visualization framework”. In: *Geoinformatics Conference*. 2008, pp. 1–11 (cit. on p. 54).

[123] Paw Kristiansen, Jan Horbach, Ralph Döhrmann, and Joachim Heuer. “Vibration measurements of high-heat-load monochromators for DESY PETRA III extension”. In: *Journal of synchrotron radiation* 22.4 (2015), pp. 879–885 (cit. on p. 60).

[124] Christian G. Schroer et al. “Hard X-ray nanoprobe at beamline P06 at PETRA III”. In: *Nuclear Instruments and Methods in Physics Research Section A: Accelerators, Spectrometers, Detectors and Associated Equipment* 616.2-3 (2010), pp. 93–97 (cit. on p. 61).

[125] Lukas Grote. “X-Ray Fluorescence Nanotomography on an Integrated Circuit”. Masterthesis. Universität Hamburg, 2017 (cit. on pp. 77, 85).

[126] Center for X-ray Optics. *X-ray Properties of Elements*. URL: http://henke.lbl.gov/optical_constants/pert_form.html (visited on 03/05/2020) (cit. on p. 80).

[127] P. Van Espen, K. Janssens, and J. Nobels. “AXIL-PC, software for the analysis of complex X-ray spectra”. In: *Chemometrics and intelligent laboratory systems* 1.1 (1986), pp. 109–114 (cit. on p. 81).

[128] Bart Vekemans, K. Janssens, Laszlo Vincze, F. Adams, and P. Van Espen. “Analysis of X-ray spectra by iterative least squares (AXIL): New developments”. In: *X-Ray Spectrometry* 23.6 (1994), pp. 278–285 (cit. on pp. 81, 82).

[129] V.A. Solé and E. Papillon. *PyMCA–X-Ray Spectrum Analysis in Python*. 2004 (cit. on p. 81).

[130] Jan Pallon, CG Ryan, N. Arteaga Marrero, Mikael Elfman, Per Kristiansson, E.J.C. Nilsson, and Christer Nilsson. “STIM evaluation in GeoPIXE to complement the quantitative dynamic analysis”. In: *Nuclear Instruments and Methods in Physics Research Section B: Beam Interactions with Materials and Atoms* 267.12-13 (2009), pp. 2080–2084 (cit. on p. 81).

[131] Manne Siegbahn. “Relations between the K and L Series of the High-Frequency Spectra”. In: *Nature* 96.2416 (1916), pp. 676–676 (cit. on p. 82).

[132] R.D. Bonetto and J.A. Riveros. “Measuring the dead time of an x-ray spectrometer by means of the first-and second-order reflections method”. In: *X-Ray Spectrometry* 13.1 (1984), pp. 44–45 (cit. on p. 83).

[133] Ran Yan, Yu Bing Liu, and Ping Dai. “Determination and Evaluation of Dead Time for X-ray Fluorescence Spectrometer”. In: *Key Engineering Materials*. Vol. 544. Trans Tech Publ. 2013, pp. 445–449 (cit. on p. 83).

[134] Christian G. Schroer. “Reconstructing x-ray fluorescence microtomograms”. In: *Applied Physics Letters* 79.12 (2001), pp. 1912–1914 (cit. on pp. 84, 85).

[135] H.O. Sørensen. “PolyXSim-3DXRD Far-field Simulation of Polycrystals”. In: *Risø National Laboratory for Sustainable Energy, Technical University of Denmark* (2008) (cit. on p. 91).

[136] *PolyXSim*. URL: https://sourceforge.net/p/fable/wiki/PolyXSim/ (visited on 02/28/2018) (cit. on p. 91).

[137] *Topas*. URL: https://www.bruker.com/de/products/x-ray-diffraction-and-elemental-analysis/x-ray-diffraction/xrd-software/topas.html (visited on 11/12/2020) (cit. on p. 93).

[138] H.B. Nie et al. “Structural and electrical properties of tantalum nitride thin films fabricated by using reactive radio-frequency magnetron sputtering”. In: *Applied Physics A* 73.2 (2001), pp. 229–236 (cit. on p. 97).

[139] Søren Schmidt. “GrainSpotter: a fast and robust polycrystalline indexing algorithm”. In: *Journal of Applied Crystallography* 47.1 (2014), pp. 276–284 (cit. on p. 102).

[140] *Grainspotter*. URL: https://sourceforge.net/p/fable/wiki/grainspotter/ (visited on 03/01/2017) (cit. on p. 102).

[141] *ImageD11*. URL: https://sourceforge.net/p/fable/wiki/imaged11%20-%20overview/ (visited on 03/01/2017) (cit. on p. 102).

[142] *Mtex toolbox*. URL: https://mtex-toolbox.github.io/ODFInversePoleFigure.html (visited on 11/28/2020) (cit. on p. 105).

[143] James Diebel. "Representing attitude: Euler angles, unit quaternions, and rotation vectors". In: *Matrix* 58.15-16 (2006), pp. 1–35 (cit. on p. 105).

[144] *Intro to X-ray Pole Figures*. URL: http://pajarito.materials.cmu.edu/rollett/27750/L4-Xray_PFs-26Jan16.pdf (visited on 11/10/2020) (cit. on p. 105).

[145] *Inverse Pole Figures*. URL: http://www.ebsd.com/popup/inversepolefigure.htm (visited on 09/08/2020) (cit. on p. 105).

[146] Philipp M. Pelz, Manuel Guizar-Sicairos, Pierre Thibault, Ian Johnson, Mirko Holler, and Andreas Menzel. "On-the-fly scans for X-ray ptychography". In: *Applied Physics Letters* 105.25 (2014), p. 251101 (cit. on p. 111).

[147] Mikhail Lyubomirskiy et al. "Diamond nanofocusing refractive X-ray lenses made by planar etching technology". In: *Journal of Synchrotron Radiation* 26.5 (Sept. 2019), pp. 1554–1557. DOI: 10.1107/S1600577519007082 (cit. on p. 111).

[148] Y. D. Wang, L. Zuo, Z. D. Liang, C. Laruelle, A. Vadon, and J. J. Heizmann. "Quantitative Texture Analysis from X-ray Diffraction Spectra". In: *Journal of Applied Crystallography* 30.4 (Aug. 1997), pp. 443–448. DOI: 10.1107/S0021889897000186 (cit. on p. 112).

[149] Silvio Achilles. "3D Scanning X-ray Diffraction Microscopy on the Nano-Scale". Masterthesis. Universität Hamburg, 2020 (cit. on p. 113).

[150] Maik Kahnt et al. "Coupled ptychography and tomography algorithm improves reconstruction of experimental data". In: *Optica* 6.10 (2019), pp. 1282–1289 (cit. on p. 114).

[151] Mirko Holler et al. "High-resolution non-destructive three-dimensional imaging of integrated circuits". In: *Nature* 543.7645 (2017), pp. 402–406 (cit. on p. 114).

[152] Xiaogang Yang et al. "Tomographic reconstruction with a generative adversarial network". In: *Journal of Synchrotron Radiation* 27.2 (Mar. 2020), pp. 486–493. DOI: 10.1107/S1600577520000831 (cit. on p. 114).

[153] Yaakov Tsaig and David L. Donoho. *Compressed sensing*. 2004 (cit. on p. 114).

[154] Zhanli Hu, Dong Liang, Dan Xia, and Hairong Zheng. "Compressive sampling in computed tomography: Method and application". In: *Nuclear Instruments and Methods in Physics Research Section A: Accelerators, Spectrometers, Detectors and Associated Equipment* 748 (2014), pp. 26–32 (cit. on p. 114).

[155] Yan Kaganovsky et al. "Compressed sampling strategies for tomography". In: *JOSA A* 31.7 (2014), pp. 1369–1394 (cit. on p. 114).

[156] Martti Kalke and Samuli Siltanen. "Sinogram interpolation method for sparse-angle tomography". In: *Applied Mathematics* 2014 (2014) (cit. on p. 114).

[157] M.E. Stuckelberger et al. "Challenges and opportunities with highly brilliant X-ray sources for multi-modal in-situ and operando characterization of solar cells". In: *Microscopy and Microanalysis* 24.S2 (2018), pp. 434–435 (cit. on p. 115).

[158] Christina Ossig, Tara Nietzold, Bradley West, Mariana Bertoni, Gerald Falkenberg, Christian G. Schroer, and Michael E. Stuckelberger. "X-ray beam induced current measurements for multi-modal x-ray microscopy of solar cells". In: *JoVE (Journal of Visualized Experiments)* 150 (2019), e60001 (cit. on p. 115).

[159] *X-ray Data Booklet*. URL: https://xdb.lbl.gov/ (visited on 03/10/2017) (cit. on p. 121).

[160] *Interpretation of XRF Spectra*. URL: https://chem.libretexts.org/Bookshelves/Analytical_Chemistry/Supplemental_Modules_(Analytical_Chemistry)/Analytical_Sciences_Digital_Library/JASDL/Courseware/Introduction_to_XRF-_An_Analytical_Perspective/2._Interpretation_of_XRF_Spectra (visited on 10/01/2020) (cit. on p. 121).

[161] Lih J. Chen. *Silicide technology for integrated circuits*. Vol. 5. Iet, 2004 (cit. on p. 122).

Own Publications

Andreas Schropp, Ralph Döhrmann, Stephan Botta, Dennis Brückner, Maik Kahnt, Mikhail Lyubomirskiy, Christina Ossig, Scholz, Maria, Martin Seyrich, Michael E Stuckelberger, et al. “PtyNAMi: ptychographic nano-analytical microscope”. In: *Journal of applied crystallography* 53.4 (2020), pp. 957–971.

Ralph Doehrmann, Stephan Botta, Gerald Falkenberg, Jan Garrevoet, Maik Kahnt, Mikhail Lyubomirskiy, Scholz, Maria, Christian G. Schroer, Andreas Schropp, Martin Seyrich, et al. “PtyNAMi: Ptychographic Nano-Analytical Microscope at PETRA III-How to Achieve Sub-nanometer Sample Stability”. In: (2018).

Gerald Falkenberg, Gerta Fleissner, Philipp Alraun, Juliane Reinhardt, Scholz, Maria, Andreas Schropp, Kathryn Spiers, Jan Garrevoet, Christian G. Schroer, and Gunther Fleissner. “Correlative Imaging of Melanosoms with Ptychography, X-ray Fluorescence and Light Microscopy”. In: *Microscopy and Microanalysis* 24.S2 (2018), pp. 390–391.

Gerald Falkenberg, Gerta Fleissner, Philip Alraun, Juliane Reinhardt, Scholz, Maria, Andreas Schropp, Kathryn Spiers, Jan Garrevoet, Christian G. Schroer, and Gunther Fleissner. “Correlative XRF, ptychography and light microscopy on shielding pigments of Clunio larval ocelli”. In: *Journal of Instrumentation* 13.07 (2018), p. C07001.

Maik Kahnt, Gerald Falkenberg, Jan Garrevoet, Jana Hartmann, Thilo Krause, Michael Niehle, Scholz, Maria, Martin Seyrich, Achim Trampert, Andreas Waag, et al. “Simultaneous hard X-ray ptychographic tomography and X-ray fluorescence tomography of isolated hollow core-shell GaN rods”. In: *Microscopy and Microanalysis* 24.S2 (2018), pp. 32–33.

Frank Seiboth, Felix Wittwer, Scholz, Maria, Maik Kahnt, Martin Seyrich, Andreas Schropp, Ulrich Wagner, Christoph Rau, Jan Garrevoet, Gerald Falkenberg, et al. “Nanofocusing with aberration-corrected rotationally parabolic refractive X-ray lenses”. In: *Journal of synchrotron radiation* 25.1 (2018), pp. 108–115.

Felix Wittwer, Robert Hoppe, Frank Seiboth, Juliane Reinhardt, Scholz, Maria, and Christian G Schroer. “Ptychography with a Virtually Enlarged Illumination”. In: *Microscopy and Microanalysis* 24.S2 (2018), pp. 46–47.

Jens Patommel, Susanne Klare, Robert Hoppe, Stephan Ritter, Dirk Samberg, Felix Wittwer, Andreas Jahn, Karola Richter, Christian Wenzel, Johann W. Bartha, Scholz, Maria, Frank Seiboth, Ulrike Boesenberg, Gerald Falkenberg, and Christian G. Schroer. “Focusing hard x rays beyond the critical angle of total reflection by adiabatically focusing lenses”. In: *Applied Physics Letters* 110.10 (2017), p. 101103.

Christian G Schroer, Martin Seyrich, Maik Kahnt, Stephan Botta, Ralph Döhrmann, Gerald Falkenberg, Jan Garrevoet, Mikhail Lyubomirskiy, Scholz, Maria, Andreas Schropp, et al. “PtyNAMi: ptychographic nano-analytical microscope at PETRA III: interferometrically tracking positions for 3D x-ray scanning microscopy using a ball-lens retroreflector”. In: *X-Ray Nanoimaging: Instruments and Methods III*. Vol. 10389. International Society for Optics and Photonics. 2017, 103890E.

Frank Seiboth, Andreas Schropp, Scholz, Maria, Felix Wittwer, Christian Rödel, Martin Wünsche, Tobias Ullsperger, Stefan Nolte, Jussi Rahomäki, Karolis Parfeniukas, et al. “Aberration correction for hard x-ray focusing at the nanoscale”. In: *Advances in X-Ray/EUV Optics and Components XII*. Vol. 10386. International Society for Optics and Photonics. 2017, 103860A.

Frank Seiboth, Andreas Schropp, Scholz, Maria, Felix Wittwer, Christian Rödel, Martin Wünsche, Tobias Ullsperger, Stefan Nolte, Jussi Rahomäki, Karolis Parfeniukas, et al. “Perfect X-ray focusing via fitting corrective glasses to aberrated optics”. In: *Nature Communications* 8.1 (2017), pp. 1–5.

Sina Baier, Christian D. Damsgaard, Scholz, Maria, Federico Benzi, Amélie Rochet, Robert Hoppe, Torsten Scherer, Junjie Shi, Arne Wittstock, Britta Weinhausen, et al. “In situ ptychography of heterogeneous catalysts using hard x-rays: High resolution imaging at ambient pressure and elevated temperature”. In: *Microscopy and Microanalysis* 22.1 (2016), pp. 178–188.

Sina Baier, Christian Danvad Damsgaard, Juliane Reinhardt, M. Klumpp, Federico Benzi, Scholz, Maria, Thomas Sheppard, Zoltan Imre Balogh, Takeshi Kasama, Jakob Birkedal Wagner, et al. “Studying a bifunctional Cu/ZnO-zeolite catalyst for direct production of dimethyl ether with in situ ptychography and ETEM”. In: *17th Nordic Symposium on Catalysis 2016: Surface science and catalysis for sustainable development and the use of large scale facilities for catalysis research*. 2016.

Christian G. Schroer, Christoph Baumbach, Ralph Döhrmann, Susanne Klare, Robert Hoppe, Maik Kahnt, Jens Patommel, Juliane Reinhardt, Stephan Ritter, Dirk Samberg, Scholz, Maria, Andreas Schropp, Frank Seiboth, Martin Seyrich, Felix Wittwer, and G. Falkenberg. “Hard x-ray nanoprobe of beamline P06 at PETRA III”. In: *AIP conference proceedings*. Vol. 1741. 1. AIP Publishing LLC. 2016, p. 030007.

Frank Seiboth, Maik Kahnt, Scholz, Maria, Martin Seyrich, Felix Wittwer, Jan Garrevoet, Gerald Falkenberg, Andreas Schropp, and Christian G. Schroer. “Quantitative characterization of aberrations in x-ray optics”. In: *Advances in X-Ray/EUV Optics and Components XI*. Vol. 9963. International Society for Optics and Photonics. 2016, 99630P.

Sina Baier, Federico Benzi, Amélie Rochet, Scholz, Maria, Robert Hoppe, Junjie Shi, Arne Wittstock, M. Bäumer, Christian Danvad Damsgaard, Christian G. Schroer, et al. “In situ ptychography during the annealing treatment of heterogeneous nanoporous gold catalysts”. In: *5th International Congress on Operando Spectroscopy*. 2015.

Frank Seiboth, Scholz, Maria, Jens Patommel, Robert Hoppe, Felix Wittwer, Juliane Reinhardt, Jens Seidel, M. Knaut, Andreas Jahn, K. Richter, et al. “Hard x-ray nanofocusing by refractive lenses of constant thickness”. In: *Applied Physics Letters* 105.13 (2014), p. 131110.

Danksagung – Acknowledgement

Seit Juni 2014 bin ich für meine Promotion in Hamburg und am DESY. Diese in vielfacher Hinsicht interessante Zeit ließ mich persönlich und mein Wissen wachsen. Ich blicke gern auf all die Erfahrung durch die verschiedenen Messzeiten, zum Teil verbunden mit Dienstreisen und dem Kennenlernen neuer Menschen und Orte, sowie verschiedenen Herausforderungen im Laufe des Doktorandendaseins zurück.

Als allererstes danke ich meinem Doktorvater Prof. Dr. Christian G. Schroer für die Möglichkeit, in seiner Gruppe dieses Projekt durchzuführen, für die interessanten Themen ebenso wie für die spontane Alternative zum ursprünglichen Thema kurz vor Start der entscheidenden Messzeit und das schier unerschöpfliche Wissen, das er immer gern mit uns teilt. Außerdem danke ich Christian dafür, dass er sich stets seine positive und unterstützende Haltung bewahrt und uns in dem gelegentlichen Gedankenchaos den Wind aus den Segeln nimmt und uns sonst freie Hand in unserer Arbeit lässt.

Des Weiteren danke ich Dr. habil. Thomas Keller herzlich, nicht nur für die Übernahme des Zweitgutachtens, sondern auch für die Zusammenarbeit bei der Abbildung des Microchips mit dem Elektronenmikroskop und die zeitnahe Eintaktung mehrerer Präparations- und Abbildungsstunden am Elektronenmikroskop und FIB.

Insgesamt danke ich allen Prüfern in der Prüfungskommission, Prof. Dr. Daniela Pfannkuche, Prof. Dr. Dorota Koziej, Prof. Dr. Markus Drescher, und den zuvor genannten für die schnelle Bereitschaft, diese Aufgabe zu übernehmen und die freundliche Rückmeldung dazu.

Ein großer Dank richtet sich auch an meine früheren Kollegen von Infineon Technologies Dresden GmbH und Co. KG, Karsten Mai und Jakob Kriz für die Probe(n) und die Informationen darüber, deren Zeit und Antworten auf meine Fragen, sowie für die Kommentare zu meiner Arbeit. Ebenso danke ich in diesem Zusammenhang auch Eric Neubert, der dafür verantwortlich war, die Wafer nach meinen Wünschen vorzubereiten und mir zuzusenden.

Ohne unsere Ingenieure wäre jede Messzeit undenkbar und ihnen gilt daher großer Dank, egal ob durch langfristig geplante oder spontane Umsetzung unserer Wünsche. Vielen Dank für alle Vorbereitungen für das ursprünglich geplante Projekt – den Keil und Probenhalter für den ersten Laminographieaufbau – an Dirk Samberg, sowie für die Anpassung und Verbesserung an Stephan Botta. Ein wesentlicher Teil des aktuellen Aufbaus der P06 Nanoprobe wurde von Ralph Döhrmann geplant und geleitet. Bei dem multimodalen Experiment hat Ralph innerhalb einer Woche alle notwendigen Änderungen, inlusive der Organisation und dem Einbau der Diode in einen Beamstop, umgesetzt. Vielen Dank.

Danke an die Beamline P06 Gruppe um Gerald Falkenberg für die vielen Möglichkeiten zusätzlicher Messzeit und all die Erfahrung an der Beamline, sowie die Unterstützung bei akuten Problemen, allen voran danke ich dabei Jan Garrevoet. Gerald gilt zudem noch der Dank, für die Einweisung in AXIL.

Ein herzlicher Dank gilt am Nanolab neben Thomas Keller auch Satishkumar Kulkarni. Mit Satish habe ich mehrere Tage am SEM und FIB verbracht um Querschnitte zu machen, abzubilden und auszumessen, sowie um Proben (nicht nur den Microchip) für Messungen am Synchrotron vorzubereiten.
Für das multimodale Experiment brauchten wir kurzerhand eine Referenzprobe, einen sogenannten Standard (CeO_2). Dieser wurde uns von der Gruppe um Hans-Peter Liermann zur Verfügung gestellt und wir bekamen in dem Zusammenhang auch die Programme und eine Einweisung in die Auswertung des Standards. Vielen Dank für diese schnelle, vorausschauende und unkomplizierte Hilfe.
Die Auswertung der XRD-Daten wäre ohne die umfangreiche Hilfe von Ulrich Lienert und Johan Hektor für die Grain Analyse sowie Martin Etter bezüglich der Pulveranalyse nicht oder nicht in dem Umfang möglich gewesen. Vielen Dank für die Einweisung in die Themen und Programme, die Unterstützung und den fachlichen Austausch.
Der größte Dank gilt meinen Kollegen Juliane Reinhardt, Maik Kahnt, Felix Wittwer, Martin Seyrich, Andreas Schropp und Johannes Hagemann, welche mir als Diskussionspartner, durch fachliche Hilfe (meist instantan), durchr ihre Ideen, aber auch im privaten Bereich – unter anderem mit Kaffee – wichtige Anker geworden und sehr ans Herz gewachsen sind. Ebendiese waren auch beim Gegenlesen der Arbeit unentbehrlich und haben dazu beigetragen, dass der Arbeit noch an manchen Stellen das i-Tüpfelchen aufgesetzt wurde.
Ich danke Juliane darüber hinaus für ihre Freundschaft, die vielen Frauengespräche im Büro in dem zeitweise stark männerdominierten Umfeld und für vieles mehr.
Ich danke auch Frank, der Juliane im Büro abgelöst hat, für die angenehme und unkomplizierte Art, das Büro zu teilen und die vielen Gespräche zur Kaffeezeit.
Während meiner Doktorarbeit haben Lukas Grote and Silvio Achilles zu Teilen meines Projekts ihre Masterarbeit geschrieben. Sie haben beide phantastische Arbeit geleistet und mit ihren Fragen und ihrer Zielstrebigkeit auch bei mir verschiedene Aspekte der Arbeit angeregt und vorangetrieben. Ich danke beiden für die Zusammenarbeit, die Unterstützung und die interessanten Fragen.
Ich danke all meinen Kollegen für die vielen Gespräche, Diskussionen, den Einblick in ihre Themen, gemeinsame Veranstaltungen, gemeinsame Essen, besonders dem vielen Käse, und vieles mehr. Dazu gehören, zu den bereits erwähnten, Mikhail Lyubomirskiy, Christina Ossig, Xiaogang Yang, Michael Stückelberger, Dennis Brückner, Saba Alizadeh, Samanehalsadat Ehteram, Peter Modregger und Patrick Willjes.
Für die vielen Stunden des schönsten Englisch, sowie für ihre immer gutmütige und ruhige Art danke ich Louise Kennedy von Herzen.
Vielen Dank an meinen André für seine Geduld, seine Unterstützung und die Ermöglichung etlicher Schreibnächte, so wie an meinen Edgar für den strikten zeitlichen Tagesablauf, die ausgleichende Ablenkung, vor allem durch sein sonniges Gemüt und die viele frische Luft.
Auch meiner Familie und meinen Freunden danke ich für das unerschöpfliche Vertrauen und die mentale Unterstützung.
Zuletzt danke ich allen, die in den letzten Jahren auf irgendeine Art zu dieser Arbeit beigetragen haben und die hier leider unbeabsichtigt unerwähnt blieben.

Eidesstattliche Versicherung / Declaration on Oath

Hiermit versichere ich an Eides statt, die vorliegende Dissertationsschrift selbst verfasst und keine anderen als die angegebenen Hilfsmittel und Quellen benutzt zu haben.

Die eingereichte schriftliche Fassung entspricht der auf dem elektronischen Speichermedium.

Die Dissertation wurde in der vorgelegten oder einer ähnlichen Form nicht schon einmal in einem früheren Promotionsverfahren angenommen oder als ungenügend beurteilt.

I hereby declare, in lieu of an oath, that I have written the present dissertation by my own and have not used other than the acknowledged resources and aids.

The written version is consistent with the one handed in electronically.

The dissertation has not been accepted in this or a comparable version in an earlier doctoral procedure or judged as insufficient.

Maria Scholz
Hamburg, December 22th, 2020